POLITECNICO
MILANO 1863

SCUOLA DI INGEGNERIA INDUSTRIALE
E DELL'INFORMAZIONE

Optimization of Multi-Impulse Earth–Moon Transfers in High-Fidelity Models

Tesi di Laurea Magistrale in
Space Engineering - Ingegneria Spaziale

Author: **Guido Grossi**

Student ID: 969103
Advisor: Francesco Topputo
Co-advisors: Dr. Carmine Giordano, Carmine Buonagura
Academic Year: 2022-23

Alle Persone che amo

e che mi amano

così come sono

Abstract

The Artemis program is just the beginning of a new era of lunar exploration, wherein mankind will not only be engaged in discovering new frontiers but also exploiting the resources from space. Within this framework, improving lunar transfer trajectories is a fundamental measure towards achieving more economical and efficient missions. Particularly, the aim of this thesis is to minimize the fuel consumption of Earth–Moon transfer trajectories in high-fidelity models, by means of a semi-analytical approach.
In the first part of the thesis, the possibility of reducing the fuel cost of two-impulse Earth–Moon transfers in a four-body model is addressed. Primer Vector theory is applied to identify which trajectories could benefit from the introduction of an additional intermediate impulse. Then, three-impulse transfers are computed with a direct numerical optimization method. Despite the majority of the trajectories being improved by a negligible amount, the cost of the transfers characterized by an initial gravity assist at the Moon is reduced by tens of m/s placing a corrective maneuver after the lunar encounter.
The second part of the thesis deals with the problem of continuing multi-impulse Earth–Moon transfers from a four-body model to a complete ephemeris-based model of the solar system, written in a rotopulsating frame. The innovative algorithm presented, based on a direct transcription and multiple shooting strategy, successfully transform in the real solar system different families of Earth–Moon trajectories. In particular, the focus is on ballistic low-energy Earth–Moon transfers, due to their numerous advantages. The methodology described is suitable for generating nominal trajectories for real missions starting from solutions obtained with simplified, but still meaningful, astrodynamical models.

Keywords: Space trajectory optimization · Earth–Moon transfers · Primer Vector theory · Four-body problem · Rotopulsating n-body problem · Low-energy transfers

Sommario

Il programma Artemis è solo l'inizio di una nuova era di esplorazione in cui l'umanità non solo si impegnerà a scoprire nuove frontiere, ma anche a sfruttare le risorse dello spazio. Di conseguenza, migliorare le traiettorie di trasferimento lunare è un passo fondamentale per la realizzazione di missioni spaziali sempre più economiche ed efficienti. In particolare, l'obiettivo di questa tesi è minimizzare il consumo di carburante di traiettorie lunari in modelli astrodinamici ad alta fedeltà, utilizzando un approccio semi-analitico.
Nella prima parte, si discute la possibilità di ridurre il consumo di carburante per trasferimenti Terra-Luna a due impulsi in un modello a quattro corpi. La teoria del Vettore Primo viene applicata per identificare quali traiettorie potrebbero beneficiare dell'introduzione di un ulteriore impulso. Successivamente, i trasferimenti a tre impulsi sono calcolati con un metodo di ottimizzazione numerica diretta. Nonostante la maggior parte delle traiettorie siano migliorate di un fattore trascurabile, il costo dei trasferimenti che sfruttano l'effetto fionda gravitazionale della Luna, è ridotto di decine di m/s inserendo una manovra correttiva successiva al sorvolo lunare.
La seconda parte della tesi affronta il problema della continuazione di trasferimenti lunari multi-impulso da un modello a quattro corpi ad uno completo del sistema solare, descritto dalle effemeridi in un sistema di riferimento rotopulsante. L'algoritmo presentato, basato su una strategia di trascrizione diretta e di shooting multiplo, adatta con successo diverse famiglie di traiettorie Terra–Luna nel sistema solare. In particolare, l'attenzione è posta sui trasferimenti balistici a bassa energia, dotati di numerosi vantaggi. La procedura descritta è atta a generare traiettorie nominali di missioni reali partendo da soluzioni ottenute in modelli astrodinamici semplificati, ma comunque significativi.

Parole chiave: Ottimizzazione di traiettorie spaziali · Trasferimenti Terra-Luna · Teoria del Vettore Primo · Problema dei quattro corpi · Problema degli n corpi · Trasferimenti a bassa energia

Contents

List of Figures

List of Theorems, Propositions and Problems

List of Tables

List of Algorithms

Acronyms

1 | Introduction

The history of lunar transfers is a rich and captivating story that has fascinated people for decades. The challenge of reaching the Moon has inspired generations of scientists, engineers, and space enthusiasts, and marked the first great step in space exploration. From the first successful robotic missions to the Moon in the late 1950s to the historic Apollo program and the recent resurgence of interest in lunar exploration, the story of lunar transfers is one of human achievement and exploration. The quest to explore and study the Moon has led to many technological advancements and scientific discoveries.
However, reaching the Moon still remains a difficult and costly task, and optimizing transfer trajectories is a crucial step towards making lunar exploration more accessible and sustainable. In the past, simplified models have been widely used to study the dynamics of the cislunar environment, and continue to play a crucial role in the preliminary phases of space missions. Nonetheless, with the increasing understanding of the solar system, it has become clear that these simplified models are inadequate for accurately planning complex missions. To address these limitations, more realistic models based on ephemerides have been developed. They opened up new avenues of research into more complex dynamics and trajectories that are not present in simplified models. The transition from easier formulations to more complete models is a crucial step in guaranteeing the success of future lunar missions, while also preserving the accumulated knowledge of the dynamics of the cislunar environment over time.
The focus of this thesis is to refine optimal lunar transfer trajectories in high-fidelity models using a semi-analytical approach and advanced optimization algorithms.

1.1. Context

Exploration of the Moon has been an area of interest for many years, with the Apollo missions paving the way for further study and research. Nowadays, the perspective on lunar missions has shifted, including not only scientific research and human exploration, but also resource utilization.

A cornerstone of this new era of lunar exploration is the Artemis program[1], led by NASA, which aims to land the first woman and the next man on the Moon by 2024. The primary goal of the program is to establish a sustainable human presence on the Moon and to develop new technologies that will enable future missions to explore deeper into the solar system. To achieve this, Artemis will leverage the Lunar Gateway[2], a small space station that will orbit the Moon and serve as a staging point for lunar landings and deep space exploration. The station will also serve as a platform for scientific research and technology demonstrations, facilitating international cooperation in space exploration.
One crucial factor for the incoming era of space utilization and exploration will be maximizing the payload mass of each transfer. The first approach to increase the useful mass consists in reducing the propulsion system requirements in terms of fuel. Therefore, finding optimal transfer trajectories is essential for maximizing the scientific and exploratory potential of future missions.

1.1.1. Earth to Moon Transfers

Several established techniques exist for transferring a spacecraft from a low Earth orbit (LEO) to a lunar orbit [10]. These include direct transfers, low-thrust transfers, and low-energy ballistic transfers. Direct transfers, such as those used in the Apollo program, have the advantage of a short transfer time (3-6 days) but require a high amount of fuel. A second class of transfers makes use of low-thrust propulsion to spiral away from the Earth and toward the Moon [33]. A low-thrust transfer involves employing engines that use fuel more efficiently but requires longer transfer times (many months) and complex mission design. Low-energy ballistic trajectories are also of great interest, as they offer a balance between the advantages and disadvantages of the first two methods: they require less fuel than a direct transfer and less time than a low-thrust transfer [48].
In an exterior low-energy transfer the spacecraft is injected into an orbit having the apogee at approximately four Earth–Moon distances. In this region, called weak stability boundary, the perturbation of the Sun can be exploited to approach the Moon from the exterior, and to perform a lunar ballistic capture [3–6, 11]. Specifically, the gravity gradient of the Sun can be used in a favorable way only when the orbit is properly oriented with respect to the Sun, the Earth, and the Moon [8, 12]. Many strategies have been studied to design low energy transfers [20, 49], and also some missions have already flight on these trajectories [2, 31, 57]. For example, Koon showed in [38] how it is possible using invariant manifold techniques to construct low energy transfer paths to the Moon.

[1] `https://www.nasa.gov/specials/artemis/`, retrieved on March 20, 2023.
[2] `https://www.nasa.gov/gateway/overview`, retrieved on March 20, 2023.

Also, the performances of the transfer can be improved by introducing a lunar gravity assist at departure [45, 55].
Since the discovery of low-energy transfers, the problem of finding alternative, efficient Earth–Moon transfers has been approached with a focus on a small class of solutions, typically compared only to the Hohmann transfer. Topputo in [62] answered the question on the existence of other solutions, possibly having intermediate features between the solution at hand and the Hohmann transfer. The paper succeeded in framing all these kinds of transfers and many others as special points of a more general picture. This global set of solutions for the two-impulse Earth–Moon transfers in a four-body model is the starting point for the first part of the thesis.

1.1.2. High-Fidelity Models and Trajectory Continuation

As space missions become more complex, the trajectory design must meet increasingly stringent requirements. Accordingly, high-fidelity models are employed in the early stages of trajectory design to exploit their unique features [19]. Moreover, as the complexity of such models increases, new solutions appear due to the richer content of the vector field and open up new scenarios for spacecraft characterized by very limited thrust authority (e.g., interplanetary CubeSats). The drawback is that no analytical solution is available, and consequently it is very difficult to have a general insight into the dynamics. Furthermore, they are less prone to the extensive computational searches which are usually required to design an optimal trajectory.
The most popular model for designing orbits in the cislunar environment is the restricted three-body model [61]. However, when the three-body orbits are reproduced in more comprehensive gravitational models, large errors emerge. Especially if orbits are defined in the regions of phase space where two main gravitational accelerations balance, the sensitivity is high and any additional perturbation produces large effects. The first extension to the three-body model is the four-body model, which accounts also for the perturbations of a fourth body [59, 67]. It was shown that this model is deemed appropriate to catch the basic dynamics characterizing the Sun–Earth–Moon problem [44, 62].
By the way, in turn, the mission will eventually have to fly in the real scenario. Hence, flying orbits must be studied, tested and validated in the real dynamics, that is the solar system n-body problem modeled through precise ephemeris data. Therefore continuation from simplified to more complex models is a critical step in trajectory design [18]. Gómez succeeded in describing the complete solar system dynamics in a co-rotating Earth–Moon system, which is a direct extension of the simplified models with three and four bodies [26]. Dei Tos in [17] established a clear hierarchy in the gravitational models available to

the designer, and shows that the equations for the spacecraft motion in simpler models can be readily obtained as particular cases of the most complete model. Additionally, the study proved that a gradual increase in the dynamics complexity benefits accuracy, the chances of success and the convergence rate of a continuation algorithm.

1.1.3. Trajectory Optimization

At its core, the optimization of spacecraft trajectories involves finding a trajectory that fulfills specified starting and ending conditions while accomplishing a given mission and minimizing a chosen significant factor. Typically, the primary goal is to reduce propellant usage or maximize the amount of the spacecraft not used for propellant. However, there are other scenarios where minimizing flight time is paramount or where minimizing both propellant usage and flight time are equivalent (e.g., low thrust trajectories).
Space trajectory optimization typically falls in the class of convoluted continuous optimization problems. The complexities involved are numerous, including [16]: nonlinear dynamical systems; potential discontinuities in state variables; unclear explicit knowledge of terminal conditions; presence of time-dependent forces; fundamental structure of the optimal trajectory unknown a priori.
In addition, as there exist various kinds of spacecraft trajectories (such as those propelled impulsively with chemical rockets or those with low-thrust electric propulsion) distinct solution methods must be explored, that are best suited to the unique characteristics of each trajectory [41]. For instance, impulsive transfer scenarios, even including flybys, are frequently translated into a parameter optimization problem. Conversely, continuous thrust situations require an optimal control approach, as both the thrust magnitude and direction have time histories that are continuous and must be modeled and determined.
The calculus of variations can be used to derive some necessary optimality conditions for each type of spacecraft trajectory optimization problem. Unfortunately, solving the resulting system of equations and boundary conditions is usually difficult or even impossible. For certain simplified but still valuable cases of either impulsive-thrust or continuous-thrust transfers, analytical necessary conditions can be described using Primer Vector theory. This was first formulated by Lawden [39], then Lion extended the definition of the primer vector to include nonoptimal trajectory [40], and Jezewski showed under which conditions an optimal impulsive trajectory could be improved by the addition of another impulse or by allowing a terminal coast [37].

Nonetheless, the vast majority of researchers today use numerical optimization, which, for continuous optimal control problems, can be generally classified into two types:

- **Indirect solutions** use the analytical necessary conditions from the calculus of variations, requiring the addition of costate variables equal in number to the state variables, and their governing equations. This doubles the size of the dynamical system, making it more challenging to solve. Other drawbacks include: optimality conditions must be analytically derived for each problem; the domain of convergence is small; construction of an initial guess solution may not be intuitive.
- **Direct solutions**, on the other hand, convert the continuous optimal control problem into a parameter optimization problem. To satisfy the system equations, the parameters are integrated stepwise using either implicit or explicit rules. This generates nonlinear constraint equations that must be fulfilled by the parameters, which are the discrete representations of the state and control time histories. The problem is thus transformed into a nonlinear programming (NLP) problem. The method is relatively robust and simpler for implementation. Nonetheless, a disadvantage can originate from the definition of an objective function. Indeed, NLP solvers utilize the gradient of the objective function with respect to NLP variables and its computation would fail when the derivatives face a singularity.

Although Betts presents in [9] a comprehensive survey on the relationship and evolution of both direct and indirect optimization, it should be noted that significant advancements have been made in direct numerical solutions for optimal control problems. One such approach that has become popular is the use of evolutionary algorithms (e.g., genetic algorithms and Particle Swarm Optimizer) which offers a qualitatively different solution to these problems [50]. Additionally, progress has been made in analytical solutions, including "shape-based" trajectories [64].

1.2. Motivations

Optimizing lunar transfer trajectories is a crucial step towards enabling more efficient and cost-effective lunar missions. The Artemis program and the Lunar Gateway are just the beginning of a new era of lunar exploration, wherein mankind will not only be engaged in discovering new frontiers but also exploiting the resources from space. The ultimate aim of this thesis is to contribute to the development of new and improved methods for designing optimal lunar transfers in high-fidelity models and to profit from their complex dynamics to get unique trajectories.

1.2.1. Research Questions

The first part of the work focuses on refining the rich database of two-impulse lunar transfers built up by Topputo in [62]. Indeed, these trajectories were obtained using a direct method, so the local optimality of each solution was proved only from a numerical viewpoint and against the same class of transfers. This last is actually a crucial point, and it is reasonable to think that enlarging the class of solutions should bring benefits in terms of fuel-efficiency. For instance, if some necessary conditions suggest that an additional maneuver could lower the overall cost of a transfer, then the two-impulse solution is no more optimal. For this reason, Lawden's Primer Vector theory is used to develop this kind of necessary conditions, which are applied together with a direct optimization method to obtain optimal three-impulse transfers.
All in all, the first part of this work aims to answer the following research question:

Research Question I:

To what extent does the addition of a midcourse-impulse through a semi-analytical approach can bring improvements to the global picture of two-impulse Earth–Moon transfers in a four-body model?

In order to give a proper answer, some intermediate steps should be covered:

1. Use an analytical approach (i.e., Primer Vector theory) to develop a set of first-order optimality necessary conditions for a lunar transfer in the four-body model;
2. Check whether each solution from the database of two-impulse transfers satisfies the previous necessary conditions;
3. Built an automated process able to refine sub-optimal solutions by adding a mid-course impulse, such that the final three-impulse trajectory is more cost-effective.

The second part of the thesis concerns the use of a high-fidelity ephemeris-based model of the solar system written in a rotopulsating Earth–Moon frame. The aim is to design an algorithm that transforms the multi-impulse transfers from the four-body model to an n-body model, retaining as far as possible their particular geometrical features. Given the unique advantages offered by exterior low-energy transfers, the focus of this second part is mainly on this particular family (see Fig. 1.1a). Moreover, here the perturbation of the Sun plays a more relevant role with respect to interior ones, where most of the trajectory is defined within the Moon orbit, and the solar effect is not crucial (Fig. 1.1b). Thus, the transition between the two paradigms wherein Sun's effects are modeled differently is expected to be more challenging and impactful on the final solution.

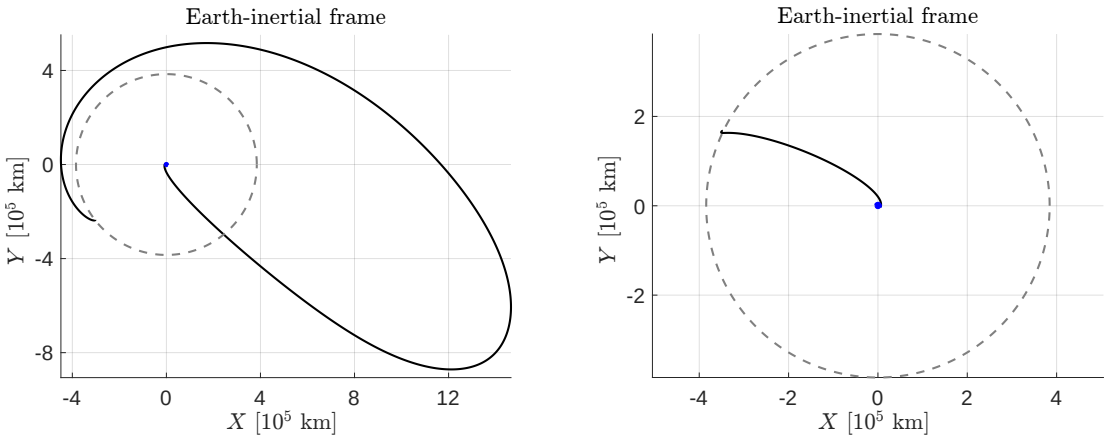

(a) Exterior transfer (b) Interior transfer

Figure 1.1: Sample solutions of exterior and interior Earth–Moon transfers in a restricted four-body model. The trajectories are represented in an inertial, Earth-centered, reference frame, and the Moon's orbit is depicted with a gray, dashed line

The second research question can be resumed in:

Research Question II:

How does an impulsive low-energy Earth–Moon transfer can be designed in an ephemeris-based model of the solar system, starting from a trajectory in a simplified four-body model?

Again, some intermediate steps are necessarily embedded:

1. Define the new boundary conditions for the transfer in the real solar system;
2. Analyze the main differences between the two models and exploit their similarities to get a reliable initial seed orbit;
3. Built an algorithm to import the geometry of the four-body trajectory to a more complete model;
4. Refine automatically the trajectory until a desired feasible transfer is achieved and the fuel consumption is locally minimized.

1.2.2. Expected Results

The expected result of Part I is to provide an updated global picture of optimal multi-impulse Earth–Moon transfers in a four-body model, and to asses in which families of trajectories the addition of a third impulse is beneficial for the total cost of the mission.

Concerning Part II, the final aim is to design an algorithm that takes a trajectory from the four-body model, and returns a similar transfer in the most complete astrodynamical model, based on real ephemerides.

1.3. Structure of the Thesis

The thesis is divided into two parts: the first is devoted to the application of the primer vector theory to impulsive Earth–Moon transfer in a four-body model, whilst the second concerns the continuation of multi-impulse trajectories from the four-body model to a full-ephemeris model of the solar system. If the first part is intended to have a more theoretical orientation, dealing with basic research, the second part is more geared towards practical real-world application.

Part I

Chapter 2 deals with the detailed description of the Planar Bicircular Four Body Problem. Subsequently, the reference two-impulse Earth–Moon transfers are defined and classified. Finally, Lawden's Primer Vector theory is recalled and adapted to a four-body model.

Chapter 3 presents the methodology used to reduce the cost of two-impulse Earth–Moon transfers with an additional midcourse impulse. Two main phases are individuated: the construction of a perturbed trajectory with the addition of the midcourse impulse, and the iterative refinement of this last until a local minimum of the cost function is achieved.

Chapter 4 discusses how the methodology is implemented within a numerical framework, and shows the results obtained. Importance is given to the flexibility and efficiency of the algorithm, which must optimize thousands of different transfers in an automatic fashion.

Part II

Chapter 5 introduces a high-fidelity ephemeris-based model of the solar system and shifts the focus to low-energy Earth–Moon transfers, describing their main features.

Chapter 6 gives a definition of the trajectory continuation problem and describes the original methodology used to obtain an initial seed orbit in the n-body model. Subsequently, an automated procedure refines the initial guess solution until a feasible transfer is found.

Chapter 7 deals with the numerical implementation and solution to the continuation problem. Some final trajectories in the real solar system are shown and discussed, with emphasis on low-energy transfers.

Chapter 8 concludes the thesis with a summary of the results. Critical evaluation is provided for the adopted strategies and some hints for further developments are given.

1.4. Conventions

For clarity, the conventions used in the thesis are listed in this remainder.

- **Scalar quantities** are in italic and lower or upper case letters (e.g., m or M). Barred letters (e.g., $\overline{T}$) are used for mean values and reference quantities.
- **Vectors and matrices:** vectors (and vectorial functions) are assembled column-wise and are written in bold and lower case letters (e.g., $\mathbf{r}$). Upper case bold letters are used only for vectorial quantities view from an inertial system (e.g., $\mathbf{R}$). Matrices are indicated with capital letters (e.g., A).
- **Vectorial operations:** vectorial scalar product is indicated either transposing the first vector (e.g., $\mathbf{r}^\top\mathbf{v}$) or using the symbol '$\cdot$'. Vectorial cross product is indicated by '$\times$'. Euclidean vectorial norm (2-norm) is denoted as $\|\cdot\|$.
- **Special matrices:** the identity matrix and null matrix of dimensions $(n \times n)$ are denoted as I_n and 0_n, respectively.
- **Derivatives:** conventional time derivatives are indicated by dots (e.g., $\dot{k}$, $\ddot{k}$). Derivatives of column-vectors with respect to scalars are organized in row-vectors (e.g., $\mathbf{v}^\top = \mathrm{d}\mathbf{x}/\mathrm{d}t$). Accordingly, gradient matrices are assembled row-wise.
- **Class of functions:** the class of continuous real functions is indicated by $\mathcal{C}[\cdot]$, where the domain of the function might be specified between parentheses. $\mathcal{C}^1$ and $\hat{\mathcal{C}}$ are used for continuously differentiable and piecewise continuous functions, respectively.

1.5. Hardware and Software Specifications

Data processing and implementations are performed using the commercial software Matlab® by MathWorks, version Matlab 2022b. Precise data about the celestial bodies are retrieved from the planetary and lunar ephemerides DE432 of the JPL [21]. Access to these is provided through the JPL's SPICE toolkit [1].
Serial calculations are carried out on a MacBookPro (2017), with macOS 13.2.1 operating system and powered by an Intel® Core i7 quad-core CPU @2.90 GHz with 16 GB of RAM. Parallel computations are run on a Dell XPS 9550 with Windows 10 Pro 22H2 and powered by an Intel® Core i7 quad-core CPU @2.60 GHz with 32 GB of RAM.

Part I

Impulsive Earth–Moon Transfers in a Four-Body Model

2 | Background

In this second chapter, the main peculiarities of the Planar Bicircular Restricted Four Body Problem are reviewed. Then, Earth–Moon transfers in the planar bicircular restricted four-body model are defined. Finally, the Primer Vector Theory is recalled and applied to derive the analytical conditions for the optimality of a trajectory.

2.1. Planar Bicircular Restricted Four Body Problem

In the hierarchy of the astrodynamical models, the Planar Bicircular Restricted Four-Body Problem (PBRFBP) occupies a medium position on a scale of complexity and fidelity. The bicircular problem is a simplified version of the restricted four-body problem. This model is used to describe the motion of a maleness particle under the gravitational attraction of the Earth, Moon and Sun, whose orbits are assumed to be circular. Many of its characteristics are inherited from the Circular Restricted Three Body Problem, to which the perturbations of the Sun is superposed. In this section, the geometry of the model is outlined, together with the equations of motion.

2.1.1. Geometry of the Model

In the paradigm of the PBRFBP, there are two celestial bodies that move under their mutual gravity on co-planar circular orbits about their common center of mass. These two *primaries*, P_1 and P_2, with masses $M_1 > M_2$, rotates counterclockwise with a constant angular velocity ω. On the same plane, the model also incorporates the periodic perturbation of a third celestial body, P_3, that is assumed to revolve in a circular orbit around the center of mass of the primaries. In the present case, P_1 represents the Earth, P_2 the Moon and P_3 the Sun. All these three are assumed to be point masses and to possess spherically symmetric gravity fields. The last body, P, represents the spacecraft (SC) and moves under the gravity of the other three bodies. In reason of the large difference between the masses of the probe and the celestial bodies, the problem is *restricted*: the infinitesimal mass of P does not affect the motions of the other bodies. The geometry of the problem is depicted in Fig. 2.1, where evidently neither the distances between the

bodies nor their sizes are to scale. Despite the model is not coherent, i.e., the motion does not satisfy Newton's equations, it catches the insights of the real four-body dynamics [59] and it allows to design some particular orbits, such as low-energy transfers [67]. The reason why, is that the previous assumptions are actually well justified, since they represent a good approximation of the real environment. In fact, the eccentricities of the Earth and Moon orbits are 0.0167 and 0.0549, respectively, and the Moon orbit inclination on the ecliptic is about 5 deg.

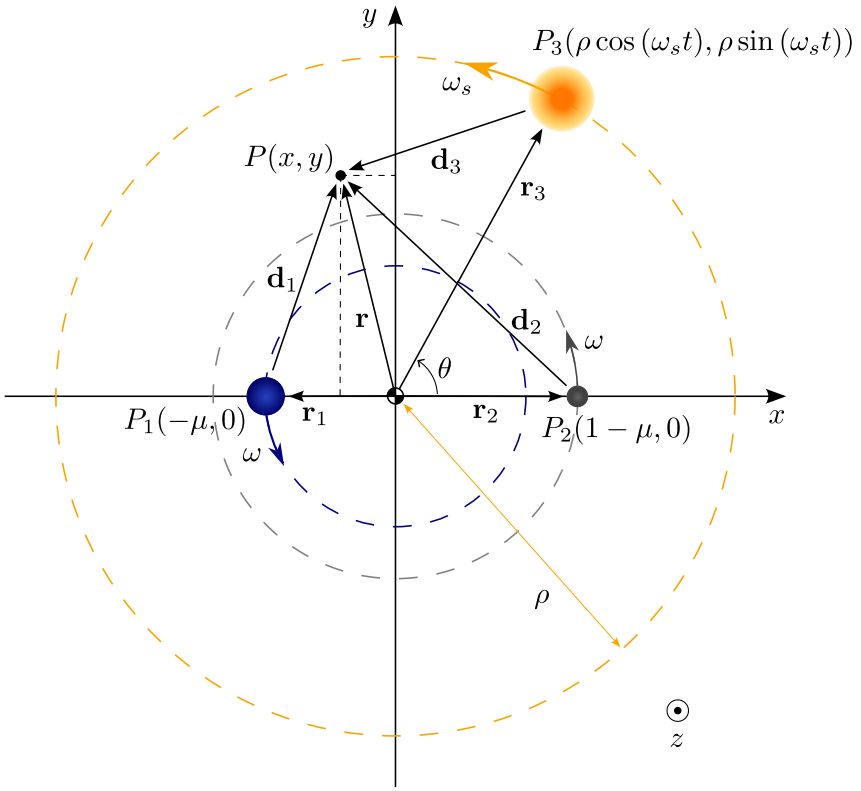

Figure 2.1: Geometry of the PBRFBP in rotating Earth–Moon coordinates, drawing not to scale; here a positive ω_S is represented, but for the Earth–Moon–Sun system its value is negative (see Table 1)

2.1.2. Nondimensionalization

A nondimensional formulation of the problem accomplishes both the generalization of results to any primary system and the simplification of subsequent mathematical developments [35]. A characteristic value is assigned to each one of the basic quantities of the problem: length, mass and time. The reference length $\overline{L}$ is set equal to ℓ_{EM}, the mean distance between the two primaries, and the characteristic mass $\overline{M}$ is selected as the sum

of M_1 and M_2. The nondimensional time is chosen as

$$\overline{T} = \sqrt{\frac{{\ell_{\mathrm{EM}}}^3}{G\left(M_1 + M_2\right)}} = \sqrt{\frac{\overline{L}^3}{G\overline{M}}} \ . \tag{2.1}$$

G is the universal gravitational constant, and from Eq. (2.1), its nondimensional value is unity. Moreover, from Kepler's equation, the mean motion ω_{EM} of the primaries is

$$\omega_{\mathrm{EM}} = \sqrt{\frac{G\left(M_1 + M_2\right)}{{\ell_{\mathrm{EM}}}^3}} \ . \tag{2.2}$$

Note that ω_{EM} coincides with the angular velocity of the synodic reference frame. As the nondimensional value of G, ℓ_{EM} and $M_1 + M_2$ is one, ω, the nondimensional counterpart of ω_{EM}, inherits a unitary value. Also, let define the mass ratio of P_2 to the total mass of the two primaries as the mass-ratio parameter of the problem:

$$\mu \equiv \frac{M_2}{M_1 + M_2} \ . \tag{2.3}$$

It follows that the nondimensional masses of the primaries can be written as

$$m_1 = 1 - \mu \ , \tag{2.4a}$$

$$m_2 = \mu \ . \tag{2.4b}$$

The main consequence of this formulation is the advantage of having the Earth and the Moon at two fixed points on the rotating x-axis, at nondimensional coordinates $(-\mu,\, 0)$ for the Earth and $(1 - \mu,\, 0)$ for the Moon (see Fig. 2.1).
Concerning the third body P_3, its orbital radius ρ is a mean value of the distance between the Sun and the Earth–Moon barycenter. Its mean angular velocity ω_S relative to the rotating frame is negative, so it rotates clockwise, and the Sun's angle with respect to the x-axis is denoted as $\theta = \omega_S t$.

The values of the physical quantities used in this study are taken from [59], and are collected in Table 1, together with the associated units of distance, time, mass and velocity (this last defined as $\overline{V} = \overline{L}/\overline{T}$).

Table 1: Physical and characteristic quantities used in the PBRFBP

Symbol	Value	Units	Meaning
μ	$1.21506683 \times 10^{-2}$	-	Earth–Moon mass parameter
m_S	3.28900541×10^{5}	-	Scaled mass of the Sun*
ρ	3.88811143×10^{5}	-	Scaled Sun–(Earth–Moon) distance*
ω_S	$-9.25195985 \times 10^{-1}$	-	Scaled angular velocity of the Sun*
ℓ_{EM}	3.84405000×10^{5}	km	Mean Earth–Moon distance
ω_{EM}	$2.66186135 \times 10^{-6}$	s^{-1}	Mean Earth–Moon angular velocity
$\overline{L}$	3.84405000×10^{5}	km	Reference distance
$\overline{M}$	$6.04765089 \times 10^{24}$	kg	Reference mass
$\overline{T}$	4.34811305	days	Reference time
$\overline{V}$	1.02323281	km s $^{-1}$	Reference velocity

* The constants used to describe the Sun perturbation meet the length, time, and mass normalization of the PBRFBP

2.1.3. Coordinate Systems

An advantageous frame for describing the motion of P rotates together with the two primaries. Nonetheless, sometimes also an inertial frame is needed. These coordinate systems are defined hereafter.

Synodic Frame

A co-rotating coordinate system $(\boldsymbol{x}, \boldsymbol{y}, \boldsymbol{z})$ can be adopted to describe the motion of P. This reference frame has its origin at the center of mass of the Earth–Moon system. The x-axis is parallel to the line joining the two primaries and is directed from the barycenter to P_2. The z-axis is perpendicular to the plane of motion of the primaries. Finally, the y-axis completes the right-handed trial. As the frame rotates with an angular velocity equal to that of the Earth–Moon system, it is also called *synodic*.

Sidereal Frame

For the subsequent discussion, it is useful also to introduce a frame that does not rotate and is centered in one of the two primaries. Actually, two inertial coordinate systems $(\boldsymbol{X}_1, \boldsymbol{Y}_1, \boldsymbol{Z}_1)$ and $(\boldsymbol{X}_2, \boldsymbol{Y}_2, \boldsymbol{Z}_2)$, called *sidereal* frames, are defined. The origin is either the Earth P_1 or the Moon P_2, while the directions of the axes are fixed, and coincide with those of the synodic frame at the time $t = 0$ (see Fig. 2.2).

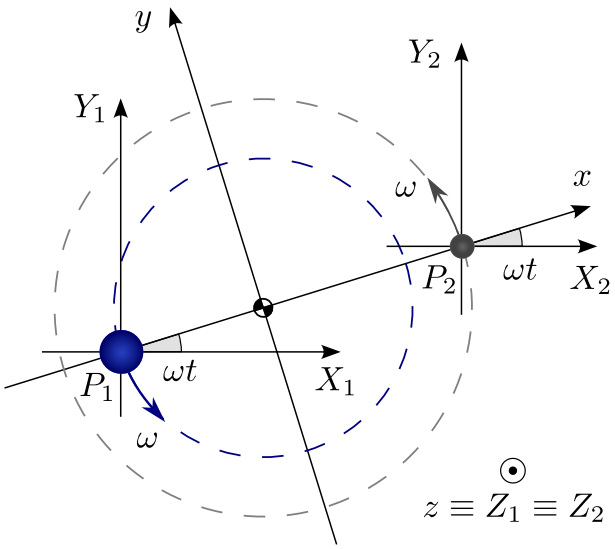

Figure 2.2: Synodic $(\boldsymbol{x}, \boldsymbol{y}, \boldsymbol{z})$ and sidereal $(\boldsymbol{X}_1, \boldsymbol{Y}_1, \boldsymbol{Z}_1)$, $(\boldsymbol{X}_2, \boldsymbol{Y}_2, \boldsymbol{Z}_2)$ coordinate systems

Coordinate Transformation

Let $(x, y, \dot{x}, \dot{y})$ be the nondimensional position and velocity of P in the synodic frame[1]. The position in the P_1-centered sidereal frame is obtained by subtracting the coordinates of the Earth from those of P, and by applying the following rotation matrix (remember that the dimensionless angular velocity is ω is unitary)

$$C = \begin{bmatrix} \cos t & -\sin t & 0 \\ \sin t & \cos t & 0 \\ 0 & 0 & 1 \end{bmatrix} . \tag{2.5}$$

As a consequence, the corresponding state $(X_1, Y_1, \dot{X}_1, \dot{Y}_1)$ is

$$\begin{aligned} X_1(t) &= (x(t) + \mu)\cos t - y(t)\sin t \ , \\ Y_1(t) &= (x(t) + \mu)\sin t + y(t)\cos t \ , \\ \dot{X}_1(t) &= (\dot{x}(t) - y(t))\cos t - (\dot{y}(t) + x(t) + \mu)\sin t \ , \\ \dot{Y}_1(t) &= (\dot{x}(t) - y(t))\sin t + (\dot{y}(t) + x(t) + \mu)\cos t \ ; \end{aligned} \tag{2.6}$$

where t is the present, scaled time and the last two equations are the time derivatives of the first two. The transformation into the P_2-centered inertial frame is attained from Eq. (2.6) by replacing 'μ' with '$\mu - 1$'.

[1]The third coordinate z and its derivative $\dot{z}$ are not considered due to the planar nature of the model.

2.1.4. Equations of Motion

The complete derivation of the equations of motion through a Newtonian formalism in the absence of the perturbation of the Sun, so for the Planar Circular Restricted Three-Body Problem (PCRTBP), can be found in [61]. Indeed, this is the starting point also for the case of four bodies, to which the perturbation of the Sun is added.
According to [62, 67], the set of two, second-order, scalar, differential equations describing the motion of a massless particle in the PBRFBP are

$$\begin{cases} \ddot{x} - 2\dot{y} = \dfrac{\partial \Omega}{\partial x} & \text{(2.7a)} \\ \ddot{y} + 2\dot{x} = \dfrac{\partial \Omega}{\partial y} & \text{(2.7b)} \end{cases}$$

where Ω is a pseudo-potential of the model, defined as

$$\Omega(x, y, t) := \frac{1}{2}\left(x^2 + y^2\right) + \frac{1-\mu}{d_1} + \frac{\mu}{d_2} + \frac{1}{2}\mu\left(1-\mu\right) + \frac{m_S}{d_3} - \frac{m_S}{\rho^2}\left(x\cos\left(\omega_S t\right) + y\sin\left(\omega_S t\right)\right) \ . \quad (2.8)$$

Moreover, the distances of P from P_1 and P_2 are, respectively,

$$d_1(t) = \sqrt{\left(x(t)+\mu\right)^2 + y(t)^2} \ , \quad (2.9)$$

$$d_2(t) = \sqrt{\left(x(t)+\mu-1\right)^2 + y(t)^2} \ . \quad (2.10)$$

Instead, differently from the two primaries, the present location of the Sun is time-dependent, $P_3 = (\rho\cos(\omega_S t), \rho\sin(\omega_S t))$, and therefore the Sun-spacecraft distance is

$$d_3(t) = \sqrt{\left(x(t) - \rho\cos(\omega_S t)\right)^2 + \left(y(t) - \rho\sin(\omega_S t)\right)^2} \ . \quad (2.11)$$

Let the state vector of P in dimensionless rotating coordinates be

$$\mathbf{x}(t) \equiv \left(\mathbf{r}(t), \mathbf{v}(t)\right)^\top = \left(x(t), y(t), \dot{x}(t), \dot{y}(t)\right)^\top \ , \quad (2.12)$$

where $\mathbf{r}(t)$ is the SC position vector and $\mathbf{v}(t)$ is its velocity vector. For the subsequent analysis, it is convenient to express Eq. (2.7) in a first order form

$$\dot{\mathbf{x}}(t) \equiv \begin{bmatrix} \dot{\mathbf{r}}(t) \\ \dot{\mathbf{v}}(t) \end{bmatrix} = \begin{bmatrix} \mathbf{v}(t) \\ \mathbf{g}(\mathbf{x}, t) \end{bmatrix} ; \quad (2.13)$$

where the *coastal acceleration* $\mathbf{g}$ is defined as

$$\mathbf{g}(\mathbf{x}, t) \equiv \begin{bmatrix} +2\dot{y} + \dfrac{\partial \Omega}{\partial x} \\ -2\dot{x} + \dfrac{\partial \Omega}{\partial y} \end{bmatrix}, \tag{2.14}$$

and contains both the gravitational acceleration as well as the terms due to the relative motion of the rotating frame with respect to an inertial one. The partial derivatives of Ω with respect to x and y are computed analytically; they are not reported here for conciseness but they can be found in appendix A.1. The dynamics may be written also with a general and compact notation

$$\dot{\mathbf{x}} = \mathbf{f}_4(\mathbf{x}, t) \ , \tag{2.15}$$

where the subscript indicates the number of bodies taken into account by the model. Even though Eq. (2.15) does not possess an analytical solution, the system can be integrated numerically. Provided an initial condition of the states $\mathbf{x}_i = (\mathbf{r}_i, \mathbf{v}_i)^\top$ at a time t_i, the flow of the PBRFBP, i.e., the solution of Eq. (2.7), is indicated by $\varphi(\mathbf{x}_i, t_i; t)$[2].

Before continuing, some remarks can be done. First of all, one notes that, even if the potential forces of the model are functions only of the position (gravitational forces), the acceleration $\mathbf{g}$ depends on the velocity due to the non-inertial nature of the synodic frame. Secondly, being the Sun not at rest in the reference frame adopted, the autonomy of the problem is lost, and thus the PBRFBP becomes a time-dependent model. Finally, regarding Ω, it is worth noticing that the perturbations due to the Sun represent a great departure from the PCRTBP as both the equilibrium points and the Jacobi integral that were present in the three-body model vanish [62].

2.1.5. Variational Equations

The variational equations are associated with the equations of motion. They express a sensitivity analysis of how the final integrated state can have a variation caused by little perturbations on the initial state. In particular, the state transition matrix (STM) is a key result which provides fast and accurate (up to the first-order) information on how the system responds to changes in the initial conditions. Indeed, differential information is of paramount importance for convergence and numerical efficiency of optimization processes. Also, the STM will play a relevant role in the Primer Vector theory.

[2] In the second part of the thesis the symbol φ_4 is used to distinguish from the flows of other models.

Consider a reference trajectory $\overline{\mathbf{x}}(t) = \varphi(\overline{\mathbf{x}}_i, t_i; t)$. The variational analysis aims to study the behavior of the state $\mathbf{x}(t)$ when a small perturbation $\delta\mathbf{x}_i$ is applied to the initial condition $\overline{\mathbf{x}}_i$. The new trajectory $\mathbf{x}(t)$ will deviate from the reference one by a quantity $\delta\mathbf{x}(t)$, so it can be expressed as

$$\mathbf{x}(t) = \overline{\mathbf{x}}(t) + \delta\mathbf{x}(t) = \varphi(\overline{\mathbf{x}}_i + \delta\mathbf{x}_i, t_i; t) \ . \tag{2.16}$$

If $\overline{\mathbf{x}}(t)$ and $\mathbf{x}(t)$ are sufficiently close such that a linear analysis is justified, substituting in Eq. (2.16) the first order expansion of φ with respect to $\delta\mathbf{x}_i$ leads to

$$\delta\mathbf{x}(t) = \frac{\partial\varphi}{\partial\mathbf{x}_i}(\overline{\mathbf{x}}_i, t_i; t)\, \delta\mathbf{x}_i \ . \tag{2.17}$$

Equation (2.17) is often written in terms of the *state transition matrix*:

$$\delta\mathbf{x}(t) = \Phi(t_i, t)\, \delta\mathbf{x}_i \ , \tag{2.18}$$

where each element $\Phi(t_i, t)$ represents the variation of a final state due to a change in one of the initial states. Thus, by definition, the STM is the jacobian of the flow:

$$\Phi(t_i, t) \equiv \frac{\partial\varphi}{\partial\mathbf{x}_i}(\overline{\mathbf{x}}_i, t_i; t) \ . \tag{2.19}$$

Sometimes it may be useful to partition the STM into four blocks

$$\Phi(t_i, t) = \begin{bmatrix} \Phi_{rr}(t_i, t) & \Phi_{rv}(t_i, t) \\ \\ \Phi_{vr}(t_i, t) & \Phi_{vv}(t_i, t) \end{bmatrix} = \begin{bmatrix} \dfrac{\partial\varphi_r}{\partial\mathbf{r}_i}(\overline{\mathbf{x}}_i, t_i; t) & \dfrac{\partial\varphi_r}{\partial\mathbf{v}_i}(\overline{\mathbf{x}}_i, t_i; t) \\ \dfrac{\partial\varphi_v}{\partial\mathbf{r}_i}(\overline{\mathbf{x}}_i, t_i; t) & \dfrac{\partial\varphi_v}{\partial\mathbf{v}_i}(\overline{\mathbf{x}}_i, t_i; t) \end{bmatrix} . \tag{2.20}$$

where φ_r and φ_v are the position and velocity components of φ. The dynamics of $\delta\mathbf{x}(t)$ is attained from Eq. (2.15), taking the first order Taylor expansion of $\mathbf{f}$ with respect to $\mathbf{x}$ about the reference trajectory $\overline{\mathbf{x}}$. This leads to the *variational state equations*

$$\delta\dot{\mathbf{x}}(t) = A(t)\, \delta\mathbf{x}_i \ , \tag{2.21}$$

where $A(t)$, usually referred to as state propagation matrix (SPM), is

$$A(t) \equiv \frac{\mathrm{d}}{\mathrm{d}t}\left(\frac{\partial\varphi}{\partial\mathbf{x}_i}(\overline{\mathbf{x}}_i, t_i; t)\right) = \left.\frac{\partial\mathbf{f}(\mathbf{x}, t)}{\partial\mathbf{x}}\right|_{\mathbf{x}=\overline{\mathbf{x}}} . \tag{2.22}$$

Putting together Eq. (2.18) and Eq. (2.21), it can be shown that the dynamics of $\Phi(t_i, t)$ is described by the first order variational equation

$$\dot{\Phi}(t_i, t) = A(t)\,\Phi(t_i, t)\ . \tag{2.23}$$

Eq. (2.23) represents a set of 16 differential equations, because the dimension of the state vector is 4 (the problem is planar). Recalling the definition of $\Phi(t_i, t)$, its initial condition cannot be else than the identity matrix: $\Phi(t_i, t_i) = I_4$. Moreover, being the SPM a time dependent function, it is evident that the variational equation cannot be integrated independently from the equations of motion (2.7). Thus, a total number of 20 first-order differential equations must be solved. Note also, that Eq. (2.18) is actually the solution of the variational equation (2.21) in terms of the STM.

In the case of the PBRFBP, the jacobian of the dynamics is

$$A_4(t) = \frac{\partial \mathbf{f}_4(\mathbf{x}, t)}{\partial \mathbf{x}} = \begin{bmatrix} 0_3 & I_3 \\ G_r & G_v \end{bmatrix}, \tag{2.24}$$

where G_r, known as *gravity-gradient matrix*, is

$$G_r(\mathbf{x}, t) \equiv \frac{\partial \mathbf{g}(\mathbf{x}, t)}{\partial \mathbf{r}} = \frac{\partial^2 \Omega}{\partial \mathbf{r}^2} = \begin{bmatrix} \dfrac{\partial^2 \Omega}{\partial x^2} & \dfrac{\partial^2 \Omega}{\partial x \partial y} \\ \dfrac{\partial^2 \Omega}{\partial y \partial x} & \dfrac{\partial^2 \Omega}{\partial y^2} \end{bmatrix} \tag{2.25}$$

and

$$G_v(\mathbf{x}, t) \equiv \frac{\partial \mathbf{g}(\mathbf{x}, t)}{\partial \mathbf{v}} = \begin{bmatrix} 0 & +2 \\ -2 & 0 \end{bmatrix}. \tag{2.26}$$

The pseudo-potential Ω, defined in Eq. (2.8), is a continuous function in its domain, i.e., the entire space except the coordinates occupied by the celestial bodies P_1, P_2 and P_3. Moreover, this property is inhered by its partial derivatives with respect to x and y. Thus, from a known theorem of calculus, being the second partial derivatives continuous (where they are defined), the Hessian matrix is a symmetric matrix: $G_r = {G_r}^\top$ The reader can refer to appendix A.1 for the analytical expressions of the components of G_r.
Finally, it is convenient to express the variational state equations (2.21) of the PBRFBP in a second-order form:

$$\delta\ddot{\mathbf{r}} = G_r \delta\mathbf{r} + G_v \delta\dot{\mathbf{r}}\ . \tag{2.27}$$

Indeed, as a similar equation will emerge during the derivation of the primer vector dynamics, the same results concerning its solution in terms of the STM will be employed.

2.2. Earth–Moon Transfers in a Four-Body Model

In the first part of this thesis, Primer Vector theory is applied to refine Earth–Moon transfers. However, before entering the details of the methodology, it is convenient to introduce here the kind of transfers that will be analyzed. The problem of transferring a spacecraft from an orbit around the Earth to the Moon represents a main challenge from the origin of space exploration and many approaches have been studied till today (a complete survey can be found in [20, 49]). The complexity of these ranges from simple Hohmann transfers in a two-body model to complex weak stability boundary transfers with ballistic capture at the Moon in high-fidelity solar system models [2–4, 12, 31, 47]. Also the nature of the propulsion technology of the spacecraft plays an important role during the design of a transfer. Indeed, the assumption of either low- or high-thrust propulsion generates very different solutions [16, 33].

2.2.1. Reference Earth–Moon Trajectories

The present work will discuss exclusively high-thrust missions, where impulsive maneuvers are separated by ballistic arcs, i.e., phases during which the spacecraft is subject to the coastal acceleration of the gravitational model only. The main starting point is the results in [62]. Here, two-impulse Earth–Moon transfers are treated in the restricted four-body problem with the Sun, the Earth, and the Moon as primaries (i.e., the present PBRFBP). The optimization problem is solved through direct transcription and multiple shooting strategy, and thousands of (locally) optimal solutions are found. Also, the author succeeded in framing known cases as special points of a more general picture, and in classifying many families of solutions depending on their features (e.g., cost, time of flight, number of revolutions and gravity assists, interior- and exterior-like transfers).

The transfers found by Topputo in [62] are actually the seeding trajectories of this thesis, and thus they will be named *reference trajectories*. These are obtained in the same PBRFBP presented in section 2.1, and are defined as follows.

1. The spacecraft is initially in a circular, low-altitude, parking orbit around the Earth, whose altitude is $h_i = 167$ km;
2. At the initial time t_i, a first impulse $\Delta\mathbf{v}_i$ parallel to the velocity of the parking orbit, places the spacecraft on the transfer orbit;
3. At the final time t_f, a second impulse $\Delta\mathbf{v}_f$ parallel to the local velocity inserts the spacecraft into a circular lunar orbit, of altitude $h_f = 100$ km;

Note that maneuvering in the direction of the local velocity is a requirement consistent with a fuel-optimal problem as it maximizes the variations of spacecraft energy [51]. As reported in [62], the altitude of the departure and arrival orbits are chosen consistently with the existing literature [2–4, 12, 31, 47–49]. In fact, the paper aims to frame existing Earth–Moon transfers depending on their time of flight and cost, and this is a meaningful operation only if the compared trajectories share equal initial and final energies (i.e., same altitude assuming circular orbits). Moreover, a mission profile including a low-Earth orbit is consistent with major architecture requirements (e.g., use of small/medium size launchers, in-orbit assembly of large structures, etc.) [52]. Instead, concerning the orientation of the parking obits in [62], they all lie on the (x, y)-plane of the synodic frame (see section 2.1.3). Similarly, also the transfers discussed in the first part of this thesis will inherit the same boundary conditions to allow a significant comparison with other previous works, especially with [62].

The solution database of [62] is made of almost 300 000 trajectories, many of which are reported in Fig. 2.3. Solutions with a time-of-flight of up to 200 days exist in literature [46], and also Earth–Moon transfers requiring as much as 2 years have been found [11]. However, in this work, a lunar transfer requiring hundreds of days is not deemed a viable option for real missions, and thus an upper bound on the maximum transfer duration of 100 days is applied. Each point of Fig. 2.3 is associated to a locally optimal solution with duration $\Delta t = t_f - t_i$ and cost $\Delta v = \|\Delta \mathbf{v}_i\| + \|\Delta \mathbf{v}_f\|$. In particular, only transfers with $\Delta t < 100$ days and $\Delta v < 4150$ m/s are reported in Fig. 2.3.
This general picture suggests that the solutions are organized into families, which constitute a well-defined structure in the (Δt, Δv) plane. To ease the analysis, the total set of solutions is subdivided into two regions that enclose "Short" and "Long" transfers ('S' and 'L' squares in Fig. 2.3). The same distinction will be maintained in the present work. Short transfers are characterized by a time of flight lower than 50 days, and a cost below 4150 m/s. Instead, long transfers have a time of flight between 50 and 100 days, and a cost lower than 3950 m/s. Note that, as the cost tends to reduce for increasing transfer time, only solutions of practical interest (with $\Delta v < 3950$ m/s) are included within the L region. Indeed, it is reasonable that a higher Δt is justified by a lower cost.

It is evident, that the reference transfers are accomplished in a purely ballistic fashion, so neither mid-course maneuvers nor other means of propulsion are considered during the cruise. Therefore, the following theory and the methodology presented will explore when and how an intermediate impulse could improve such trajectories.

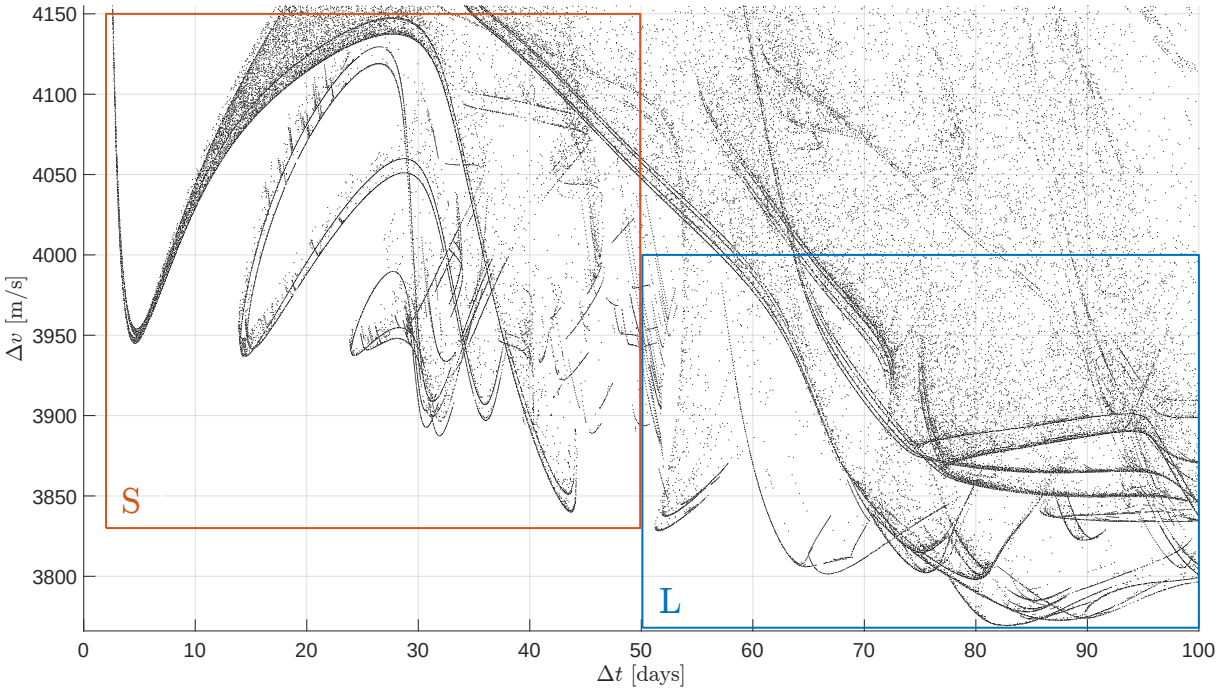

Figure 2.3: Two-impulse Earth–Moon transfers of [62] shown in the (Δt, Δv) plane. The two regions S and L enclose "Short" and "Long" transfer solutions, respectively

2.3. Primer Vector Theory

This section presents the derivation of a theory for trajectory optimization through an *indirect method*. The optimal trajectory is determined by meeting a set of necessary conditions (NC), obtained with an analytical approach. In fact, even when a direct method is employed (e.g., in [62]), it is beneficial to verify if the solution satisfies the NC; otherwise, it cannot be considered an optimal solution.

Hereafter, the set of NC are derived using the optimal control theory, a generalization of the calculus of variations. This theory deals with problems of infinite dimensions where the parameters and the unknowns are time-dependent functions, and aims to find a multi-dimensional vector that minimizes a specified functional. In space applications, of special concern are minimum fuel trajectories: if less propellant can be carried, then more payload weight can be thrust into orbit, or a smaller spacecraft can be used.
In 1963, D. F. Lawden first formulated, in his pioneering work [39], the general optimization problem in space navigation as a problem of Mayer. He developed the so-called *Primer Vector Theory*: a collection of first-order necessary conditions for optimality of both impulsive and continuous-thrust trajectories. These conditions are expressed in terms of a particular vector comprised of the adjoin variables associated with the velocity,

denoted as *primer vector*. The most completely developed theory is for impulsive and fixed-time trajectories, where the primer vector can indicate the appropriate timing for the addition of midcourse impulses or terminal coasting periods to minimize fuel consumption. The purpose of this section is to recall the derivation of Lawden's necessary conditions for an impulsive trajectory with fixed initial and final times, positions and velocities. The novelty is that Lawden's theory was derived in the framework Restricted Two-Body Problem, but here is extended to the PBRFBP.

First, the fuel-optimal problem of interest is described. Then, the necessary conditions for a generic thrust profile are obtained by means of Pontryagin's Maximum Principle (a key result of optimal control theory). Lastly, NC are adapted to the specific case of an impulsive mission and are expressed in terms of the primer vector only.

2.3.1. Fuel-Optimal Problem Formulation

Consider a spacecraft equipped with an engine and immersed in a perfectly general gravitational field, where neither the thrust direction nor thrust magnitude programs are predetermined. The motion is assumed to take place in vacuum. Two classes of variables are identified: the state variables, $\mathbf{x}(t) \in \mathbb{R}^{n_x}$ and the control variables $\mathbf{u}(t) \in \mathbb{R}^{n_u}$, where n_x and n_u are the dimensions of the vectors $\mathbf{x}$ and $\mathbf{u}$, respectively. Let the state vector at the time t be

$$\mathbf{x}(t) \equiv \left(\mathbf{r}(t), \mathbf{v}(t), m(t)\right)^\top , \tag{2.28}$$

where $\mathbf{r}(t)$ and $\mathbf{v}(t)$ are the SC position and velocity vectors, respectively, while $m(t)$ is the mass of the probe. The control variables $\mathbf{u}(t)$ are related to the action of the engine

$$\mathbf{u}(t) \equiv \left(\mathrm{T}(t), \boldsymbol{\alpha}(t), q\right)^\top , \tag{2.29}$$

where $\mathrm{T}(t)$ is the thrust magnitude produced by the engine and $\boldsymbol{\alpha}(t)$, also known as *thrust pointing vector*, is a unitary vector whose components are in the direction of the thrust. Lastly, q is a slack variable, whose role will be clarified later. Depending on the astrodynamical model, the dynamics of the state variables is a function of $\mathbf{x}(t)$, $\mathbf{u}(t)$ and the time t. In a generic compact notation it can be expressed as

$$\dot{\mathbf{x}}(t) = \mathbf{f}(\mathbf{x}(t), \mathbf{u}(t), t) \ . \tag{2.30}$$

Alternatively, the equations of motion written in a state-space form read

$$\dot{\mathbf{x}}(t) = \begin{bmatrix} \dot{\mathbf{r}}(t) \\ \dot{\mathbf{v}}(t) \\ \dot{m}(t) \end{bmatrix} = \begin{bmatrix} \mathbf{v}(t) \\ \mathbf{g}(\mathbf{x}, t) + \dfrac{\mathrm{T}(t)}{m(t)}\,\boldsymbol{\alpha}(t) \\ -\dfrac{\mathrm{T}(t)}{I_{sp} g_0} \end{bmatrix}, \tag{2.31}$$

where $\mathbf{g}(\mathbf{x}, t)$ is the coastal acceleration of the gravitational model. The last equation is needed to express the change in mass of the spacecraft due to the generation of thrust. Indeed, from the conservation of the mass, the mass variation is equal end opposite to the mass flow rate of the engine β:

$$\dot{m}(t) = -\beta(t) \equiv -\frac{\mathrm{T}(t)}{I_{sp} g_0}\,, \tag{2.32}$$

where I_{sp} is the specific impulse of the engine, while $g_0 = 9.807$ m/s^2 is the standard gravitational acceleration. The problem to be solved is to minimize a specific *performance criterion* $J \in \mathbb{R}$, also called *cost functional*, or simply *cost*, representing the minimum propellant consumption. This can be expressed by the integral of the thrust acceleration (thrust per unit mass) in time $\Gamma(t) \equiv \mathrm{T}(t)/m(t)$

$$J = \int_{t_i}^{t_f} \Gamma(t)\,\mathrm{d}t, = \int_{t_i}^{t_f} \frac{\mathrm{T}(t)}{m(t)}\,\mathrm{d}t\,. \tag{2.33}$$

In the case of a constant specific impulse (CSI) engine, using the equation of mass conservation (2.32), the cost can be written also as

$$J = -c \int_{t_i}^{t_f} \frac{\dot{m}(t)}{m(t)}\,\mathrm{d}t\,, \tag{2.34}$$

where $c = I_{sp} g_0$ is the effective exhaust velocity relative to the engine. Let $m_i = m(t_i)$ and $m_f = m(t_f)$ be the initial and final mass of the probe, respectively. Integrating Eq. (2.34) yields the final expression of the cost function for a fuel-optimal problem

$$J = c \ln\left(\frac{m_i}{m_f}\right)\,. \tag{2.35}$$

It is evinced that, for a fixed initial mass, minimizing the integral of the thrust acceleration in time, is equivalent to minimizing the mass of propellant consumed. It will be shown later, that this particular definition of the cost function is advantageous as, assuming only

impulsive maneuvers are permitted, the cost is equivalent to the sum of the maneuvers' magnitudes ($\sum_k \|\Delta \mathbf{v}_k\|$). Note also, that J is a function only of the final value of the state variable m (still assuming prescribed initial conditions on the mass).

In finding the histories of the state and control variables minimizing the cost, one must also take into account the finite authority of the engine. So, the values that $\mathbf{u}(t)$ is allowed to assume are actually bounded by the state-of-the-art technology. In particular, for a CSI engine, the expelled mass flow rate is assumed to be limited. This reflects in a constant maximum thrust magnitude allowable (i.e., $\mathrm{T}_{\max} = I_{sp}\, g_0\, \beta_{\max}$). Hence, the control function $\mathrm{T}(t)$ is subject to the inequality constraints

$$0 \leq \mathrm{T}(t) \leq \mathrm{T}_{\max} \ . \tag{2.36}$$

In order to transform the constraints (2.36) into equality constraints, another control variable, known as *slack variable*, $q \in \mathbb{R}$ is introduced. As a consequence, $\mathrm{T}(t)$ is required to satisfy the following equation

$$\mathrm{T}(t)\ (\mathrm{T}_{\max} - \mathrm{T}(t)) - q(t)^2 = 0 \ . \tag{2.37}$$

One notes that, since $q^2 \geq 0$, Eq. (2.36) is equivalent to Eq. (2.37). Also, by its definition, the thrust direction $\boldsymbol{\alpha}(t)$ is constrained to have unit magnitude:

$$\boldsymbol{\alpha}(t)^\top \boldsymbol{\alpha}(t) = 1 \ . \tag{2.38}$$

Therefore, the values that can be assumed by the control variables of Eq. (2.29) are restricted to a specific region $U \in \mathbb{R}^{n_u}$

$$U \coloneqq \left\{ \mathbf{u} \in \mathbb{R}^{n_u} :\ \mathrm{T}\,(\mathrm{T}_{\max} - \mathrm{T}) - q^2 = 0,\ \boldsymbol{\alpha}(t)^\top \boldsymbol{\alpha}(t) - 1 = 0 \right\} . \tag{2.39}$$

A continuous (or piecewise continuous) control $\mathbf{u}(t) \in \hat{\mathcal{C}}\,[t_i, t_f]$ satisfying Eq. (2.37) and Eq. (2.38) is said to be an *admissible control*. The class of admissible control functions in the time interval between t_i and t_f, is indicated by $\mathcal{U}\,[t_i, t_f]$.

$$\mathcal{U}\,[t_i, t_f] \coloneqq \left\{ \mathbf{u}(t) \in \hat{\mathcal{C}}\,[t_i, t_f] :\ \mathbf{u}(t) \in U \text{ for } t_i \leq t \leq t_f \right\} . \tag{2.40}$$

As this theory will be applied to Earth–Moon transfers discussed in section 2.2.1, it is pertinent to maintain consistent boundary conditions. Consequently, the problem of minimizing the fuel consumption is formulated for a spacecraft path between two specific

times, with assigned initial state and certain final states (position and velocity).

Problem 2.1 (Fuel-Optimal Problem). — *Let the state and control variables of a spacecraft be defined in Eqs.* (2.28) *and* (2.29)*, and let the dynamics* $\dot{\mathbf{x}}(t) = \mathbf{f}(\mathbf{x}(t), \mathbf{u}(t), t)$ *be governed by the equations of motion Eq.* (2.31)*. Given an initial state* $\mathbf{x}_i$ *at time* t_i *and a final position and velocity* $\{\mathbf{r}_f, \mathbf{v}_f\}$ *at time* t_f*, the cost functional* $J = c \ln (m_i/m_f)$ *must be minimized over the set of admissible controls* $\mathbf{u}(t) \in \mathcal{U}[t_i, t_f]$*, defined in Eq.* (2.40)*.*

$$\min_{\mathbf{u}(t) \in \mathcal{U}[t_i, t_f]} \quad J = c \ln \left(\frac{m_i}{m_f} \right), \quad \textit{subject to} \quad \begin{cases} \dot{\mathbf{x}}(t) = \mathbf{f}(\mathbf{x}(t), \mathbf{u}(t), t) \\ \mathbf{x}(t_i) = \mathbf{x}_i \\ \mathbf{r}(t_f) = \mathbf{r}_f \\ \mathbf{v}(t_f) = \mathbf{v}_f \end{cases} .$$

2.3.2. First-Order Necessary Conditions

The kind of problem described in the previous section falls under the class of optimal control problems with control equality constraints. This family of problems is notoriously hard to solve, and even the theory is not unambiguous, since there exist many forms of necessary conditions for optimality [41].

Lawden derived the first-order necessary conditions for a fuel-optimal CSI trajectory using classical calculus of variations. Despite that, an optimal control theory formulation is used in the subsequent derivation, but the final conclusions are analogous to those of Lawden. The following discussion is mainly inspired by Hiday, who developed in 1992 the primer vector necessary conditions for an impulsive, fuel-optimal, trajectory in the Elliptic Restricted Three-Body Problem [35]. Together with it, also the works of Bell [7], Jezewski [36] and Guzman [27] are used for an exhaustive derivation. Specifically, the *Pontryagin Maximum Principle* [22, 54] is employed to derive the first-order necessary conditions for optimality. The reader is referred to [30] for a survey of the various forms of the maximum principle.
For the sake of completeness, it must be pointed out that also other approaches are found in literature. For example, one significant difference is that in [16, 32, 41] the mass is not considered a state variable, but is kept track of separately.

In order to threaten the state equations (2.31) as differential constraints, a new set of variables $\boldsymbol{\lambda}(t) \in \mathbb{R}^{n_x}$ is introduced. These are called *Lagrange multiplier*, or *adjoint variables*, or *costates*, and are defined as $\boldsymbol{\lambda}(t) \equiv (\boldsymbol{\lambda}_r(t), \boldsymbol{\lambda}_v(t), \lambda_m(t))^\top$. The vectorial functions $\boldsymbol{\lambda}_r(t)$ and $\boldsymbol{\lambda}_v(t)$ and the scalar function $\lambda_m(t)$ are the adjoint to the spacecraft position, velocity and mass, respectively. Additionally, other two Lagrange multipliers

$\sigma_1(t)$ and $\sigma_2(t)$ are introduced in conjunction with the thrust constraints of Eqs. (2.37) and (2.38). One possible approach to derive the first-order conditions of Problem 2.1 is by means of the *Lagrangian* and *Hamiltonian* functions. The Hamiltonian $\mathcal{H}$ is defined as the summation of the path-dependent terms of J, and each adjoint variable multiplied by the right-hand side of the corresponding state equation. In the present case, since J is a function only of the final state, the Hamiltonian is

$$\mathcal{H}(\mathbf{x}, \mathbf{u}, \boldsymbol{\lambda}, t) \coloneqq \boldsymbol{\lambda}^\top \mathbf{f} = \boldsymbol{\lambda}_r^\top \mathbf{v} + \boldsymbol{\lambda}_v^\top \left[\mathbf{g} + \frac{\mathrm{T}}{m} \boldsymbol{\alpha} \right] - \lambda_m \frac{\mathrm{T}}{c} \ . \tag{2.41}$$

Note, that on the right side, the dependence upon the time and the state vector is omitted in favor of a more compact notation. The Lagrange expression $\mathcal{F}$ is defined by the subtraction of the Hamiltonian from the sum of the products of each σ variable with the corresponding control constraint

$$\mathcal{F}(\mathbf{x}, \mathbf{u}, \boldsymbol{\lambda}, t) \coloneqq \sigma_1 \left[\mathrm{T} \left(\mathrm{T}_{\max} - \mathrm{T} \right) - q^2 \right] + \sigma_2 \left(\boldsymbol{\alpha}^\top \boldsymbol{\alpha} - 1 \right) - \mathcal{H} \ . \tag{2.42}$$

The necessary conditions for the optimality of a solution are stated in the following theorem, which here is adapted to the fuel-optimal case described in Problem 2.1. Many proofs of Pontryagin's Principle exist in literature, but in general they are very long and technically difficult (see [34] or [54]).

Theorem 2.1 (Maximum Principle). — *Consider Problem 2.1. Suppose that* $\mathbf{u}^\star(t) \in \mathcal{U}$ *is a minimizer for the cost function* J*, and let* $\mathbf{x}^\star(t)$ *denote the state vector associated with the optimal trajectory. Then, there exist a* n_x*-dimensional vectorial function* $\boldsymbol{\lambda}^\star(t) \in \hat{\mathcal{C}}^1[t_i, t_f]$ *and a* n_u*-dimensional vectorial function* $\boldsymbol{\sigma}^\star(t) \in \hat{\mathcal{C}}^1[t_i, t_f]$*, such that* $(\boldsymbol{\lambda}^\star(t), \boldsymbol{\sigma}^\star(t)) \neq \mathbf{0} \ \forall \ t \in [t_i, t_f]$*, and:*

(a) the quadruple $\{\mathbf{u}^\star, \mathbf{x}^\star, \boldsymbol{\lambda}^\star, \boldsymbol{\sigma}^\star\}$ *verifies the equations*

$$\begin{cases} \dot{\mathbf{x}}^\star(t)^\top = \dfrac{\partial \mathcal{F}}{\partial \boldsymbol{\lambda}} \left(t, \mathbf{x}^\star, \mathbf{u}^\star, \boldsymbol{\lambda}^\star, \boldsymbol{\sigma}^\star \right) & \text{(2.43a)} \\ \dot{\boldsymbol{\lambda}}^\star(t)^\top = -\dfrac{\partial \mathcal{F}}{\partial \mathbf{x}} \left(t, \mathbf{x}^\star, \mathbf{u}^\star, \boldsymbol{\lambda}^\star, \boldsymbol{\sigma}^\star \right) & \text{(2.43b)} \\ \mathbf{0}^\top = \dfrac{\partial \mathcal{F}}{\partial \mathbf{u}} \left(t, \mathbf{x}^\star, \mathbf{u}^\star, \boldsymbol{\lambda}^\star, \boldsymbol{\sigma}^\star \right) & \text{(2.43c)} \end{cases}$$

at each instant t *of continuity of* $\mathbf{u}^\star$*, and the following transversal conditions hold:*

$$\boldsymbol{\lambda}^{\star\top}(t_f) = -\frac{\partial J}{\partial \mathbf{x}}(t_f, \mathbf{x}^\star(t_f)). \tag{2.44}$$

(b) the function $\mathcal{H}(\mathbf{x}^\star, \mathbf{u}, \boldsymbol{\lambda}^\star, t)$ *defined in Eq.* (2.41) *attains its maximum on* $\mathcal{U}[t_i, t_f]$ *at* $\mathbf{u}(t) = \mathbf{u}^\star(t)$ *for every* $t \in [t_i, t_f]$*:*

$$\mathcal{H}(\mathbf{x}^\star, \mathbf{u}^\star, \boldsymbol{\lambda}^\star, t) \geq \mathcal{H}(\mathbf{x}^\star, \mathbf{u}, \boldsymbol{\lambda}^\star, t) \quad \forall\ \mathbf{u}(t) \in \mathcal{U}[t_i, t_f]\,, \tag{2.45}$$

where $\mathcal{U}[t_i, t_f]$ *is the class of admissible control functions defined in Eq.* (2.40)*.*

Equation (2.43) is a system of differential algbraic equations (DAE), because Eqs. (2.43a) and (2.43b) represent $2n_x$ first-order differential equations and Eq. (2.43c) is a set of n_u algebraic equations. This kind of problem is known as two point boundary value problem (TPBVP), because the boundary conditions for the state vector are assigned both at the initial and final time, whilst the boundary conditions for the adjoint vector are given only at the final time. The adjoint differential equations (2.43b) originate from the Euler-Lagrange equations of optimal control [41]. For the present case, in a more explicit form, they read (superscript '$\star$' is dropped to ease notation)

$$\begin{cases} \dot{\boldsymbol{\lambda}}_r^\top = -\dfrac{\partial \mathcal{H}}{\partial \mathbf{r}} = -\boldsymbol{\lambda}_v^\top G_r\ , & \text{(2.46a)} \\[2ex] \dot{\boldsymbol{\lambda}}_v^\top = -\dfrac{\partial \mathcal{H}}{\partial \mathbf{v}} = -\boldsymbol{\lambda}_r^\top - \boldsymbol{\lambda}_v^\top G_v\ , & \text{(2.46b)} \\[2ex] \dot{\lambda}_m = -\dfrac{\partial \mathcal{H}}{\partial m} = \dfrac{\mathrm{T}}{m^2}\,\boldsymbol{\lambda}_v^\top \boldsymbol{\alpha}\ . & \text{(2.46c)} \end{cases}$$

where the two matrices G_r and G_v were defined in Eqs. (2.25) and (2.26). Lawden developed the solution to the problem in terms of inertial coordinates, therefore the vector $\mathbf{g}$ in his derivation is a function only of position and time, so $G_v = 0_{n_x}$. However, this term is nonzero in the general case, as the motion may be described in a rotating frame. Concerning Eq. (2.43c), the components of the vectorial algebraic equation are

$$\begin{cases} 0 = \dfrac{\partial \mathcal{F}}{\partial\, \mathrm{T}} = \sigma_1^\star\,(\mathrm{T}_{\max} - 2\,\mathrm{T}^\star) - \dfrac{1}{m^\star}\boldsymbol{\lambda}_v^{\star\top}\boldsymbol{\alpha}^\star + \dfrac{\lambda_m^\star}{c}\ , & \text{(2.47a)} \\[2ex] \mathbf{0}^\top = \dfrac{\partial \mathcal{F}}{\partial \boldsymbol{\alpha}} = 2\sigma_2^\star \boldsymbol{\alpha}^{\star\top} - \dfrac{\mathrm{T}^\star}{m^\star}\boldsymbol{\lambda}_v^{\star\top}\ , & \text{(2.47b)} \\[2ex] 0 = \dfrac{\partial \mathcal{F}}{\partial q} = -2\sigma_1^\star q^\star\ . & \text{(2.47c)} \end{cases}$$

The state and control variables that satisfy Eqs. (2.43b) and (2.43c) are termed *extremals* [35], for these solutions render the cost function an extremum. However, by the nature of the space trajectory problem, there is clearly no upper bound to the fuel that could

be consumed on a feasible trajectory. So, one may be confident that a solution is a local minimum and not a local maximum [16].

Equation (2.47c) requires either $\sigma_1^\star$, $q^\star$, or both should vanish. If $q^\star = 0$, then, in accordance with Eq. (2.37), either $\mathrm{T}^\star = 0$ or $\mathrm{T}^\star = \mathrm{T}_{\max}$. If $\sigma_1^\star = 0$, the thrust magnitude can assume intermediate values. Thus, the optimal trajectory may be comprised of the following types of arcs:

(i) Null Thrust Arcs (NT-arcs) when $\mathrm{T}^\star = 0$,

(ii) Intermediate Thrust Arcs (IT-arcs) when $0 < \mathrm{T}^\star < \mathrm{T}_{\max}$,

(iii) Maximum Thrust Arcs (MT-arcs) when $\mathrm{T}^\star = \mathrm{T}_{\max}$.

Consider now Eq. (2.47b). Provided that $\sigma_2^\star$ and $\mathrm{T}^\star$ are both non-zero, $\boldsymbol{\alpha}^\star$ and $\boldsymbol{\lambda}_v^\star$ must be parallel. Let the adjoint vector to the velocity be termed the *primer vector* and, hereafter, be denoted as

$$\mathbf{p}(t) \equiv \boldsymbol{\lambda}_v(t) \ . \tag{2.48}$$

Then, the optimal thrust direction is always parallel to the primer, and since $\|\boldsymbol{\alpha}^\star\| = 1$

$$\boldsymbol{\alpha}^\star(t) = \frac{\mathbf{p}^\star(t)}{\|\mathbf{p}^\star(t)\|} \ . \tag{2.49}$$

As it will be clearer later, the renaming of $\boldsymbol{\lambda}_v$ is not arbitrary, but rather this distinctive vector plays a relevant role in facilitating the understanding of optimal trajectories. If $\mathrm{T}^\star = 0$, the motor is not operating, and the components of $\boldsymbol{\alpha}^\star$ are indeterminate; additionally, if $\sigma_2^\star = 0$, the primer vanishes.

The optimal control is now chosen according to Pontryagin's Maximum Principle stated in (2.45), and affirming that the Hamiltonian should be maximized over the choice of admissible control variables in order to minimize the cost function. Note that, as empathized by [53], the inequality (2.45) does not imply $\mathcal{H}(\mathbf{x}, \mathbf{u}^\star, \boldsymbol{\lambda}, t) \geq \mathcal{H}(\mathbf{x}, \mathbf{u}, \boldsymbol{\lambda}, t)$ for arbitrary (i.e., non-optimal) $\mathbf{x}(t)$, $\boldsymbol{\lambda}(t)$. Substituting the definition of $\mathcal{H}$ reported in Eq. (2.41) into Eq. (2.45), utilizing the definition of the primer and simplifying,

$$\left[\frac{1}{m}\mathbf{p}^{\star\top}\boldsymbol{\alpha}^\star - \frac{1}{c}\lambda_m^\star\right]\mathrm{T}^\star \geq \left[\frac{1}{m}\mathbf{p}^{\star\top}\boldsymbol{\alpha} - \frac{1}{c}\lambda_m^\star\right]\mathrm{T} \ , \tag{2.50}$$

where superscript '$\star$' still denotes the value that a quantity assumes on the minimal cost trajectory. Inequality Eq. (2.50) is also recognized as the Weierstrass necessary conditions in calculus of variations, and it is the starting point employed by Lawden in [39]. At every point on the optimal trajectory, condition (2.50) must be valid for all possible values of $\boldsymbol{\alpha}$

and T satisfying constraints (2.37) and (2.38). Hence, following Hilday [35], Weierstrass inequality can be analyzed in each extremal of the optimal trajectory.

- Over an NT-arc, $\mathrm{T}^\star = 0$, and inequality (2.50) reduces to

$$\frac{1}{c}\lambda_m^\star \geq \frac{1}{m}\mathbf{p}^{\star\top}\boldsymbol{\alpha} \ . \tag{2.51}$$

  Imposing the greatest restriction on the above necessary conditions, the upper bound on the right-hand side of (2.51) is sought. The maximum value of the quantity $\mathbf{p}^{\star\top}\boldsymbol{\alpha}$ is obtained when $\boldsymbol{\alpha}$ is aligned with the primer vector; consequently, this maximum value is just the magnitude of the primer. Hence, the Weierstrass necessary condition on an NT-arc simplifies to

$$\lambda_m^\star \geq \frac{c\,\|\mathbf{p}^\star\|}{m} \ . \tag{2.52}$$

- Over a MT-arc, $\mathrm{T}^\star = \mathrm{T}_{\max}$, and (2.50) becomes

$$\left[\frac{1}{m}\mathbf{p}^{\star\top}\boldsymbol{\alpha}^\star - \frac{1}{c}\lambda_m^\star\right]\mathrm{T}_{\max} \geq \left[\frac{1}{m}\mathbf{p}^{\star\top}\boldsymbol{\alpha} - \frac{1}{c}\lambda_m^\star\right]\mathrm{T} \ . \tag{2.53}$$

  Taking $\mathrm{T} = \mathrm{T}_{\max}$ in order to maximize the right side of (2.53) requires that

$$\mathbf{p}^{\star\top}\boldsymbol{\alpha}^\star \geq \mathbf{p}^{\star\top}\boldsymbol{\alpha} \ . \tag{2.54}$$

  Additionally, taking $\boldsymbol{\alpha} = \boldsymbol{\alpha}^\star$ to determine an upper bound on the right side of (2.53)

$$\left[\frac{1}{m}\mathbf{p}^{\star\top}\boldsymbol{\alpha}^\star - \frac{1}{c}\lambda_m^\star\right]\mathrm{T}_{\max} \geq \left[\frac{1}{m}\mathbf{p}^{\star\top}\boldsymbol{\alpha}^\star - \frac{1}{c}\lambda_m^\star\right]\mathrm{T} \ ; \tag{2.55}$$

  moreover, since $\mathrm{T} \leq \mathrm{T}_{\max}$, the quantity in parentheses must be positive in order for the necessary condition to be satisfied. Thus,

$$\lambda_m{}^\star \leq \frac{c}{m}\mathbf{p}^{\star\top}\boldsymbol{\alpha}^\star \ . \tag{2.56}$$

  Conditions (2.54) and (2.56) are sufficient to ensure the validity of necessary condition (2.50). Inequality (2.54) will be satisfied for all $\boldsymbol{\alpha}$ if, and only if, $\mathbf{p}^{\star\top}\boldsymbol{\alpha}^\star$ assumes its maximum value. Hence, in agreement with the early results for the NT-arc, $\mathbf{p}^\star$ and $\boldsymbol{\alpha}^\star$ must be aligned. Conditions (2.56) then reduces to

$$\lambda_m^\star \leq \frac{c\,\|\mathbf{p}^\star\|}{m} \ . \tag{2.57}$$

- Over an IT-arc, the optimal thrust magnitude $\mathrm{T}^\star$ can assume values either greater or lower then T. Taking $\boldsymbol{\alpha} = \boldsymbol{\alpha}^\star$ in condition (2.50) makes clear that the inequality

$$\left[\frac{1}{m}\mathbf{p}^{\star\top}\boldsymbol{\alpha}^\star - \frac{1}{c}\lambda_m^\star\right]\mathrm{T}^\star \geq \left[\frac{1}{m}\mathbf{p}^{\star\top}\boldsymbol{\alpha}^\star - \frac{1}{c}\lambda_m^\star\right]\mathrm{T} \tag{2.58}$$

  cannot be valid fo all permissible T; however, equality is possible provided

$$\lambda_m{}^\star = \frac{c}{m}\mathbf{p}^{\star\top}\boldsymbol{\alpha}^\star \ . \tag{2.59}$$

  Substituting the value of $\lambda_m^\star$ from Eq. (2.59) into condition (2.50) and rearranging further, requires that

$$\lambda_m{}^\star \geq \frac{c}{m}\mathbf{p}^{\star\top}\boldsymbol{\alpha} \tag{2.60}$$

  for all permissible values of $\boldsymbol{\alpha}$. An upper bound on the right side of (2.60) is obtained when the primer and thrust directions are identical; consequently, necessary condition (2.60) becomes

$$\lambda_m^\star \geq \frac{c\,\|\mathbf{p}^\star\|}{m} \ . \tag{2.61}$$

  Note, however, that (2.59) implies that

$$\lambda_m^\star \leq \frac{c\,\|\mathbf{p}^\star\|}{m} \ , \tag{2.62}$$

  where equality occurs only when the primer and thrust directions are aligned. Hence, in order for both to be valid,

$$\lambda_m^\star = \frac{c\,\|\mathbf{p}^\star\|}{m} \ , \tag{2.63}$$

  and the thrust must be parallel to the primer vector. In the special case when the primer vanishes, Eq. (2.63) is still valid.

Consideration of the necessary conditions on each of the three extremal arcs is concluded; hence, the superscript '$\star$' will henceforth be dropped, and the subsequent states, controls and Lagrange multipliers are assumed to be evaluated on the optimal trajectory.
The results obtained from the Maximum Principle can be summarized as follows:

1. Whenever the thrust is operative and $\|\mathbf{p}\| \neq 0$, the thrust must act in the direction and sense of the primer vector

$$\boldsymbol{\alpha} = \frac{\mathbf{p}}{\|\mathbf{p}\|} \ ; \tag{2.64}$$

2. Defining the function S as

$$\mathcal{S} \coloneqq \frac{c\,\|\mathbf{p}\|}{m} - \lambda_m \ , \tag{2.65}$$

then it is necessary that

- $\mathcal{S} \leq 0$ over an NT-arc;
- $\mathcal{S} \geq 0$ over a MT-arc;
- $\mathcal{S} = 0$ over an IT-arc.

Because the function $\mathcal{S}$ delineates the amount of thrust on extremal arcs, $\mathcal{S}$ is identified as the *thrust magnitude switching function.*

It remains to take into account Eqs. (2.46c) and (2.47a). They are employed to eliminate the adjoint λ_m from consideration, by expressing it in terms of the thrust magnitude switching function. Differentiating Eq. (2.65) and solving for the derivative of the adjoint,

$$\dot{\lambda}_m = \frac{c}{m}\,\|\dot{\mathbf{p}}\| - \frac{c\,\|\mathbf{p}\|}{m^2}\dot{m} - \dot{\mathcal{S}} \ . \tag{2.66}$$

Equating the two expressions of $\dot{\lambda}_m$ in Eqs. (2.46c) and (2.66) produces

$$\frac{c}{m}\,\|\dot{\mathbf{p}}\| - \frac{c\,\|\mathbf{p}\|}{m^2}\dot{m} - \dot{\mathcal{S}} = \frac{\mathrm{T}}{m^2}\,\|\mathbf{p}\| \ . \tag{2.67}$$

Utilizing the conservation of mass expression (2.32) for the term $\dot{m}$, renders

$$\dot{\mathcal{S}} = \frac{c}{m}\,\|\dot{\mathbf{p}}\| - \frac{c\,\|\mathbf{p}\|}{m^2}\left(-\frac{\mathrm{T}}{c}\right) - \frac{\mathrm{T}}{m^2}\,\|\mathbf{p}\|\,, \tag{2.68}$$

which reduces to

$$\dot{\mathcal{S}} = \frac{c}{m}\,\|\dot{\mathbf{p}}\| \ . \tag{2.69}$$

Also, substituting Eq. (2.65) into Eq. (2.47a)

$$0 = \sigma_1\,(\mathrm{T}_{\max} - 2\,\mathrm{T}) - \frac{\|\mathbf{p}\|}{m} + \frac{1}{c}\left(\frac{c\,\|\mathbf{p}\|}{m} - \mathcal{S}\right) \ , \tag{2.70}$$

simplifying and rearranging

$$\mathcal{S} = c\,\sigma_1\,(\mathrm{T}_{\max} - 2\,\mathrm{T}) \ . \tag{2.71}$$

Hence, the constraints on the Lagrange multipliers λ_m and σ_1 have been replaced by the specification of the switching function and its derivative according to Eqs. (2.69) and (2.71). On NT- and MT-arcs, Eq. (2.71) serves only to determine the value of σ_1.

Since the spacecraft mass is constant on an NT-arc, Eq. (2.69) is integrable to yield

$$\mathcal{S} = \frac{c}{m} \|\mathbf{p}\| + \text{constant} \ . \tag{2.72}$$

Instead, on an IT-arc the conditions about $\mathcal{S}$ further simplify. Recall that for an IT-arc, $\sigma_1 = 0$; therefore, from Eq. (2.71), $\mathcal{S} = 0$. In order for the switching function to remain zero throughout the duration of the IT-arc, the derivative of the switching function must also be identically zero. Accordingly, Eq. (2.69) implies that $\|\dot{\mathbf{p}}\| = 0$ or $\|\mathbf{p}\| = \text{constant}$.

The results of this section will now be collected together. The necessary conditions for an optimal solution of Problem 2.1, which are also expressed by Theorem 2.1, can be stated in terms of the primer vector $\mathbf{p}$ and the thrust magnitude switching function $\mathcal{S}$.

Proposition 2.1 (Necessary Conditions for a General Fuel-Optimal Trajectory). — *An optimal trajectory for Problem 2.1 is such that:*

1. *Whenever the engine of the spacecraft is operative and $\|\mathbf{p}\| \neq 0$, the thrust must act in the direction and sense of the primer vector*

$$\boldsymbol{\alpha} = \frac{\mathbf{p}}{\|\mathbf{p}\|} \ .$$

2. *$\mathcal{S}$ must respect the following specification on the three types of extremal arcs:*
   - *(i) On a NT-arc, $\mathcal{S}$ is negative and is determined by Eq. (2.72)*

$$\mathcal{S} = \frac{c}{m} \|\mathbf{p}\| + \text{constant} \quad \textit{and} \quad \mathcal{S} \leq 0 \ ;$$

   - *(ii) On a MT-arc, $\mathcal{S}$ is positive and it respects Eq. (2.69)*

$$\dot{\mathcal{S}} = \frac{c}{m} \|\dot{\mathbf{p}}\| \quad \textit{and} \quad \mathcal{S} \geq 0 \ ;$$

   - *(iii) On an IT-arc, $\mathcal{S}$ is identically zero and the primer magnitude is constant*

$$\mathcal{S} = \dot{\mathcal{S}} = 0 \quad \textit{and} \quad \|\dot{\mathbf{p}}\| = 0 \ .$$

Note that these conditions apply for either high- or low-thrust engines, as no assumption has been made on the thrust profile. Moreover, their validity holds irrespective of the astrodynamical model employed.

2.3.3. Primer Differential Equations

Before discussing further the necessary conditions for optimality, it is useful to develop the differential equations for the primer vector. Writing the second adjoint differential equation (2.46b) in terms of $\mathbf{p}$ and differentiating

$$\ddot{\mathbf{p}}^\top = -\dot{\boldsymbol{\lambda}}_r^\top - \dot{\mathbf{p}}^\top G_v - \mathbf{p}^\top \dot{G}_v \ . \tag{2.73}$$

Then, substituting the first adjoint differential equation (2.46a) inside Eq. (2.73) and simplifying, yields to

$$\ddot{\mathbf{p}}^\top = \mathbf{p}^\top \left(G_r - \dot{G}_v \right) - \dot{\mathbf{p}}^\top G_v \ , \tag{2.74}$$

which, transposed, results in

$$\ddot{\mathbf{p}} = \left(G_r - \dot{G}_v \right)^\top \mathbf{p} - G_v^\top \dot{\mathbf{p}} \ . \tag{2.75}$$

Eq. (2.75) is valid for every astrodynamical model, but in the framework of the PBRFBP, it reduces even more. Indeed, being G_v, defined in Eq. (2.26), a constant matrix, $\dot{G}_v$ is identically zero. Moreover, it was already pointed out, that owing to the regularity of the pseudo-potential Ω, G_r is symmetric. Thus, in the present case:

$$\left(G_r - \dot{G}_v \right)^\top = G_r \ . \tag{2.76}$$

Furthermore, it should be observed that G_v is an antisymmetric matrix

$$-G_v^\top = \begin{bmatrix} 0 & +2 \\ -2 & 0 \end{bmatrix} = G_v \ . \tag{2.77}$$

The second order differential equation for the primer vector in a PBRFBP simplifies to

$$\ddot{\mathbf{p}} = G_r \mathbf{p} + G_v \dot{\mathbf{p}} \ . \tag{2.78}$$

Lawden's approach to the primer differential equation for transfers in the two-body problem results in a matrix G_v that is always zero. However, in the PBRFBP, the second derivative of the primer vector depends also on its first derivative. A notable advantage of the primer vector equation, is that it obviates the need for simultaneous integration of Eq. (2.78) and both the state and the variational dynamics, Eqs. (2.7) and (2.23), respectively. Indeed, Eq. (2.78) and Eq. (2.27) are actually the same second-order differential equation. Hence, if the initial conditions for $\mathbf{p}$ and $\dot{\mathbf{p}}$ are known, the history of the primer

vector in time can be computed by means of the STM:

$$\begin{bmatrix} \mathbf{p}(t) \\ \dot{\mathbf{p}}(t) \end{bmatrix} = \begin{bmatrix} \Phi_{rr}(t_i,t) & \Phi_{rv}(t_i,t) \\ \Phi_{vr}(t_i,t) & \Phi_{vv}(t_i,t) \end{bmatrix} \begin{bmatrix} \mathbf{p}(t_i) \\ \dot{\mathbf{p}}(t_i) \end{bmatrix} . \tag{2.79}$$

Unfortunately, instead of $\dot{\mathbf{p}}(t_i)$, the values of $\mathbf{p}$ at the initial and final times are very often available (especially for a trajectory with two impulsive maneuvers at the ending points). Nevertheless, if matrix equation (2.79) is evaluated at $t = t_f$, and the sub-matrix $\Phi_{rv}(t_i, t_f)$ is nonsingular, the first equation of (2.79) can be rearranged to have:

$$\dot{\mathbf{p}}(t_i) = \Phi_{rv}^{-1}(t_i,t_f)\left[\mathbf{p}(t_f) - \Phi_{rr}(t_i,t_f)\mathbf{p}(t_i)\right] . \tag{2.80}$$

Thus, knowing the values of the primer vector at the endpoints of the trajectory ($\mathbf{p}_i = \mathbf{p}(t_i)$, $\mathbf{p}_f = \mathbf{p}(t_f)$), the solution for the primer is given by Eqs. (2.79) and (2.80):

$$\mathbf{p}(t) = \left[\Phi_{rr}(t_i,t) - \Phi_{rv}(t_i,t)\,\Phi_{rv}^{-1}(t_i,t_f)\,\Phi_{rr}(t_i,t_f)\right]\mathbf{p}_i + \Phi_{rv}(t_i,t)\,\Phi_{rv}^{-1}(t_i,t_f)\mathbf{p}_f . \tag{2.81}$$

2.3.4. Adjoint Equation

When a system possess an integral of motion, theoretical developments are facilitated and also checks on the accuracy of numerical computations can be performed. For instance, in the two-body problem or in the circular three-body problem, the Hamiltonian is constant on a coastal arc. However, in the case of the planar bicircular rotating four-body problem, the Hamiltonian is time varying ($\dot{\mathcal{H}}(t) \neq 0$) and so it does not represent an integral of motion. The main reason for this is that the system is non-autonomous, therefore $\mathbf{g}(\mathbf{x}, t)$, and consequently $\mathcal{H}(t)$, are explicit functions of time. The extension of the primer vector theory to the PBRFBP is complicated by the non-constancy of the Hamiltonian. Nonetheless, a useful variational expression can be rendered constant by contemporaneous variations between a perturbed and a reference trajectory. Once again, the following derivation is inspired by [35].

Let $\overline{\gamma}$ and γ represent a reference trajectory and a trajectory slightly perturbed from the reference, respectively. Assume also, that both trajectories satisfy the same boundary conditions. If δ symbolizes a *contemporaneous variation*, then the difference between the states on the perturbed and reference trajectory is:

$$\delta\mathbf{x}(t) = \mathbf{x}(t) - \overline{\mathbf{x}}(t) , \tag{2.82}$$

where $\mathbf{x}(t) = (\mathbf{r}(t), \mathbf{v}(t))^\top$ and $\overline{\mathbf{x}}(t) = (\overline{\mathbf{r}}(t), \overline{\mathbf{v}}(t))^\top$ denote the state vectors of γ and $\overline{\gamma}$, respectively. The equations of motion of a spacecraft on a coastal arc are obtained by setting $\mathrm{T} = 0$ in Eq. (2.31). If γ and $\overline{\gamma}$ are sufficiently close such that a linear analysis is justified, then the contemporaneous variation in the velocity and in the accelerations on the null-thrust arc can be expressed as

$$\delta\dot{\mathbf{r}}(t) = \dot{\mathbf{r}}(t) - \dot{\overline{\mathbf{r}}}(t) = \delta\mathbf{v} \ , \tag{2.83}$$

$$\delta\dot{\mathbf{v}}(t) = \dot{\mathbf{v}}(t) - \dot{\overline{\mathbf{v}}}(t) = \delta\mathbf{g} = \frac{\partial\mathbf{g}}{\partial\mathbf{r}}\delta\mathbf{r} + \frac{\partial\mathbf{g}}{\partial\mathbf{v}}\delta\mathbf{v} \ . \tag{2.84}$$

Substituting the definitions of Eqs. (2.25) and (2.26), the state variational equations (2.83) and (2.84) can be written in a second order form as

$$\delta\ddot{\mathbf{r}} = \delta\dot{\mathbf{v}} = G_r\delta\mathbf{r} + G_v\delta\mathbf{v} \ . \tag{2.85}$$

Equation (2.85) is equivalent to the variational equation (2.27), therefore its solution can be written in terms of the STM

$$\begin{bmatrix}\delta\mathbf{r}(t)\\ \delta\mathbf{v}(t)\end{bmatrix} = \begin{bmatrix}\Phi_{rr}(\tau,t) & \Phi_{rv}(\tau,t)\\ \Phi_{vr}(\tau,t) & \Phi_{vv}(\tau,t)\end{bmatrix}\begin{bmatrix}\delta\mathbf{r}(\tau)\\ \delta\mathbf{v}(\tau)\end{bmatrix} . \tag{2.86}$$

Recall now from Eq. (2.75), that the second order differential equation for the primer vector on the reference trajectory is

$$\ddot{\overline{\mathbf{p}}} = \left(G_r - \dot{G}_v\right)^\top \overline{\mathbf{p}} - G_v^\top\dot{\overline{\mathbf{p}}} \ . \tag{2.87}$$

Pre-multiplying Eq. (2.85) by $\overline{\mathbf{p}}^\top$ and Eq. (2.75) by $\delta\mathbf{r}^\top$ and subtracting,

$$\overline{\mathbf{p}}^\top\delta\ddot{\mathbf{r}} - \delta\mathbf{r}^\top\ddot{\overline{\mathbf{p}}} = \overline{\mathbf{p}}^\top G_r\delta\mathbf{r} + \overline{\mathbf{p}}^\top G_v\delta\mathbf{v} - \delta\mathbf{r}^\top G_r^\top\overline{\mathbf{p}} + \delta\mathbf{r}^\top\dot{G}_v^\top\overline{\mathbf{p}} + \delta\mathbf{r}^\top G_v^\top\dot{\overline{\mathbf{p}}} \ . \tag{2.88}$$

Canceling the first and third terms on the right side

$$\overline{\mathbf{p}}^\top\delta\ddot{\mathbf{r}} - \delta\mathbf{r}^\top\ddot{\overline{\mathbf{p}}} - \overline{\mathbf{p}}^\top G_v\delta\mathbf{v} - \delta\mathbf{r}^\top\dot{G}_v^\top\overline{\mathbf{p}} - \delta\mathbf{r}^\top G_v^\top\dot{\overline{\mathbf{p}}} = 0 \ . \tag{2.89}$$

Adding and subtracting the quantity $\dot{\overline{\mathbf{p}}}^\top\delta\mathbf{v}$

$$\overline{\mathbf{p}}^\top\delta\ddot{\mathbf{r}} + \dot{\overline{\mathbf{p}}}^\top\delta\mathbf{v} - \delta\mathbf{r}^\top\ddot{\overline{\mathbf{p}}} - \dot{\overline{\mathbf{p}}}^\top\delta\mathbf{v} - \overline{\mathbf{p}}^\top G_v\delta\mathbf{v} - \delta\mathbf{r}^\top\dot{G}_v^\top\overline{\mathbf{p}} - \delta\mathbf{r}^\top G_v^\top\dot{\overline{\mathbf{p}}} = 0 \ . \tag{2.90}$$

Recalling that $\delta\dot{\mathbf{r}} = \delta\mathbf{v}$ and $\delta\ddot{\mathbf{r}} = \delta\dot{\mathbf{v}}$ and transposing the third, sixth and last terms, yield

$$\left(\overline{\mathbf{p}}^\top \delta\dot{\mathbf{v}} + \dot{\overline{\mathbf{p}}}^\top \delta\mathbf{v}\right) - \left(\ddot{\overline{\mathbf{p}}}^\top \delta\mathbf{r} + \dot{\overline{\mathbf{p}}}^\top \delta\dot{\mathbf{r}}\right) - \left(\dot{\overline{\mathbf{p}}}^\top G_v \delta\mathbf{r} + \overline{\mathbf{p}}^\top \dot{G}_v \delta\mathbf{r} + \overline{\mathbf{p}}^\top G_v \delta\dot{\mathbf{r}}\right) = 0 \ . \tag{2.91}$$

At this point, one can note that the left side is an exact differential; hence,

$$\frac{\mathrm{d}}{\mathrm{d}t}\left(\overline{\mathbf{p}}^\top \delta\mathbf{v} - \dot{\overline{\mathbf{p}}}^\top \delta\mathbf{r} - \overline{\mathbf{p}}^\top G_v \delta\mathbf{r}\right) = 0 \ , \tag{2.92}$$

which can be integrated to yield

$$\overline{\mathbf{p}}^\top \delta\mathbf{v} - \left(\dot{\overline{\mathbf{p}}}^\top + \overline{\mathbf{p}}^\top G_v\right) \delta\mathbf{r} = \text{constant} \ . \tag{2.93}$$

Equation (2.93) is named *adjoint equation*: it is the basis for the analysis in [40] and it will be used extensively in the subsequent derivations.

2.3.5. Impulsive Thrust

Consider a high-thrust CSI engine, which, for instance, employs conventional chemical propulsion. On such a transfer, the duration of an arc of maximum thrust is negligible if compared to the total time of the mission. Accordingly, for the purpose of finding an optimal trajectory, the motion of the spacecraft during a MT-arc can be neglected. So, a MT-arc can be approximated as an impulse (i.e., Dirac delta function δ_D) useful to change the velocity of the probe, without affecting its position. Such (ideal) impulsive maneuver, is modeled by allowing the maximum thrust magnitude to be infinite: $\mathrm{T}_{\max} \to \infty$. It is shown hereafter, how this assumption simplifies the necessary conditions just found.

Cost Function

In the case of impulsive trajectory, $\Gamma(t) = \|\Delta\mathbf{v}(t)\| \ \delta_D(t - t_k)$, where t_k is the time of the k-th impulse and $\|\Delta\mathbf{v}(t)\|$ is the variation of the velocity achieved. From Eq. (2.33)

$$J = \int_{t_i}^{t_f} \Gamma(t)\,\mathrm{d}t = \int_{t_i}^{t_f} \|\Delta\mathbf{v}(t)\| \ \delta_D(t - t_k)\,\mathrm{d}t = \sum_{k=1}^{n_k} \|\Delta\mathbf{v}_k\| \ . \tag{2.94}$$

where n_k is the number of impulsive maneuvers. J is referred to as the *characteristic velocity* of the transfer. Therefore, minimizing the fuel expenditure, and minimizing the characteristic velocity (i.e., the sum of the magnitude of the velocity changes), are equivalent optimization criteria for the impulsive thrust problem. Furthermore, by definition, the velocity change $\|\Delta\mathbf{v}_k\|$ is aligned to the thrust direction $\boldsymbol{\alpha}$ at time t_k.

Corner Conditions

Consider a MT-arc which is preceded and succeeded by NT-arcs. As determined at the end of section 2.3.2, a MT-arc is characterized by $\mathcal{S} \geq 0$, and a NT-arc by $\mathcal{S} \leq 0$. In the case of a MT-arc of non-negligible duration (finite T_{max}), the graph of the thrust magnitude switching function has the form illustrated in Fig. 2.4a. Instead, if the thrust is impulsive ($T_{max} \to \infty$) and the duration of the MT-arc is negligible, then the graph of $\mathcal{S}$ resembles the one reported in Fig. 2.4b. It is evident that the switching function attains its maximum value, equal to zero, at the instant of application of the impulsive thrust, denoted as $t = t_k$. Hence, the shape of Fig. 2.4b necessarily implies that

$$\mathcal{S}(t_k) = \dot{\mathcal{S}}(t_k) = 0 \ . \tag{2.95}$$

Moreover, if either or both the NT-arcs are replaced by IT-arcs, over which $\mathcal{S} = 0$, the conclusion (2.95) is unaltered. Summarizing, for the case of impulsive thrust maneuvers, $T = 0$ when $\mathcal{S} < 0$ and the impulses occur when $\mathcal{S}$ is maximum and tangent to $\mathcal{S} = 0$.

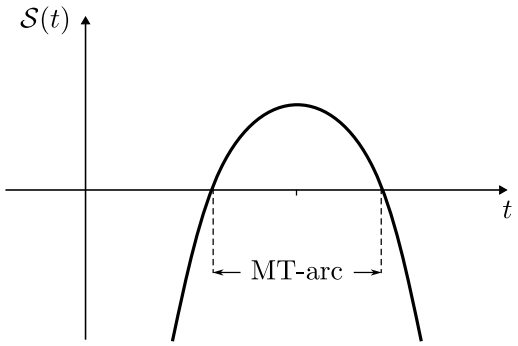

(a) General thrust: MT-arc of finite duration

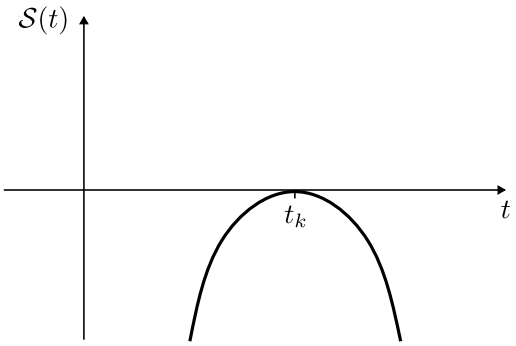

(b) Impulsive thrust case: MT-arc of infinitesimal duration and $\dot{\mathcal{S}}$ continuous at $t = t_k$

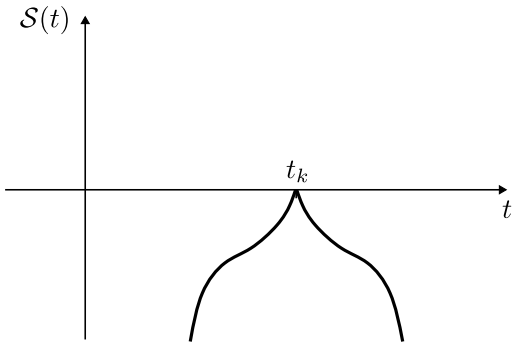

(c) Impulsive thrust case: MT-arc of infinitesimal duration with a cusp ($\dot{\mathcal{S}}$ discontinuous)

Figure 2.4: Switching function of a NT-arcs preceding and succeeding a MT-arc

However, as the preceding arguments do not preclude the existence of a cusp at $t = t_k$ in the $\mathcal{S}$-graph (see Fig. 2.4c), a more rigorous demonstration of Eq. (2.95) is needed. According to the calculus of variations terminology, a *corner* exists if an instantaneous change in the control variable (i.e., an impulse) causes some or all of the state variables to experience a discontinuity. The theorem that follows, from calculus of variations, outlines the conditions that must be met at the corner points of an optimal solution.

Theorem 2.2 (Weierstrass-Erdmann Corner Conditions). — *Consider the fuel-optimal problem described in Problem 2.1, and suppose that the quadruple* $\{\mathbf{u}^\star, \mathbf{x}^\star, \boldsymbol{\lambda}^\star, \boldsymbol{\sigma}^\star\}$ *are associated to the optimal trajectory (i.e., they satisfy the necessary conditions reported in Theorem 2.1). At every possible corner point* $t_k \in (t_i, t_f)$ *of* $\mathbf{u}^\star(t) \in \mathcal{U}[t_i, t_f]$*, the following conditions must hold:*

$$\boldsymbol{\lambda}^\star(t_k^-) = \boldsymbol{\lambda}^\star(t_k^+) \ , \tag{2.96}$$

$$\mathcal{H}\left(t_k^-, \mathbf{x}^\star(t_k^-), \mathbf{u}^\star(t_k^-), \boldsymbol{\lambda}^\star(t_k^-)\right) = \mathcal{H}\left(t_k^+, \mathbf{x}^\star(t_k^+), \mathbf{u}^\star(t_k^+), \boldsymbol{\lambda}^\star(t_k^+)\right) \ . \tag{2.97}$$

where $\mathcal{H}$ *is defined by Eq.* (2.41)*, and* t_k^-*,* t_k^+ *denote the time instant just before and after the corner, respectively.*

Conditions (2.96) stipulate that the adjoint variables must be continuous at a corner. As a consequence, also the primer vector $\mathbf{p} \equiv \boldsymbol{\lambda}_v$ must be continuous across the impulse

$$\mathbf{p}^- = \mathbf{p}^+ \ , \tag{2.98}$$

where the superscripts '+' and '−' denote the evaluation of the quantity prior to and subsequent to the corner, respectively. Furthermore, using the definition of $\mathbf{p}$, the second adjoint equation (2.46b) becomes

$$\dot{\mathbf{p}}^\top = -\boldsymbol{\lambda}_r^\top - \mathbf{p}^\top G_v \ . \tag{2.99}$$

The derivative of the primer is expressed solely in terms of the continuous adjoint variables $\boldsymbol{\lambda}_r$ and $\mathbf{p}$, and the matrix G_v, which is a constant in the PBRFBP. Hence, another outcome of the Weierstrass-Erdmann corner conditions is that also the derivative of the primer must be continuous at a corner

$$\dot{\mathbf{p}}^- = \dot{\mathbf{p}}^+ \ . \tag{2.100}$$

A further consequence, from Eq. (2.69), is that the derivative of the switching function is continuous across the impulse

$$\dot{\mathcal{S}}^- = \dot{\mathcal{S}}^+ \ . \tag{2.101}$$

This, for an optimal trajectory, excludes the existence of a cusp in the graph of $\mathcal{S}$, which was present in Fig. 2.4c.

The second corner condition requires that the Hamiltonian is continuous across the discontinuity of the control variable:

$$\mathcal{H}^- = \mathcal{H}^+ \ . \tag{2.102}$$

The Hamiltonian defined in Eq. (2.41) can be rewritten in terms of $\mathbf{p}$ and $\dot{\mathbf{p}}$ by using the second adjoint equation (2.46b)

$$\mathcal{H} = \mathbf{p}^\top \mathbf{g} - \left(\dot{\mathbf{p}}^\top + \mathbf{p}^\top G_v\right) \mathbf{v} + \left(\frac{c\,\|\mathbf{p}\|}{m} - \lambda_m\right) \frac{\mathrm{T}}{c} \ . \tag{2.103}$$

As T is discontinuous at a corner, the only possibility for $\mathcal{H}$ to be continuous is that

$$\frac{c\,\|\mathbf{p}\|}{m} - \lambda_m = 0 \ , \tag{2.104}$$

which, from the definition of $\mathcal{S}$ in Eq. (2.65), is equivalent to state that

$$\mathcal{S}(t_k) = \mathcal{S}^- = \mathcal{S}^+ = 0 \ . \tag{2.105}$$

Up to this point, it was proved rigorously that $\mathcal{S}$ and $\dot{\mathcal{S}}$ are continuous at a corner, and $\mathcal{S} = 0$. In order to demonstrate all the results obtained by geometrical considerations, it is still needed to show that also $\dot{\mathcal{S}} = 0$.

To this aim, leave aside for a moment the corner conditions and consider the following case where a NT-arc joins two impulsive thrusts. Let P denote the magnitude of the primer vector at the instant of one of the two maneuvers. Equation (2.72) is valid over the entire NT-arc. Because at the boundaries of the arc $\mathcal{S} = 0$ and $\mathcal{S} \in \mathcal{C}$, evaluating Eq. (2.72) at an extreme point yields

$$\mathcal{S} = 0 = \frac{c}{m}\mathrm{P} + \text{constant} \ . \tag{2.106}$$

So, the values of the constant are determined to be equal to $-\frac{c}{m}\mathrm{P}$, and Eq. (2.72) becomes

$$\mathcal{S} = \frac{c}{m}\left(\|\mathbf{p}\| - \mathrm{P}\right) \ . \tag{2.107}$$

From Eq. (2.107), valid over the entire NT-arc, the magnitude of $\mathbf{p}$ must equal P at the other terminal as well (where still $\mathcal{S} = 0$). Hence, if an optimal trajectory is composed

of NT-arcs separated by impulsive maneuvers, then $\|\mathbf{p}\| = \mathrm{P}$ at every application of an impulsive thrust. If one or both of the impulsive maneuvers is replaced by an IT-arc, the previous conclusion is unaffected. Indeed, over an IT-arc, $\mathcal{S} = \dot{\mathcal{S}} = \|\dot{\mathbf{p}}\| = 0$; therefore, an IT-arc on an optimal trajectory behaves exactly as an impulsive maneuver. Consequently, at all impulsive maneuvers and over all IT-arcs $\|\mathbf{p}\| = \mathrm{P}$; also, over all NT-arcs $\|\mathbf{p}\| \leq \mathrm{P}$. The value of P can be computed applying the transversality conditions (2.44). According to Problem 2.1, the only state variable unspecified at the final time is the mass. The missing boundary condition for the final mass is

$$\lambda_m(t_f) = -\frac{\partial J}{\partial m_f} = \frac{c}{m_f} \ . \tag{2.108}$$

Using the definition of $\mathcal{S}$ (Eq. (2.65)) the final value of the switching function is

$$\mathcal{S}(t_f) = \frac{c}{m_f} \left(\|\mathbf{p}_f\| - 1 \right) \ . \tag{2.109}$$

If the final arc of the trajectory is a NT-arc, Eq. (2.107) can be evaluated at $t = t_f$

$$\mathcal{S} = \frac{c}{m} \left(\|\mathbf{p}_f\| - \mathrm{P} \right) \ . \tag{2.110}$$

The value of the constant P is inferred comparing Eqs. (2.109) and (2.110), resulting in

$$\mathrm{P} = 1 \ . \tag{2.111}$$

Alternatively, if the final arc is an IT-arc, then $\mathcal{S}(t_f) = 0$ and condition (2.109) is satisfied provided $\|\mathbf{p}\| = \mathrm{P} = 1$. Recalling that $\|\mathbf{p}\| = \mathrm{P}$ at every application of an impulsive thrust, the following conclusions can be drawn: on a fuel-optimal trajectory, the magnitude of the primer must not exceed unity on any NT-arc (where $\mathcal{S} < 0$), and, whenever the engine is operative, the primer is a unit vector aligned in the thrust direction $\boldsymbol{\alpha}$.

It is now possible to investigate further the second Weierstrass-Erdmann corner conditions, and to prove that at a corner $\dot{\mathcal{S}} = 0$. According to the result of Eqs. (2.103) and (2.104), the second corner condition $\mathcal{H}^+ - \mathcal{H}^- = 0$ is

$$\mathbf{p}^{-\top}\mathbf{g}^- - \left(\dot{\mathbf{p}}^{-\top} + \mathbf{p}^{-\top}G_v{}^-\right)\mathbf{v}^- - \mathbf{p}^{+\top}\mathbf{g}^+ - \left(\dot{\mathbf{p}}^{+\top} + \mathbf{p}^{+\top}G_v{}^+\right)\mathbf{v}^+ = 0 \ . \tag{2.112}$$

Re-grouping terms and using Eqs. (2.98) and (2.100), the previous equation simplifies to

$$\mathbf{p}^\top \left[\left(\mathbf{g}^+ - G_v\mathbf{v}^+\right) - \left(\mathbf{g}^- - G_v\mathbf{v}^-\right) \right] - \dot{\mathbf{p}}^\top \left[\mathbf{v}^+ - \mathbf{v}^-\right] = 0 \ , \tag{2.113}$$

where the superscripts of G_v are removed as it is a constant matrix in the present case. In the PBRFBP, the quantity $(\mathbf{g} - G_v\mathbf{v})$ is evaluated employing Eqs. (2.14) and (2.26).

$$\mathbf{g} - G_v\mathbf{v} = \begin{bmatrix} +2\dot{y} + \dfrac{\partial\Omega}{\partial x} \\ -2\dot{x} + \dfrac{\partial\Omega}{\partial y} \end{bmatrix} - \begin{bmatrix} 0 & +2 \\ -2 & 0 \end{bmatrix} \begin{bmatrix} \dot{x} \\ \dot{y} \end{bmatrix} = \begin{bmatrix} \dfrac{\partial\Omega}{\partial x} \\ \dfrac{\partial\Omega}{\partial y} \end{bmatrix} . \tag{2.114}$$

From the definition of the pseudo-potential in Eq. (2.8), it is evident that Ω is a function only of the time t and the position vector $\mathbf{r}$. Similarly, its partial derivatives are dependent solely on the position coordinates of the spacecraft (see appendix A.1). Since these last are continuous across an impulsive maneuver so does the quantity $(\mathbf{g} - G_v\mathbf{v})$. Thus, the corresponding term in Eq. (2.113) vanishes, yielding to

$$\mathcal{H}^+ - \mathcal{H}^- = -\dot{\mathbf{p}}^\top \Delta\mathbf{v} = 0 \ , \tag{2.115}$$

where $\Delta\mathbf{v} = \mathbf{v}^+ - \mathbf{v}^-$ is the velocity discontinuity at the corner. As $\|\Delta\mathbf{v}\| \neq 0$ at an impulse, Eq. (2.115) is satisfied either if $\|\dot{\mathbf{p}}\| = 0$ or if $\dot{\mathbf{p}}$ and $\Delta\mathbf{v}$ are orthogonal each other. Recalling the first necessary condition stated in Proposition 2.1, the thrust direction, which in turn is parallel to $\Delta\mathbf{v}$, is aligned with the primer vector at the instant of the impulsive maneuver. Thus, Eq. (2.115) is equivalent to

$$\dot{\mathbf{p}}^\top \mathbf{p} = 0 \ . \tag{2.116}$$

Remember also that the magnitude of $\mathbf{p}$ has been previously determined to equal unity at the instant of an impulsive maneuver. Then, Eq. (2.116) is met when the derivative of the magnitude of the primer vector is zero at a corner. Moreover, from Eq. (2.69), the derivative of the switching function must also vanish at a corner.

This concludes the proof that, what was observed from graphical considerations (i.e., $\mathcal{S}$ and $\dot{\mathcal{S}}$ vanish and $\dot{\mathcal{S}}$ is continuous at a corner) is actually an outgrowth of the Weierstrass-Erdmann corner conditions.

Lawden's Impulsive Necessary Conditions

Finally, the first-order necessary conditions for an optimal impulsive transfer in the PBRFBP can be expressed entirely in terms of the primer vector.

Proposition 2.2 (Necessary Conditions for an Impulsive Fuel-Optimal Trajectory in the PBRFBP). — *Consider the Problem 2.1 in a planar bicircular rotating four-body model, where only impulsive maneuvers are allowed. Denote with t_k the instants when the impulses are applied, and so $\Delta\mathbf{v}(t_k) \neq \mathbf{0}$. The necessary conditions for an optimal trajectory, i.e., satisfying Theorem 2.1, require that:*

1. *The primer vector is continuous, has a continuous first derivative and satisfies the second order differential equation* (2.78)

$$\mathbf{p}(t) \in \mathcal{C}^1[t_i, t_f] \quad \textit{and} \quad \ddot{\mathbf{p}} = G_r\mathbf{p} + G_v\dot{\mathbf{p}} \ ;$$

2. *The magnitude of the primer vector is always less or equal than one, with impulses occurring at those instants when the magnitude of the primer is one*

$$\|\mathbf{p}(t)\| \leq 1 \quad \forall\, t \in [t_i, t_f] \quad \textit{and} \quad \|\mathbf{p}(t_k)\| = 1 \quad \forall\, t_k \in [t_i, t_f] \ ;$$

3. *At all impulses, the primer is a unit vector aligned in the thrust direction*

$$\mathbf{p}(t_k) = \frac{\Delta\mathbf{v}(t_k)}{\|\Delta\mathbf{v}(t_k)\|} \quad \forall\, t_k \in [t_i, t_f] \ ;$$

4. *At all interior impulses (not at the initial or final time), the scalar product between the primer vector and its first derivative is null; so, either the two are orthogonal or the magnitude of the primer vector derivative is null*

$$\dot{\mathbf{p}}(t_k)^\top \mathbf{p}(t_k) = 0 \quad \forall\, t_k \in (t_i, t_f) \ .$$

The previous conditions coincide with those derived by [7, 35, 36]. Also, except for the inclusion of the matrix G_v in the differential primer equation, the necessary conditions in Proposition 2.2 are identical to those obtained by Lawden for optimal transfers in a two-body problem [39]. Because of this, henceforward they will be referred to as Lawden's necessary conditions (LNC).

Only now, the renaming of the velocity adjoint variable is justified because of the key role played in this theory. Lawden explained the origin of the term primer vector in a personal letter in 1990: "In regard to the term *primer vector*, you are quite correct in your supposition. I served in the artillery during the war [World War II] and became familiar with the initiation of the burning of cordite by means of a primer charge. Thus, $p = 1$ is the signal for the rocket motor to be ignited."

3 | Methodology

In this chapter, Primer Vector theory is applied to the two-impulse Earth–Moon transfers described in section 2.2.1. Starting from an analytical result, a procedure is developed to further optimize the solutions that do not meet LNC. The selected trajectories are modified by adding a midcourse impulse such that the new three-impulse transfers are less expensive than the reference ones.

3.1. Non-Optimal Trajectories

It was already pointed out the difference between direct and indirect methods for space-trajectory optimization and the importance of checking whether some necessary conditions for optimality are met or not. The reference trajectories of [62] are computed with a direct method and the NLP problem is solved with a sequential quadratic programming algorithm implementing an active-set strategy (see [23] for details). The convergence of the algorithm guarantees local optimality (up to a fixed tolerance) but it is not known if these solutions also satisfy the analytical necessary conditions. Presumably, among the thousand reference solutions, some of them already meet LNC, but others can be further optimized. The litmus paper is the history of the primer vector associated with each reference trajectory. If a transfer path does not comply with the conditions stipulated for a fuel-optimal trajectory, ways of improving the non-optimal path are sought. Note that, henceforward, the term "optimal" is used as a substitute for "meets the first-order Lawden's necessary conditions".
The following methodology to improve non-optimal trajectories in the PBRFBP is inspired by [35], and it parallels Lion and Handselman's extension of primer vector theory to non-optimal trajectories in the two-body problem [40].

3.1.1. Primer Vector Magnitude

Let $\overline{\gamma}(\overline{\mathbf{x}}_i, t_i) = \{\varphi(\overline{\mathbf{x}}_i, t_i; t)\ \forall t \in [t_i, t_f]\}$ be a two-impulse reference trajectory, which connects two given states $\overline{\mathbf{x}}_i$ and $\overline{\mathbf{x}}_f$. The impulses are provided at the initial and final times: $\Delta\overline{\mathbf{v}}_i$ at $t = t_i$ and $\Delta\overline{\mathbf{v}}_f$ at $t = t_f$. The primer $\overline{\mathbf{p}}$ is defined as the solution to Eq. (2.81)

which satisfies the following boundary conditions (from LNC)

$$\overline{\mathbf{p}}(t_i) = \overline{\mathbf{p}}_i = \frac{\Delta\overline{\mathbf{v}}_i}{\|\Delta\overline{\mathbf{v}}_i\|} \ , \qquad \overline{\mathbf{p}}(t_f) = \overline{\mathbf{p}}_f = \frac{\Delta\overline{\mathbf{v}}_f}{\|\Delta\overline{\mathbf{v}}_f\|} \ . \tag{3.1}$$

Lion and Handselman showed in [40] that the primer vector gives a clear indication of how a trajectory can be improved. They observed from numerical results [29, 40] that the primer magnitude behavior falls into one of the first five categories shown in Fig. 3.1. These categories are meant to be representative of the qualitative history of the primer rather than exhaustive. It can be noted that each of the first four graphs (Figs. 3.1a to 3.1d) violates the second LNC reported in Proposition 2.2, according to which the magnitude of the primer must not exceed unity. Consequently, the corresponding trajectories for sure will not be optimal. Instead, Fig. 3.1e and Fig. 3.1f satisfy LNC. In particular, Fig. 3.1f represents an optimal three-impulse trajectory, because at the time of the midcourse impulse, both the primer and its derivative are continuous, the primer magnitude is unitary and its derivative is zero (in agreement with LNC).

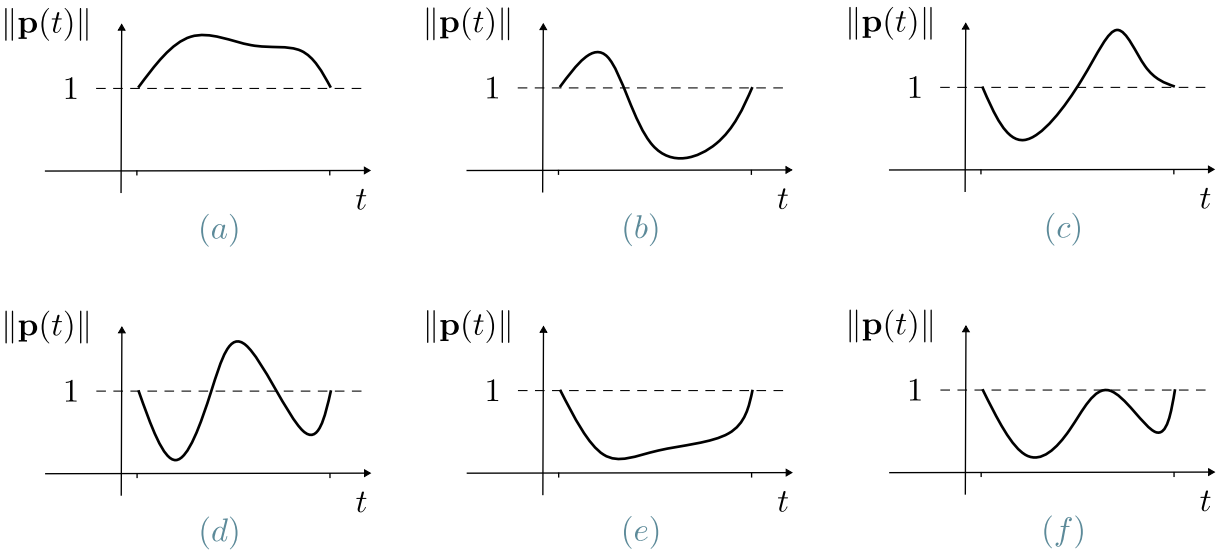

Figure 3.1: Different cases of primer vector qualitative behavior according to [40]; note that only case (e) and (f) satisfy LNC; this last is also the only one with three impulses

Given a specific set of boundary conditions and a fixed transfer time, an impulsive trajectory can be modified in two ways. One method involves allowing for a terminal coast, while the other entails incorporating a midcourse impulse.
An initial coast may be employed in the case of the former, where the first impulse takes place after the initial time, and the spacecraft coasts along its original trajectory until the initial impulse is executed. Alternatively, a final coast may be utilized, which involves the spacecraft reaching its destination before the final time, followed by coasting along its

final orbit until the designated endpoint is reached. Since it is wanted to keep the same boundary conditions, the addition of a terminal coast is not the focus of the present work. However, further discussions about this approach can be found in [7, 16, 27, 35, 36, 40], but the criteria for adding a terminal coast are reported for the sake of completeness.

Proposition 3.1 (Criteria for a Terminal Coast). — *If* $\|\dot{\mathbf{p}}(t_i)\| > 0$*, an initial coast will lower the total cost. Similarly, if* $\|\dot{\mathbf{p}}(t_f)\| < 0$*, a final coast will diminish the cost.*

Fore instance, these principles may be employed to lower the cost of the trajectories in Figs. 3.1a to 3.1c. Nevertheless, the current analysis aims to post-process a two-impulse reference solution whose primer behavior resembles the one in Fig. 3.1d, and to compute a neighboring three-impulse reference solution with a primer history similar to Fig. 3.1f. The problem of adding a new midcourse impulse to $\overline{\gamma}$ is addressed in the following section.

3.2. Criterion for an Additional Impulse

Besides terminal coasts, the addition of one or more midcourse impulses is another potential way of lowering the cost of an impulsive trajectory. First, an analytical criterion is developed to determine if adding an impulse will reduce the cost. Then, the optimal location and timing for the new impulse are computed in two steps: identifying a first initial guess for the position and time of the third impulse; iterating on these values until a minimum in the cost is achieved.

3.2.1. Definition of Perturbed Three-Impulse Trajectory

In order to investigate the effect of an additional impulse on the cost of the transfer, the reference two-impulse trajectory $\overline{\gamma}$ is compared with a neighboring trajectory γ, named *perturbed trajectory*, to which an interior impulse is added (see Fig. 3.2). Let indicate with the subscripts i^- and i^+ a quantity evaluated just before and after the first impulse, respectively. Analogously, f^- and f^+ represent a quantity across the final impulse. Both trajectories connects the same terminal states: $\overline{\mathbf{x}}_{i^-} = \mathbf{x}_{i^-}$ at $t = t_{i^-}$ and $\overline{\mathbf{x}}_{f^+} = \mathbf{x}_{f^+}$ at $t = t_{f^+}$. However, at an intermediate time $t = t_m$, $\overline{\gamma}$ and γ pass thorough two different midpoints: $\overline{\mathbf{x}}_m$ and $\mathbf{x}_m$, respectively. Of course, this is possible only assuming different terminal impulses, so also $\overline{\mathbf{v}}_{i^+} \neq \mathbf{v}_{i^+}$ and $\overline{\mathbf{v}}_{f^-} \neq \mathbf{v}_{f^-}$. Note that, as the maneuvers are impulsive, the positions are always continuous and do not necessitate the previous notation (e.g., $\mathbf{r}_i = \mathbf{r}_{i^+} = \mathbf{r}_{i^-}$).

Consider the first segment of γ, denoted as $\gamma^{(1)}$, which originates at $\{\mathbf{x}_{i^+}, t_{i^+}\}$ and terminates at $\{\mathbf{x}_{m^-}, t_{m^-}\}$. The position vector on $\gamma^{(1)}$ can be described as a Taylor series

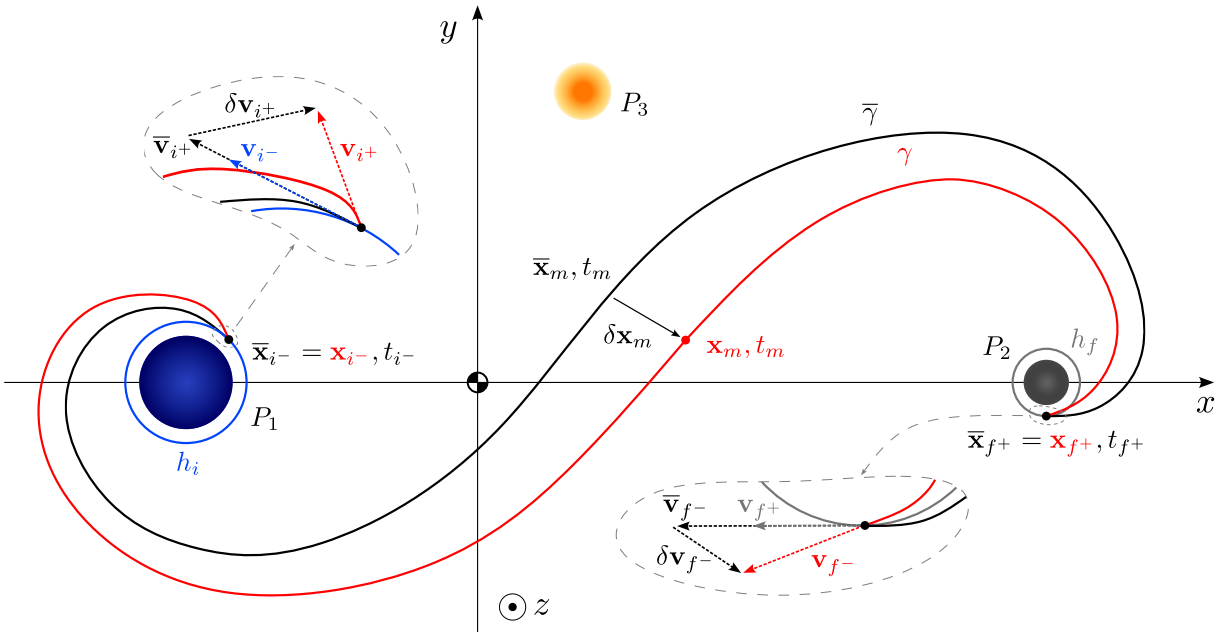

Figure 3.2: Two-impulse reference and three-impulse perturbed transfers (in *black* and *red*, respectively); the two trajectories share the same terminal conditions and transfer time, the midcourse impulse of the latter is located at time t_m

expansion, which, to the first order, reads

$$\mathbf{r}(t) = \overline{\mathbf{r}}(t) + \frac{\partial \overline{\mathbf{r}}(t)}{\partial \overline{\mathbf{r}}_i}\delta\mathbf{r}_i + \frac{\partial \overline{\mathbf{r}}(t)}{\partial \overline{\mathbf{v}}_{i+}}\delta\mathbf{v}_{i+} \ , \tag{3.2}$$

where it is recalled that the symbol δ is used to express the difference between the perturbed and the reference trajectory (e.g., $\delta\mathbf{r}(t) = \mathbf{r}(t) - \overline{\mathbf{r}}(t)$). Since $\gamma^{(1)}$ and $\overline{\gamma}$ have the same initial position, then $\delta\mathbf{r}_i(t) = \mathbf{0}$; therefore Eq. (3.2) can be evaluated at $t = t_{m^-}$ and rearranged to yield

$$\delta\mathbf{v}_{i+} = \left[\frac{\partial \overline{\mathbf{r}}_{m^-}}{\partial \overline{\mathbf{v}}_{i+}}\right]^{-1} \delta\mathbf{r}_{m^-} \ . \tag{3.3}$$

Next, consider the second segment $\gamma^{(2)}$, which originates at $\{\mathbf{x}_{m^+}, t_{m^+}\}$ and terminates at $\{\mathbf{x}_{f^-}, t_{f^-}\}$. Once again, the position vector of $\gamma^{(2)}$ can be expressed with a first-order Taylor expansion with respect to the final state $\mathbf{x}_{f^-}$

$$\mathbf{r}(t) = \overline{\mathbf{r}}(t) + \frac{\partial \overline{\mathbf{r}}(t)}{\partial \overline{\mathbf{r}}_f}\delta\mathbf{r}_f + \frac{\partial \overline{\mathbf{r}}(t)}{\partial \overline{\mathbf{v}}_{f^-}}\delta\mathbf{v}_{f^-} \ , \tag{3.4}$$

Now, $\gamma^{(2)}$ and $\overline{\gamma}$ have the same final position, so $\delta\mathbf{r}_f(t) = \mathbf{0}$; Eq. (3.4), evaluated at $t = t_{m^+}$ and rearranged, results in

$$\delta\mathbf{v}_{f^-} = \left[\frac{\partial\overline{\mathbf{r}}_{m^+}}{\partial\overline{\mathbf{v}}_{f^-}}\right]^{-1}\delta\mathbf{r}_{m^+} \ . \tag{3.5}$$

The partial derivatives in Equations (3.3) and (3.5) coincide with the sub-matrices of the STM associated to $\overline{\gamma}$:

$$\delta\mathbf{v}_{i^+} = \overline{\Phi}_{rv}^{-1}(t_{i^+}, t_{m^-})\delta\mathbf{r}_{m^-} \ , \tag{3.6a}$$

$$\delta\mathbf{v}_{f^-} = \overline{\Phi}_{rv}^{-1}(t_{f^-}, t_{m^+})\delta\mathbf{r}_{m^+} \ . \tag{3.6b}$$

Thus, a neighboring three-impulse trajectory exists if both $\overline{\Phi}_{rv}(t_{i^+}, t_{m^-})$ and $\overline{\Phi}_{rv}(t_{f^-}, t_{m^+})$ are nonsingular. Their values are evaluated integrating together Eqs. (2.7) and (2.23) forward in time from $t_{i^+} \to t_{m^-}$ and backward in time from $t_{f^-} \to t_{m^+}$.

3.2.2. Cost Function

Suppose that the reference trajectory $\overline{\gamma}$ is one of the Earth–Moon transfers described in section 2.2.1; its cost is

$$J_{\overline{\gamma}} = \|\Delta\overline{\mathbf{v}}_i\| + \|\Delta\overline{\mathbf{v}}_f\| \ , \tag{3.7}$$

where $\Delta\overline{\mathbf{v}}_i$ and $\Delta\overline{\mathbf{v}}_f$ are the impulsive maneuvers at the initial and final time, respectively. Instead, the perturbed trajectory γ is composed of three impulses:

$$J_\gamma = \|\Delta\mathbf{v}_i\| + \|\Delta\mathbf{v}_m\| + \|\Delta\mathbf{v}_f\| \ , \tag{3.8}$$

with the intermediate impulse occurring at time $t = t_m$. The cost J_γ can be written in terms of the variations with respect to the reference trajectory

$$J_\gamma = \|\Delta\overline{\mathbf{v}}_i + \delta\Delta\mathbf{v}_i\| + \|\Delta\overline{\mathbf{v}}_m + \delta\Delta\mathbf{v}_m\| + \|\Delta\mathbf{v}_f + \delta\Delta\mathbf{v}_f\| \ . \tag{3.9}$$

However, as long as the two trajectories share the same terminal states (before the initial impulse and after the final impulse): $\overline{\mathbf{v}}_{i^-} = \mathbf{v}_{i^-}$ and $\overline{\mathbf{v}}_{f^+} = \mathbf{v}_{f^+}$. Thus

$$\delta\Delta\mathbf{v}_i = \Delta\mathbf{v}_i - \Delta\overline{\mathbf{v}}_i = (\mathbf{v}_{i^+} - \mathbf{v}_{i^-}) - (\overline{\mathbf{v}}_{i^+} - \overline{\mathbf{v}}_{i^-}) = \mathbf{v}_{i^+} - \overline{\mathbf{v}}_{i^+} = \delta\mathbf{v}_{i^+} \ , \tag{3.10a}$$

$$\delta\Delta\mathbf{v}_f = \Delta\mathbf{v}_f - \Delta\overline{\mathbf{v}}_f = (\mathbf{v}_{f^+} - \mathbf{v}_{f^-}) - (\overline{\mathbf{v}}_{f^+} - \overline{\mathbf{v}}_{f^-}) = -\mathbf{v}_{f^-} + \overline{\mathbf{v}}_{f^-} = -\delta\mathbf{v}_{f^-} \ . \tag{3.10b}$$

Moreover, being the velocity of the reference trajectory continuous at $t = t_m$, $\Delta\overline{\mathbf{v}}_m = \mathbf{0}$. Accordingly, the cost of the perturbed trajectory simplifies to

$$J_\gamma = \|\Delta\overline{\mathbf{v}}_i + \delta\mathbf{v}_{i^+}\| + \|\delta\Delta\mathbf{v}_m\| + \|\Delta\mathbf{v}_f - \delta\mathbf{v}_{f^-}\| \ . \tag{3.11}$$

The difference in cost, indicated with ΔJ, is computed subtracting Eq. (3.7) to Eq. (3.11)

$$\Delta J = J_\gamma - J_{\overline{\gamma}} = \|\Delta\overline{\mathbf{v}}_i + \delta\mathbf{v}_{i^+}\| - \|\Delta\overline{\mathbf{v}}_i\| + \|\delta\Delta\mathbf{v}_m\| + \|\Delta\mathbf{v}_f - \delta\mathbf{v}_{f^-}\| - \|\Delta\overline{\mathbf{v}}_f\| \ . \quad (3.12)$$

Let denote with δJ the first-order approximation of the cost variation ΔJ. The analytical expression of δJ is hereafter derived in order to examine the feasibility of implementing an additional impulse such that the overall fuel expenditure is reduced. First, note that Eq. (3.12) contains the differences between the magnitudes of some vectors. It is proved in appendix A.2, that these differences can be written, to the first order, as

$$\|\Delta\overline{\mathbf{v}}_i + \delta\mathbf{v}_{i^+}\| - \|\Delta\overline{\mathbf{v}}_i\| = \frac{\Delta\overline{\mathbf{v}}_i^\top}{\|\Delta\overline{\mathbf{v}}_i\|}\delta\mathbf{v}_{i^+} \ , \quad (3.13a)$$

$$\|\Delta\overline{\mathbf{v}}_f - \delta\mathbf{v}_{f^-}\| - \|\Delta\overline{\mathbf{v}}_f\| = -\frac{\Delta\overline{\mathbf{v}}_f^\top}{\|\Delta\overline{\mathbf{v}}_f\|}\delta\mathbf{v}_{f^-} \ . \quad (3.13b)$$

Substituting Eqs. (3.13a) and (3.13b) into Eq. (3.12), and renaming ΔJ into δJ

$$\delta J = \frac{\Delta\overline{\mathbf{v}}_i^\top}{\|\Delta\overline{\mathbf{v}}_i\|}\delta\mathbf{v}_{i^+} + \|\delta\Delta\mathbf{v}_m\| - \frac{\Delta\overline{\mathbf{v}}_f^\top}{\|\Delta\overline{\mathbf{v}}_f\|}\delta\mathbf{v}_{f^-} \ . \quad (3.14)$$

From Eq. (3.1), at the endpoints of the reference trajectory, the primer is a unit vector aligned with the velocity increments; hence, the cost variation results in

$$\delta J = \overline{\mathbf{p}}_{i^+}^\top\delta\mathbf{v}_{i^+} + \|\delta\Delta\mathbf{v}_m\| - \overline{\mathbf{p}}_{f^-}^\top\delta\mathbf{v}_{f^-} \ . \quad (3.15)$$

Recall, that the adjoint equation (2.93) was previously determined to be valid everywhere on a coastal arc of a perturbed trajectory. Therefore it can be evaluated at the boundaries of the two coastal arcs of γ.

- On the first arc, $\gamma^{(1)}$:

$$\text{for } t = t_{i^+} \qquad \overline{\mathbf{p}}_{i^+}^\top\delta\mathbf{v}_{i^+} - \left(\dot{\overline{\mathbf{p}}}_{i^+}^\top + \overline{\mathbf{p}}_{i^+}^\top G_{v_{i^+}}\right)\delta\mathbf{r}_{i^+} = c_1 \ , \quad (3.16a)$$

$$\text{for } t = t_{m^-} \qquad \overline{\mathbf{p}}_{m^-}^\top\delta\mathbf{v}_{m^-} - \left(\dot{\overline{\mathbf{p}}}_{m^-}^\top + \overline{\mathbf{p}}_{m^-}^\top G_{v_{m^-}}\right)\delta\mathbf{r}_{m^-} = c_1 \ , \quad (3.16b)$$

where c_1 is a constant. Recalling that $\delta\mathbf{r}_{i^+} = \mathbf{0}$ and equating the two expressions

$$\overline{\mathbf{p}}_{i^+}^\top\delta\mathbf{v}_{i^+} = \overline{\mathbf{p}}_{m^-}^\top\delta\mathbf{v}_{m^-} - \left(\dot{\overline{\mathbf{p}}}_{m^-}^\top + \overline{\mathbf{p}}_{m^-}^\top G_{v_{m^-}}\right)\delta\mathbf{r}_{m^-} \ . \quad (3.17)$$

- On the second arc, $\gamma^{(2)}$:

$$\text{for } t = t_{m^+} \qquad \overline{\mathbf{p}}_{m^+}^\top \delta\mathbf{v}_{m^+} - \left(\dot{\overline{\mathbf{p}}}_{m^+}^\top + \overline{\mathbf{p}}_{m^+}^\top G_{v_{m^+}}\right)\delta\mathbf{r}_{m^+} = c_2 \ , \tag{3.18a}$$

$$\text{for } t = t_{f^-} \qquad \overline{\mathbf{p}}_{f^-}^\top \delta\mathbf{v}_{f^-} - \left(\dot{\overline{\mathbf{p}}}_{f^-}^\top + \overline{\mathbf{p}}_{f^-}^\top G_{v_{f^-}}\right)\delta\mathbf{r}_{f^-} = c_2 \ , \tag{3.18b}$$

where c_2 is another constant. Since $\delta\mathbf{r}_{f^-} = \mathbf{0}$, equating the two expressions yields

$$\overline{\mathbf{p}}_{f^-}^\top \delta\mathbf{v}_{f^-} = \overline{\mathbf{p}}_{m^+}^\top \delta\mathbf{v}_{m^+} - \left(\dot{\overline{\mathbf{p}}}_{m^+}^\top + \overline{\mathbf{p}}_{m^+}^\top G_{v_{m^+}}\right)\delta\mathbf{r}_{m^+} \ . \tag{3.19}$$

Subtracting Eq. (3.19) from Eq. (3.17)

$$\overline{\mathbf{p}}_{i^+}^\top \delta\mathbf{v}_{i^+} - \overline{\mathbf{p}}_{f^-}^\top \delta\mathbf{v}_{f^-} = \left[\overline{\mathbf{p}}_m^\top \delta\mathbf{v}_m - \left(\dot{\overline{\mathbf{p}}}_m^\top + \overline{\mathbf{p}}_m^\top G_{v_m}\right)\delta\mathbf{r}_m\right]_+^- \ . \tag{3.20}$$

Since the primer vector and its derivative are evaluated on the reference trajectory $\overline{\gamma}$, which is a coastal arc (i.e., no impulses exist interior to the terminal impulses), $\overline{\mathbf{p}}_m$ and $\dot{\overline{\mathbf{p}}}_m$ are continuous. Additionally, also G_v is computed on the reference trajectory, and being the state $\overline{\mathbf{x}}$ continuous at $t = t_m$, also G_{v_m} must be continuous. Thus, for these three quantities the '+' and '–' subscripts can be dropped and Eq. (3.20) simplifies to

$$\overline{\mathbf{p}}_{i^+}^\top \delta\mathbf{v}_{i^+} - \overline{\mathbf{p}}_{f^-}^\top \delta\mathbf{v}_{f^-} = \overline{\mathbf{p}}_m^\top \left(\delta\mathbf{v}_{m^-} - \delta\mathbf{v}_{m^+}\right) + \left(\dot{\overline{\mathbf{p}}}_m^\top + \overline{\mathbf{p}}_m^\top G_{v_m}\right)\left(\delta\mathbf{r}_{m^+} - \delta\mathbf{r}_{m^-}\right) \ . \tag{3.21}$$

Moreover, despite a discontinuity in the velocity is allowed for γ at $t = t_m$, the position on the perturbed trajectory still requires to be continuous at such instant (i.e., $\delta\mathbf{r}_{m^+} = \delta\mathbf{r}_{m^-}$); thus, the last term of Eq. (3.21) vanishes and the previous equation becomes

$$\overline{\mathbf{p}}_{i^+}^\top \delta\mathbf{v}_{i^+} - \overline{\mathbf{p}}_{f^-}^\top \delta\mathbf{v}_{f^-} = \overline{\mathbf{p}}_m^\top \left(\delta\mathbf{v}_{m^-} - \delta\mathbf{v}_{m^+}\right) \ . \tag{3.22}$$

At this point, Eq. (3.22) is replaced into the first-order variation of the cost (Eq. (3.15)):

$$\delta J = -\overline{\mathbf{p}}_m^\top \left(\delta\mathbf{v}_{m^+} - \delta\mathbf{v}_{m^-}\right) + \left\|\delta\mathbf{v}_{m^+} - \delta\mathbf{v}_{m^-}\right\| \ . \tag{3.23}$$

Equation (3.23) expresses δJ solely in terms of the primer vector at the interior impulse, and the intermediate velocity increment, but this last coincides with $\Delta\mathbf{v}_m$. Indeed,

$$\delta\mathbf{v}_{m^+} - \delta\mathbf{v}_{m^-} = \delta\Delta\mathbf{v}_m = \Delta\mathbf{v}_m - \Delta\overline{\mathbf{v}}_m = \Delta\mathbf{v}_m \ , \tag{3.24}$$

because in the reference trajectory no mid-course impulse is present ($\Delta\overline{\mathbf{v}}_m = \mathbf{0}$). Let κ denote the magnitude of the intermediate impulse, and $\hat{\boldsymbol{\kappa}}$ be a unit vector in the direction of the impulse. Substituting $\delta\mathbf{v}_{m^+} - \delta\mathbf{v}_{m^-} = \Delta\mathbf{v}_m \equiv \kappa\hat{\boldsymbol{\kappa}}$ into Equation (3.23)

$$\delta J = \kappa \left(1 - \overline{\mathbf{p}}_m^\top \hat{\boldsymbol{\kappa}}\right) \ . \tag{3.25}$$

If δJ can be made negative, then γ represents an improvement in the cost over $\overline{\gamma}$. Looking at Eq. (3.25), this is possible only if the magnitude of the primer vector at $t = t_m$ is greater than unity. Therefore, Eq. (3.25) can be interpreted as an alternate proof of LNC for $\overline{\gamma}$ to be optimal. Indeed, if $\|\overline{\mathbf{p}}_m\|$ is always less than unity, there is no chance that a neighboring three-impulse trajectory presents a lower cost; thus $\overline{\gamma}$ itself is already optimal. Furthermore, Eq. (3.25) is used to develop the criterion for the inclusion of an intermediate impulse on a reference trajectory in order to reduce the overall cost.

Proposition 3.2 (Criterion for an Additional Midcourse Impulse). — *Consider a reference trajectory $\overline{\gamma}$, generated by an initial and a final impulsive maneuver, whose total characteristic velocity is $J_{\overline{\gamma}}$. Let γ be a neighboring perturbed trajectory, with the same terminal conditions of $\overline{\gamma}$ but with an additional intermediate impulse. A perturbed trajectory γ with a cost J_γ lower than $J_{\overline{\gamma}}$ exists if the primer vector magnitude evaluated over $\overline{\gamma}$ exceeds unity at an intermediate time.*

$$\textit{If } \exists\ t_m \in (t_i, t_f)\ \textit{ s.t. }\ \|\overline{\mathbf{p}}(t_m)\| > 1,\ \textit{ then } \exists\ \gamma\ \textit{ s.t. } J_\gamma < J_{\overline{\gamma}}\ .$$

Moreover, the cost difference between the two is, to the first-order:

$$\delta J = \kappa \left(1 - \overline{\mathbf{p}}_m^\top \hat{\boldsymbol{\kappa}}\right) \ ,$$

where κ denotes the magnitude of the intermediate maneuver, and $\hat{\boldsymbol{\kappa}}$ its direction.

Equation (3.25) suggests that the greatest improvement in cost, to first-order, is obtained when the product $\overline{\mathbf{p}}_m^\top \hat{\boldsymbol{\kappa}}$ is maximum. This can be obtained by applying the intermediate impulse in the direction of the primer, at the instant when the primer magnitude is maximum. However, the position, as well as the magnitude of the interior impulse, are yet to be determined. The location of the new impulse in space and time is done in two steps. The first step is to determine initial values for position and time midcourse impulse that will lower the cost. The second step is to iterate on the values of position and time until a minimum in the cost is achieved.

3.2.3. Insertion of a Midcourse Impulse

In order to build a perturbed-three impulse trajectory, a first guess for the position and time of the midcourse impulse is necessary. The time of maximum primer magnitude is selected as an initial estimate of t_m. Note, that this choice does not guarantee that the decrease in cost is maximized, because the value of $\Delta\mathbf{v}_m$ in the expression for δJ depends on the value of t_m. However, what is needed is just an initial position and time of the midcourse impulse to begin an iteration process. So, as long as the initial choice represents a decrease in the cost, it is decided for the simple device of choosing t_m as the time of maximum primer magnitude. Instead, the initial position of the impulse, namely the value $\delta\mathbf{r}_m$ to be added to $\bar{\mathbf{r}}_m$, is chosen so that the velocity change is in the direction of the primer vector. Indeed, this sounds familiar because it is one of the LNC derived previously, but how to determine $\bar{\mathbf{r}}_m$ is not straightforward.

First, let investigate the effect that the initial and final impulses have on the position and velocity of the mid-course impulse. Using the results of Eq. (2.86), the state transition matrix can be evaluated on the reference trajectory from $t_{i^+} \to t_{m^-}$, yielding to

$$\delta\mathbf{r}_{m^-} = \overline{\Phi}_{rv}(t_{i^+}, t_{m^-})\delta\mathbf{v}_{i^+} \ , \tag{3.26a}$$

$$\delta\mathbf{v}_{m^-} = \overline{\Phi}_{vv}(t_{i^+}, t_{m^-})\delta\mathbf{v}_{i^+} \ , \tag{3.26b}$$

where it is also used that $\delta\mathbf{r}_i = \mathbf{0}$. Again, evaluating Eq. (2.86) from $t_{f^-} \to t_{m^+}$ and recalling that $\delta\mathbf{r}_f = \mathbf{0}$,

$$\delta\mathbf{r}_{m^+} = \overline{\Phi}_{rv}(t_{f^-}, t_{m^+})\delta\mathbf{v}_{f^-} \ , \tag{3.27a}$$

$$\delta\mathbf{v}_{m^+} = \overline{\Phi}_{vv}(t_{f^-}, t_{m^+})\delta\mathbf{v}_{f^-} \ . \tag{3.27b}$$

Equations (3.26b) and (3.27b) are substituted into Eq. (3.24):

$$\Delta\mathbf{v}_m = \delta\mathbf{v}_{m^+} - \delta\mathbf{v}_{m^-} = \overline{\Phi}_{vv}(t_{f^-}, t_{m^+})\delta\mathbf{v}_{f^-} - \overline{\Phi}_{vv}(t_{i^+}, t_{m^-})\delta\mathbf{v}_{i^+} \ . \tag{3.28}$$

The values of $\delta\mathbf{v}_{f^-}$ and $\delta\mathbf{v}_{i^+}$ can be expressed by inverting Eqs. (3.26a) and (3.27a), and noting that the position continuity requires $\delta\mathbf{r}_{m^-} = \delta\mathbf{r}_{m^+} = \delta\mathbf{r}_m$. It results

$$\Delta\mathbf{v}_m = \left[\overline{\Phi}_{vv}(t_{f^-}, t_{m^+})\overline{\Phi}_{rv}^{-1}(t_{f^-}, t_{m^+}) - \overline{\Phi}_{vv}(t_{i^+}, t_{m^-})\overline{\Phi}_{rv}^{-1}(t_{i^+}, t_{m^-})\right]\delta\mathbf{r}_m \ . \tag{3.29}$$

Hence, the variation of the position of the mid-course maneuver can be written as a function of the intermediate impulse itself:

$$\delta\mathbf{r}_m = K^{-1}\Delta\mathbf{v}_m \ , \tag{3.30}$$

where the matrix K must be nonsingular and is defined as

$$K \equiv \overline{\Phi}_{vv}(t_{f^-}, t_{m^+})\overline{\Phi}_{rv}^{-1}(t_{f^-}, t_{m^+}) - \overline{\Phi}_{vv}(t_{i^+}, t_{m^-})\overline{\Phi}_{rv}^{-1}(t_{i^+}, t_{m^-}) \ . \tag{3.31}$$

For the maximum improvement in cost $\Delta\mathbf{v}_m \equiv \kappa\hat{\boldsymbol{\kappa}}$ should be aligned with $\overline{\mathbf{p}}_m$. Hence

$$\delta\mathbf{r}_m = \kappa K^{-1}\frac{\overline{\mathbf{p}}_m}{\|\overline{\mathbf{p}}_m\|} \ . \tag{3.32}$$

If the value of κ is selected small enough to justify a first order analysis, the previous choice for $\delta\mathbf{r}_m$ ensures that $\Delta\mathbf{v}_m$ and $\overline{\mathbf{p}}_m$ are aligned at the time t_m when $\|\overline{\mathbf{p}}(t)\|$ is maximum, which is compliant with the third LNC.

3.2.4. Building a Perturbed Three-Impulse Trajectory

Once the location in time and space of the midcourse impulse is determined, it is needed to build a trajectory connecting the prescribed initial and final states with the newly computed position of the intermediate maneuver. Therefore, a double shooting problem must be set up, which consists in solving two Lambert's problems:

- connecting the states $\{\overline{\mathbf{r}}_i,\, t_i\}$ with $\{\overline{\mathbf{r}}_m + \delta\mathbf{r}_m,\, t_m\}$;
- connecting the states $\{\overline{\mathbf{r}}_f,\, t_f\}$ with $\{\overline{\mathbf{r}}_m + \delta\mathbf{r}_m,\, t_m\}$;

where $\delta\mathbf{r}_m$ is chosen accordingly to Eq. (3.32), and t_m is the time on the reference trajectory when the primer magnitude attains its maximum.
As the terminal positions and times must coincide with those of the reference trajectory, the only unknowns of the problem are the initial velocity just after the first impulse $\mathbf{v}_{i^+}$, and the final one before the last maneuver $\mathbf{v}_{f^-}$. Indeed, as the states $\mathbf{x}_{i^-}$ and $\mathbf{x}_{f^+}$ are prescribed and coincide with those of $\overline{\gamma}$, the values of the new impulses $(\Delta\mathbf{v}_i, \Delta\mathbf{v}_f)$ can be recovered later. Note, that the shooting problem could also have been set up with the velocity variations as unknowns, but this would have implied more cumbersome computations of the jacobian of the objective function.

The idea of the solution method, represented in Fig. 3.3, consists in guessing the values of $\mathbf{v}_{i^+}$ and $\mathbf{v}_{f^-}$ and propagating the two states (forward and backward in time) until the continuity on the position is satisfied. Moreover, the two red arcs of Fig. 3.3 must meet at a precise position specified by $\delta\mathbf{r}_m$. The problem is actually a root-finding problem with 4 unknowns and a 4-dimensional objective function (recall that the current model is planar, so only two coordinates are of interest), and it can be stated as follows.

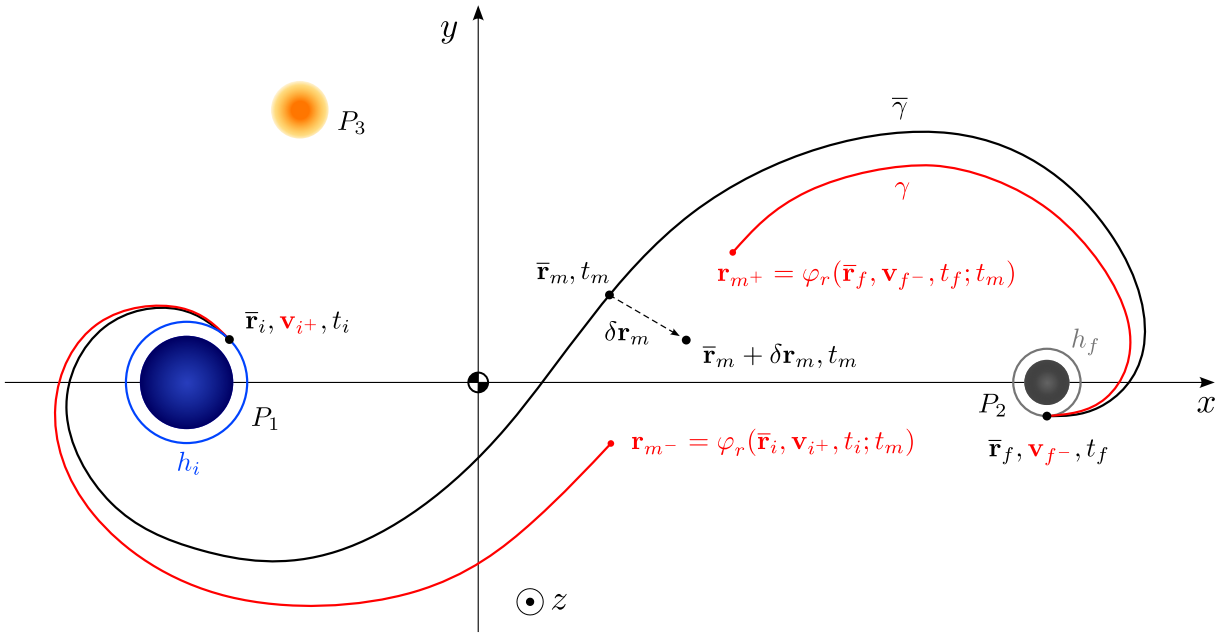

Figure 3.3: Representation of the forward-backward shooting problem solved to build the perturbed trajectory (in *red*), whose midcourse impulse occurs at $t = t_m$ and is located at $\mathbf{r}_m = \bar{\mathbf{r}}_m + \delta\mathbf{r}_m$; the unknowns of the problem are the velocities $\mathbf{v}_{i^+}$ and $\mathbf{v}_{f^-}$

Problem 3.1 (Forward-Backward Shooting). — *Consider a two-impulse reference trajectory $\overline{\gamma}$ connecting the states $\{\bar{\mathbf{x}}_i, t_i\}$ and $\{\bar{\mathbf{x}}_f, t_f\}$. Find $\mathbf{v}_{i^+}$ and $\mathbf{v}_{f^-}$ such that their propagation forward and backward in time, respectively, have a position matching $\mathbf{r}_m = \bar{\mathbf{r}}_m + \delta\mathbf{r}_m$ at time $t = t_m$.*

$$\textit{Given } \mathbf{r}_m, \textit{ find } \{\mathbf{v}_{i^+}, \mathbf{v}_{f^-}\} \textit{ s.t. } \mathbf{F} := \begin{bmatrix} \varphi_r(\bar{\mathbf{r}}_i, \mathbf{v}_{i^+}, t_i; t_m) - \mathbf{r}_m \\ \varphi_r(\bar{\mathbf{r}}_f, \mathbf{v}_{f^-}, t_f; t_m) - \mathbf{r}_m \end{bmatrix} = \mathbf{0} \ .$$

Once the values of the unknowns are found, the perturbed trajectory is completely determined, and its cost can be computed:

$$J_\gamma = \|\mathbf{v}_{i^+} - \bar{\mathbf{v}}_{i^-}\| + \kappa + \|\bar{\mathbf{v}}_{f^+} - \mathbf{v}_{f^-}\| \tag{3.33}$$

As it will be described in section 4.3.1, Problem 3.1 is solved by means of an iterative procedure; so the values for the first guess of the unknowns are needed. These are computed from the velocities of the reference trajectory, to which the first order variations generated by $\delta\mathbf{r}_m$ are added:

$$\mathbf{v}_{i^+}^{(0)} = \bar{\mathbf{v}}_{i^+} + \bar{\Phi}_{rv}^{-1}(t_i, t_m)\delta\mathbf{r}_m \ , \qquad \mathbf{v}_{f^-}^{(0)} = \bar{\mathbf{v}}_{f^-} + \bar{\Phi}_{rv}^{-1}(t_f, t_m)\delta\mathbf{r}_m \ . \tag{3.34a}$$

Moreover, as a gradient-based algorithm will be employed, the jacobian of the objective function $\mathbf{F}$ is computed analytically for higher computational efficiency. Thanks to the choice of the unknowns, the expressions of the derivatives are quite simple:

$$\frac{\partial \mathbf{F}}{\partial \mathbf{v}_{i^+}} = \begin{bmatrix} \overline{\Phi}_{rv}(t_i, t_m) \\ 0_2 \end{bmatrix} , \qquad \frac{\partial \mathbf{F}}{\partial \mathbf{v}_{f^-}} = \begin{bmatrix} 0_2 \\ \overline{\Phi}_{rv}(t_f, t_m) \end{bmatrix} . \tag{3.35}$$

3.2.5. Movement of the Interior Impulse

It was previously mentioned, that the primer magnitude on a reference two-impulse trajectory that requires an additional impulse may resemble qualitatively the behavior of Fig. 3.4a. However, the inclusion of an additional impulse (as it was discussed up to this point) does not necessarily yield an optimal three-impulse trajectory. The time history of the primer vector magnitude on the newly computed perturbed trajectory must be examined again, in order to verify the compliance with LNC. Although the primer is continuous and is a unit vector at each impulse, a typical non-optimal trajectory is characterized by a cusp at the location of the intermediate impulse, as in Fig. 3.4b. Therefore, the necessary condition for optimality which requires $\dot{\mathbf{p}}$ to be continuous at each interior impulse is not met, and a neighboring three-impulse solution with a lower cost must exist (see Fig. 3.4c). This optimal solution is named *refined trajectory*, and hereafter the second and last step for the optimization procedure is described.

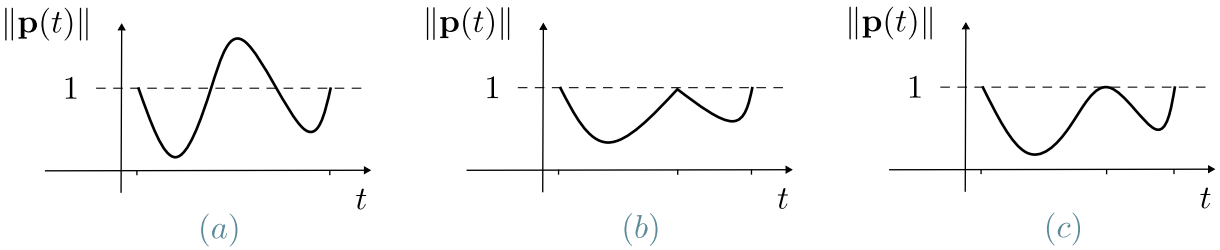

Figure 3.4: Primer vector magnitude on a reference two-impulsive trajectory (a), a perturbed three-impulse trajectory (b), and an optimal three-impulse trajectory (c)

Let $\tilde{\gamma}$ denote a refined three-impulse trajectory, that shares the same terminal conditions with $\overline{\gamma}$ and γ, but, differently from the perturbed trajectory, the midcourse impulse is allowed to be located at $\tilde{t}_m \neq t_m$. $\tilde{\gamma}$ consists of two ballistic arcs connecting the states

$$\{\overline{\mathbf{r}}_i,\, t_i\} \rightarrow \left\{\tilde{\mathbf{r}}_m\, \tilde{t}_m\right\} ,$$
$$\left\{\tilde{\mathbf{r}}_m\, \tilde{t}_m\right\} \rightarrow \{\overline{\mathbf{r}}_f,\, t_f\} .$$

If the symbol ‘d’ indicates a *non-contemporaneous variation*, then the position and time

of the intermediate maneuver on the refined trajectory can be expressed as

$$\tilde{t}_m = \bar{t}_m + \mathrm{d}t_m = t_m + \mathrm{d}t_m \ , \tag{3.36a}$$

$$\tilde{\mathbf{r}}_m = \bar{\mathbf{r}}_m + \mathrm{d}\mathbf{r}_m \ . \tag{3.36b}$$

As usual, the cost of $\tilde{\gamma}$ is the sum of the velocity increments of all the maneuvers

$$J_{\tilde{\gamma}} = \|\Delta\tilde{\mathbf{v}}_i\| + \|\Delta\tilde{\mathbf{v}}_m\| + \|\Delta\tilde{\mathbf{v}}_f\| \ . \tag{3.37}$$

The following expression for the cost difference between the refined and the reference three-impulse trajectory is developed in [35] and [37]:

$$\mathrm{d}J = J_{\tilde{\gamma}} - J_{\gamma} = \left[\dot{\mathbf{p}}_{m^+}^{\top} - \dot{\mathbf{p}}_{m^-}^{\top}\right] \mathrm{d}\mathbf{r}_m + \left[\mathcal{H}_{m^+} - \mathcal{H}_{m^-}\right] \mathrm{d}t_m \ . \tag{3.38}$$

If the refined trajectory is an optimum, $\mathrm{d}J = 0$; consequently both the Hamiltonian and the primer derivative must be continuous across the intermediate impulse. This is consistent with the results of Weierstrass-Erdmann conditions for an optimal trajectory and constitutes an alternate proof of the last LNC.

3.2.6. Building a Refined Three-Impulse Trajectory

The idea now is to iterate on the position and time of the mid-course impulse, in the neighborhood of the perturbed trajectory γ, until a local minimum of $J_{\tilde{\gamma}}$ is reached (see Fig. 3.5). This can be done by setting up a NLP problem, whose unknowns are $\tilde{\mathbf{r}}_m$ and $\tilde{t}_m$. However, the two arcs of the solution must meet at the position of the second impulse (i.e., it must be $\tilde{\mathbf{r}}_{m^-} = \tilde{\mathbf{r}}_{m^+}$ in Fig. 3.5) and this depends on the velocities just after the initial impulse, and before the last one. Therefore, to avoid solving a shooting problem at each iteration of the NLP problem, both $\tilde{\mathbf{v}}_{i^+}$ and $\tilde{\mathbf{v}}_{f^-}$ are considered among the unknowns of the problem. These are collected in a vector of NLP variables $\mathbf{y} \in \mathbb{R}^7$

$$\mathbf{y} \equiv \left(\tilde{\mathbf{v}}_{i^+},\, \tilde{\mathbf{v}}_{f^-},\, \tilde{\mathbf{r}}_m,\, \tilde{t}_m\right)^{\top} \ . \tag{3.39}$$

In such a way, the continuity on the position at $\tilde{t}_m$ is treated as a nonlinear equality constraint. Also, the time of the midcourse impulse must be within the interval delimited by t_i and t_f. Theoretically, one could also think to include some constraints about $\dot{\mathbf{p}}_m$ and $\mathcal{H}_m$ in order to respect LNC. Unfortunately, with this choice, it would not possible to compute analytically the jacobians of the constraints, and the required calculations would burden the numerical resolution.

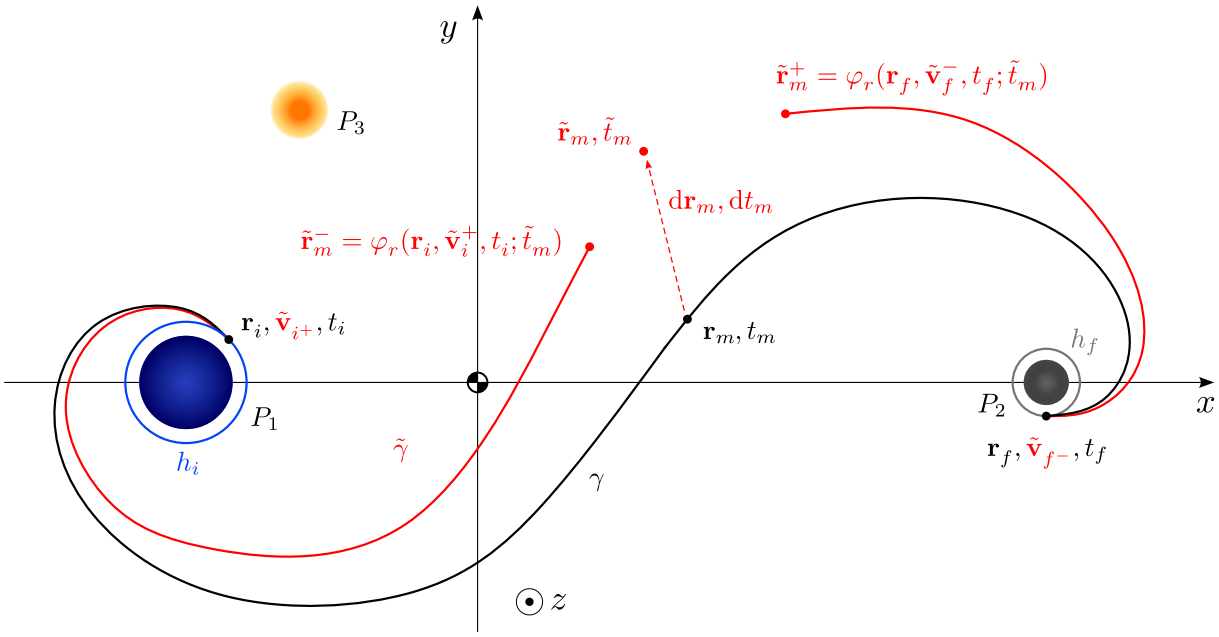

Figure 3.5: Optimization problem solved to compute the three-impulse refined trajectory (*red*), starting from a three-impulse perturbed trajectory (*black*)

So, the problem is converted into a parameter optimization problem, with a scalar objective function, four scalar equality constraints and two inequality constraints.

Problem 3.2 (Three-Impulse Trajectory Optimization). — *Consider a three-impulse trajectory γ connecting the states $\{\mathbf{x}_i, t_i\}$ and $\{\mathbf{x}_f, t_f\}$. Find the location in time and space of the midcourse impulse $\{\tilde{\mathbf{r}}_m, \tilde{t}_m\}$, and the values of the initial and final velocities $\{\tilde{\mathbf{v}}_{m^+}, \tilde{\mathbf{v}}_{f^-}\}$, such that the two ballistic arcs of the refined three-impulse trajectory meet at $\tilde{\mathbf{r}}_m$, and its cost $J_{\tilde{\gamma}}$ is (locally) minimized.*

$$\min_{\mathbf{y}} \; J_{\tilde{\gamma}}(\mathbf{y}) \coloneqq \|\Delta\tilde{\mathbf{v}}_i\| + \|\Delta\tilde{\mathbf{v}}_m\| + \|\Delta\tilde{\mathbf{v}}_f\|$$

subject to the constraints

$$\begin{cases} \mathbf{h}_{m^-}(\mathbf{y}) \coloneqq \varphi_r(\mathbf{r}_i, \tilde{\mathbf{v}}_{i^+}, t_i; \tilde{t}_m) - \tilde{\mathbf{r}}_m = \mathbf{0} \ , \\ \mathbf{h}_{m^+}(\mathbf{y}) \coloneqq \varphi_r(\mathbf{r}_f, \tilde{\mathbf{v}}_{f-}, t_f; \tilde{t}_f) - \tilde{\mathbf{r}}_m = \mathbf{0} \ , \\ t_i < \tilde{t}_m < t_f \ . \end{cases}$$

Problem 3.2 will be solved numerically, with an iterative approach (see section 4.4). The components of the first guess solution $\mathbf{y}^{(0)}$ are taken from the perturbed three-impulse trajectory γ: $\mathbf{y}^{(0)} = (\mathbf{v}_{m^+}, \mathbf{v}_{f^-}, \mathbf{r}_m, t_m)^\top$.

Analytical Computation of the Jacobians

Also in this case, the analytical computation of the derivatives of the cost $J_{\tilde{\gamma}}$ and the nonlinear equality constraints $\mathbf{h}_{m^-}$, $\mathbf{h}_{m^+}$ is of paramount importance for numerical efficiency.

Consider the cost function in Eq. (3.37); recalling that the terminal velocities are prescribed and coincide with those of the nominal and reference trajectories (i.e., $\tilde{\mathbf{v}}_{i^-} = \overline{\mathbf{v}}_{i^-} = \mathbf{v}_{i^-}$ and $\tilde{\mathbf{v}}_{f^+} = \overline{\mathbf{v}}_{f^+} = \mathbf{v}_{f^+}$), the characteristic velocity can be written as

$$J_{\tilde{\gamma}} = \|\tilde{\mathbf{v}}_{i^+} - \mathbf{v}_{i^-}\| + \|\tilde{\mathbf{v}}_{m^+} - \tilde{\mathbf{v}}_{m^-}\| + \|\tilde{\mathbf{v}}_{f^+} - \mathbf{v}_{f^-}\| \ . \tag{3.40}$$

The velocities at the intermediate impulses are obtained propagating the states at the times t_{i^-} and t_{f^+} forward and backward in time, respectively

$$\mathbf{v}_{m^-} = \varphi_v(\mathbf{r}_i, \tilde{\mathbf{v}}_{i^+}, t_i; \tilde{t}_m) \ , \qquad \mathbf{v}_{m^+} = \varphi_v(\mathbf{r}_f, \tilde{\mathbf{v}}_{f^-}, t_f; \tilde{t}_m) \ . \tag{3.41a}$$

The jacobian of $J_{\tilde{\gamma}}$ with respect to the NLP variables of Problem 3.2 is

$$\frac{\partial J_{\tilde{\gamma}}}{\partial \mathbf{y}} \equiv \left(\frac{\partial J_{\tilde{\gamma}}}{\partial \tilde{\mathbf{v}}_{i^+}}, \frac{\partial J_{\tilde{\gamma}}}{\partial \tilde{\mathbf{v}}_{f^-}}, \frac{\partial J_{\tilde{\gamma}}}{\partial \tilde{\mathbf{r}}_m}, \frac{\partial J_{\tilde{\gamma}}}{\partial \tilde{t}_m} \right) \ . \tag{3.42}$$

Hereafter, the analytical expression of each component of $\partial J_{\tilde{\gamma}}/\partial \mathbf{y}$ is developed.
Recalling the chain rule for the partial derivatives, the first quantity in Eq. (3.42) is

$$\begin{aligned} \frac{\partial J_{\tilde{\gamma}}}{\partial \tilde{\mathbf{v}}_{i^+}} &= \frac{\partial J_{\tilde{\gamma}}}{\partial \Delta\tilde{\mathbf{v}}_i} \cdot \frac{\partial \Delta\tilde{\mathbf{v}}_{i^+}}{\partial \tilde{\mathbf{v}}_{i^+}} + \frac{\partial J_{\tilde{\gamma}}}{\partial \Delta\tilde{\mathbf{v}}_m} \cdot \frac{\partial \Delta\tilde{\mathbf{v}}_m}{\partial \tilde{\mathbf{v}}_{i^+}} \\ &= \frac{\partial \|\Delta\tilde{\mathbf{v}}_i\|}{\partial \Delta\tilde{\mathbf{v}}_i} \cdot \frac{\partial \Delta\tilde{\mathbf{v}}_{i^+}}{\partial \tilde{\mathbf{v}}_{i^+}} + \frac{\partial \|\Delta\tilde{\mathbf{v}}_m\|}{\partial \Delta\tilde{\mathbf{v}}_m} \cdot \frac{\partial \Delta\tilde{\mathbf{v}}_m}{\partial \tilde{\mathbf{v}}_{i^+}} \ . \end{aligned} \tag{3.43}$$

Using the argument that

$$\frac{\mathrm{d}\,\|\mathbf{x}\|}{\mathrm{d}\mathbf{x}} = \frac{\mathbf{x}}{\|\mathbf{x}\|} \tag{3.44}$$

where $\mathbf{x}$ is a generic vector, Eq. (3.43) reduces to

$$\frac{\partial J_{\tilde{\gamma}}}{\partial \tilde{\mathbf{v}}_{i^+}} = \frac{\Delta\tilde{\mathbf{v}}_i}{\|\Delta\tilde{\mathbf{v}}_i\|} \cdot \frac{\partial \Delta\tilde{\mathbf{v}}_{i^+}}{\partial \tilde{\mathbf{v}}_{i^+}} + \frac{\Delta\tilde{\mathbf{v}}_m}{\|\Delta\tilde{\mathbf{v}}_m\|} \cdot \frac{\partial \Delta\tilde{\mathbf{v}}_m}{\partial \tilde{\mathbf{v}}_{i^+}} \ . \tag{3.45}$$

Since $\Delta\tilde{\mathbf{v}}_{i^+} = \tilde{\mathbf{v}}_{i^+} - \mathbf{v}_{i^-}$, the first partial derivatives remaining in Eq. (3.45) is simply

$$\frac{\partial \Delta\tilde{\mathbf{v}}_{i^+}}{\partial \tilde{\mathbf{v}}_{i^+}} = I_2 \ . \tag{3.46}$$

Instead, as $\Delta\tilde{\mathbf{v}}_m = \tilde{\mathbf{v}}_{m^+} - \tilde{\mathbf{v}}_{m^-}$ but only $\tilde{\mathbf{v}}_{m^-}$ depends upon $\tilde{\mathbf{v}}_{i^+}$, the second derivative in Eq. (3.45) reduces to

$$\frac{\partial \Delta\tilde{\mathbf{v}}_m}{\partial \tilde{\mathbf{v}}_{i^+}} = -\frac{\partial \tilde{\mathbf{v}}_{m^-}}{\partial \tilde{\mathbf{v}}_{i^+}} = -\tilde{\Phi}_{vv}(t_i; \tilde{t}_m) \ , \tag{3.47}$$

where $\tilde{\Phi}_{vv}(t_i; \tilde{t}_m)$ is a partition of the state transition matrix associated with the refined three-impulse trajectory. Thus, the analytical expression for the first component of the jacobian of $J_{\tilde{\gamma}}$ is

$$\frac{\partial J_{\tilde{\gamma}}}{\partial \tilde{\mathbf{v}}_{i^+}} = \frac{\Delta\tilde{\mathbf{v}}_i^\top}{\|\Delta\tilde{\mathbf{v}}_i\|} - \frac{\Delta\tilde{\mathbf{v}}_m^\top}{\|\Delta\tilde{\mathbf{v}}_m\|}\tilde{\Phi}_{vv}(t_i; \tilde{t}_m) \ . \tag{3.48}$$

With similar reasoning, it can be shown that the derivative of $J_{\tilde{\gamma}}$ with respect to $\tilde{\mathbf{v}}_{f^-}$ is

$$\frac{\partial J_{\tilde{\gamma}}}{\partial \tilde{\mathbf{v}}_{f^-}} = -\frac{\Delta\tilde{\mathbf{v}}_f^\top}{\|\Delta\tilde{\mathbf{v}}_f\|} + \frac{\Delta\tilde{\mathbf{v}}_m^\top}{\|\Delta\tilde{\mathbf{v}}_m\|}\tilde{\Phi}_{vv}(t_f; \tilde{t}_m) \ . \tag{3.49}$$

Concerning the derivative with respect to $\tilde{\mathbf{r}}_m$, this is identically null

$$\frac{\partial J_{\tilde{\gamma}}}{\partial \tilde{\mathbf{r}}_m} = \mathbf{0}^\top \ . \tag{3.50}$$

Indeed, it is evident also from Eq. (3.41), that none of the quantities appearing in Eq. (3.40) depends directly upon $\tilde{\mathbf{r}}_m$. The last component of the jacobian can be expressed using the chain rule and the result of Eq. (3.44)

$$\frac{\partial J_{\tilde{\gamma}}}{\partial \tilde{t}_m} = \frac{\partial J_{\tilde{\gamma}}}{\partial \Delta\tilde{\mathbf{v}}_m} \cdot \frac{\partial \Delta\tilde{\mathbf{v}}_m}{\partial \tilde{t}_m} = \frac{\Delta\tilde{\mathbf{v}}_m}{\|\Delta\tilde{\mathbf{v}}_m\|} \cdot \frac{\partial \Delta\tilde{\mathbf{v}}_m}{\partial \tilde{t}_m} \ . \tag{3.51}$$

The derivative of $\Delta\tilde{\mathbf{v}}_m$ with respect to $\tilde{t}_m$ can be developed using Eq. (3.41):

$$\Delta\tilde{\mathbf{v}}_m = \tilde{\mathbf{v}}_{m^+} - \tilde{\mathbf{v}}_{m^-} = \varphi_v(\mathbf{r}_f, \tilde{\mathbf{v}}_{f^-}, t_i; \tilde{t}_m) - \varphi_v(\mathbf{r}_i, \tilde{\mathbf{v}}_{i^+}, t_i; \tilde{t}_m) \ . \tag{3.52}$$

Then, recalling the definition of the flow (i.e., the integral of the dynamics), one notes that the derivative of the flow with respect to the final time of the integration ($\tilde{t}_m$ in the present case) is actually the dynamical field $\mathbf{f}(\mathbf{x}, t)$ evaluated at the ending state of the flow [19]. In particular, the derivatives of the last two components of the flow coincide with the gravitational acceleration $\mathbf{g}(\mathbf{x}, t)$

$$\frac{\partial}{\partial \tilde{t}_m}\varphi_v(\mathbf{r}_i, \tilde{\mathbf{v}}_{i^+}, t_i; \tilde{t}_m) = \mathbf{g}(\varphi(\mathbf{r}_i, \tilde{\mathbf{v}}_{i^+}, t_i; \tilde{t}_m), \tilde{t}_m) = \mathbf{g}(\tilde{\mathbf{x}}_{m^-}, \tilde{t}_m) \ , \tag{3.53a}$$

$$\frac{\partial}{\partial \tilde{t}_m}\varphi_v(\mathbf{r}_f, \tilde{\mathbf{v}}_{f^-}, t_f; \tilde{t}_m) = \mathbf{g}(\varphi(\mathbf{r}_f, \tilde{\mathbf{v}}_{f^-}, t_f; \tilde{t}_m), \tilde{t}_m) = \mathbf{g}(\tilde{\mathbf{x}}_{m^+}, \tilde{t}_m) \ . \tag{3.53b}$$

Thus,

$$\frac{\partial J_{\tilde{\gamma}}}{\partial \tilde{t}_m} = \frac{\Delta\tilde{\mathbf{v}}_m^\top}{\|\Delta\tilde{\mathbf{v}}_m\|}\left(\mathbf{g}(\tilde{\mathbf{x}}_{m^+}, \tilde{t}_m) - \mathbf{g}(\tilde{\mathbf{x}}_{m^-}, \tilde{t}_m)\right) \ . \tag{3.54}$$

Putting together Eqs. (3.48) to (3.50) and (3.54), the jacobian of the objective function with respect to the NLP variable $\mathbf{y}$ is

$$\frac{\partial J_{\tilde{\gamma}}}{\partial \mathbf{y}} = \begin{bmatrix} \dfrac{\Delta\tilde{\mathbf{v}}_i}{\|\Delta\tilde{\mathbf{v}}_i\|} - \tilde{\Phi}_{vv}(t_i;\tilde{t}_m)\dfrac{\Delta\tilde{\mathbf{v}}_m}{\|\Delta\tilde{\mathbf{v}}_m\|} \\ -\dfrac{\Delta\tilde{\mathbf{v}}_f}{\|\Delta\tilde{\mathbf{v}}_f\|} + \ \tilde{\Phi}_{vv}(t_f;\tilde{t}_m)\dfrac{\Delta\tilde{\mathbf{v}}_m}{\|\Delta\tilde{\mathbf{v}}_m\|} \\ \mathbf{0} \\ \left(\mathbf{g}(\tilde{\mathbf{x}}_{m^+}, \tilde{t}_m) - \mathbf{g}(\tilde{\mathbf{x}}_{m^-}, \tilde{t}_m)\right)^\top \dfrac{\Delta\tilde{\mathbf{v}}_m}{\|\Delta\tilde{\mathbf{v}}_m\|} \end{bmatrix}^\top , \tag{3.55}$$

where one notes that the components computed previously are transposed and the transpose symbol is taken out of the vector parentheses.

Consider now the derivatives of the constraints $\mathbf{h}_{m^-}$ and $\mathbf{h}_{m^+}$ defined in Problem 3.2. Their jacobians are two (2×7)-dimensional matrices defined as

$$\frac{\partial \mathbf{h}_{m^-}}{\partial \mathbf{y}} \equiv \left(\frac{\partial \mathbf{h}_{m^-}}{\partial \tilde{\mathbf{v}}_{i^+}}, \frac{\partial \mathbf{h}_{m^-}}{\partial \tilde{\mathbf{v}}_{f^-}}, \frac{\partial \mathbf{h}_{m^-}}{\partial \tilde{\mathbf{r}}_m}, \frac{\partial \mathbf{h}_{m^-}}{\partial \tilde{t}_m}\right) \ , \tag{3.56a}$$

$$\frac{\partial \mathbf{h}_{m^+}}{\partial \mathbf{y}} \equiv \left(\frac{\partial \mathbf{h}_{m^+}}{\partial \tilde{\mathbf{v}}_{i^+}}, \frac{\partial \mathbf{h}_{m^+}}{\partial \tilde{\mathbf{v}}_{f^-}}, \frac{\partial \mathbf{h}_{m^+}}{\partial \tilde{\mathbf{r}}_m}, \frac{\partial \mathbf{h}_{m^+}}{\partial \tilde{t}_m}\right) \ . \tag{3.56b}$$

Since each constraint concerns one arc of the three-impulse trajectory (see Fig. 3.5), it is evident that the components of $\mathbf{h}_{m^-}$ are not influenced by the values taken by $\tilde{\mathbf{v}}_{f^-}$ and similarly $\mathbf{h}_{m^+}$ does not depend upon $\tilde{\mathbf{v}}_{i^+}$. Hence, two quantities in Eq. (3.56) are null

$$\frac{\partial \mathbf{h}_{m^-}}{\partial \tilde{\mathbf{v}}_{f^-}} = \frac{\partial \mathbf{h}_{m^+}}{\partial \tilde{\mathbf{v}}_{i^+}} = 0_2 \ . \tag{3.57}$$

Moreover, both $\mathbf{h}_{m^-}$ and $\mathbf{h}_{m^+}$ depend linearly upon $\tilde{\mathbf{r}}_m$ and so

$$\frac{\partial \mathbf{h}_{m^-}}{\partial \tilde{\mathbf{r}}_m} = \frac{\partial \mathbf{h}_{m^+}}{\partial \tilde{\mathbf{r}}_m} = -I_2 \ . \tag{3.58}$$

Concerning the quantities $\partial \mathbf{h}_{m^-}/\partial \tilde{\mathbf{v}}_{i^+}$ and $\partial \mathbf{h}_{m^+}/\partial \tilde{\mathbf{v}}_{f^-}$, these are the derivatives of the

flow with respect to the initial states, which, by definition, are the elements of the STM

$$\frac{\partial \mathbf{h}_{m^-}}{\partial \tilde{\mathbf{v}}_{i^+}} = \frac{\partial}{\partial \tilde{\mathbf{v}}_{i^+}} \varphi_r(\mathbf{r}_i, \tilde{\mathbf{v}}_{i^+}, t_i; \tilde{t}_m) = \tilde{\Phi}_{rv}(t_i; \tilde{t}_m) \ , \tag{3.59a}$$

$$\frac{\partial \mathbf{h}_{m^+}}{\partial \tilde{\mathbf{v}}_{f^-}} = \frac{\partial}{\partial \tilde{\mathbf{v}}_{f^-}} \varphi_r(\mathbf{r}_f, \tilde{\mathbf{v}}_{f^-}, t_f; \tilde{t}_m) = \tilde{\Phi}_{rv}(t_f; \tilde{t}_m) \ . \tag{3.59b}$$

The last two terms in Eq. (3.56), $\partial \mathbf{h}_{m^-}/\partial \tilde{t}_m$ and $\partial \mathbf{h}_{m^+}/\partial \tilde{t}_m$, are, once again, the derivative of the flow with respect to the final time at which the flow is evaluated. Therefore, they coincide with the dynamical field evaluated at the state of the intermediate impulse. Since the interest is on the first two components of $\mathbf{f}(\mathbf{x}, t)$, and these are the velocities:

$$\frac{\partial \mathbf{h}_{m^-}}{\partial \tilde{t}_m} = \frac{\partial}{\partial \tilde{t}_m} \varphi_r(\mathbf{r}_i, \tilde{\mathbf{v}}_{i^+}, t_i; \tilde{t}_m) = \varphi_v(\mathbf{r}_i, \tilde{\mathbf{v}}_{i^+}, t_i; \tilde{t}_m) = \tilde{\mathbf{v}}_{m^-} \ , \tag{3.60a}$$

$$\frac{\partial \mathbf{h}_{m^+}}{\partial \tilde{t}_m} = \frac{\partial}{\partial \tilde{t}_m} \varphi_r(\mathbf{r}_f, \tilde{\mathbf{v}}_{f^-}, t_f; \tilde{t}_m) = \varphi_v(\mathbf{r}_f, \tilde{\mathbf{v}}_{f^-}, t_f; \tilde{t}_m) = \tilde{\mathbf{v}}_{m^+} \ . \tag{3.60b}$$

Finally, combining Eqs. (3.57) to (3.60), the jacobians of the constraints read

$$\frac{\partial \mathbf{h}_{m^-}}{\partial \mathbf{y}} = \begin{bmatrix} \tilde{\Phi}_{rv}(t_i; \tilde{t}_m) \\ 0_2 \\ -I_2 \\ \tilde{\mathbf{v}}_{m^-} \end{bmatrix}^\top , \qquad \frac{\partial \mathbf{h}_{m^+}}{\partial \mathbf{y}} = \begin{bmatrix} 0_2 \\ \tilde{\Phi}_{rv}(t_f; \tilde{t}_m) \\ -I_2 \\ \tilde{\mathbf{v}}_{m^+} \end{bmatrix}^\top . \tag{3.61a}$$

4 | Simulations and Results

This chapter illustrates the results of the optimization process that takes a non-optimal two-impulse Earth–Moon transfer of [62], and adds an intermediate impulse to get an improved three-impulse trajectory.

4.1. Numerical Integration

It was anticipated in section 2.1.4 that the equations of motion of the PBRFBP do not possess an analytical solution; therefore, Eq. (2.15) must be integrated numerically, and the Matlab® suite `ode113` is used to this aim. This integration scheme is a variable-step, variable-order Adams-Bashforth-Moulton PECE (predict, evaluate, correct, evaluate) solver of orders 1 to 13 [58]. Both absolute and relative error tolerances[1] are set to 10×10^{-12}. Recalling that all variables are nondimensional, this corresponds to a tolerance on the position lower than 1 mm.
Very often, the equations of motion are integrated together with the variational equation for the state transition matrix (Eq. (2.23)), and the resulting system of twenty first-order ODEs is solved by means of `ode113`. Once the history of the STM is known (at some discrete time instants), the values for the primer vector and its derivatives can be obtained by solving the algebraic equation (2.79), and using the boundary conditions in Eq. (3.1). However, another way to compute $\mathbf{p}(t)$ is necessary if the primer is required at a specific time when the STM is not available, or if the variational equation has not been solved yet. In these cases, both the dynamics of the states and the primer, Eq. (2.15) and Eq. (2.78), respectively, should be integrated together. So, an augmented state vector collecting the components of the states, the primer, and the primer derivative, is assembled

$$\mathbf{z}(t) \equiv \left(\mathbf{r}(t), \mathbf{v}(t), \mathbf{p}(t), \dot{\mathbf{p}}(t)\right)^{\top} \quad . \tag{4.1}$$

Then, Eq. (2.15) and Eq. (2.78) (written in a first-order form) compose a system of eight first-order ODEs, that, again, is solved with `ode113`.

[1] Relative and absolute tolerances are defined at `https://www.mathworks.com/help/matlab/ref/odeset.html`, retrieved on March 06, 2023.

4.1.1. Model Verification

The Earth–Moon transfers of [62] serve also as a solid benchmark to validate the correct implementation of the PBRFBP. Indeed, the database provided contains much information about each of the almost 300 000 transfers, including the total cost, the initial state, and the final one. Each initial state $\mathbf{x}_i$ at the time t_i is propagated numerically up to the corresponding final time t_f; then, the final states obtained, as well as the costs of the transfers, are compared with the values reported in the database. An almost perfect match is found, validating the implementation of the four-body dynamics. Consider, for instance, the difference between the costs of the data set and the costs of the trajectories just propagated. As an illustrative example, none of the almost 80 thousand trajectories in the L region, shows a cost discrepancy higher than 0.1 m/s (when the cost of each transfer is in the order of 4×10^3 m/s). Moreover, after the propagation of each solution it is verified that, on its path, the spacecraft does not impact any celestial body.
Hereafter, Fig. 4.1 shows the geometry of some samples taken from different families of [62], both prograde and retrograde. Family a, b, c, and d collect interior transfers, while family o and p contain exterior transfer solutions. These last, as it will be shown later, are the solutions of interest for the second part of the present work.

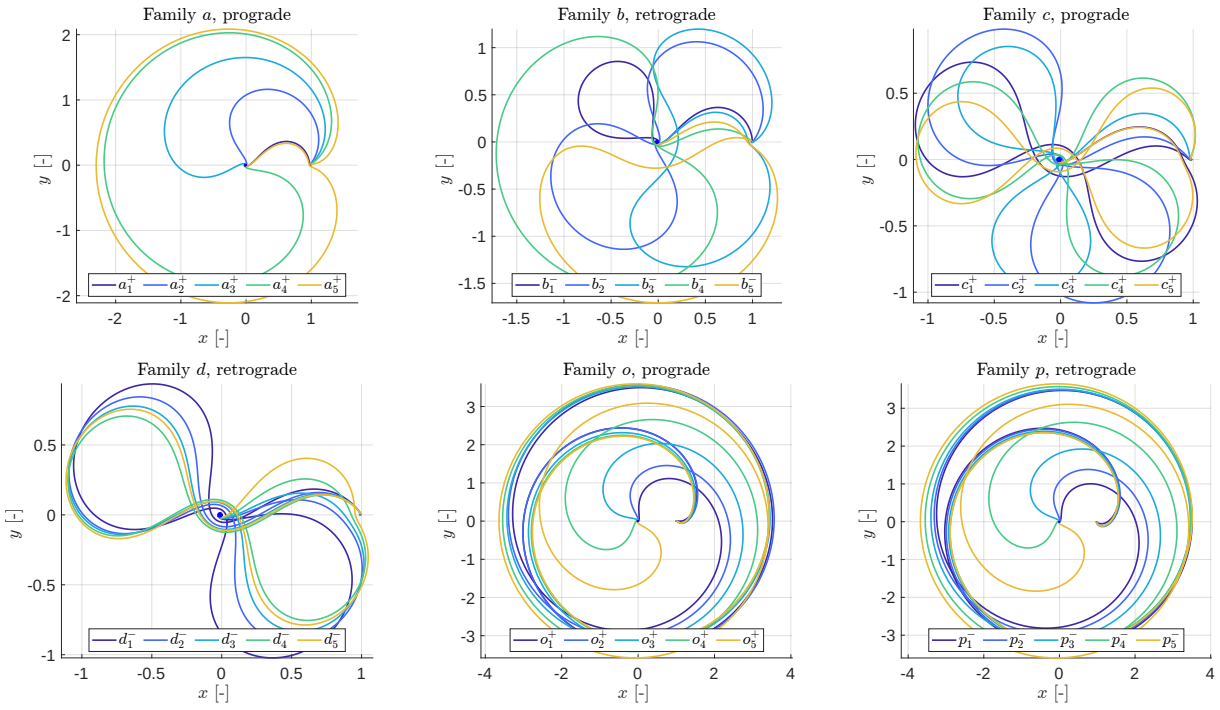

Figure 4.1: Samples of two-impulse Earth–Moon transfers from different families in the synodic frame; coordinates are nondimensional according to the PBRFBP; the Earth and the Moon are located at $(-\mu, 0)$ and $(1-\mu, 0)$, respectively

4.2. Non-Optimal Two-Impulse Transfers

The primer magnitude associated with each of the reference trajectories can be analyzed to verify the optimality of the solutions according to the LNC. Consider for example the solution sample in Fig. 4.2a. The transfer is represented in the synodic frame (top-left) and in the Earth-sidereal frame (top-right). Besides the SC trajectory, these two plots report the apparent orbit of the Sun (orange dashed line, not to scale). The initial and final positions of the Sun are labeled with a filled and an empty circle, respectively. Note also, that in the synodic frame, the Sun moves clockwise, whilst in the Earth-centered inertial frame it rotates counterclockwise.

The bottom graph represents the history of the primer magnitude during the transfer. It is evident that in this specific case, LNC are not satisfied. Indeed, the maximum magnitude of the primer, indicated by a red cross, exceeds unity. Figure 4.2a is an example of a reference transfer belonging to the L region that is not optimal and therefore can be improved with an additional midcourse impulse. On the contrary, Fig. 4.1b represents a sample solution that respects LNC, and so the two-impulse transfer is already optimal.

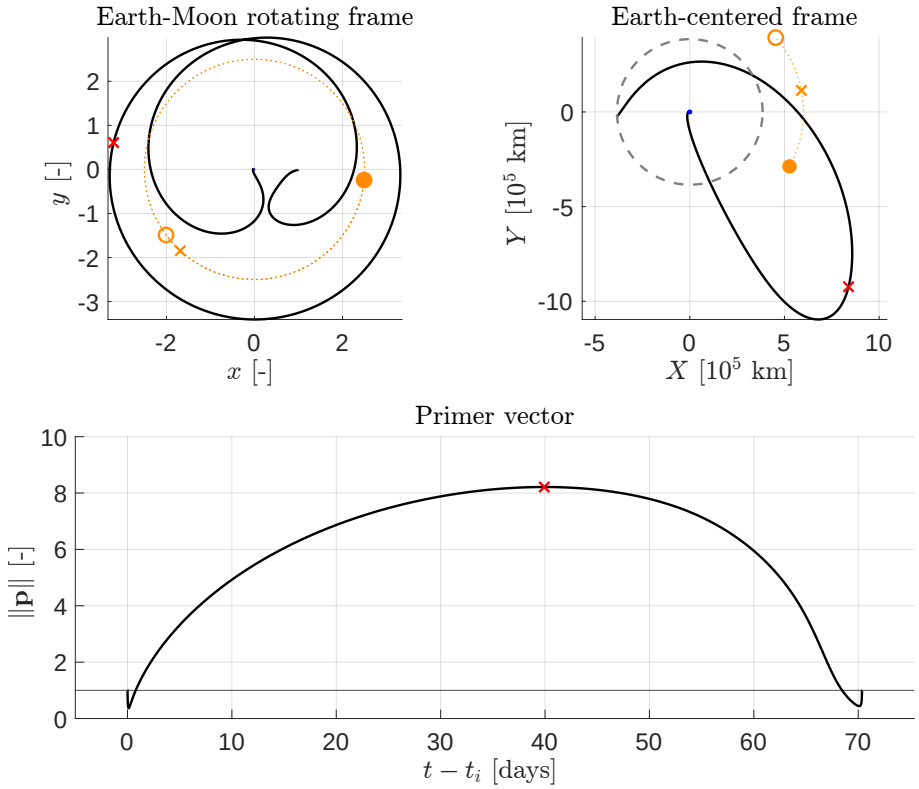

(a) Non-optimal two-impulse transfer

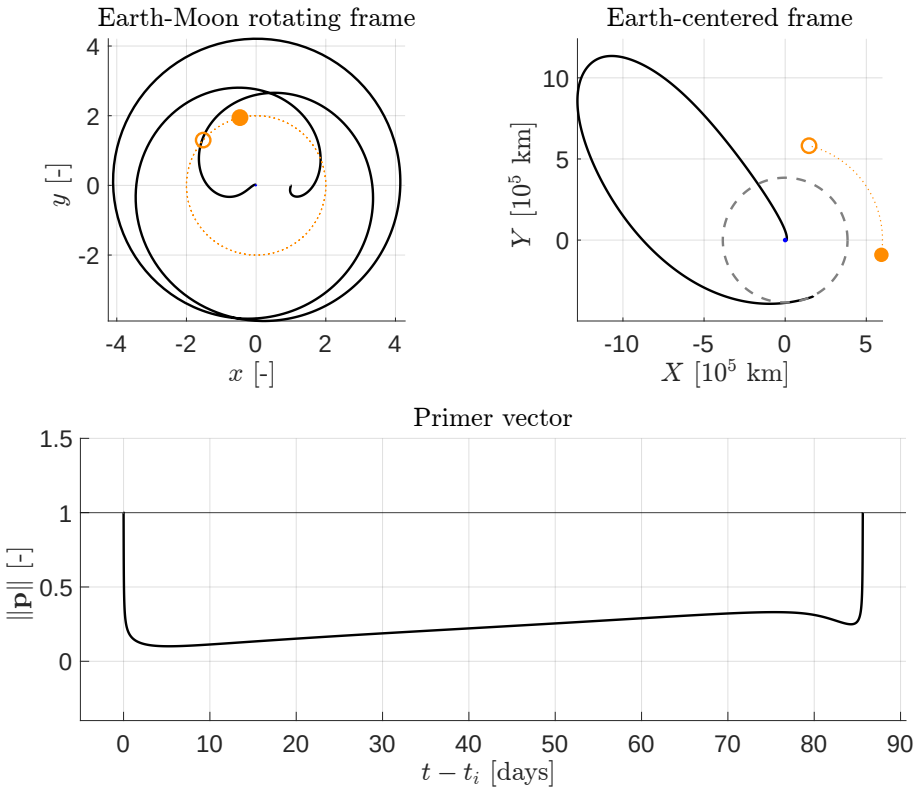

(b) Optimal two-impulse transfer

Figure 4.1: Geometry of samples reference transfers in both synodic (top-left) and Earth-sidereal (top-right) frame, together with the primer magnitude history (bottom graph); Moon's orbit is depicted with a dashed-gray line in the sidereal frame; the apparent orbit of the Sun (not to scale) is represented in orange; the initial and final position of the Sun are indicated by a filled and an empty circle, respectively; the red cross in Fig. 4.2a denotes the instant when the primer magnitude is maximum, and the orange cross specifies the position of the Sun at that time

4.2.1. Filtered Two-Impulse Transfers

Instead of focusing on single samples, it is more interesting to look at the global picture (Fig. 2.3), and to have an overall view of the trajectories that do not satisfy LNC. However, since the total number of solutions is very high (284 013, to be exact) some preliminary remarks must be made. First, it is decided to focus only on the transfers inside the S and L regions, due to their more interesting characteristics from the viewpoint of a real mission. Then, with the aim of finding more non-optimal solutions, the L region is enlarged with respect to that of [62], and transfers with a cost up to 4000 m/s are included (instead of 3950 m/s). Finally, for numerical reasons, the threshold for the primer magnitude that discriminates the optimality of a solution is set to 1.01. An automated algorithm verifies

the maximum primer magnitude for all the previous transfers. All the colored (gray, red, and blue) points in Fig. 4.2 correspond to the *short* and *long* transfers whose primer vector magnitude exceeds 1.01.

Actually, not all these trajectories will be further improved with a midcourse impulse. Many of them are still not of practical interest for a real-life mission to the Moon (gray points in Fig. 4.2). For instance, long transfers that perform many flybys at the Earth are never implemented, as the recursive passage inside the Van Allen belts must be avoided to preserve the hardware of the spacecraft. Moreover, it is observed that the maximum primer magnitude of these trajectories occurs in the vicinity of the Earth. Here the pseudo-potential of the PBRFBP shows very high gradients [17], and thus a first-order analysis based on the STM loses accuracy (this has also repercussions on numerical computations). Hence, non-optimal transfers are further filtered and only solutions respecting the following requirements are retained:

1. the trajectory must pass at a distance lower than 40 000 km from the Earth (estimated extension of the outer Van Allen belt) only once, at the departure;
2. during *long* transfers the spacecraft must not perform more than 2 revolutions about the Earth, while for *short* transfers the threshold is lowered to 1.5 revolutions.

Red and blue dots reported in Fig. 4.2 are the retained solutions to which a further impulse is added, whilst the gray dots are the non-optimal solution discarded by the filter.

- The solutions contained in the **S region** are 166 813. Almost 35 % of them do not respect LNC, but only 1.5 % (2355 solutions) are retained after the filtering. This happens because, in the center of this area, many transfers belonging to families b and c perform Earth flybys, and so are discarded (note the high number of gray dots at the middle of the red rectangle in Fig. 4.2). Moreover, looking at Fig. 4.2 one notes that none of the direct transfers (solutions with $\Delta t < 10$ day, family a) requires an additional impulse, as they are already optimal.
- The solutions within the **L region** are 76 392, and 13 % of them do not respect LNC. In this case, many of these last pass the filter (8218 solutions), corresponding to 10.7 % of the total number inside the region. However, the majority of the most interesting solutions (Pareto-efficient front with $\Delta v < 3850$ m/s and $\Delta t > 70$ days, made of low energy transfers with ballistic capture) do not require a third-maneuver. On the contrary, the bigger cluster of improvable solutions is shifted to the top-left corner of the L region. Additionally, there are two vertical blue arcs on the left side of the L region, made of solutions which perform an initial lunar gravity assist.

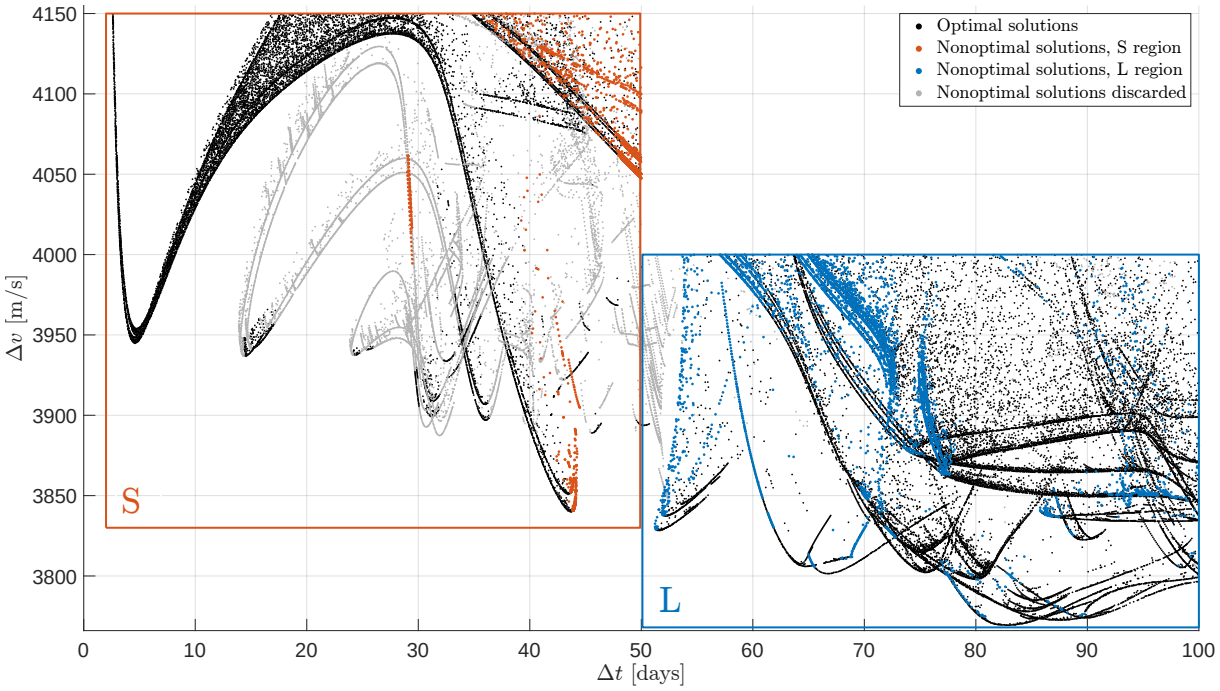

Figure 4.2: Earth–Moon transfers of [62] shown in the $(\Delta t, \Delta v)$. Black dots represent solutions that already satisfy LNC; red and blue points denote non-optimal trajectories belonging to the S and L region that will be improved with a midcourse impulse; gray dots indicate non-optimal transfers that are filtered out due to their geometry

4.3. Perturbed Three-Impulse Transfers

Once a non-optimal reference transfer is individuated, a perturbed three-impulse trajectory is built by adding a midcourse impulse. Recalling the discussion in section 3.2.3, the only parameter that is still to be chosen is the magnitude of the midcourse impulse κ. Indeed, once this is fixed, the position of the midcourse impulse is obtained through Eq. (3.32). Then, Problem 3.1 can be solved to connect the two ballistic arcs and obtain a continuous trajectory.

4.3.1. Solution to the Forward-Backward Shooting Problem

For a given value of κ, the forward-backward shooting problem is solved by means of Matlab®'s suite `fsolve`, implementing a `trust-region` algorithm. The tolerance on the minimum step, as well as the termination tolerance on the function value, are both set to 10×10^{-10}; consequently, the maximum error accepted on the midcourse position is about 0.04 m. Moreover, to improve numerical efficiency and convergence performances, the algorithm is provided with the analytical expression for the derivatives of the objective

function, reported in Eq. (3.35). It is also checked that the analytical gradients match the ones computed numerically by the solver using a central finite difference scheme. Relative errors obtained are in the order of 10^{-7} adimensional units.

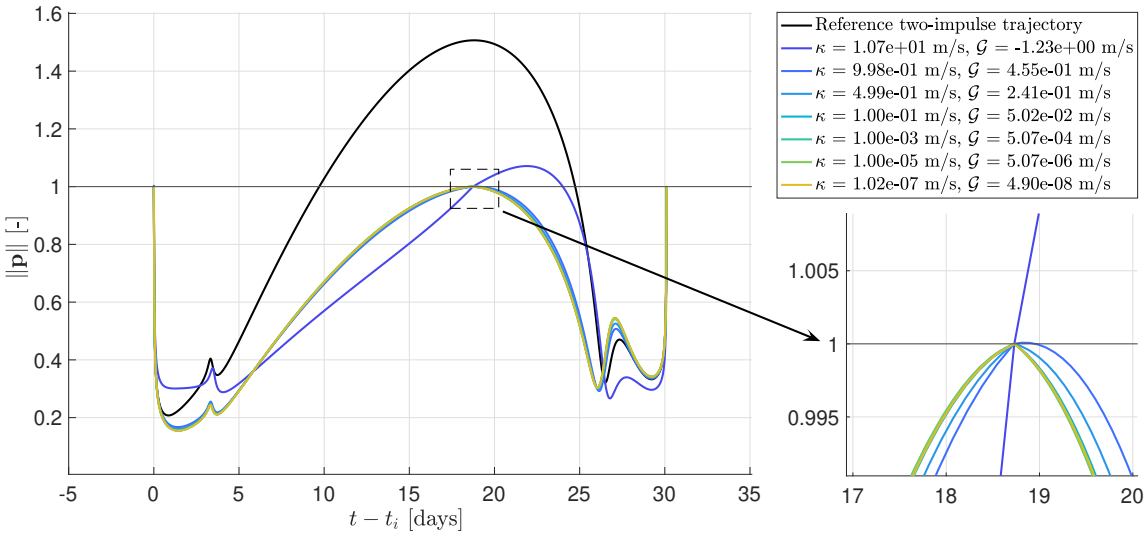

Figure 4.3: Primer magnitude on some perturbed trajectories obtained from the same reference transfer, but for different values of κ

Fig. 4.3 shows the primer magnitude on some perturbed trajectories obtained from the same reference transfer, but for different values of κ. It is pointed out that these trajectories do not satisfy LNC, because either the primer magnitude exceeds unity or the primer derivative is discontinuous at the intermediate impulse. However, this must not surprise, as it was already anticipated that a perturbed trajectory is not necessarily optimal. Together with the primer, it is reported also the *gain* $\mathcal{G}$, in m/s, associated with each solution. The gain is defined as the opposite of ΔJ:

$$\mathcal{G} \equiv -\Delta J = J_{\bar{\gamma}} - J_{\gamma} \ . \tag{4.2}$$

In such a way, intuitively, a positive gain indicates that a perturbed trajectory is more convenient. In agreement with the first-order cost variation in Eq. (3.25), Fig. 4.3 shows that the gain is proportional to the value of κ.
Of course, the solution with the highest gain is desirable, as it represents the best first-guess trajectory for the subsequent optimization problem. Thus, one can think of using always the same (high) κ for all the trajectories of the global picture. Nevertheless, still from Fig. 4.3, it can be noticed that too high values for the magnitude of the midcourse

impulse generate negative gains[2], and this must be avoided. Furthermore, thousands of trajectories must be processed, and the same value for κ might produce a positive gain for some solutions and a negative one for others. In short, an algorithm is needed to select κ for each solution, keeping in mind that, as reported in [16], one should never accept a midcourse impulse position that does not decrease the cost, because a sufficiently small κ will always provide a lower cost.

4.3.2. Magnitude of the Intermediate Impulse

The idea to compute a perturbed trajectory, sketched in Algorithm 1, is to solve Problem 3.1 starting with a high value of κ, which is the same for all the trajectories and is indicated with $\kappa_{\max}$. If the cost of the perturbed trajectory is lower than the reference one (i.e., $\mathcal{G} > 0$), then a suitable three-impulse trajectory is found. On the contrary, if $\mathcal{G}$ is negative, κ is reduced and the forward-backward shooting problem is solved again; this is repeated until a positive gain is obtained. κ is reduced also when the function `fsolve` used to solve the shooting problem does not converge (i.e., the perturbed trajectory γ has a discontinuity on the position at $t = t_m$).

Algorithm 1 Perturbed Trajectory Computation

1: Initialize $\mathcal{G} = 0$ and $\kappa = \kappa_{\max}$
2: **while** $\mathcal{G} \leq 0$ **do**
3: Compute $\delta\mathbf{r}_m(\kappa)$ using Eq. (3.32)
4: Compute γ solving the shooting problem, with $\mathbf{r}_m = \overline{\mathbf{r}}_m + \delta\mathbf{r}_m(\kappa)$
5: Update the gain $\mathcal{G}$
6: **if** $\mathcal{G} \leq 0$ **or** γ is not continuous at t_m **then**
7: Reduce κ ▷ *γ is continuous if the shooting problem converged*
8: **end if**
9: **end while**

At this point, it remains to select $\kappa_{\max}$ and to decide how to reduce κ at each iteration. It was observed that high values for $\kappa_{\max}$, such as 10 m/s, might yield positive gains in some cases. Even so, in these cases, a first-order analysis is no more justified, and consequently, $\Delta\mathbf{v}_m$ and $\overline{\mathbf{p}}_m$ are no more aligned at the time t_m (in contrast with LNC). Furthermore, since $\delta\mathbf{r}_m$ is proportional to κ, the bigger κ, the longer the convergence of the shooting algorithm. Thus, a conservative choice is made, setting the value of $\kappa_{\max}$ to 1 m/s.
Concerning the reduction of κ, on the one hand, a broader decrease might generate large steps in the gain, losing useful solutions; but on the other hand, a finer decrement might result in a waste of computational time and resources (especially for solutions that need

[2]This result is not related to the particular sample solution in Fig. 4.3, but has general validity.

many iterations). A compromise must be reached, and it has opted for a 10 % reduction at each step, so that at the k-th iteration $\kappa_k = 0.9\kappa_{k-1}$.

Nevertheless, it is recalled that the perturbed trajectory serves as the initial guess for Problem 3.2, so it is unnecessary to put a lot of effort into finding the best value of κ for each solution. Rather, as a large number of solutions must be processed automatically (and this is not the last step of the optimization), fast computations were preferred. For the same reason, also the maximum number of the iterations for the `fsolve` algorithm is kept small (just 50 iterations) to avoid the algorithm to stuck at this preliminary step.

4.4. Refined Three-Impulse Transfers

Problem 3.2 is solved by means of Matlab®'s routine `fmincon`[3]. The tolerances about the objective function value, the constraints functions, and the first-order optimality are set to 10^{-9} adimensional units, while the tolerance on the minimum step-size is an order of magnitude lower[4]. The solver is provided with the analytical expressions of the jacobians derived in section 3.2.6. Also in this case, once and for all, they are compared with those computed with a central finite difference scheme, and the resulting discrepancy is in the order of 10^{-7} adimensional units.
Two optimization algorithms are used for a performing and robust code. The first 1000 iterations are carried out implementing an `active-set` algorithm. Then, the trajectories that do not reach convergence are further optimized with an `interior-point` algorithm. Indeed, the `active-set` scheme allows for larger steps in the variables space, which adds speed. However, a too-large step may make the solution diverge, especially in proximity to high-gradients of the pseudo-potential. In these cases, an interior-point method could recover a feasible solution, as it takes smaller steps and satisfies bounds at all iterations. For its part, `interior-point` algorithm often gets stuck taking smaller and smaller steps in the attempt to satisfy the constraints.

Figure 4.4 shows an illustrative example of a refined transfer returned by the optimization algorithm. In particular, an exterior low-energy transfer with an initial flyby at the Moon is reported. The asterisk on each three-impulse trajectory highlights the instant of the midcourse impulse. One can appreciate how the NLP solver modified the location of the intermediate maneuver of the perturbed trajectory.

[3]For more details about the optimization method implemented by each algorithm visit: `https://it.mathworks.com/help/optim/ug/constrained-nonlinear-optimization-algorithms.html`, retrieved on March 08, 2023.

[4]Definitions of tolerances and stopping criteria can be found at `https://it.mathworks.com/help/optim/ug/tolerances-and-stopping-criteria.html`, retrieved on March 08, 2023.

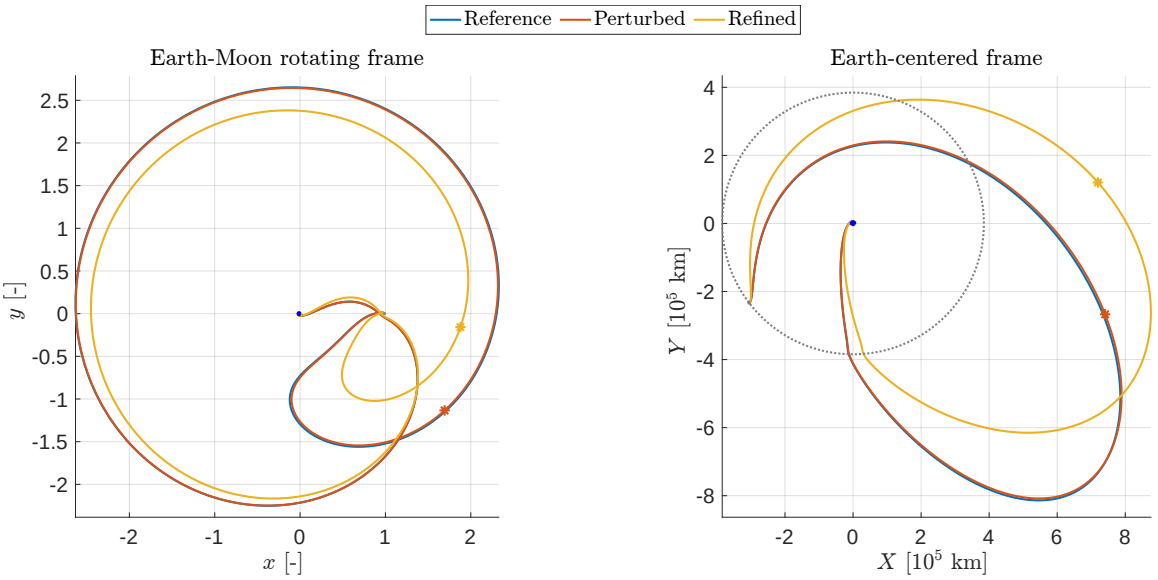

Figure 4.4: Illustrative example of a reference, perturbed and refined transfer; the asterisks denote the positions of the intermediate impulses on the three-impulse trajectories

In order to assess the optimality of the final solution, the history of the primer vector magnitude is represented in Fig. 4.5. Evidently, the original two-impulse trajectory is not optimal, as the primer magnitude exceeds one. In this case, also the perturbed trajectory does not satisfy LNC, because either the primer exceeds unity and also a cusp is present at t_m. Nonetheless, the refined trajectory is optimal, as all LNC are met.

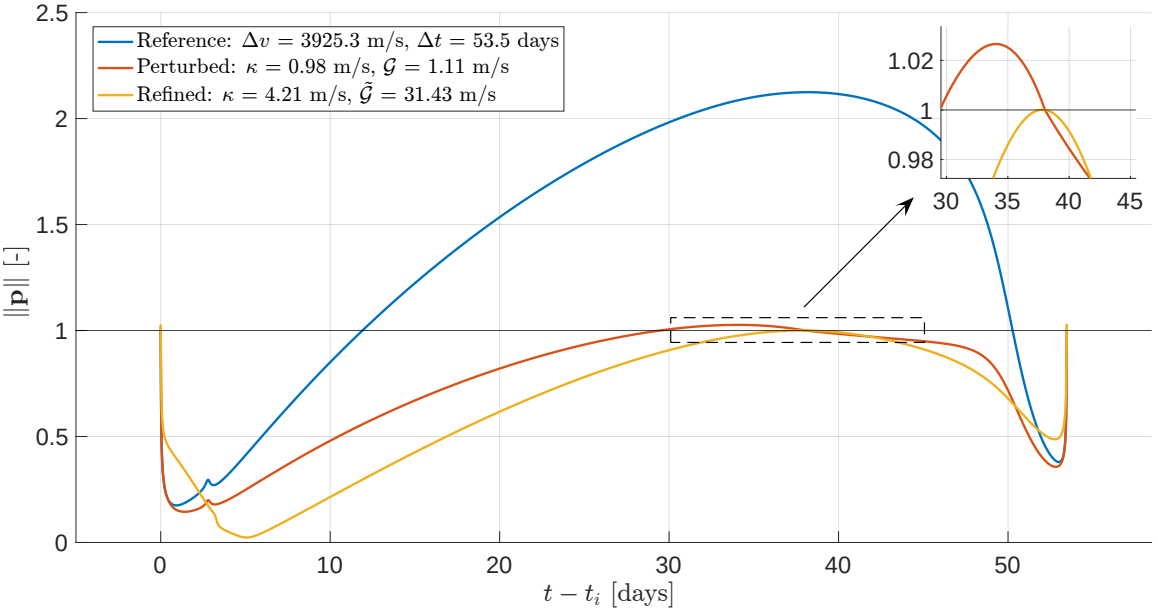

Figure 4.5: Primer vector magnitude associated with a reference, perturbed and refined transfer; an enlarged view highlights how the refined trajectory satisfies LNC

The same conclusion is also confirmed by Fig. 4.6. Here, the Hamiltonian function and the magnitude of the primer derivative are reported for each transfer. Even if both $\mathcal{H}$ and $\|\dot{\mathbf{p}}\|$ are discontinuous in γ, Weierstrass-Erdmann corner conditions are satisfied by $\tilde{\gamma}$ (see Theorem 2.2). The noteworthy aspect is that this outcome is achieved autonomously by the optimization algorithm, without any specific constraints on $\mathcal{H}$ or $\|\dot{\mathbf{p}}\|$.

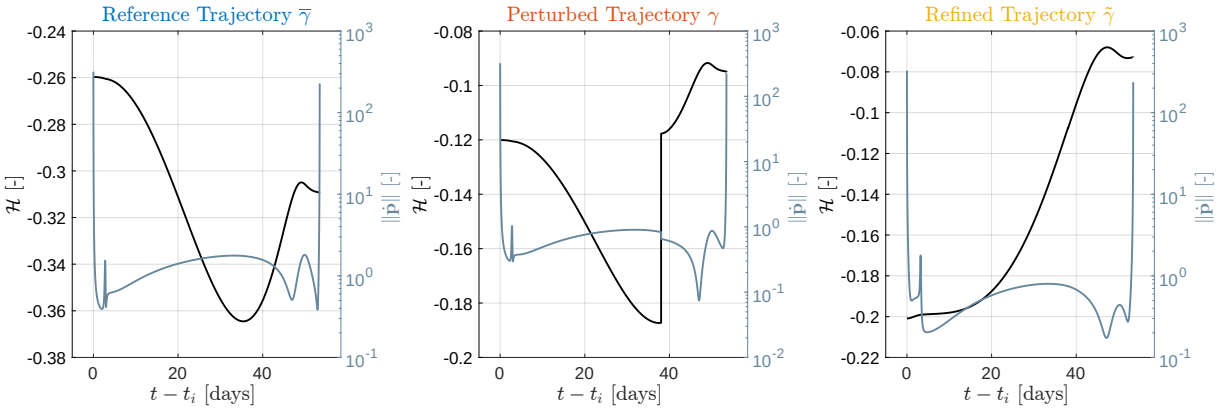

Figure 4.6: Hamiltonian function and magnitude of the primer vector derivative evaluated on a reference, perturbed and refined transfer

Finally, Fig. 4.7 shows the absolute value of each impulsive maneuver for all three transfers. The most relevant part of the budget is spent to leave the initial orbit around the Earth, and its absolute value is similar for all the trajectories. Instead, in the refined transfer, a little intermediate maneuver allows for saving fuel at the arrival, as the spacecraft velocity is closer to that of the Moon. Consequently, in this specific case, ballistic capture at the Moon is more efficient.

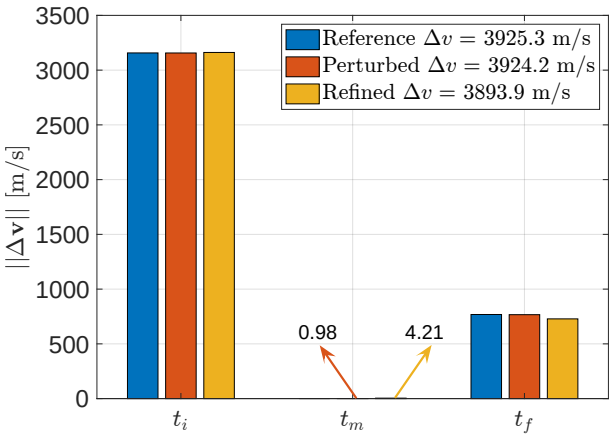

Figure 4.7: Cost breakdown for a reference, perturbed and refined transfer

4.5. Global Results

A total number of 10 573 trajectories are automatically optimized by utilizing the Parallel Computing Toolbox of Matlab®, which reduces the computation time by almost four times. All the solutions reach convergence, and, to analyze the improvement of each refined three-impulse transfer, the gain $\tilde{\mathcal{G}}$ is defined as

$$\tilde{\mathcal{G}} \equiv J_{\bar{\gamma}} - J_{\tilde{\gamma}} \ , \tag{4.3}$$

where the reference is still the two-impulse trajectory $\bar{\gamma}$.

Figure 4.8 shows the updated global picture of [62], where nonoptimal two-impulse solutions are replaced with improved three-impulse transfers. These are represented by colors associated with the value of the gain in Fig. 4.8a and with the magnitude of the midcourse impulse in Fig. 4.8b.

The gain $\tilde{\mathcal{G}}$ ranges from values as low as 10^{-6} m/s, up to the maximum improvement of 63 m/s. While the most efficient trajectories (Pareto-optimal region) are not modified appreciably, some other trajectories are notably improved. In particular, the family of transfers where an additional impulse provides a real benefit (represented by the two vertical arcs of red dots in Fig. 4.8a) are characterized by an initial flyby at the Moon. This was already proved to be a key feature to obtain an Earth–Moon transfer with a cost that approaches the theoretical minimum of 3726 m/s estimated by [60]. For example, the best trajectories found in literature, with costs lower than 3800 m/s [45, 68], exploit the presence of the Moon to achieve an exterior low-energy transfer. However, the current results show that inserting an additional maneuver after the lunar gravity assist could reduce the cost of the transfer by tens of m/s. A possible interpretation is that the extra degree of freedom represented by $\Delta\mathbf{v}_m$ allows for more effective use of the flyby, because modification of the spacecraft path after the Moon encounter is beneficial to recover a feasible transfer. Conversely, in the absence of an intermediate maneuver, the lunar gravity assist is utilized as much as possible to enable a workable transfer.

Figure 4.8b shows the same graph of Fig. 4.8a but this time the color of the three-impulse trajectories is associated with the magnitude of the midcourse impulse $\|\Delta\mathbf{v}_m\|$. The first aspect that leaps out is the similarity between the values of $\|\Delta\mathbf{v}_m\|$ and $\tilde{\mathcal{G}}$: as predicted by the theoretical discussion, the more consistent the intermediate maneuver, the more affected the cost of the final trajectory. It is important to note that extremely low values of $\|\Delta\mathbf{v}_m\|$ are not practically feasible in an real mission due, for example, to the limitations on the minimum impulse bit of a chemical thruster. Therefore, when examining Fig. 4.8b,

values that are too low must be considered with caution, but are still part to the results of the present analysis.

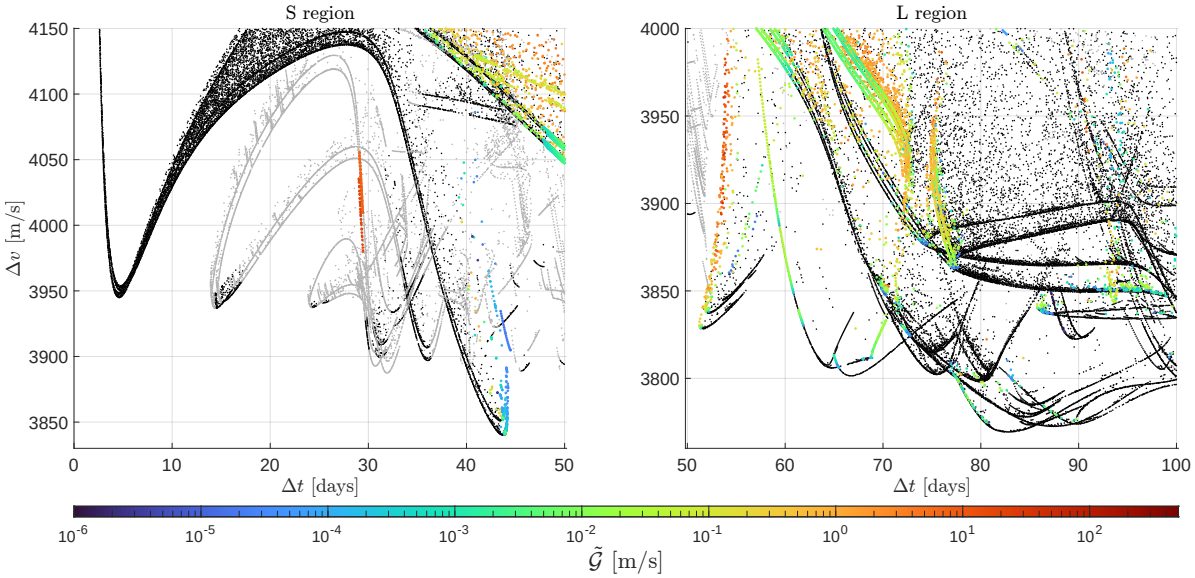

(a) Colors of three-impulse transfer associated with the gain $\tilde{\mathcal{G}}$

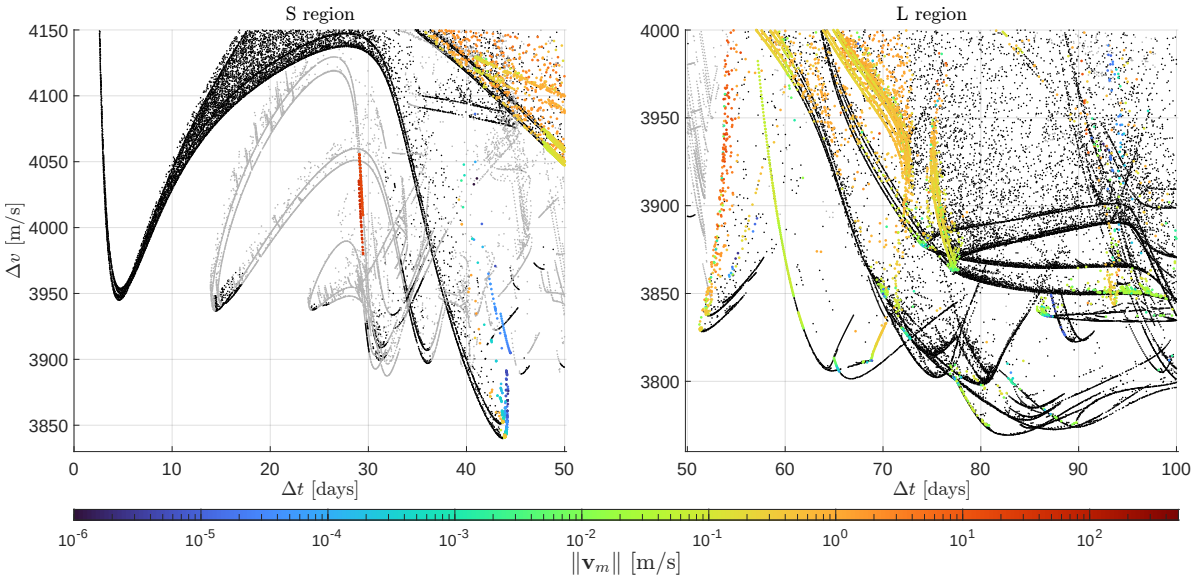

(b) Colors of three-impulse transfer associated with the intermediate impulse $\|\Delta\mathbf{v}_m\|$

Figure 4.8: Optimal multi-impulse Earth–Moon in a $(\Delta t,\ \Delta v)$ graph. Black and gray dots represent two-impulse solutions; the former do not necessitate an additional impulse, and the latter are not of interest to the present analysts (because discarded by the filter); colored dots are refined-three impulse transfers, whose color is associated with some parameter of the trajectory, such as the gain with respect to the reference trajectory and the magnitude of the intermediate impulse

The significance of the optimization process in obtaining a refined transfer from a perturbed one is emphasized in Fig. 4.9. The graphs present the difference in gain between the two trajectories. Note also, that since $\kappa_{\max} = 1$ m/s, the absolute values for $\mathcal{G}$ are limited, particularly the maximum found is about 4 m/s. Hence, the optimization algorithm brings significant improvement, especially for solutions with gains up to tens m/s. However, this fact does not question the importance of selecting a suitable initial guess solution, which is already an improvement on its own.

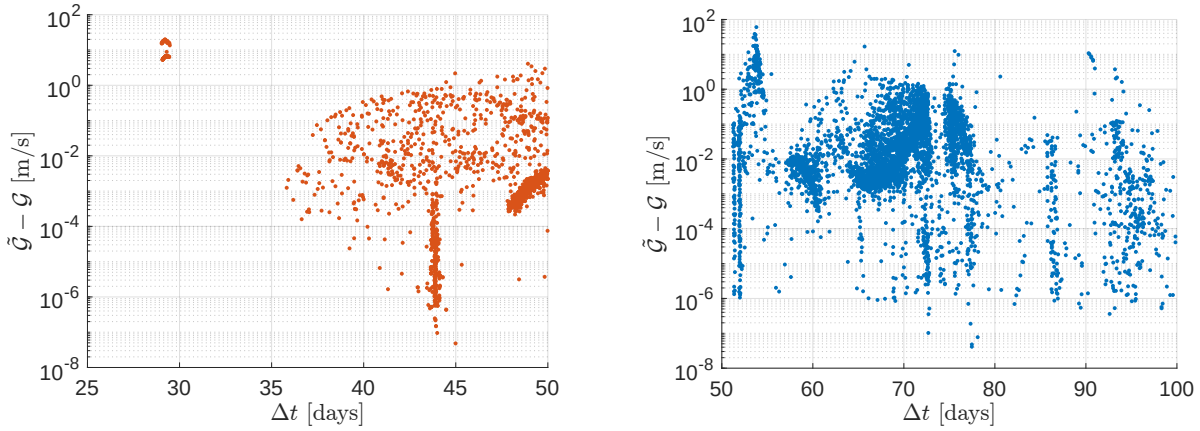

(a) S region (b) L region

Figure 4.9: Differential gain between the perturbed trajectory and the refined trajectory

Lastly, Fig. 4.10 shows the final gain of the refined trajectories. It can be appreciated that the melioration is, on average, more relevant in the L region, as the denser part of the point cloud in Fig. 4.10b has a slightly higher gain compared to Fig. 4.10a.

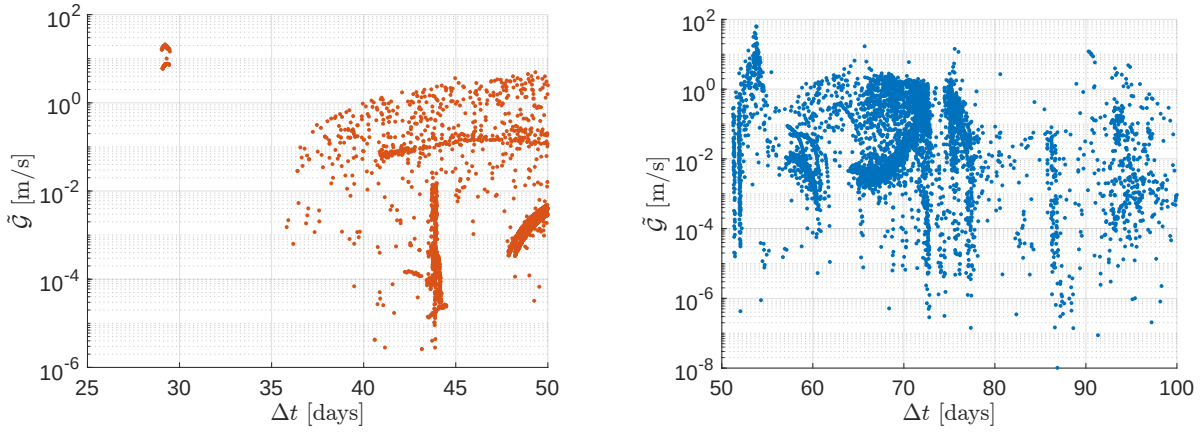

(a) S region (b) L region

Figure 4.10: Gain of the refined trajectory for each solution modified with a third impulse

Part II

Trajectory Continuation in a High-Fidelity Model

5 | Background

The first chapter of the second part of the thesis is devoted to the description of the Rotopulsating Restricted n-Body Problem, which is used to model the real solar system environment. Furthermore, low-energy transfers from the Earth to the Moon are described, together with their main advantages.

5.1. Rotopulsating Restricted n-Body Problem

In the last part of the present study, it is required to describe the motion of a spacecraft in the real solar system. The astrodynamical model selected for this aim is the Rotopulsating Restricted n-Body Problem (RPRnBP). This originates from the Inertial Restricted n-Body Model (IRnBM), which describes the motion of n bodies subjected to their mutual gravitational interaction with respect to an inertial reference frame. However, since the aim is to adapt to the real environment the trajectories obtained in the PBRFBP, while retaining as much as possible their features, an inertial model is not indicated. Instead, it would be optimal if the motion were described in a local system which rotates with the Earth and the Moon. Here the RPRnBP comes into play. Indeed, in the RPRnBP, the solar system n-body problem is written as a perturbation of the Circular Restricted Three Body Problem (CRTBP), by means of a time-dependent transformation [26]. However, before describing this model, it is convenient to introduce the IRnBM.

5.1.1. Inertial Restricted n-Body Problem

In the framework of the Inertial Restricted n-Body Problem, the motion of a massless particle P (i.e., the spacecraft) is described under the gravitational attraction of $n-1$ celestial bodies P_j, whose motions are not affected by P. Through the full work, the set of bodies considered to model the solar system environment will be denoted as

$$S = \{P_1, \ldots, P_{11}\} \ , \tag{5.1}$$

where, in continuation with the PBRFBP, P_1 denotes the Earth, P_2 the Moon, P_3 the Sun, and from P_4 to P_{11} the remaining planets (Pluto included). The mass of the i-th celestial body m_i is retrieved through JPL's SPICE.
The motion of the spacecraft is described in the International Celestial Reference Frame (ICRF), also called J2000 frame (see Fig. 5.1). This is an inertial reference frame whose axes $(\boldsymbol{X}, \boldsymbol{Y}, \boldsymbol{Z})$ are defined as follows:

- the X-axis points the Vernal Equinox, the intersection between the celestial equator and the ecliptic on January 01, 2000, 12:00 Barycentric Dynamical Time (TDB);
- the Z-axis is normal to the Earth equatorial plane on January 01, 2000, 12:00 TDB, which is approximately Earth's spin axis orientation at that epoch;
- the Y-axis completes the right-handed orthonormal reference frame.

If not specified, the origin of this frame is the Solar System Barycenter (SSB). However, it is also possible to choose the Earth as the center for the reference system, and this frame takes the name of Earth-Centered Inertial frame (ECI2000).

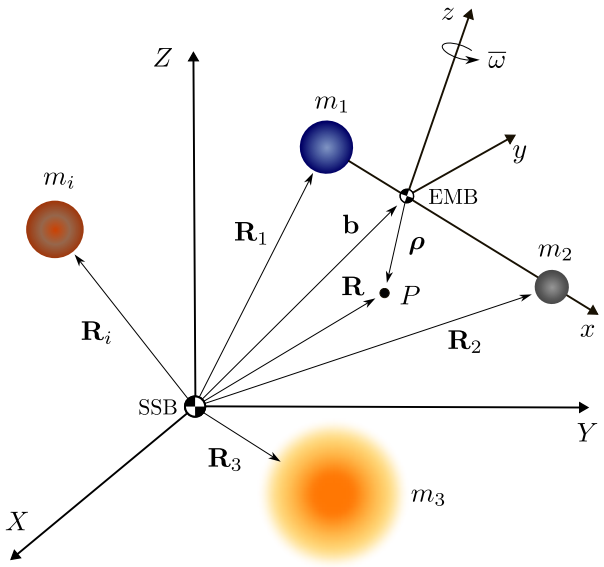

Figure 5.1: Sketch of the Inertial Restricted n-Body Model in the ICRF frame

Let indicate with $\mathbf{R}_i = (X_i, Y_i, Z_i)^\top$ and $\mathbf{V}_i = (\dot{X}_i, \dot{Y}_i, \dot{Z}_i)^\top$ the position and the velocity of the i-th celestial body in the ICRF frame; SPICE toolkit is used to read the states of the celestial bodies from the JPL ephemeris data DE432 at any epoch.
The equations of motion of a massless particle, derived through a Lagrangian formalism, can be written in a very compact form as [19]

$$\ddot{\mathbf{R}} + \nabla V = \mathbf{a}_{\text{SRP}} \ , \tag{5.2}$$

where $\mathbf{R} = (X, Y, Z)^\top$ is the position of P in the inertial frame. ∇V appearing in Eq. (5.2) is the gradient of the gravitational potential V derived from Newton's equation (so it is a function only of the positions of the bodies). In the PBRFBP presented before, the attractors have been considered as point masses. Actually, in the real world, all bodies have a distributed mass. This fact must be taken into account in a high-fidelity model, and thus there is the need to define a potential that accounts for the oblateness of the celestial bodies. According to [19], ∇V is equal to

$$\nabla V = \sum_{i \in S} \mu_i \left[\frac{\mathbf{R} - \mathbf{R}_i}{\|\mathbf{R} - \mathbf{R}_i\|^3} + \frac{3}{2} J_{2_i} R_{B_i}^2 \left(\frac{I_3 + 2I_z}{\|\mathbf{R} - \mathbf{R}_i\|^5} - \frac{5I_3(\mathbf{R} - \mathbf{R}_i)^\top I_z (\mathbf{R} - \mathbf{R}_i)}{\|\mathbf{R} - \mathbf{R}_i\|^7} \right) (\mathbf{R} - \mathbf{R_i}) \right] . \tag{5.3}$$

where μ_i is the gravitational parameter of the i-th primary, R_{B_i} its mean equatorial radius, and J_{2_i} is the second harmonic coefficient related to inhomogeneous mass distribution (accurate values for these physical parameters are provided by SPICE); instead, I_z is a 3×3 null matrix except for the third diagonal component, which is one.

On top of the conservative terms in Eq. (5.2), a high-fidelity model also requires the inclusion of nonconservative forces. In this work, the effect of solar radiation pressure (SRP) is considered, which imparts a net acceleration $\mathbf{a}_{\text{SRP}}$ to the spacecraft. Using a simple model where the flux decreases with the square of the distance from the source, the perturbation (aligned with the Sun-SC direction) can be estimated as

$$\mathbf{a}_{\text{SRP}} = \text{SP}_0 \frac{\mathbf{R} - \mathbf{R}_3}{\|\mathbf{R} - \mathbf{R}_3\|^3} . \tag{5.4}$$

SP_0 is the SRP parameter, defined as

$$\text{SP}_0 \equiv (1 + c_r) \frac{A}{m} \frac{\Phi_0 d_0^2}{c} , \tag{5.5}$$

where Φ_0 is the solar flux intensity at a distance d_0 from the Sun, c is the speed of light, c_r is the reflectivity coefficient of the spacecraft, and A/m its area to mass ratio. In this work d_0 corresponds to 1 AU, Φ_0 is a constant equal to 1368 W/m^2 and the values for c_r and A/m are taken from the ESA mission LUMIO [13]. In particular it is used $c_r = 0.3$, and $A/m = 0.00958$ m^2/kg.

5.1.2. Definition of the Rotopulsating Frame

Inertial frames represent a comfortable reference to write equations of motion, however, these frames are not always the most appropriate choice. The idea developed by the Barcelona group [25, 26] is to introduce a suitable reference system and units such that, after selecting two bodies of the Solar System as primaries, the complete n-body equations of the Solar System are set as a perturbation of the CRTBP. This new set of coordinates, named rotopulsating frame (RPF), is chosen such that its origin always coincide with the barycenter of the two primaries, and the three axes are hereafter defined.

- The x-axis is aligned, at every time, with the conjunction of the two bodies, and originates from the more massive body (assume $m_1 > m_2$);
- the z-axis is aligned with the relative angular momentum of the two primaries, so it is perpendicular to their common instantaneous plane of motion;
- the y-axis completes the right-handed orthonormal reference frame.

In the present case, the two primaries are the Earth and the Moon (see Fig. 5.1), and now the analogy with the PBRFBP is evident. Indeed, the rotating frame follows the motion of the primaries around their common barycenter. Moreover, with proper adimensionalization, the two bodies always occupy the same positions on the x-axis. In particular, the scaling factor k, which is the actual distance between the primaries, adjusts their positions so that P_1 is fixed at $(-\mu, 0, 0)$, and P_2 at $(1-\mu, 0, 0)$, where the mass parameter μ is defined as in the PBRFBP (see Eq. (2.3)). Hence, the new frame rotates and pulsates in a non-uniform fashion (this explains the name of the frame).

5.1.3. Coordinate Transformation and Adimensionalization

In order to describe the motion of P in a rotating frame, that by definition is no more inertial, it is useful to define some new adimensional quantities. Let $\{\varepsilon, \mathbf{R}, \mathbf{V}\}$ be the dimensional time[1], position, and velocity of P in the inertial frame, respectively, and let $\{\tau, \boldsymbol{\rho}, \boldsymbol{\eta}\}$ be their nondimensional counterparts in the RPF. Following [26], the transformation between sidereal coordinates (inertial), and synodic ones (non-inertial) is:

$$\mathbf{R}(\varepsilon) = \mathbf{b}(\varepsilon) + k(\varepsilon) C(\varepsilon) \boldsymbol{\rho}(\tau) \ , \tag{5.6}$$

[1]The symbol ε is used to represent a dimensional epoch expressed in TDB, and to distinguish from the symbol t used for the adimensional time of the PBRFBP. In the context of the RPRnBP, dots indicate derivation with respect to ε.

where the quantities appearing in Eq. (5.6) are defined as follows:

- $\mathbf{b}(\varepsilon)$ represents the translation from the SSB to the Earth–Moon barycenter (EMB), and it is defined as
$$\mathbf{b}(\varepsilon) = \frac{m_1\mathbf{R}_1(\varepsilon) + m_2\mathbf{R}_2(\varepsilon)}{m_1 + m_2} \ ; \tag{5.7}$$

- $k(\varepsilon)$ is the space adimensionalization factor and coincides with the instantaneous distance between the primaries
$$k(\varepsilon) = \|\mathbf{R}_2(\varepsilon) - \mathbf{R}_1(\varepsilon)\| \ ; \tag{5.8}$$

- $C(\varepsilon) = [\mathbf{e}_1(\varepsilon), \mathbf{e}_2(\varepsilon), \mathbf{e}_3(\varepsilon)]$ is an orthonormal rotation matrix, whose components are the unit vectors aligned with the axes of the RPF but seen from the ICRF:
$$\mathbf{e}_1(\varepsilon) = \frac{\mathbf{R}_2(\varepsilon) - \mathbf{R}_1(\varepsilon)}{k(\varepsilon)} \ , \tag{5.9a}$$
$$\mathbf{e}_2(\varepsilon) = \mathbf{e}_3(\varepsilon) \times \mathbf{e}_1(\varepsilon) \ , \tag{5.9b}$$
$$\mathbf{e}_3(\varepsilon) = \frac{(\mathbf{R}_2(\varepsilon) - \mathbf{R}_1(\varepsilon)) \times (\mathbf{V}_2(\varepsilon) - \mathbf{V}_1(\varepsilon))}{\|(\mathbf{R}_2(\varepsilon) - \mathbf{R}_1(\varepsilon)) \times (\mathbf{V}_2(\varepsilon) - \mathbf{V}_1(\varepsilon))\|} \ . \tag{5.9c}$$

It is important to remark that this change of coordinates is non-autonomous since $\mathbf{b}$, k and C depend on time through the components of $\mathbf{R}_1$ and $\mathbf{R}_2$, which, in turns, are read from ephemeris data. Note, also, that the definition of the cosine matrix C is consistent with the description of the RPF. In fact, it sets the primaries on the x–axis and rotates the instantaneous plane of motion into the (x, y)-plane by requiring that the relative velocity between the primaries has its third component equal to zero (see Fig. 5.2).

The relation linking the velocities $\mathbf{V}$ and $\boldsymbol{\eta}$ can be obtained deriving in time Eq. (5.6):

$$\mathbf{V}(\varepsilon) = \dot{\mathbf{b}}(\varepsilon) + \dot{k}(\varepsilon)C(\varepsilon)\boldsymbol{\rho}(\tau) + k(\varepsilon)\dot{C}(\varepsilon)\boldsymbol{\rho}(\tau) + k(\varepsilon)C(\varepsilon)\boldsymbol{\eta}(\tau)\dot{\tau} \ . \tag{5.10}$$

In Eq. (5.10) it is used that $\boldsymbol{\eta} = \boldsymbol{\rho}' \coloneqq \mathrm{d}\boldsymbol{\rho}/\mathrm{d}\tau$ (where $'$ indicates the derivative with respect to the nondimensional time τ), together with the chain rule

$$\frac{\mathrm{d}\boldsymbol{\rho}}{\mathrm{d}t} = \frac{\mathrm{d}\boldsymbol{\rho}}{\mathrm{d}\tau}\frac{\mathrm{d}\tau}{\mathrm{d}\varepsilon} = \boldsymbol{\eta}\dot{\tau} \ . \tag{5.11}$$

Finally, a change of independent variables from some dynamical time ε to the adimensional time τ is expressed as

$$\tau = \overline{\omega}(\varepsilon - \varepsilon_0) \ , \tag{5.12}$$

where $\overline{\omega}$ is the mean motion of P_2 with respect to P_1, and ε_0 is a fixed epoch[2], used to shift the non-autonomous problem to a null initial nondimensional time [17]. With this choice of the scaling factor $\overline{\omega}$, the revolution period of the primaries is 2π time units, like in the PBRFBP. The numerical value used for the mean motion is 2.6653143788e-06 s^{-1}, estimated from the mean distance between the primaries ($\overline{a}$) using Kepler's third law:

$$\overline{\omega} = \sqrt{\frac{G(m_1 + m_2)}{\overline{a}^3}} \ . \tag{5.13}$$

G is the universal gravitational constant and the mean distance, in turn, is obtained by averaging ephemeris data over a long time window (e.g., 400 years). Finally, note that $\dot{\tau} = \overline{\omega}$ is a constant, and this will simplify substantially the following computations.

5.1.4. Equations of Motion and Variational Equation

Once the new adimensional quantities have been introduced, the next step is to derive the equations for the restricted n-body model in the RPF. These can be obtained substituting the coordinate transformations of Eqs. (5.6), (5.10) and (5.12) into Eq. (5.2), and by using the definitions of ∇V and $\mathbf{a}_{\text{SRP}}$ (Eqs. (5.3) and (5.4)). After some manipulations, the equations of motion for the RPRnBM are [19]

$$\begin{aligned} \boldsymbol{\rho}'' + \frac{1}{\overline{\omega}}\left(\frac{2\dot{k}}{k} I_3 + 2C^\top \dot{C}\right)\boldsymbol{\rho}' + \frac{1}{\overline{\omega}^2}\left(\frac{\ddot{k}}{k} I_3 + 2\frac{\dot{k}}{k} C^\top \dot{C} + C^\top \ddot{C}\right)\boldsymbol{\rho} \\ + \frac{C^\top \ddot{\mathbf{b}}}{k\overline{\omega}^2} = \nabla\Omega + \frac{\mathrm{SP}_0}{\overline{\omega}^2 k^3} \frac{\boldsymbol{\delta}_3}{\|\boldsymbol{\delta}_3\|^3} \ , \end{aligned} \tag{5.14}$$

where $\nabla\Omega = \partial\Omega/\partial\boldsymbol{\rho}$ is the gradient of the pseudopotential

$$\Omega = \sum_{i \in S} \frac{m_i}{(m_1 + m_2)\|\boldsymbol{\delta}_i\|} \left[1 + \frac{J_{2_i} R_{B_i}^2}{2k^2 \|\boldsymbol{\delta}_i\|^2}\left(1 - \frac{3\boldsymbol{\delta}_i^\top C^\top I_z C \boldsymbol{\delta}_i}{\|\boldsymbol{\delta}_i\|^2}\right)\right] \ . \tag{5.15}$$

As can be seen from the sketch of the RPRnBP in Fig. 5.2, $\boldsymbol{\delta}_i = \boldsymbol{\rho} - \boldsymbol{\rho}_i$ is the distance between the spacecraft and the i-th celestial body in the RPF. Appendix A.3 reports the analytical expressions for the derivatives of k, C, and $\mathbf{b}$ appearing in Eq. (5.14).

[2]The reference epoch ε_0 is set arbitrarily to January 01, 2025.

Let $\boldsymbol{x} \equiv (\boldsymbol{\rho}\,, \boldsymbol{\eta})^\top$ be the state vector of P in the RPRnBP[3]. Equation (5.14) can be written in a first-order form as

$$\boldsymbol{x}' = \mathbf{f}_n(\boldsymbol{x}, \tau) = \begin{bmatrix} \mathbf{f}_{n\rho} \\ \mathbf{f}_{n\eta} \end{bmatrix} = \begin{bmatrix} \boldsymbol{\eta} \\ \boldsymbol{\rho}'' \end{bmatrix} \ , \tag{5.16}$$

where $\boldsymbol{\rho}''$ can be isolated from Eq. (5.14) itself.
The solution of Eq. (5.16) at time τ starting from an initial condition $\boldsymbol{x}_i$ at τ_i is indicated by $\boldsymbol{x}(\tau) = \varphi_n(\boldsymbol{x}_i, \tau_i; \tau)$ and is referred to as the flow of the RPRnBP. Analogously to what has been done for the PBRFBP, the STM of Eq. (5.16), i.e., $\Phi(\tau_i, \tau) \equiv \partial\varphi_n/\partial\boldsymbol{x}_i$, can be obtained integrating the variational equation Eq. (2.23), always with the same initial conditions $\Phi(\tau_i, \tau_i) = I_6$.
For the sake of completeness, the jacobian of the dynamical field $\mathbf{f}_n$ is hereafter reported:

$$\frac{\partial \mathbf{f}_n}{\partial \boldsymbol{x}} = \begin{bmatrix} 0_3 & I_3 \\ \dfrac{\partial \mathbf{f}_{n\eta}}{\partial \boldsymbol{\rho}} & \dfrac{\partial \mathbf{f}_{n\eta}}{\partial \boldsymbol{\eta}} \end{bmatrix} \ , \tag{5.17}$$

where, it can be shown, that the last two components are [19]

$$\begin{aligned} \frac{\partial \mathbf{f}_{n\eta}}{\partial \boldsymbol{\rho}} = &-\frac{1}{\overline{\omega}^2}\left(\frac{\ddot{k}}{k} I_3 + 2\frac{\dot{k}}{k} C^\top \dot{C} + C^\top \ddot{C}\right) \\ &- \sum_{i \in S} \frac{m_i}{(m_1 + m_2)} \left\{ \frac{1}{\|\boldsymbol{\delta}_i\|^3} - \frac{3}{\boldsymbol{\delta}_i^\top \boldsymbol{\delta}_i} \|\boldsymbol{\delta}_i\|^5 + \frac{3 J_{2_i} R_{B_i}^2}{2k^2} \left[\frac{I_3 + 2C^\top I_z C}{\|\boldsymbol{\delta}_i\|^5} \right.\right. \\ &- \frac{(5I_3 + 10 C^\top I_z C)\boldsymbol{\delta}_i \boldsymbol{\delta}_i^\top}{\|\boldsymbol{\delta}_i\|^7} - \frac{5 \boldsymbol{\delta}_i^\top C^\top I_z C \boldsymbol{\delta}_i I_3}{\|\boldsymbol{\delta}_i\|^7} - \frac{10 \boldsymbol{\delta}_i \boldsymbol{\delta}_i^\top C^\top I_z C}{\|\boldsymbol{\delta}_i\|^7} + \\ &\left.\left. 35 \boldsymbol{\delta}_i C^\top I_z C \boldsymbol{\delta}_i^\top \frac{\boldsymbol{\delta}_i \boldsymbol{\delta}_i^\top}{\|\boldsymbol{\delta}_i\|^9} \right] \right\} + \frac{\mathrm{SP}_0}{\overline{\omega}^2 k^3} \left[\frac{I_3}{\|\boldsymbol{\delta}_3\|^3} - \frac{\boldsymbol{\delta}_3 \boldsymbol{\delta}_3^\top}{\|\boldsymbol{\delta}_3\|^5} \right] \ , \end{aligned} \tag{5.18}$$

and

$$\frac{\partial \mathbf{f}_{n\eta}}{\partial \boldsymbol{\eta}} = -\frac{2}{\overline{\omega}} \left(\frac{\dot{k}}{k} I_3 + C^\top \dot{C} \right) \ . \tag{5.19}$$

Also in this case the variational equation must be integrated together with the state equation, yielding a system of 42 first-order differential equations. Being this model based on ephemerides data, the solution to the equations of motion must be obtained numerically. Furthermore, the computational heaviness of this problem is much higher compared to the PBRFBP due to, at least, three reasons: first, the problem is no longer

[3]Differently from the PBRFBP, where the state vector is represented by $\mathbf{x}$, in the RPRnBP the symbol $\boldsymbol{x}$ is used.

planar and the number of equations is more than double (42 versus 20); then, the analytical expression of the right-hand side of the dynamics is much involved; lastly, data must be retrieved from ephemerides at each integration step, and this absorbs many resources.

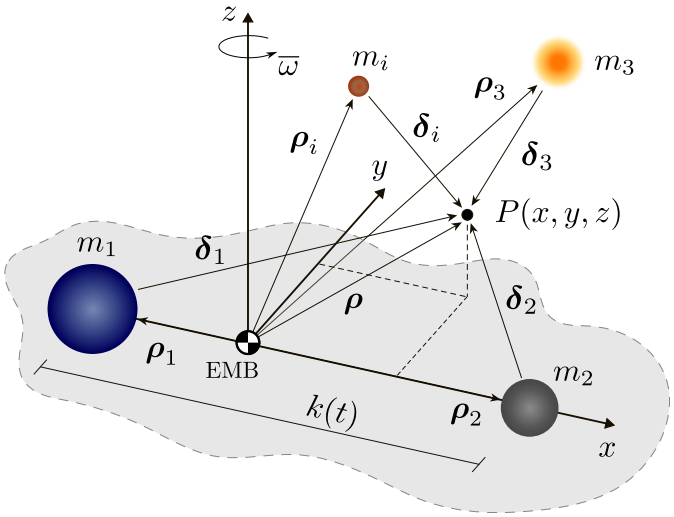

Figure 5.2: Sketch of the Rotopulsating Restricted n-Body Model

5.2. Low-Energy Transfers

The advancement of trajectory design techniques has made it possible to create novel categories of low-energy Earth–Moon transfers. These involve trajectories that put the spacecraft beyond the orbit of the Moon, and take advantage of the Sun's gravity to reduce the transfer fuel costs [48]. Indeed, when the spacecraft falls back toward the Earth, it arrives at the Moon with a velocity that closely matches the Moon's orbital velocity and it is ballistically captured by the Moon (i.e., the spacecraft two-body energy becomes negative). The result is that the lunar orbit insertion requires much less fuel compared with a conventional, direct transfer. The interested reader can find a review of low-energy transfer in [20].

The main theory to construct this kind of transfer was developed during the late 1980s and early 1990s by Belbruno and Miller, and is called weak stability boundary (WSB) theory [2–4]. The method involves targeting a specific area in space where the gravitational forces of the Sun, Earth, and Moon are in balance [5, 6], without utilizing any three-body periodic orbits or other dynamic structures.

Many approaches can be found in literature about designing low-energy transfers to low-altitude lunar orbits [12, 14, 15, 47, 66], and some missions have already flown on such trajectories (e.g., the Japanese Hiten Mission in 1991, NASA's ARTEMIS in 2009 and NASA's GRAIL in 2011).

Nevertheless, also [62] found a high number of exterior transfers which can be classified as low-energy transfers[4]. These can be easily identified, and are characterized by:

- a cost lower than the Hohmann Earth–Moon Transfer, that is about 3950 m/s with the present orbits (167 km at the Earth, 100 km for the Moon);
- a transfer time of about three months;
- a ballistic capture at the Moon.

The algorithm that will be developed in the second part of the thesis is mainly employed to continue these low-energy transfers in the real solar system, due to their more challenging and innovative nature. Indeed, for such trajectories, the Sun's effect is of paramount importance, and it is much more interesting to assess how these are modified once adapted to a full-ephemeris model.

5.2.1. Features of Low-Energy Transfers

Low-energy transfers provide many benefits to missions when compared with conventional transfers. Some example advantages include the following [48]:

1. They require less fuel to achieve the same orbit than it would be following a conventional, 3–6 day direct transfer (for example the lunar orbit insertion maneuver is at least 100 m/s smaller when the spacecraft destination is a 100 km circular orbit about the Moon [49]).
2. Low-energy transfers are more flexible than conventional transfers and may be used to transfer spacecraft to many more orbits on a given date.
3. They have extended launch periods: very little fuel is required to establish a launch period of 21 days or more for a mission to the Moon [47].
4. Low-energy transfers have a relaxed operational timeline. A spacecraft may typically wait a week before performing a maneuver, giving ample time to be checked out and prepare for its cruise operations.
5. Low-energy transfers may place several vehicles into very different orbits at the Moon using a single launch vehicle (the GRAIL mission [31, 57] separated two lunar-orbit insertions by over a day using very little fuel, see Fig. 5.3).
6. Low-energy trajectories may be used to transfer a spacecraft from the Moon directly to any location on the surface of the Earth using relatively small quantities of fuel.

[4]For example both the solutions reported in Figs. 4.1b and 4.2a are low-energy transfers.

The typical drawbacks of low-energy transfers between the Earth and the Moon are the longer transfer duration (making them not suitable for very time-critical missions, e.g., missions with human passengers) and the longer link distances, as the spacecraft travels as far as 2 million kilometers away from the Earth.

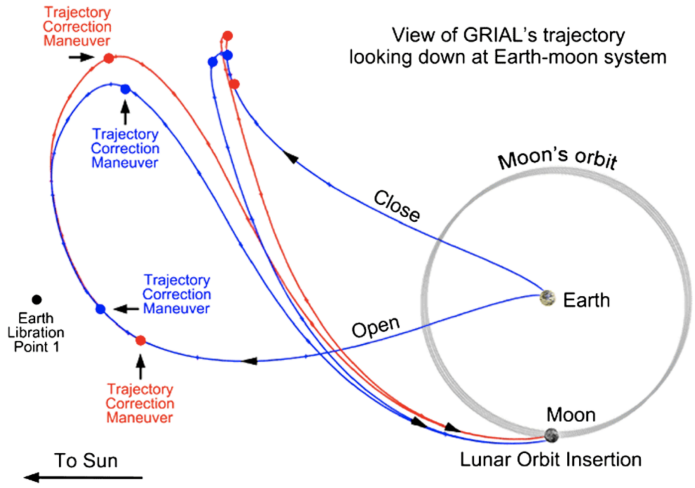

Figure 5.3: GRAIL-A and GRAIL-B trajectories for a launch at the open and close of the launch period (from [20]); note how the two orbits separate at the arrival even if they were lunched together

6 | Methodology

Nowadays there are numerous astrodynamical models at the disposal of designers. As these models become more intricate, they offer new solutions resulting from a more comprehensive vector field. However, since there is no analytical solution, gaining a comprehensive understanding of the dynamics is challenging. Typically, simplified models are employed in the early design phases of space missions. Indeed, they offer a deeper grasp of the dynamics of the system, and also the lighter computational effort required is more suitable to perform extensive optimization searches. By the way, a real mission will eventually fly in the real scenario, so the ultimate nominal trajectory must be studied, tested, and validate in a real solar system model.

The primary aim of the algorithm developed in the second part of this study is to facilitate the transition from orbits in a simplified model to more complex environments (this is what is intended for "continuation"). In particular, the present chapter describes the procedure adopted to import an Earth–Moon transfer from a simplified four-body model to a high-fidelity, ephemeris-based model of the solar system. The analysis carried out in this chapter is inspired by the works by Dei Tos and Topputo [17–19].

6.1. Description of the Continuation Problem

Before discussing the solution method, it is convenient to state the continuation problem and to describe the starting point as well as the expected final solution. Special attention is also given to the boundary conditions of the trajectory in the solar system.

6.1.1. Initial Trajectory in the Four-Body Model

Let γ_4[1] be an Earth–Moon transfer in the PBRFBP that embeds either two or three impulsive maneuvers, depending on whether it has been improved or not by means of the Primer Vector theory. As the starting point of each trajectory is a solution of [62], γ_4 satisfies the following conditions on the initial and final state:

[1]The subscript indicates the number of bodies in the model used to design the trajectory.

- at the departure time t_i the spacecraft is in a circular orbit around the Earth, at an altitude of 167 km;
- at the arrival time t_f an impulse of magnitude Δv_f inserts the spacecraft in a circular orbit around the Moon, whose altitude is 100 km.

Moreover, if γ_4 is an optimal two-impulse trajectory, i.e., it has not been further optimized with a mid-course impulse, then the two impulses are aligned with the local circular velocities of the initial and final orbits.

6.1.2. Final Trajectory in the n-Body Model

Analogously, let γ_n denote an impulsive trajectory in the RPRnBP made of an initial impulse in the proximity of the Earth, a final impulse at the Moon, and, in case, an intermediate maneuver.
Let $\boldsymbol{x}_i$ be the state of the spacecraft before the first maneuver, at the departure from the Earth, and $\boldsymbol{x}_f$ be the very last state at the arrival to the Moon, after the final impulse. In the original PBRFBP, these positions and velocities belong to the aforementioned initial and final circular orbits. However, the boundary conditions of the transfer in the n-body model still need to be specified. To this aim, let $\mathcal{D} \in \mathbb{R}^6$ and $\mathcal{A} \in \mathbb{R}^6$ be two sets containing the admissible states at the departure and arrival, respectively. They are defined as:

$$\mathcal{D} \equiv \left\{ \boldsymbol{x} \in \mathbb{R}^6 : \mathbf{h}_{\mathcal{D}}(\boldsymbol{x}) = \mathbf{0} \right\}, \qquad \mathcal{A} \equiv \left\{ \boldsymbol{x} \in \mathbb{R}^6 : \mathbf{h}_{\mathcal{A}}(\boldsymbol{x}) = \mathbf{0} \right\}, \tag{6.1}$$

where $\mathbf{h}_{\mathcal{D}}$ and $\mathbf{h}_{\mathcal{A}}$ are two vectorial functions collecting the conditions, yet to be defined, that $\boldsymbol{x}$ must respect in order to belong to $\mathcal{D}$ and $\mathcal{A}$. Moreover, let denote with $n_{\mathcal{D}}$ and $n_{\mathcal{A}}$ the number of scalar equations of the two sets.

The following paragraphs aim to discuss which is the most suitable frame where these constraints can be written. Many possibilities exist, but three general strategies can be identified: fixing the boundary conditions in an inertial frame (centered at the Earth or the Moon), writing them directly in the rotopulsating frame, or using both the previous approaches at the same time for different constraints.

Inertial Boundary Conditions

The boundary conditions of the transfer might be expressed in a local-inertial frame centered at the Earth or the Moon, for instance defining the altitude and orientation of two circular orbits. The first advantage that leaps out is the physical meaning of the boundary conditions: it is clear to see and it is the same during all the possible epochs. In fact,

independently of the departure and arrival dates, the initial and final states are fixed with respect to the two primaries. So, the convergence of the optimization algorithm intrinsically guarantees compliance with two a priori well-known conditions.
This approach is almost mandatory when the aim is to compare the costs of many trajectories that must share the same ending conditions. Moreover, it should be applied to a real mission wherein, either there are few available initial parking orbits, or there are very strict requirements (e.g., for scientific purposes) on the arriving orbit around the Moon. In this case, the two orbits are fixed and must be specified in an inertial frame.
The disadvantages are mainly from a numerical implementation viewpoint. Indeed, the optimization is performed in the RPRnBP and therefore the inertial boundary constraints must be converted into the RPF, becoming functions of the current epoch: $\mathbf{h}_{\mathcal{D}} = \mathbf{h}_{\mathcal{D}}(\boldsymbol{x}, \tau)$, $\mathbf{h}_{\mathcal{A}} = \mathbf{h}_{\mathcal{A}}(\boldsymbol{x}, \tau)$. Consequently, the sensitivity of the constraint functions with respect to the optimization variables is more involved.

Rotopulsating Boundary Conditions

On the other hand, the boundary conditions might be specified in the RPF from the beginning. The advantage is that no transformation is needed, because the states are already written in the reference system of the problem. Unfortunately, a direct physical meaning is lost, because the frame is rotating and pulsating in a non-uniform fashion; thus the reference distance and velocity used for the adimensionalization change with time. For instance, fixing a dimensionless final distance from one of the two primaries is like allowing the actual dimensional distance from the celestial body to vary over a bounded range. Again, because the orientation of the RPF changes with time, a constant orientation of the orbital plane (e.g., the (x, y)-plane) means that the inertial orientation of the final orbit around the celestial body is allowed to vary.
In such a way, the boundary conditions, seen from an interesting viewpoint (i.e., an inertial frame), change with the date and could not be known a priori (as the epoch of the transfer will be itself an optimization variable). This makes also more difficult to compare the costs of different transfers because their initial and final Kepler energies relative to the Earth and the Moon could be different.

Mixed Boundary Conditions

The last possibility is to write some conditions in an inertial frame and others in the RPF. This approach could be useful when some mission requirements are more strict, while others are less severe. An example is when the arrival orbit around the Moon is specified and it is an important requirement for the mission, whilst there are more degrees

of freedom in choosing the departure orbit around the Earth. In this case, the initial constraints can be written in the RPF and the final ones in the inertial frame. Actually, the meaning of these mixed conditions can be also extended to different quantities at the same boundary. For instance, fixing the size of the orbit from an inertial viewpoint but allowing the orbital plane to vary with time.

Recalling that the focus of this part of the thesis is to produce nominal trajectories for potential future missions, the approach chosen for the present work is to use inertial boundary conditions. Indeed, in a real-life scenario, it is likely that, depending on the mission goals, specific requirements are imposed on the altitude and the inclination of the lunar orbit, and these are defined in a local inertial frame.
Section 6.4 will be devoted to the detailed description of such boundary conditions. It will be also shown that the transformation between the RPF and the inertial frame is linear, so it does not introduce notable difficulties from a computational viewpoint.

6.1.3. Statement of the Problem

For the time being, leave aside the detailed definition of the boundary conditions, and focus on the continuation problem sketched in Fig. 6.1, which can be stated as follow.

Problem 6.1 (Trajectory Continuation Problem). — *Given an Earth–Moon transfer γ_4 in the* PBRFBM*, find its continuation γ_n in the* RPRnBM*, such that:*

- *the geometrical features of γ_4 are retained by γ_n;*
- *the spacecraft departs from an orbit around the Earth and arrives to an orbit around the Moon (specified by given boundary conditions);*
- *the same number of impulsive maneuvers of γ_4 is used;*
- *the total characteristic velocity (or cost) of γ_n is locally minimized.*

Problem 6.1 consists in an optimal control problem [16]. In this thesis, it is solved with a direct transcription and multiple shooting technique. Accordingly, the optimization is transcribed into a NLP problem and solved for a finite set of variables [9]. The algorithm presented is a versatile and effective method, providing improved accuracy, robustness, parallel computing, and ease of implementation. Especially in the case of high-sensitive nonlinear dynamics, multiple shooting is more reliable than simple shooting, where all the degrees of freedom are related to the initial conditions.
Indeed, the basic concept of the multiple shooting is to subdivide a trajectory into intervals and for each of them to solve a TPBVP, with successive iterations until the boundary

conditions and some continuity properties are satisfied. The higher number of decision variables is beneficial, as the sensitivity of the cost function is shared between more degrees of freedom; however, one must also consider the computational load required to handle large-scale optimization problems.
The methodology presented in this thesis to tackle Problem 6.1 consists of two steps, that will be described in detail in the following sections:

1. the generation of an initial seed trajectory;
2. the recursive correction of this last with a modified multiple shooting.

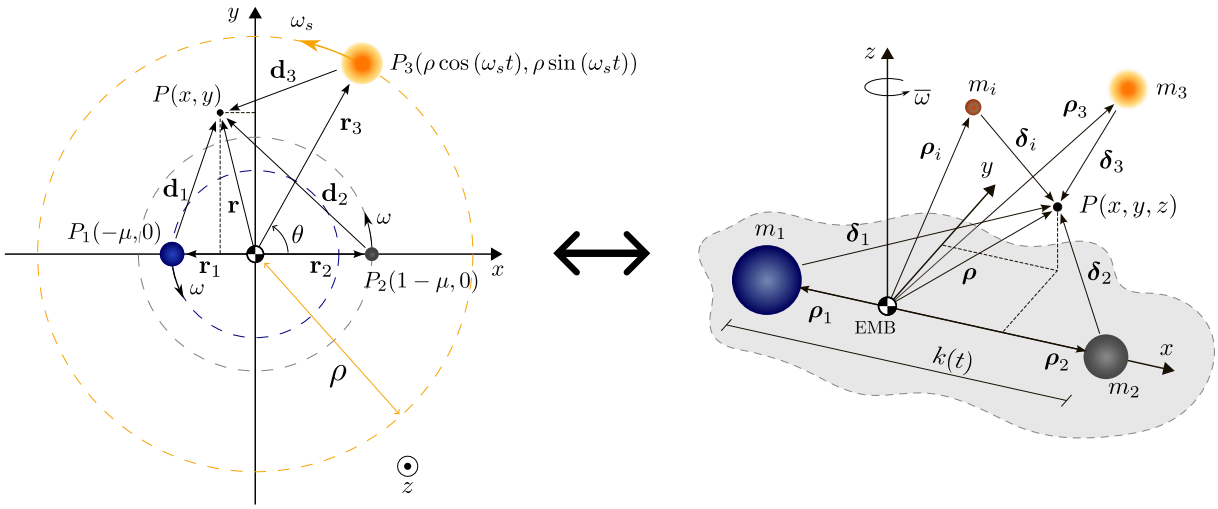

Figure 6.1: Continuation problem from the PBRFBM (*left*) to the RPRnBP (*right*)

6.2. Generation of an Initial Seed Trajectory

The initial guess for the multiple shooting algorithm is generated from the trajectory γ_4. First, a suitable epoch must be computed to define the RPF. Then, a method to transform the states of γ_4 into the nondimensional quantities of the RPRnBP is described. However, the representation of γ_4 in the solar system is no more a trajectory in the narrowest sense of the term. In fact, a (feasible) trajectory is defined as a series of positions and velocities obtained by solving the equations of motion. But when the states of γ_4 are adapted to the RPF, the current dynamics is that of the n-body model. Thus, the new series of states should be indicated as a curve (recalling the geometrical acceptance of the world) rather than a trajectory. To this aim, the symbol Γ_n is used, where the capital letter stresses that this sequence of positions and velocities is no more justified by the current astrodynamical model (expressed by the subscript).

6.2.1. Frames Alignment Problem

Henceforth, let rename the reference frame of the PBRFBP as rotating frame (RF). The positions of the Earth, the Moon, and the Sun (the celestial bodies shared between the models) in the RF of the PBRFBP and in the RPF of the RPRnBP are reported in Table 2. The way the axes of the two frames were defined, would allow for a perfect overlap of the two frames, at least for what concerns the two primaries. However, the position of the Sun is modeled in two different ways, and its effects are not negligible as the Sun's gravity is the main perturbation for a transfer in the Earth–Moon system (especially for exterior transfers).

Table 2: Position of the two primaries and the Sun in the PBRFBM and RPRnBM (coordinates are nondimensional according to the paradigm of each model)

Model	Earth	Moon	Sun
PBRFBM	$(-\mu, 0, 0)$	$(1-\mu, 0, 0)$	$(\rho\cos(\omega_s t), \rho\sin(\omega_s t), 0)$
RPRnBM	$(-\mu, 0, 0)$	$(1-\mu, 0, 0)$	$\boldsymbol{\rho}_3(\tau)$ from ephemeris data

Sun's Trajectories

Fig. 6.2 shows the trajectory of the Sun during one year in both models.

- On the one hand, in the PBRFBP, the Sun rotates with a constant radius on the (x, y)-plane and with a constant angular velocity (see Table 1). The time needed for the Sun to take a complete revolution is 29.53 days, which coincides with the mean Earth–Moon synodic month. Hence, the Sun repeats almost 12.4 times the same trajectory over a solar year (remember the motion is clockwise), so the left graph of Fig. 6.2 is a perfect circle.
- On the other, the position of the Sun depends only on the epoch at which it is observed, and things are less regular in the RPRnBP. The right graph of Fig. 6.2 shows that Sun's position from Jan 01, 2022, to Jan 01, 2023 (TDB), draws a spiraling trajectory. Here, the synodic period (the frequency associated with the in-plane circular motion) is on average 29.5 days but depends on the precise time window on which it is computed. Differently than before, also the distance of the Sun from the EMB changes depending on the epoch. Furthermore, an out-of-plane motion is present due to the relative inclination between the instantaneous Earth–Moon plane (i.e., the (x, y)-plane of the RPF) and the ecliptic. This angle changes with time, and in particular it oscillates between ± 5 deg over one year.

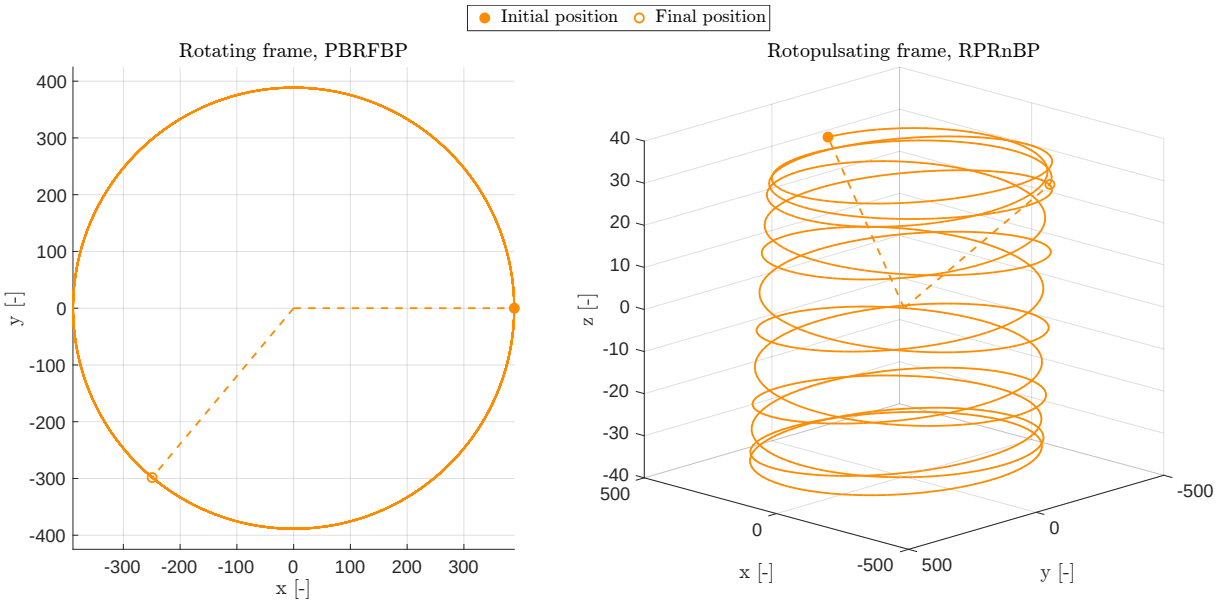

Figure 6.2: Sun's trajectory during a year in both the PBRFBP (*left*) and the PRPRnBP (*right*), where ephemerides are read from Jan 01 2022 to Jan 01 2023 TDB

Alignment Time and Alignment Epoch

Since a perfect overlap between the two models is not possible, an approach based on Sun's position is hereafter developed to find a satisfactory correspondence. This is desired because, the more the two astrodynamical models overlap, the more the curve Γ_n represents a advantageous initial seed orbit for the shooting problem, as it is closer to a real trajectory in the PBRFBP.

Unfortunately, the possibility for a precise alignment of the models during all the time of a transfer must be discarded. Indeed, the axes of the two frames rotate with different velocities: in the RF, ω is constant and always aligned with the z-axis (that consequently is fixed), whilst in the RPF, the axes are computed from the instantaneous position and velocity of the primaries. Nonetheless, this must not discourage from searching a dimensionless time t_a and an epoch ε_a when the configurations of P_1, P_2 and P_3 in the two models are as coincident as possible. Let define this time and this epoch as *alignment time* and *alignment epoch*, respectively. For a given t_a, one must find the epoch ε_a when the difference in the position of the three primaries is minimum. To this aim, a parameter is needed to quantify how much the two configurations are similar.
As the main discrepancies between the models were due to the Sun's trajectory, this parameter must be a function of the Sun's position at the generic time t and epoch ε.

Let denote with $\hat{\boldsymbol{r}}_3$ and $\hat{\boldsymbol{\rho}}_3$ the directions of the Sun in the two models (see Fig. 6.1):

$$\hat{\mathbf{r}}_3(t) \equiv \frac{\mathbf{r}_3(t)}{\|\mathbf{r}_3(t)\|} \ , \qquad \hat{\boldsymbol{\rho}}_3 \equiv \frac{\boldsymbol{\rho}_3(\varepsilon)}{\|\boldsymbol{\rho}_3(\varepsilon)\|} \ . \tag{6.2}$$

Now think of representing these directions in the same reference system, whose axes coincide with those of the RF and RPF. If a time t_a, and an epoch ε_a are found such that $\hat{\boldsymbol{r}}_3$ and $\hat{\boldsymbol{\rho}}_3$ coincide, the two configurations overlap. Therefore, the parameter required is the angle σ between the two directions: $\sigma \equiv \cos^{-1}(\hat{\boldsymbol{r}}_3 \cdot \hat{\boldsymbol{\rho}}_3)$. By the way, a more convenient quantity that introduces fewer nonlinearities can be used:

$$\sigma_{\cos} \equiv \cos(\sigma) = \hat{\mathbf{r}}_3 \cdot \hat{\boldsymbol{\rho}}_3 \ . \tag{6.3}$$

Indeed, maximizing $\sigma_{\cos}$ is equivalent to minimizing σ, but $\sigma_{\cos}$ is a linear function of $\hat{\boldsymbol{r}}_3$ and $\hat{\boldsymbol{\rho}}_3$, that is advantageous in view of a numerical optimization. At this point, the *Frames Alignment Problem* can be stated as:

Problem 6.2 (Frames Alignment Problem). — *Given a time t_a in the* PBRFBP*, find an epoch ε_a such that the angular distance between the direction of the Sun in the* PBRFBP *at time t_a and the Sun's direction in the* RPRnBP *at the epoch ε_a is minimized.*

$$\textit{Given } t_a, \ \textit{find } \varepsilon_a = \arg\max_{\varepsilon} \ \sigma_{\cos}(t_a, \varepsilon), \ \textit{where:}$$

$$\begin{cases} \sigma_{\cos} = \hat{\mathbf{r}}_3 \cdot \hat{\boldsymbol{\rho}}_3 \ , \\ \hat{\mathbf{r}}_3(t_a) = (\cos(\omega_s t_a), \sin(\omega_s t_a), 0) \ , \\ \boldsymbol{\rho}_3(\varepsilon) \textit{ is the direction of the Sun in the } \text{RPF} \textit{ at the epoch } \varepsilon \ . \end{cases}$$

In order to solve Problem 6.2, one must select before the alignment time $t_a \in [t_i, t_f]$ for each transfer. By definition, t_a is the time when the Sun's positions in the two models coincide (in the ideal case when $\sigma_{\cos} = 1$) and so also the Sun's gravitational attraction is the same (at least its direction). For all the other times $t \in [t_i, t_f] \setminus \{t_a\}$, the directions of the two perturbations do not coincide. Therefore, a careful choice is to set the alignment time when the Sun's effects on the trajectories are more relevant (relative to the attraction of the two primaries). For this reason, the alignment time on each transfer γ_4 is selected as the time when the SC distance from the EMB is maximum

$$t_a = \arg\max_{t \in [t_i t_f]} \|\mathbf{r}(t)\| \ . \tag{6.4}$$

6.2.2. Transformation Between Reference Systems

Once the Frames Alignment Problem is solved, the initial guess trajectory for the multiple shooting method can be built. As it will be described detailed in the next section, this consists of a series of states (position and velocities) at some discrete instants of time. So, the problem now is to transform γ_4 into Γ_n, or, alternatively, to convert each the state $\{t, \mathbf{r}, \mathbf{v}\}$ of γ_4 into the triplet $\{\tau, \boldsymbol{\rho}, \boldsymbol{\eta}\}$. Then, once the curve Γ_n is computed, it can be sampled to obtain a starting solution for the NLP algorithm.

The only way to represent a state in the RPF is to use the transformations in Eqs. (5.6), (5.10) and (5.12). Hence, one must necessarily pass through the ICRF. The missing link between the RF and the ICRF is named Initial Inertial frame (IIF). The origin of this frame is still the EMB, but its axes, $(\boldsymbol{i}, \boldsymbol{j}, \boldsymbol{k})$, are fixed and coincide with those of the RF at the initial time of the transfer t_i. Therefore, as depicted in see Fig. 6.3a, the IIF is an inertial frame defined for each transfer γ_4, that coincides with the RF at $t = t_i$. The conversion from the RF to the IIF is obtained using the time-dependent matrix $C_1(t)$

$$C_1(t) = \begin{bmatrix} \cos(t - t_i) & -\sin(t - t_i) & 0 \\ \sin(t - t_i) & \cos(t - t_i) & 0 \\ 0 & 0 & 1 \end{bmatrix} . \tag{6.5}$$

The advantage of this frame is that the direction cosines of $(\boldsymbol{i}, \boldsymbol{j}, \boldsymbol{k})$ in the ICRF, denoted as $(\boldsymbol{e}_1^{(i)}, \boldsymbol{e}_2^{(i)}, \boldsymbol{e}_3^{(i)})$, are constant and can be computed evaluating Eq. (5.9) at the departure epoch ε_i. Indeed, after solving the frame alignment problem ε_i can be computed assuming that the transfer time of γ_n is the same as γ_4, and so

$$\varepsilon_i = \varepsilon_a - (t_a - t_i)\overline{T} , \tag{6.6}$$

where $\overline{T}$ is the nondimensional time of the PBRFBP (see Eq. (2.1)), and it is needed to match the measurement unit of the epoch ε. Then, the change of coordinates from the IIF to the ICRF is done by means of $\mathbf{b}$ and the constant rotation matrix C_2 (see Fig. 6.3b)

$$C_2 = [\boldsymbol{e}_1^{(i)}, \boldsymbol{e}_2^{(i)}, \boldsymbol{e}_3^{(i)}] . \tag{6.7}$$

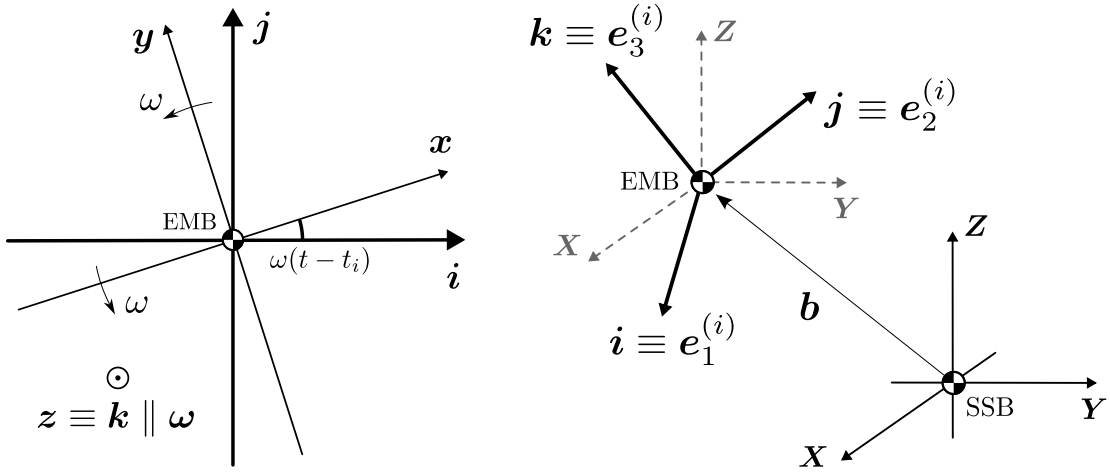

(a) RF $(\boldsymbol{x}, \boldsymbol{y}, \boldsymbol{z})$ and IIF $(\boldsymbol{i}, \boldsymbol{j}, \boldsymbol{k})$ (b) IIF $(\boldsymbol{e}_1^{(i)}, \boldsymbol{e}_2^{(i)}, \boldsymbol{e}_3^{(i)})$ and ICRF $(\boldsymbol{X}, \boldsymbol{Y}, \boldsymbol{Z})$

Figure 6.3: Graphical representation of the transformations between the reference frames; $\boldsymbol{b}$ is the position of the EMB in the ICRF, read from ephemeris data

Now that all the ingredients are defined, each step of the process to transform a state from the RF to the RPF is described.
Given a state $\{t,\, \mathbf{r}(t),\, \mathbf{v}(t)\}$ in the RF and an alignment time t_a, the corresponding state in the RPF is computed with the following procedure:

1. write the state vector in the IIF:

$$\begin{cases} \mathbf{r}^{(\mathrm{IIF})}(t) = C_1(t)\ \mathbf{r}(t) \\ \mathbf{v}^{(\mathrm{IIF})}(t) = C_1(t)\ \left(\mathbf{v}(t) + \boldsymbol{\omega} \times \mathbf{r}(t)\right) \end{cases}, \tag{6.8}$$

   where $C_1(t)$ is computed with Eq. (6.5) and $\boldsymbol{\omega} = [0, 0, \omega]^\top$;

2. restore the dimensional units of t, t_a, $\mathbf{r}^{(\mathrm{IIF})}(t)$ and $\mathbf{v}^{(\mathrm{IIF})}(t)$ multiply by the reference quantities $\overline{T}$, $\overline{L}$, $\overline{V}$;

3. solve the Frames Alignment problem and compute $\varepsilon = \varepsilon_a + (t - t_a)\overline{T}$;

4. calculate $\varepsilon_i = \varepsilon_a + (t_i - t_a)\overline{T}$ and $C_2 = [\boldsymbol{e}_1(\varepsilon_i),\, \boldsymbol{e}_2(\varepsilon_i)\,, \boldsymbol{e}_3(\varepsilon_i)]$;

5. write the state vector in the ICRF:

$$\begin{cases} \mathbf{R}(\varepsilon) = \mathbf{b}(\varepsilon) + C_2\ \mathbf{r}^{(\mathrm{IIF})}(t) \\ \mathbf{V}(\varepsilon) = \dot{\mathbf{b}}(\varepsilon) + C_2\ \mathbf{v}^{(\mathrm{IIF})}(t) \end{cases}; \tag{6.9}$$

6. compute $\{\tau,\, \boldsymbol{\rho}(\tau),\, \boldsymbol{\eta}(\tau)\}$ from $\{\varepsilon,\, \mathbf{R}(\varepsilon),\, \mathbf{V}(\varepsilon)\}$ using Eqs. (5.6), (5.10) and (5.12).

6.3. Multiple-Burn, Multiple-Shooting Formulation

A direct multiple shooting technique is developed, which accommodates two or three maneuvers (depending on the initial guess in the PBRFBP) to drive $\boldsymbol{x}(\tau)$ from $\mathcal{D}$ to $\mathcal{A}$ hypersurfaces, while respecting some continuity requirements.
The trajectory is sampled at a finite number of points, called nodes, where the state vector is taken as an unknown variable. An arc is defined as the ballistic portion of the trajectory separated by maneuvers and a segment is the portion of the trajectory separated by two consecutive nodes. With m number of maneuvers and s nodes between two maneuvers, there are $m-1$ arcs and $s-1$ segments within each arc. In particular, due to the nature of the original problem, only the cases with $m=2$ and $m=3$ are discussed.

Let $\tau_i^{(j)}$ and $\tau_f^{(j)}$ be the initial and final time of the j-th arc, with $j=1,\dots,m-1$. The time interval $[\tau_i^{(j)},\tau_f^{(j)}]$ is discretized over a uniform time grid, made up by s points $\tau_i^{(j)}=\tau_1^{(j)}<\ldots<\tau_k^{(j)}<\ldots<\tau_s^{(j)}=\tau_f^{(j)}$, with

$$\tau_k^{(j)}=\tau_i^{(j)}+\frac{k-1}{s-1}\left(\tau_f^{(j)}-\tau_i^{(j)}\right)\ ,\quad k=1,\dots,s\ . \tag{6.10}$$

The solution is sampled at each node, and the state vector is denoted as $\boldsymbol{x}_k^{(j)}=\boldsymbol{x}(\tau_k^{(j)})$. Recalling the definitions of $\boldsymbol{x}_i$ and $\boldsymbol{x}_f$ in section 6.1.2, the node $\boldsymbol{x}_1^{(1)}$ is placed after the initial impulse, while the final node $\boldsymbol{x}_s^{(m-1)}$ is located before the final impulse.
Let define the *defect vector* as

$$\boldsymbol{\zeta}_k^{(j)}\coloneqq\varphi_n(\boldsymbol{x}_k^{(j)},\tau_k^{(j)};\tau_{k+1}^{(j)})-\boldsymbol{x}_{k+1}^{(j)}\ ,\quad \begin{matrix}k=1,\dots,s-1\\ j=1,\dots,m-1\end{matrix}\ . \tag{6.11}$$

Despite the division into segments, the continuity of the solution must be respected within each arc, therefore the problem is to determine $\boldsymbol{x}_k^{(j)}$ such that $\boldsymbol{\zeta}_k^{(j)}=\mathbf{0}$. Moreover, focusing on a three-impulse trajectory ($m=3$), time and position continuity must be guaranteed also at the mid-course impulse

$$\boldsymbol{\Psi}_{\rho_m}\coloneqq\boldsymbol{\rho}_1^{(2)}-\boldsymbol{\rho}_s^{(1)}=\mathbf{0}\ ,\qquad\qquad \xi_m\coloneqq\tau_1^{(2)}-\tau_s^{(1)}=0\ . \tag{6.12}$$

Note, that the constraint $\boldsymbol{\Psi}_{\rho_m}$ leaves the door open to a possible discontinuity on the velocity, namely

$$\Delta\boldsymbol{\eta}_2=\boldsymbol{\eta}_1^{(2)}-\boldsymbol{\eta}_s^{(1)}\ . \tag{6.13}$$

This is consistent with the fact that arcs are separated by impulsive maneuvers, and the cost of these will contribute to the overall cost of the transfer.

However, another scalar constraint is considered at the time of the midcourse impulse. It is required that $\boldsymbol{\eta}_s^{(1)}$ and $\boldsymbol{\eta}_1^{(2)}$ are aligned, and so that

$$\Psi_{\eta_m} \coloneqq \boldsymbol{\eta}_1^{(2)} \cdot \boldsymbol{\eta}_s^{(1)} - \left\|\boldsymbol{\eta}_1{}^{(2)}\right\| \left\|\boldsymbol{\eta}_s{}^{(1)}\right\| = 0 \ . \tag{6.14}$$

If the two velocities are parallel, then also their difference $\Delta\boldsymbol{\eta}_2$ is in the same direction. This fact plays a crucial role in formulating the cost function for the problem, as it will be shown. Additionally, from an energetic perspective, it is desirable to maneuver in the direction of the local velocity as this maximizes the spacecraft energy variations [51]. Therefore, the constraints at the midcourse impulse are collected in a single vector:

$$\boldsymbol{\Psi}_m \coloneqq \begin{bmatrix} \boldsymbol{\Psi}_{\rho_m} \\ \Psi_{\eta_m} \end{bmatrix} = \begin{bmatrix} \boldsymbol{\rho}_1^{(2)} - \boldsymbol{\rho}_s^{(1)} \\ \boldsymbol{\eta}_1^{(2)} \cdot \boldsymbol{\eta}_s^{(1)} - \left\|\boldsymbol{\eta}_1{}^{(2)}\right\| \left\|\boldsymbol{\eta}_s{}^{(1)}\right\| \end{bmatrix} = \mathbf{0} \ . \tag{6.15}$$

Moreover, the boundary conditions at the departure and the arrival must be enforced

$$\mathbf{h}_{\mathcal{D}}(\boldsymbol{x}_i, \tau_i) = \mathbf{0} \ , \qquad \mathbf{h}_{\mathcal{A}}(\boldsymbol{x}_f, \tau_f) = \mathbf{0} \ . \tag{6.16}$$

Finally, position continuity must be imposed again behind the initial and final impulses:

$$\boldsymbol{\Psi}_i \coloneqq \boldsymbol{\rho}_1^{(1)} - \boldsymbol{\rho}_i = \mathbf{0} \ , \qquad \boldsymbol{\Psi}_f \coloneqq \boldsymbol{\rho}_f - \boldsymbol{\rho}_s^{(2)} = \mathbf{0} \ . \tag{6.17}$$

Fig. 6.4 shows a schematic representation of the multiple-burn, multiple-shooting strategy in the case of three impulsive maneuvers ($m = 3$).

6.3.1. Statement of the Optimization Problem

Within each arc there are s six-dimensional unknowns, $\boldsymbol{x}_k^{(j)}$, as well as the initial and final time $\tau_i^{(j)}$, $\tau_f^{(j)}$, for a total of $6s + 2$ scalar variables. The overall NLP variables vector, $\mathbf{y}$, is made of the collection of the free variables of each arc together with the initial and final states, $\boldsymbol{x}_i$ and $\boldsymbol{x}_f$:

$$\mathbf{y} \coloneqq \left\{ \boldsymbol{x}_i,\, \boldsymbol{x}_k^{(j)},\, \boldsymbol{x}_f,\, \tau_i^{(j)},\, \tau_f^{(j)} \right\}, \quad \begin{matrix} k = 1, \ldots, s \\ j = 1, \ldots, m-1 \end{matrix} \ . \tag{6.18}$$

The vector of equality constraints $\boldsymbol{h}$ is defined as:

$$\mathbf{h}(\mathbf{y}) \coloneqq \left\{ \boldsymbol{\zeta}_k^{(j)},\, \mathbf{h}_{\mathcal{D}} \ ,\, \mathbf{h}_{\mathcal{A}},\ \boldsymbol{\Psi}_i,\, \boldsymbol{\Psi}_f,\, \boldsymbol{\Psi}_m,\, \xi_m \right\}, \quad \begin{matrix} k = 1, \ldots, s-1 \\ j = 1, \ldots, m-1 \end{matrix} \ , \tag{6.19}$$

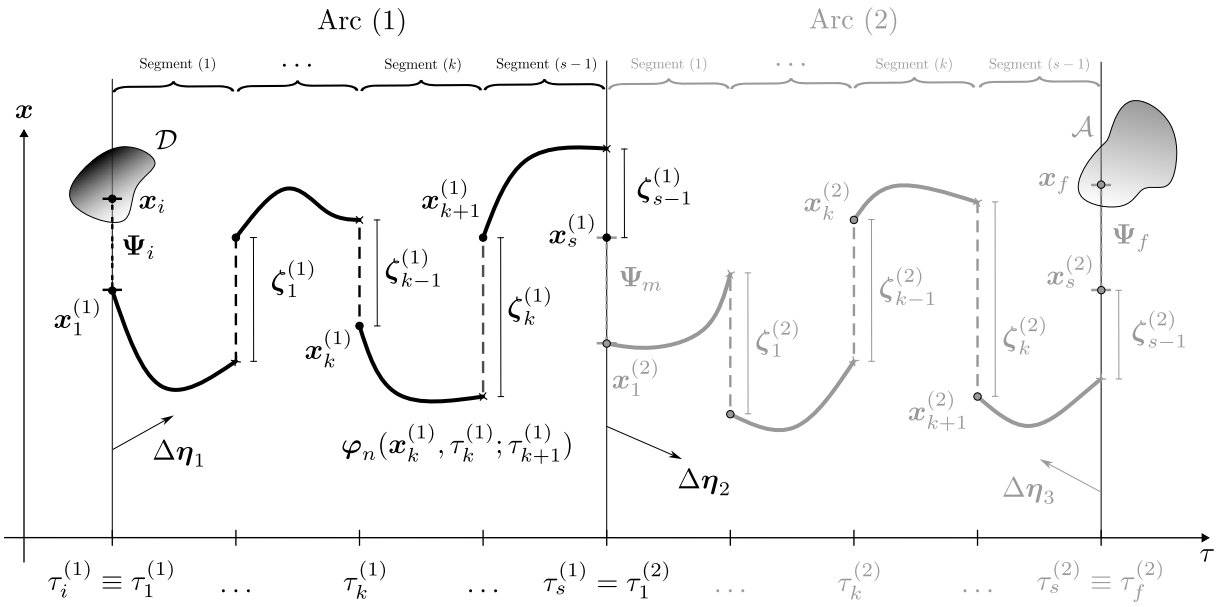

Figure 6.4: Schematic representation of the multiple-burn, multiple-shooting strategy in the case of three impulsive maneuvers ($m = 3$)

where the last two entries are present only if $m = 3$. The components of $\mathbf{h}$ are vector-valued functions and, in particular, $\mathbf{\Psi}_i$, $\mathbf{\Psi}_f$, $\mathbf{\Psi}_{\rho_m}$, ξ_m are linear functions of $\mathbf{y}$. $\mathbf{h}_\mathcal{D}$ and $\mathbf{h}_\mathcal{A}$ are still undefined and could be linear as well as nonlinear functions of $\mathbf{y}$. A set of linear inequality constraints is assembled to limit the terminal times of each arc:

$$\mathbf{g}(\mathbf{y}) \coloneqq \left\{ \tau_i^{(j)} - \tau_f^{(j)} \right\} \leq \mathbf{0} \ , \quad j = 1, \ldots, m-1 \ . \tag{6.20}$$

$\mathbf{g}(\mathbf{y})$ is made of $m - 1$ scalar linear functions, but if necessary, it could be expanded by adding other constraints, for instance on the maximum transfer duration as well as on the Δv budget of a single maneuver (maximum and minimum values), or about the minimum distance from a planet.

At this point the impulsive trajectory optimization can be stated as a NLP problem, where the cost function J to be minimized is defined in the following section, as it needs a dedicated discussion.

Problem 6.3 (Multiple Shooting NLP Problem). — *Optimal, multi-impulse Earth to Moon transfers are found by solving the* NLP *problem:*

$$\min_{\mathbf{y}} J(\mathbf{y}) \quad \textit{subject to} \quad \mathbf{h}(\mathbf{y}) = \mathbf{0} \quad \textit{and} \quad \mathbf{g}(\mathbf{y}) \leq \mathbf{0} \ .$$

Of course, the size of the problem depends on m and s. In the case of a two-impulse transfer ($m = 2$): $\mathbf{y} \in \mathbb{R}^{6s+14}$, $\mathbf{h}$ is made of $6s + n_{\mathcal{D}} + n_{\mathcal{A}}$ scalar functions, and $\mathbf{g}$ is a single scalar function; whereas, for a three-impulse transfer ($m = 3$): $\mathbf{y} \in \mathbb{R}^{12s+16}$, the number of equality constraints is $12s - 1 + n_{\mathcal{D}} + n_{\mathcal{A}}$, and $\mathbf{g}$ is composed by two scalar functions.

6.3.2. Cost Function

The purpose of the optimization process is to minimize the total characteristic velocity, i.e., the sum of the impulses $\|\Delta\mathbf{v}_i\|$, $\|\Delta\mathbf{v}_f\|$ and, if present, $\|\Delta\mathbf{v}_m\|$. This is related to the onboard propellant consumption through the Tsiolkovsky equation. Anyway, the velocity variation is a meaningful parameter only if written in an inertial frame and with the classical measurement units (e.g., m/s). Therefore the dimensional velocity should be recovered from the adimensional state $\boldsymbol{x} = \{\boldsymbol{\rho}, \boldsymbol{\eta}\}$ of the RPRnBP. The following equations express this link between adimensional and dimensional velocity variations.
At first, the dimensional velocity variation is transformed into the RPF using Eq. (5.10)

$$\begin{aligned} \|\Delta\mathbf{v}\| &= \|\mathbf{v}_+ - \mathbf{v}_-\| \\ &= \left\| \left[\dot{\mathbf{b}} + \left(\dot{k}C + k\dot{C}\right)\boldsymbol{\rho} + k\dot{\tau}C\boldsymbol{\eta}\right]_+ - \left[\dot{\mathbf{b}} + \left(\dot{k}C + k\dot{C}\right)\boldsymbol{\rho} + k\dot{\tau}C\boldsymbol{\eta}\right]_- \right\| \ , \end{aligned} \tag{6.21}$$

where the subscripts '$-$' and '$+$' indicate quantities evaluated before and after the maneuver, respectively. Assuming that the maneuver is impulsive, $\tau_+ = \tau_- = \tau$, and the position across the impulse is continuous: $\boldsymbol{\rho}_+ = \boldsymbol{\rho}_- = \boldsymbol{\rho}$. Moreover, also the quantities $\dot{\mathbf{b}}$, k, $\dot{k}$, C and $\dot{C}$ are equal before and after the impulse, as they depend only on the epoch (see appendix A.3). Thus Eq. (6.21) simplifies, yielding to

$$\|\Delta\mathbf{v}\| = \|k\dot{\tau}C\left(\boldsymbol{\eta}_+ - \boldsymbol{\eta}_-\right)\| \ . \tag{6.22}$$

Note, that C is a rotation cosine matrix and hence it does not introduce a variation in the modulus of a vector:

$$\|\Delta\mathbf{v}\| = k\dot{\tau}\,\|\boldsymbol{\eta}_+ - \boldsymbol{\eta}_-\| = k\overline{\omega}\,\|\Delta\boldsymbol{\eta}\| \ . \tag{6.23}$$

Equation (6.23) represents the relation needed to express $\|\Delta\mathbf{v}\|$ as a function of $\Delta\boldsymbol{\eta}$. Now, the objective function of the problem can be written as:

$$J(\mathbf{y}) \coloneqq \sum_{j=1}^{m} \|\Delta\mathbf{v}_j\| \ , \tag{6.24}$$

where the epoch of each node $\varepsilon_k^{(j)}$ is recovered using Eq. (5.11) and

$$\|\Delta\mathbf{v}_1\| = \overline{\omega} k(\varepsilon_i^{(1)}) \left\| \boldsymbol{\eta}_1^{(1)} - \boldsymbol{\eta}_i \right\| \ , \qquad \|\Delta\mathbf{v}_2\| = \overline{\omega} k(\varepsilon_f^{(m-1)}) \left\| \boldsymbol{\eta}_f - \boldsymbol{\eta}_s^{(m-1)} \right\| \ , \tag{6.25}$$

and, when $m = 3$ the midcourse impulse is

$$\|\Delta\mathbf{v}_3\| = \overline{\omega} \left\| k(\varepsilon_i^{(2)}) \boldsymbol{\eta}_1^{(2)} - k(\varepsilon_f^{(1)}) \boldsymbol{\eta}_s^{(1)} \right\| \ . \tag{6.26}$$

Nevertheless, this expression for $\|\Delta\mathbf{v}_3\|$ conceals an issue, as the difference between $\boldsymbol{\eta}_1^{(2)}$ and $\boldsymbol{\eta}_s^{(1)}$ appears at the denominator of some derivatives with respect to $\mathbf{y}$. This represents a problem in all those solutions with a continuous velocity at τ_m because the gradient of the objective function (used by NLP solvers) would be singular, yielding numerical errors. Indeed, note that the algorithm is not constrained to put a midcourse maneuver: it should be recovered only if necessary to further minimize the objective function. Therefore, one could think of some alternative objective functions.
In literature, this issue is often overcome using the squared magnitude of the $\Delta\mathbf{v}$ in the objective function, which can be expressed as the sum of all the $\Delta\mathbf{v}^\top\Delta\mathbf{v}$. Even so, this is not strictly equivalent to minimizing the fuel consumption, and it was observed from numerical examples that in some cases solutions with a lower cost function $J = \sum \Delta\mathbf{v}^\top\Delta\mathbf{v}$ have instead a higher $J = \sum \|\Delta\mathbf{v}\|$ (related to the real fuel expenditure).
Alternatively, a regularization method could be employed to remove the notorious singularities of the equations of motion. For example, some regularized variables, based on the Levi–Civita transformation, are used in literature [56].

Despite that, in the present case, a simpler solution can be adopted to face the singularities of $\partial J/\partial\mathbf{y}$. In particular, the constraint Ψ_{η_m} can be exploited to rewrite Eq. (6.26). Recalling that if two vectors are parallel then the magnitude of their difference coincides with the difference of their magnitudes, provided that $\Psi_{\eta_m} = 0$, then

$$\|\Delta\mathbf{v}_3\| = \overline{\omega} \left\| k(\varepsilon_i^{(2)}) \boldsymbol{\eta}_1^{(2)} \right\| - \overline{\omega} \left\| k(\varepsilon_f^{(1)}) \boldsymbol{\eta}_s^{(1)} \right\| \ . \tag{6.27}$$

In such a way, the singularities in the objective function gradient are prevented also when $\boldsymbol{\eta}_1^{(2)} = \boldsymbol{\eta}_s^{(1)}$, as only the magnitude of one velocity at a time (that is never null) appears at the denominator. Note, also, that it is not necessary to modify Eq. (6.25), because nonzero initial and final impulses are always necessary to perform a transfer.

6.3.3. Objective Functions and Constraints Jacobians

To set up an efficient multiple shooting method, the derivatives of the objective function and the constraints with respect to the NLP variables are computed analytically. When possible, the derivatives are extracted from the STM, which in turn is computed by integrating the variational equations (2.23) with the gradient of the vector field reported in Eq. (5.17). The STM provides fast and accurate information, and avoids using finite difference methods. Moreover, it allows for increased accuracy in the computation and thus enhanced robustness of the algorithm itself.
The objective function and constraints possess simple derivative expressions, except the jacobian of defect constraints, where the derivative of $\varphi_n(\boldsymbol{x}_k, \tau_k; \tau_{k+1})$ with respect to $\boldsymbol{x}_k$, τ_k and τ_{k+1} are required. The following analytical results have a key role in the next computations [17, 43, 65]:

$$\begin{aligned} \frac{\partial \varphi_n}{\partial \boldsymbol{x}_k} &= \Phi(\tau_k, \tau_{k+1}) \ , \\ \frac{\partial \varphi_n}{\partial \tau_k} &= -\Phi(\tau_k, \tau_{k+1})\, \mathbf{f}_n(\boldsymbol{x}_k, \tau_k) \ , \\ \frac{\partial \varphi_n}{\partial \tau_{k+1}} &= \mathbf{f}_n(\varphi_n(\boldsymbol{x}_k, \tau_k; \tau_{k+1}),\, \tau_{k+1}) \ , \end{aligned} \tag{6.28}$$

where $\mathbf{f}_n$ is the vector field reported in Eq. (5.16). Furthermore, it must be pointed out that in this context all the NLP variables $\mathbf{y}$ are independent. Thus, every time the variation of one component of $\mathbf{y}$ is computed with respect to another NLP variable, the resulting sensitivity is zero (for example $\partial \boldsymbol{\rho}_k / \partial \tau_i = \mathbf{0}$).

Jacobian of the Objective Functions

Before listing all the derivatives of J with respect to $\mathbf{y}$ it is useful to compute the derivative of k with respect to the dimensionless time:

$$k' \coloneqq \frac{\mathrm{d}k}{\mathrm{d}\tau} = \frac{\mathrm{d}k}{\mathrm{d}\varepsilon}\frac{\mathrm{d}\varepsilon}{\mathrm{d}\tau} = \frac{\dot{k}}{\overline{\omega}} = \frac{(\mathbf{R}_2 - \mathbf{R}_1)\cdot(\mathbf{V}_2 - \mathbf{V}_1)}{k\,\overline{\omega}} \ , \tag{6.29}$$

where $\{\mathbf{R}_1, \mathbf{V}_1\}$ and $\{\mathbf{R}_2, \mathbf{V}_2\}$ are the state vectors of the two primaries in the ICRF at the epoch ε. At this point the jacobian of J (for $m = 2$, superscripts are dropped to ease notation) is straightforward:

$$
\begin{cases}
\dfrac{\partial J}{\partial \boldsymbol{\eta}_i} = -\overline{\omega}\, k(\varepsilon_i)\, \dfrac{(\boldsymbol{\eta}_1 - \boldsymbol{\eta}_i)^\top}{\|\boldsymbol{\eta}_1 - \boldsymbol{\eta}_i\|} \\
\dfrac{\partial J}{\partial \boldsymbol{\eta}_1} = \overline{\omega}\, k(\varepsilon_i)\, \dfrac{(\boldsymbol{\eta}_1 - \boldsymbol{\eta}_i)^\top}{\|\boldsymbol{\eta}_1 - \boldsymbol{\eta}_i\|} \\
\dfrac{\partial J}{\partial \boldsymbol{\eta}_s} = -\overline{\omega}\, k(\varepsilon_f)\, \dfrac{(\boldsymbol{\eta}_f - \boldsymbol{\eta}_s)^\top}{\|\boldsymbol{\eta}_f - \boldsymbol{\eta}_s\|} \\
\dfrac{\partial J}{\partial \boldsymbol{\eta}_f} = \overline{\omega}\, k(\varepsilon_f)\, \dfrac{(\boldsymbol{\eta}_f - \boldsymbol{\eta}_s)^\top}{\|\boldsymbol{\eta}_f - \boldsymbol{\eta}_s\|} \\
\dfrac{\partial J}{\partial \tau_i} = \overline{\omega}\, k'(\varepsilon_i)\, \|\boldsymbol{\eta}_1 - \boldsymbol{\eta}_i\| \\
\dfrac{\partial J}{\partial \tau_f} = \overline{\omega}\, k'(\varepsilon_f)\, \|\boldsymbol{\eta}_f - \boldsymbol{\eta}_s\|
\end{cases}
\tag{6.30}
$$

where also the result in Eq. (3.44) was used. The other derivatives of J with respect to $\boldsymbol{\rho}_i$, $\boldsymbol{\rho}_f$, $\boldsymbol{\rho}_k$ $\forall k = 1, \ldots, s$ and $\boldsymbol{\eta}_k$ $\forall k = 2, \ldots, s-1$ are all equal to zero.

In the case, $m = 3$, the derivatives of the midcourse impulse are added to Eq. (6.30). Exploiting the expression for $\|\Delta\mathbf{v}_3\|$ in Eq. (6.29), the jacobian of J is expanded with

$$
\begin{cases}
\dfrac{\partial J}{\partial \boldsymbol{\eta}_s^{(1)}} = -\overline{\omega}\, k(\varepsilon_s^{(1)})\, \dfrac{\boldsymbol{\eta}_s^{(1)\top}}{\left\|\boldsymbol{\eta}_s^{(1)}\right\|} \\
\dfrac{\partial J}{\partial \boldsymbol{\eta}_1^{(2)}} = \overline{\omega}\, k(\varepsilon_1^{(2)})\, \dfrac{\boldsymbol{\eta}_1^{(2)\top}}{\left\|\boldsymbol{\eta}_1^{(2)}\right\|} \\
\dfrac{\partial J}{\partial \tau_s^{(1)}} = -\overline{\omega}\, k'(\varepsilon_s^{(1)})\, \left\|\boldsymbol{\eta}_s^{(1)}\right\| \\
\dfrac{\partial J}{\partial \tau_1^{(2)}} = -\overline{\omega}\, k'(\varepsilon_1^{(2)})\, \left\|\boldsymbol{\eta}_1^{(2)}\right\|
\end{cases}
\quad . \tag{6.31}
$$

One notes that, differently from Eq. (6.30), where the magnitude of a velocity increment appears in some denominators, here there is just the velocity magnitude, preventing in this way possible nonsingularities.

Jacobian of the Constraints

Some of the constraints are linear functions of $\mathbf{y}$ and thus their derivatives have simple expressions (not reported for brevity). This is the case of the inequality constraints $\mathbf{g}$, and the following equality constraints: $\boldsymbol{\Psi}_i$, $\boldsymbol{\Psi}_f$, $\boldsymbol{\Psi}_{\rho_m}$, ξ_m. The remaining functions ($\boldsymbol{\zeta}_k$, Ψ_{η_m}, $\mathbf{h}_{\mathcal{D}}$, $\mathbf{h}_{\mathcal{A}}$) are nonlinear in the NLP variables and so their derivatives must be discussed.

For what concerns the defect vectors $\boldsymbol{\zeta}_k$, with $k = 1, \dots, s-1$, their variations are more involved, and the results of Eq. (6.28) are crucial. Together with them, another remark must be done. Because among the NLP variables of each arc, there are only τ_i and τ_f, it is better to explicit the variation of the generic time τ_k with respect to them. Recalling the definition of τ_k in Eq. (6.10), its derivatives read:

$$\frac{\partial \tau_k}{\partial \tau_i} = \frac{s-k}{s-1}\,, \qquad\qquad \frac{\partial \tau_k}{\partial \tau_f} = \frac{k-1}{s-1}\,. \tag{6.32}$$

At this point, all the nonzero variations of $\boldsymbol{\zeta_k}$ with respect to $\mathbf{y}$ can be computed.

$$\begin{cases} \dfrac{\partial \boldsymbol{\zeta}_k}{\partial \boldsymbol{x}_k} = \Phi(\tau_k, \tau_{k+1}) \\ \dfrac{\partial \boldsymbol{\zeta}_k}{\partial \boldsymbol{x}_{k+1}} = -I_6 \\ \dfrac{\partial \boldsymbol{\zeta}_k}{\partial \tau_i} = \dfrac{\partial \varphi_n}{\partial \tau_k}\dfrac{\partial \tau_k}{\partial \tau_i} + \dfrac{\partial \varphi_n}{\partial \tau_{k+1}}\dfrac{\partial \tau_{k+1}}{\partial \tau_i} = \\ \qquad = -\dfrac{s-k}{s-1}\Phi(\tau_k, \tau_{k+1})\,\mathbf{f}_n(\boldsymbol{x}_k, \tau_k) + \dfrac{s-k-1}{s-1}\mathbf{f}_n(\varphi_n(\boldsymbol{x}_k, \tau_k; \tau_{k+1}),\, \tau_{k+1}) \\ \dfrac{\partial \boldsymbol{\zeta}_k}{\partial \tau_f} = \dfrac{\partial \varphi_n}{\partial \tau_k}\dfrac{\partial \tau_k}{\partial \tau_f} + \dfrac{\partial \varphi_n}{\partial \tau_{k+1}}\dfrac{\partial \tau_{k+1}}{\partial \tau_f} = \\ \qquad = -\dfrac{k-1}{s-1}\Phi(\tau_k, \tau_{k+1})\,\mathbf{f}_n(\boldsymbol{x}_k, \tau_k) + \dfrac{k}{s-1}\mathbf{f}_n(\varphi_n(\boldsymbol{x}_k, \tau_k; \tau_{k+1}),\, \tau_{k+1}) \end{cases} \tag{6.33}$$

The derivatives of Ψ_{η_m} with respect to the NLP variables are all null but those with respect to $\boldsymbol{\eta}_s^{(1)}$ and $\boldsymbol{\eta}_1^{(2)}$:

$$\begin{cases} \dfrac{\partial \Psi_{\eta_m}}{\partial \boldsymbol{\eta}_s^{(1)}} = {\boldsymbol{\eta}_1^{(2)}}^\top - \dfrac{\left\|\boldsymbol{\eta}_1{}^{(2)}\right\|}{\left\|\boldsymbol{\eta}_s{}^{(1)}\right\|}{\boldsymbol{\eta}_s}^{(1)\top} \\ \dfrac{\partial \Psi_{\eta_m}}{\partial \boldsymbol{\eta}_1^{(2)}} = {\boldsymbol{\eta}_s^{(1)}}^\top - \dfrac{\left\|\boldsymbol{\eta}_s{}^{(1)}\right\|}{\left\|\boldsymbol{\eta}_1{}^{(2)}\right\|}{\boldsymbol{\eta}_1}^{(2)\top} \end{cases}. \tag{6.34}$$

Instead, the initial and final constraints $\mathbf{h}_{\mathcal{D}}(\boldsymbol{x}_i, \tau_i)$ and $\mathbf{h}_{\mathcal{A}}(\boldsymbol{x}_f, \tau_f)$ require a dedicated analysis (see section 6.4) and can be discussed only on a case by case basis, depending on their particular definition. However, it can be anticipated that in general the only nonzero derivatives of $\mathbf{h}_{\mathcal{D}}$ are those with respect to $\boldsymbol{x}_i$ and τ_i, whilst for $\mathbf{h}_{\mathcal{A}}$ are those with respect to $\boldsymbol{x}_f$ and τ_f.

In Fig. 6.5 the structure of the jacobian of the nonlinear equality constraints is reported for $s = 5$ and $m = 3$ (4 segments, 2 arcs). The choice of repeating the node at arc interfaces is a common technique used in the construction of arc-wise structured jacobians, where the entries in each arc correspond only to the variables associated with that particular arc. The main advantage is that the construction of the jacobian matrix can be done recursively once the number of arcs m and the number of nodes per arc s are given.

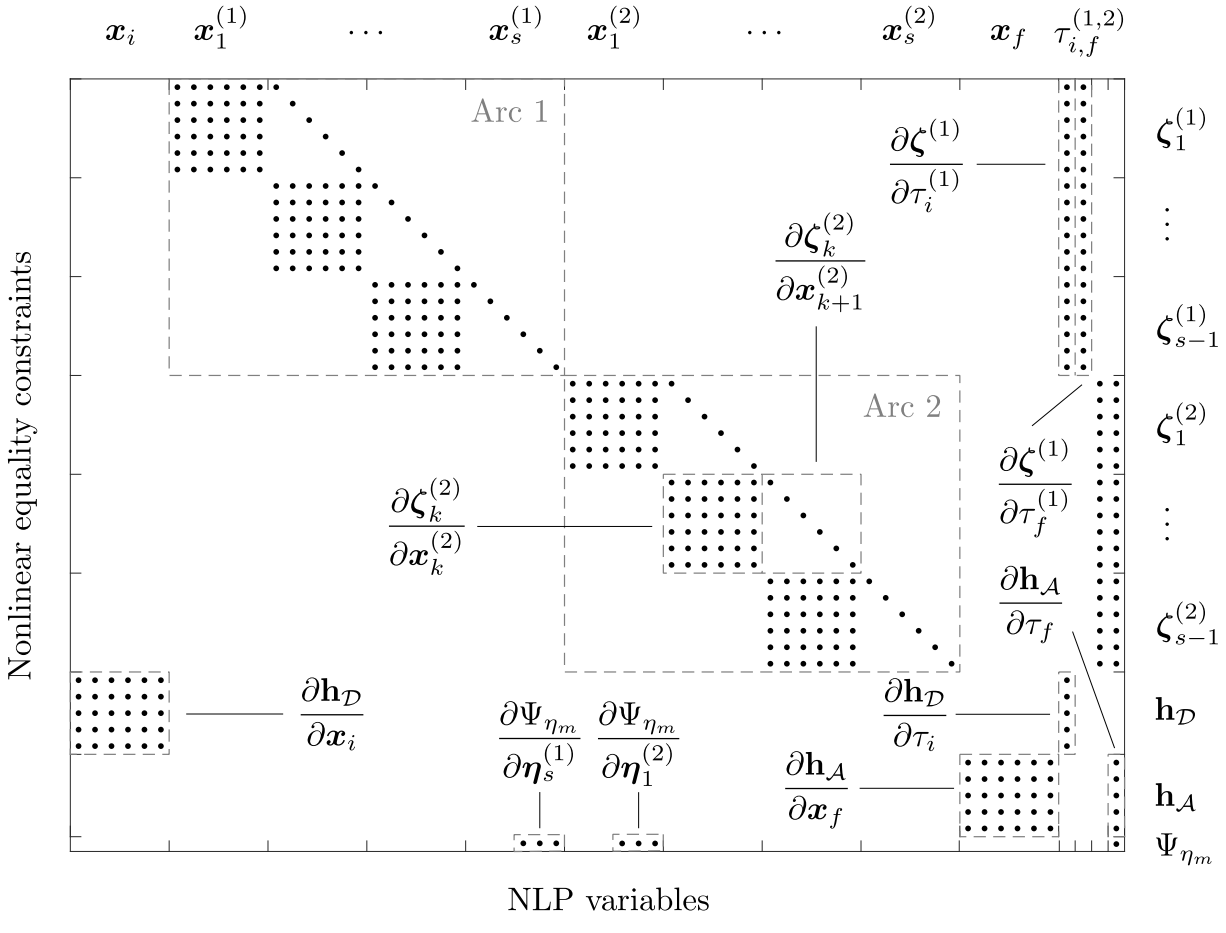

Figure 6.5: Structure of the jacobian of the nonlinear equality constraints, with $s = 5$ and $m = 3$; black dots indicates nonzero elements; the sparse and regular structure allows for a recursive construction; for the sake of generality the nonzero derivatives of $\mathbf{h}_{\mathcal{D}}$ and $\mathbf{h}_{\mathcal{A}}$ are represented as full matrices and vectors

6.4. Boundary Conditions

As it was anticipated, the boundary conditions for the Earth–Moon transfers in the real solar system model are described in an inertial frame. Actually, two of them are used: the ECI2000 for the departure conditions, and the Moon-centered Moon-equatorial at date (MCME2000) reference frame for the arrival conditions.

6.4.1. Departure from the Earth

In continuation with [62] and the existing literature, let the departure parking orbit be a circular orbit around the Earth with an altitude of $h_i = 167$ km. Concerning the orientation of the orbital plane it is decided not to put any constraint on it. This is done to limit the component of the initial impulse used to change the initial plane, which, in some cases, represents a relevant portion of the total cost of the transfer, producing final results that are strongly affected by the initial orbit inclination. Such an assumption might be justified by the extended injection capabilities of modern launch vehicles.

Let $\boldsymbol{x}_i = \{\boldsymbol{\rho}_i, \boldsymbol{\eta}_i\}$ be a state vector in the RPF at the initial time τ_i, and $\mathbf{X}_i = \mathbf{X}_i(\boldsymbol{x}_i, \tau_i) = \{\mathbf{R}_i, \mathbf{V}_i\}$ its equivalent in the ICRF at the epoch ε_i (obtained by means of the transformation from RPF to ICRF). The radius of the orbit is imposed by requiring that

$$\|\mathbf{R}_i - \mathbf{R}_1\| = R_{B_1} + h_i \ , \tag{6.35}$$

where R_{B_1} is the Earth's mean radius and $\mathbf{R}_1$ is the position of the Earth in the ICRF at the epoch ε_i. The magnitude of the relative velocity with respect to the Earth on the departure circular orbit can be computed with a two-body approximation:

$$\|\mathbf{V}_i - \mathbf{V}_1\| = \sqrt{\frac{\mu_1}{R_{B_1} + h_i}} \ , \tag{6.36}$$

where $\mathbf{V}_1$ is the velocity of the Earth in the ICRF at the epoch ε_i. Regarding the direction of the relative velocity, on a circular orbit this must be perpendicular to the radial direction. Thus, the constraint function $\mathbf{h}_\mathcal{D}$ can be assembled as:

$$\mathbf{h}_\mathcal{D}(\boldsymbol{x}_i, \tau_i) = \begin{bmatrix} \mathbf{h}_{\mathcal{D}1} \\ \mathbf{h}_{\mathcal{D}2} \\ \mathbf{h}_{\mathcal{D}3} \end{bmatrix} = \begin{bmatrix} (\mathbf{R}_i - \mathbf{R}_1)^\top (\mathbf{R}_i - \mathbf{R}_1) - (R_{B_1} + h_i)^2 \\ (\mathbf{V}_i - \mathbf{V}_1)^\top (\mathbf{V}_i - \mathbf{V}_1) - \dfrac{\mu_1}{R_{B_1} + h_i} \\ (\mathbf{R}_i - \mathbf{R}_1)^\top (\mathbf{V}_i - \mathbf{V}_1) \end{bmatrix} . \tag{6.37}$$

Particularly, $\mathbf{h}_{\mathcal{D}1}$ defines the radius of the orbit, while $\mathbf{h}_{\mathcal{D}2}$ and $\mathbf{h}_{\mathcal{D}3}$ its circular shape.

6.4.2. Arrival at the Moon

Analogously to the departure parking orbit, also the arrival one is a circular orbit with the same altitude of [62], i.e., $h_f = 100$ km.

However, to simulate some real mission requirements, here the orbital plane is assigned, and defined by two Keplerian elements: the inclination i_M and the right ascension of the ascending note Ω_M. These Keplerian parameters are given in MCME2000, see Fig. 6.6. The origin of this inertial frame is the Moon, and its axes are such that [24]:

- the Z-axis is aligned with the Moon's spin axis on January 01, 2000, TDB;
- the X-axis is aligned with the Earth mean equinox (i.e., the X-axis of the ICRF);
- the Y-axis completes the right-handed reference frame.

Therefore, the (X, Y)-plane of this frame coincides (on average) with the lunar equator, and its axes are obtained rotating the ICRF around the X-axis about $i_{\mathfrak{D}} = 24$ deg [42].

Let denote with $\hat{\boldsymbol{h}}_M$ the unit vector in the direction of the specific angular momentum of the arrival orbit (i.e., the normal direction to the orbital plane). The components of $\hat{\boldsymbol{h}}_M$ in the MCME2000 are defined by means of the Keplerian elements:

$$\hat{\mathbf{h}}_M = \left(\sin\left(i_M\right)\,\sin(\Omega_M),\ -\sin\left(i_M\right)\,\cos(\Omega_M),\ \cos\left(i_M\right)\right)^{\top}\ . \tag{6.38}$$

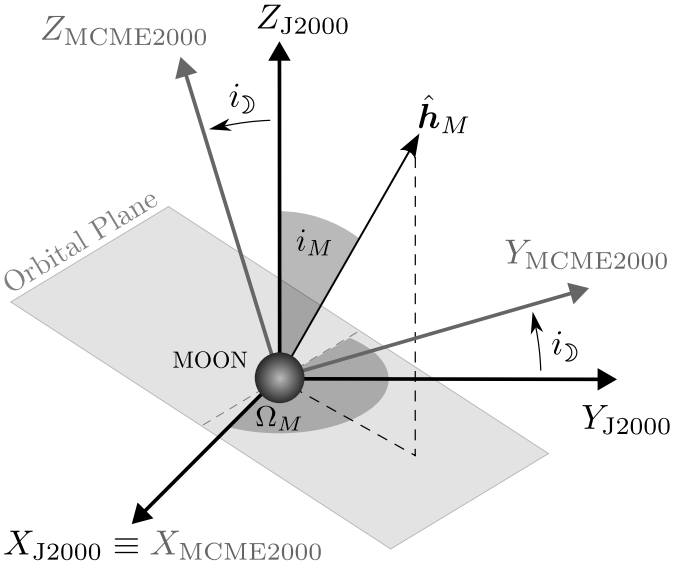

Figure 6.6: Orbital plane at the arrival date in the J2000 and MCME2000 reference frames; $\hat{\boldsymbol{h}}_M$ is the direction of the specific angular, perpendicular to the orbital plane; the dashed gray line is the intersection between the orbital plane and the (X, Y)-J2000 plane

For example, since $\hat{\boldsymbol{h}}_M$ is defined in the MCME2000, an equatorial lunar orbit is obtained setting $i_M = 0$. Then, this direction can be expressed in the ICRF with the rotation matrix T, defined as

$$T = \begin{bmatrix} 1 & 0 & 0 \\ 0 & +\cos(i_{\mathbb{D}}) & -\sin(i_{\mathbb{D}}) \\ 0 & +\sin(i_{\mathbb{D}}) & +\cos(i_{\mathbb{D}}) \end{bmatrix} . \tag{6.39}$$

Hence, the arrival constraints can be organized in the vector $\mathbf{h}_{\mathcal{A}}$

$$\mathbf{h}_{\mathcal{A}}(\boldsymbol{x}_f, \tau_f) = \begin{bmatrix} \mathbf{h}_{\mathcal{A}1} \\ \mathbf{h}_{\mathcal{A}2} \\ \mathbf{h}_{\mathcal{A}3} \\ \mathbf{h}_{\mathcal{A}4} \\ \mathbf{h}_{\mathcal{A}5} \end{bmatrix} = \begin{bmatrix} (\mathbf{R}_f - \mathbf{R}_2)^\top (\mathbf{R}_f - \mathbf{R}_2) - (R_{B_2} + h_f)^2 \\ (\mathbf{V}_f - \mathbf{V}_2)^\top (\mathbf{V}_f - \mathbf{V}_2) - \dfrac{\mu_2}{R_{B_2} + h_f} \\ (\mathbf{R}_f - \mathbf{R}_2)^\top (\mathbf{V}_f - \mathbf{V}_2) \\ (\mathbf{R}_f - \mathbf{R}_2)^\top T\hat{\boldsymbol{h}}_M \\ (\mathbf{V}_f - \mathbf{V}_2)^\top T\hat{\boldsymbol{h}}_M \end{bmatrix} , \tag{6.40}$$

where R_{B_2} is the mean lunar radius, $\{\mathbf{R}_f, \mathbf{V}_f\}$ and $\{\mathbf{R}_2, \mathbf{V}_2\}$ are the position and the velocity of the spacecraft and the Moon, respectively, at the arrival epoch ε_f in the ICRF. The meaning of the first three components of $\mathbf{h}_{\mathcal{A}}$ is analogous to the one of $\mathbf{h}_{\mathcal{D}}$. Instead, differently from the departure conditions, here the last two components of $\mathbf{h}_{\mathcal{A}}$ guarantee that the final state belongs to a specific orbital plane, defined by i_M and Ω_M.

Arrival to a Polar Lunar Orbit

Consider the case when the target orbit is a polar lunar orbit, without any prescribed right ascension of the ascending node. The formulation of the constraints in Eq. (6.40) is no more adequate because $\hat{\mathbf{h}}_M$ cannot be computed without a value for Ω_M. However, especially due to the mapping properties offered by a polar orbit, this is a frequent target employed in literature, so some new constraints must be written.
The specific angular momentum $\boldsymbol{h}_M$ of a polar orbit must be perpendicular to the z-axis of the MCME2000 reference frame, so

$$\boldsymbol{e}_3^\top \boldsymbol{h}_M = 0 , \tag{6.41}$$

where $\boldsymbol{e}_3 = (0, 0, 1)^\top$. By definition, the specific angular momentum is the cross product between the relative position and the relative velocity, but since they are defined in the ICRF, a transformation is needed

$$\boldsymbol{h}_M = T^\top \left[(\mathbf{R}_f - \mathbf{R}_2) \times (\mathbf{V}_f - \mathbf{V}_2) \right] . \tag{6.42}$$

Note that in Eq. (6.42), the rotation matrix from the ICRF to the MCME2000 is simply $T^\top$, because T is an orthonormal matrix. Hence, the condition to have a polar orbit is

$$\boldsymbol{e}_3^\top T^\top \left[(\mathbf{R}_f - \mathbf{R}_2) \times (\mathbf{V}_f - \mathbf{V}_2) \right] = 0 \,. \tag{6.43}$$

Finally, the constraint vector for a generic polar orbit $\mathbf{h}_{\mathcal{A}}^{(p)}$ is

$$\mathbf{h}_{\mathcal{A}}^{(p)}(\boldsymbol{x}_f, \tau_f) = \begin{bmatrix} \mathbf{h}_{\mathcal{A}1}^{(p)} \\ \mathbf{h}_{\mathcal{A}2}^{(p)} \\ \mathbf{h}_{\mathcal{A}3}^{(p)} \\ \mathbf{h}_{\mathcal{A}4}^{(p)} \end{bmatrix} = \begin{bmatrix} (\mathbf{R}_f - \mathbf{R}_2)^\top (\mathbf{R}_f - \mathbf{R}_2) - (R_{B_2} + h_f)^2 \\ (\mathbf{V}_f - \mathbf{V}_2)^\top (\mathbf{V}_f - \mathbf{V}_2) - \dfrac{\mu_2}{R_{B_2} + h_f} \\ (\mathbf{R}_f - \mathbf{R}_2)^\top (\mathbf{V}_f - \mathbf{V}_2) \\ \boldsymbol{e}_3^\top T^\top \left[(\mathbf{R}_f - \mathbf{R}_2) \times (\mathbf{V}_f - \mathbf{V}_2) \right] . \end{bmatrix} . \tag{6.44}$$

Once again the first three components of $\mathbf{h}_{\mathcal{A}}^{(p)}$ are used to define the altitude, velocity, and shape of the orbit, whilst the last component, $\mathbf{h}_{\mathcal{A}4}^{(p)}$ is responsible for the orbit orientation. Additionally, it is worth mentioning that, $\mathbf{h}_{\mathcal{A}1,2,3}^{(p)}$ coincide with $\mathbf{h}_{\mathcal{A}1,2,3}$.

6.4.3. Jacobian of the Boundary Conditions

Also for the boundary constraints $\mathbf{h}_{\mathcal{D}}$ and $\mathbf{h}_{\mathcal{A}}$, the variations with respect to the NLP variables are computed analytically. The two constraint functions are expressed in terms of inertial quantities, so the linear transformation made of Eqs. (5.6), (5.10) and (5.12) and the derivative reported in appendix A.3 are employed. Additionally, it is useful to compute the following variations:

$$\frac{\partial \mathbf{R}_i}{\partial \tau_i} = \frac{\partial \mathbf{R}_i}{\partial \varepsilon_i} \frac{\partial \varepsilon_i}{\partial \tau_i} = \frac{1}{\overline{\omega}} \left(\dot{\mathbf{b}}_i + \left(\dot{k}_i C_i + k_i \dot{C}_i \right) \boldsymbol{\rho}_i \right) \tag{6.45a}$$

$$\frac{\partial \mathbf{R}_f}{\partial \tau_f} = \frac{\partial \mathbf{R}_f}{\partial \varepsilon_f} \frac{\partial \varepsilon_f}{\partial \tau_f} = \frac{1}{\overline{\omega}} \left(\dot{\mathbf{b}}_f + \left(\dot{k}_f C_f + k_f \dot{C}_f \right) \boldsymbol{\rho}_f \right) \tag{6.45b}$$

$$\frac{\partial \mathbf{V}_i}{\partial \tau_i} = \frac{\partial \mathbf{V}_i}{\partial \varepsilon_i} \frac{\partial \varepsilon_i}{\partial \tau_i} = \frac{1}{\overline{\omega}} \left(\ddot{\mathbf{b}}_i + \left(\ddot{k}_i C_i + k_i \ddot{C}_i + 2 \dot{k}_i \dot{C}_i \right) \boldsymbol{\rho}_i \right) + \left(\dot{k}_i C_i + k_i \dot{C}_i \right) \boldsymbol{\eta}_i \tag{6.45c}$$

$$\frac{\partial \mathbf{V}_f}{\partial \tau_f} = \frac{\partial \mathbf{V}_f}{\partial \varepsilon_f} \frac{\partial \varepsilon_f}{\partial \tau_f} = \frac{1}{\overline{\omega}} \left(\ddot{\mathbf{b}}_f + \left(\ddot{k}_f C_f + k_f \ddot{C}_f + 2 \dot{k}_f \dot{C}_f \right) \boldsymbol{\rho}_f \right) + \left(\dot{k}_f C_f + k_f \dot{C}_f \right) \boldsymbol{\eta}_f \tag{6.45d}$$

where it is recalled that $\boldsymbol{\rho}_i$, $\boldsymbol{\rho}_f$, $\boldsymbol{\eta}_i$, $\boldsymbol{\eta}_f$ are independent variables, so their derivatives with respect to any other quantity are null.

The nonzero derivatives of $\mathbf{h}_{\mathcal{D}1}(\boldsymbol{x}_i, \tau_i)$ and $\mathbf{h}_{\mathcal{A}1}(\boldsymbol{x}_f, \tau_f)$ are:

$$\begin{cases} \dfrac{\partial \mathbf{h}_{\mathcal{D}1}}{\partial \boldsymbol{x}_i} = \begin{bmatrix} 2k_i C_i \left(\mathbf{R}_i - \mathbf{R}_1\right) \\ \mathbf{0}_{3\times 1} \end{bmatrix}^\top \\ \dfrac{\partial \mathbf{h}_{\mathcal{A}1}}{\partial \boldsymbol{x}_f} = \begin{bmatrix} 2k_f C_f \left(\mathbf{R}_f - \mathbf{R}_2\right) \\ \mathbf{0}_{3\times 1} \end{bmatrix}^\top \\ \dfrac{\partial \mathbf{h}_{\mathcal{D}1}}{\partial \tau_i} = 2\left(\mathbf{R}_i - \mathbf{R}_1\right)^\top \left(\dfrac{\partial \mathbf{R}_i}{\partial \tau_i} - \dfrac{\mathbf{V}_1}{\overline{\omega}}\right) \\ \dfrac{\partial \mathbf{h}_{\mathcal{A}1}}{\partial \tau_f} = 2\left(\mathbf{R}_f - \mathbf{R}_2\right)^\top \left(\dfrac{\partial \mathbf{R}_f}{\partial \tau_f} - \dfrac{\mathbf{V}_2}{\overline{\omega}}\right) \end{cases} . \tag{6.46}$$

The nonzero variations of $\mathbf{h}_{\mathcal{D}2}(\boldsymbol{x}_i, \tau_i)$ and $\mathbf{h}_{\mathcal{A}2}(\boldsymbol{x}_f, \tau_f)$ are:

$$\begin{cases} \dfrac{\partial \mathbf{h}_{\mathcal{D}2}}{\partial \boldsymbol{x}_i}^\top = 2\begin{bmatrix} \dot{k}_i C_i + k_i \dot{C}_i \\ \overline{\omega} k_i C_i \end{bmatrix} \left(\mathbf{V}_i - \mathbf{V}_1\right) \\ \dfrac{\partial \mathbf{h}_{\mathcal{A}2}}{\partial \boldsymbol{x}_f}^\top = 2\begin{bmatrix} \dot{k}_f C_f + k_f \dot{C}_f \\ \overline{\omega} k_f C_f \end{bmatrix} \left(\mathbf{V}_f - \mathbf{V}_2\right) \\ \dfrac{\partial \mathbf{h}_{\mathcal{D}2}}{\partial \tau_i} = 2\left(\mathbf{V}_i - \mathbf{V}_1\right)^\top \left(\dfrac{\partial \mathbf{V}_i}{\partial \tau_i} - \dfrac{\mathbf{A}_1}{\overline{\omega}}\right) \\ \dfrac{\partial \mathbf{h}_{\mathcal{A}2}}{\partial \tau_f} = 2\left(\mathbf{V}_f - \mathbf{V}_2\right)^\top \left(\dfrac{\partial \mathbf{V}_f}{\partial \tau_f} - \dfrac{\mathbf{A}_2}{\overline{\omega}}\right) \end{cases} . \tag{6.47}$$

Then, the only derivatives of $\mathbf{h}_{\mathcal{D}3}(\boldsymbol{x}_i, \tau_i)$ and $\mathbf{h}_{\mathcal{A}3}(\boldsymbol{x}_f, \tau_f)$ different from zero are:

$$\begin{cases} \dfrac{\partial \mathbf{h}_{\mathcal{D}3}}{\partial \boldsymbol{x}_i}^\top = \begin{bmatrix} \dot{k}_i C_i + k_i \dot{C}_i \\ \overline{\omega} k_i C_i \end{bmatrix} \left(\mathbf{R}_i - \mathbf{R}_1\right) + \begin{bmatrix} k_i C_i \left(\mathbf{V}_i - \mathbf{V}_1\right) \\ \mathbf{0}_{3\times 1} \end{bmatrix} \\ \dfrac{\partial \mathbf{h}_{\mathcal{A}3}}{\partial \boldsymbol{x}_f}^\top = \begin{bmatrix} \dot{k}_f C_f + k_f \dot{C}_f \\ \overline{\omega} k_f C_f \end{bmatrix} \left(\mathbf{R}_f - \mathbf{R}_2\right) + \begin{bmatrix} k_f C_f \left(\mathbf{V}_f - \mathbf{V}_2\right) \\ \mathbf{0}_{3\times 1} \end{bmatrix} \\ \dfrac{\partial \mathbf{h}_{\mathcal{D}3}}{\partial \tau_i} = \left(\mathbf{R}_i - \mathbf{R}_1\right)^\top \left(\dfrac{\partial \mathbf{V}_i}{\partial \tau_i} - \dfrac{\mathbf{A}_1}{\overline{\omega}}\right) + \left(\mathbf{V}_i - \mathbf{V}_1\right)^\top \left(\dfrac{\partial \mathbf{R}_i}{\partial \tau_i} - \dfrac{\mathbf{V}_1}{\overline{\omega}}\right) \\ \dfrac{\partial \mathbf{h}_{\mathcal{A}3}}{\partial \tau_f} = \left(\mathbf{R}_f - \mathbf{R}_2\right)^\top \left(\dfrac{\partial \mathbf{V}_f}{\partial \tau_f} - \dfrac{\mathbf{A}_2}{\overline{\omega}}\right) + \left(\mathbf{V}_f - \mathbf{V}_2\right)^\top \left(\dfrac{\partial \mathbf{R}_f}{\partial \tau_f} - \dfrac{\mathbf{V}_2}{\overline{\omega}}\right) \end{cases} . \tag{6.48}$$

The derivatives of $\mathbf{h}_{\mathcal{A}4}(\boldsymbol{x}_f, \tau_f)$ and $\mathbf{h}_{\mathcal{A}5}(\boldsymbol{x}_f, \tau_f)$ are shorter, because $T\,\hat{\boldsymbol{h}}_M$ is a constant

$$\begin{cases} \dfrac{\partial \mathbf{h}_{\mathcal{A}4}}{\partial \boldsymbol{x}_f}^\top = \begin{bmatrix} k_f C_f T\,\hat{\boldsymbol{h}}_M \\ \mathbf{0}_{3\times 1} \end{bmatrix} \\ \dfrac{\partial \mathbf{h}_{\mathcal{A}5}}{\partial \boldsymbol{x}_f}^\top = \begin{bmatrix} (\dot{k}_f C_f + k_f \dot{C}_f) T\,\hat{\boldsymbol{h}}_M \\ \overline{\omega} k_f C_f T\,\hat{\boldsymbol{h}}_M \end{bmatrix} \\ \dfrac{\partial \mathbf{h}_{\mathcal{A}4}}{\partial \tau_f} = \left(\dfrac{\partial \mathbf{R}_f}{\partial \tau_f} - \dfrac{\mathbf{V}_2}{\overline{\omega}} \right)^\top T\,\hat{\boldsymbol{h}}_M \\ \dfrac{\partial \mathbf{h}_{\mathcal{A}5}}{\partial \tau_f} = \left(\dfrac{\partial \mathbf{V}_f}{\partial \tau_f} - \dfrac{\mathbf{A}_2}{\overline{\omega}} \right)^\top T\,\hat{\boldsymbol{h}}_M \end{cases} . \tag{6.49}$$

Finally, also the derivatives of $\mathbf{h}^{(p)}_{\mathcal{A}4}$ are reported, but, due to the presence of the cross product, these are computed component-wise, with $k = 1, 2, 3$:

$$\begin{cases} \dfrac{\partial \mathbf{h}^{(p)}_{\mathcal{A}4}}{\partial \rho_{fk}} = \boldsymbol{e}_3^\top T^\top \Big((k_f C_{fk}) \times (\mathbf{V}_f - \mathbf{V}_2) + (\dot{k}_f C_{fk} + k_f \dot{C}_{fk}) \times (\mathbf{R}_f - \mathbf{R}_2) \Big) \\ \dfrac{\partial \mathbf{h}^{(p)}_{\mathcal{A}4}}{\partial \eta_{fk}} = \boldsymbol{e}_3^\top T^\top \left((k_f C_{fk}) \times \mathbf{R}_f \right) \\ \dfrac{\partial \mathbf{h}^{(p)}_{\mathcal{A}4}}{\partial \tau_f} = \boldsymbol{e}_3^\top T^\top \left(\mathbf{V}_f \times \left(\dfrac{\partial \mathbf{R}_f}{\partial \tau_f} - \dfrac{\mathbf{V}_2}{\overline{\omega}} \right) + \mathbf{R}_f \times \left(\dfrac{\partial \mathbf{V}_f}{\partial \tau_f} - \dfrac{\mathbf{A}_2}{\overline{\omega}} \right) \right) \end{cases} , \tag{6.50}$$

where C_{fk} and $\dot{C}_{fk}$ are the k-th column of C_f and $\dot{C}_f$, respectively.

7 | Simulations and Results

This chapter explains how the continuation problem to a high-fidelity model is implemented and solved. Also, some results are presented and discussed.

7.1. Numerical Implementation

The initial seed trajectory for the multiple shooting problem is computed starting from a transfer γ_4 in the PBRFBP. First, the Frames Alignment problem is solved and a suitable departure epoch is computed. Then γ_4 is transformed into Γ_n and this last is sampled at some specific instants of time (depending on the parameters s and m of the multiple shooting). Finally, a NLP optimization is carried out to obtain a feasible trajectory.

7.1.1. Numerical Integration of the n-Body Model

The RP-RnBP code included in the ULTIMAT software, initially developed under an ESA contract and subsequently improved internally [63], is used to implement the equations of motion and the variational equation of the RPRnBP. Despite in the original codes used a seventh/eight-order variable-step Dorman-Prince integration scheme [28], in this work the equations are integrated with the Matlab® suite `ode113`, with absolute and relative tolerances set to 2.5×10^{-14} (adimensional units). Due to the computational heaviness of the right-hand side of these 42 differential equations, a Matlab® mex file is used. Even so, emphasis is put on the running time required, much longer than the one needed to integrate the equations of the PBRFBP.

7.1.2. Solution to the Frames Alignment Problem

The solution to Problem 6.2 is strongly inspired by the considerations about the Sun's trajectories reported in section 6.2.1. In addition to the angle σ, it is useful also to consider the in-plane and out-of-plane angles between $\hat{\mathbf{r}}_3$ and $\hat{\boldsymbol{\rho}}_3$ (see Fig. 7.1), denoted as σ_i and σ_o, respectively.

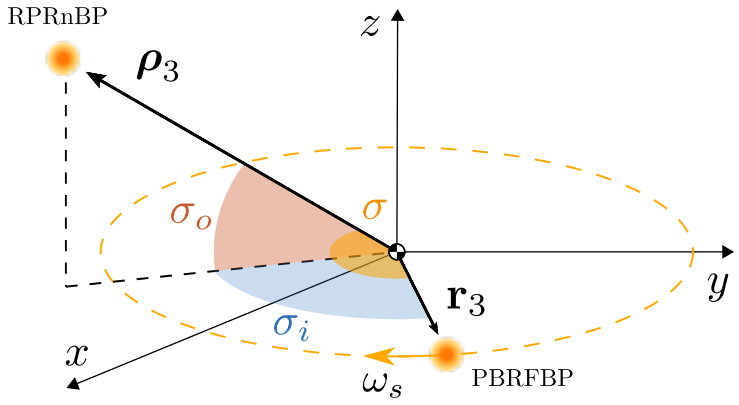

Figure 7.1: Angles between the Sun's directions in the RPF and RF; σ is the angle between the two position vector, σ_i is the angle between $\mathbf{r}_3$ and the projection of $\boldsymbol{\rho}_3$ onto the (x, y)-plane, while σ_o is the elevation angle of the real Sun (from the solar system model), still with respect to the (x, y)-plane

According to the PBRFBP, for a given time $t = t_a$, $\hat{\mathbf{r}}_3$ is a constant direction belonging to the (x, y)-plane. Figure 7.2 shows how the three angles change with time over a year, for a fixed $\hat{\mathbf{r}}_3$ and reading $\boldsymbol{\rho}_3$ from ephemeris data. As expected, the in-plane distance between the two directions has a frequency of about 29.5 days. Therefore, approximately once per synodic month, the projection of $\hat{\boldsymbol{\rho}}_3$ coincides with $\hat{\mathbf{r}}_3$, and σ has local minimum where σ_i is null. However, from Fig. 7.2b (which is an enlargement of Fig. 7.2a), it is evident that the local minima are not all the same; so another frequency affects the behavior of σ. This is due to the spiraling trajectory that the Sun draws in the RPF (see Fig. 6.2). Indeed, σ_o is strongly related to the z-component of $\boldsymbol{\rho}_3$, and it shows an oscillation period of about one year, with a 5 deg amplitude[1].
In principle, one could sift the entire ephemeris catalog looking for the best epoch when σ is minimum. Actually, rather than being a waste of computational time and resources, this is also pointless from the practical viewpoint of a real mission, whose timeline is influenced by many others factors. Furthermore, it must be recalled that this problem serves just to obtain an initial guess solution, that will be modified by the multiple shooting algorithm. For these reasons, it is chosen to focus the research on a single year, being sure that at least two minima are much smaller than the others (see Fig. 7.2b).

The idea for solving the Frame Alignment problem is to compute all the twelve local minima that σ exhibits during a year, and then to select the epoch corresponding to the absolute minimum. Algorithm 2 is a pseudo code that explains the procedure followed

[1]This explains why the hypothesis of planar motion for the celestial bodies in the PBRFBP is actually a good assumption, from the moment that the maximum inclination between the Earth–Moon plane and the ecliptic is limited to 5 deg.

to find the best alignment epoch and to compute the corresponding departure epoch. The heart of the algorithm consists in locally minimizing $-\sigma_{\cos}$, which is equivalent to maximizing $\sigma_{\cos}$. This last is computed at each time t and epoch ε through Algorithm 3. The optimization process is solved efficiently with Matlab® suite `fminunc`, implementing a quasi-Newton algorithm[2].

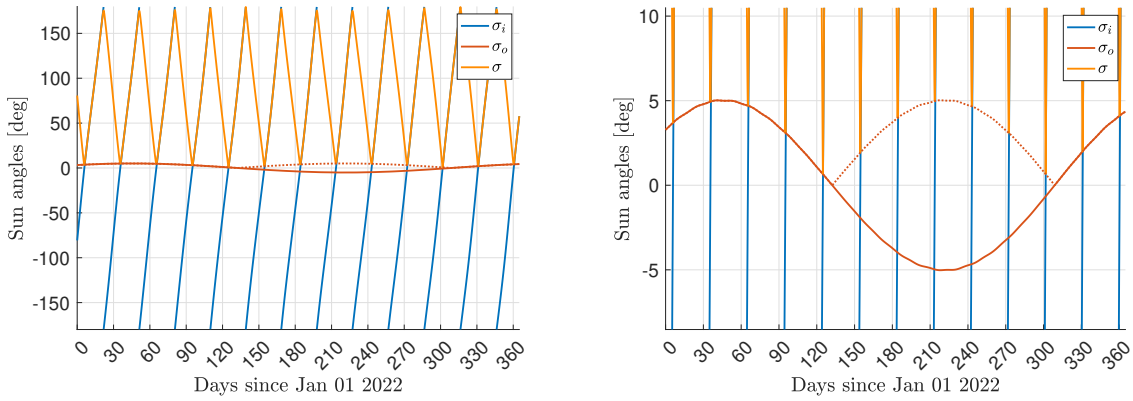

(a) (b)

Figure 7.2: Angles between the Sun's positions in the PBRFBP and in the RPRnBP over the course of a year; the angles are computed for a fixed value of t, and so $\hat{\mathbf{r}}_3$; Fig. 7.2b shows an enlarged view of Fig. 7.2a

Algorithm 2 Frames Alignment Problem

Input: Alignment time $t_a \in [t_i, t_f]$ of a trajectory in the PBRFBP
Output: Alignment epoch ε_a and departure epoch ε_i
Initialize: $\varepsilon_g \leftarrow \varepsilon_0$ ▷ *Initialize guess solution with reference epoch*
For: $m \leftarrow 1$ **to** 12 **do** ▷ *Loop over each month of a year*
  $\sigma_{\cos}, \varepsilon_a \leftarrow$ `fminunc(-AngularDistance`$(\varepsilon, t_a), \varepsilon_g)$ ▷ *Minimization*
  $E[m] \leftarrow \varepsilon_a$ ▷ *Store the current solution in a vector*
  $\sigma[m] \leftarrow \text{acos}(\sigma_{\cos})$ ▷ *Compute and store the angular distance*
  $e_g \leftarrow E[m] + 29.5$ days ▷ *Update guess solution for the next month*
End For
$M \leftarrow \arg\min(\sigma[m])$ ▷ *Select the month with the minimum angle*
$\varepsilon_a \leftarrow E[M]$ ▷ *Compute alignment epoch*
$\varepsilon_i \leftarrow \varepsilon_a - (t_a - t_i)\overline{T}$ ▷ *Compute departure epoch*

[2]Refer to `https://it.mathworks.com/help/optim/ug/fminunc.html` for more details, retrieved on March 16, 2023.

Algorithm 3 AngularDistance Function

1: **Input:** Time t and epoch ε
2: **Output:** $\sigma_{\cos}$, cosine of the angular distance
3: **Function:** `AngularDistance`(ε, t)
4: $\hat{\mathbf{r}}_3 \leftarrow (\cos(\omega_s t), \sin(\omega_s t), 0)$ ▷ *Direction of the Sun in the* RF
5: $\mathbf{R}_3 \leftarrow$ Position of the Sun in the ICRF at epoch ε ▷ *Read from ephemerides*
6: $\hat{\boldsymbol{\rho}}_3 \leftarrow$ Convert $\mathbf{R}_3$ into the RPF an normalize
7: $\sigma_{\cos} \leftarrow \hat{\mathbf{r}}_3 \cdot \hat{\boldsymbol{\rho}}_3$ ▷ *Cosine of the angle between the two directions*
8: **End**

An illustrative example of the results obtained with this algorithm is shown in Fig. 7.3. In the left graph the twelve local minima of σ are reported with also the corresponding value of σ_i (note the different scales in the values of the angles). On the right instead, the out-of-plane coordinate of the Sun, (i.e., ρ_{3_z}) is reported. The red squares highlight the absolute minimum of σ, so the solution to the problem. Observe that, according to the previous considerations, this occurs when the Sun is crossing the Earth–Moon plane (ρ_{3_z} is close to 0).

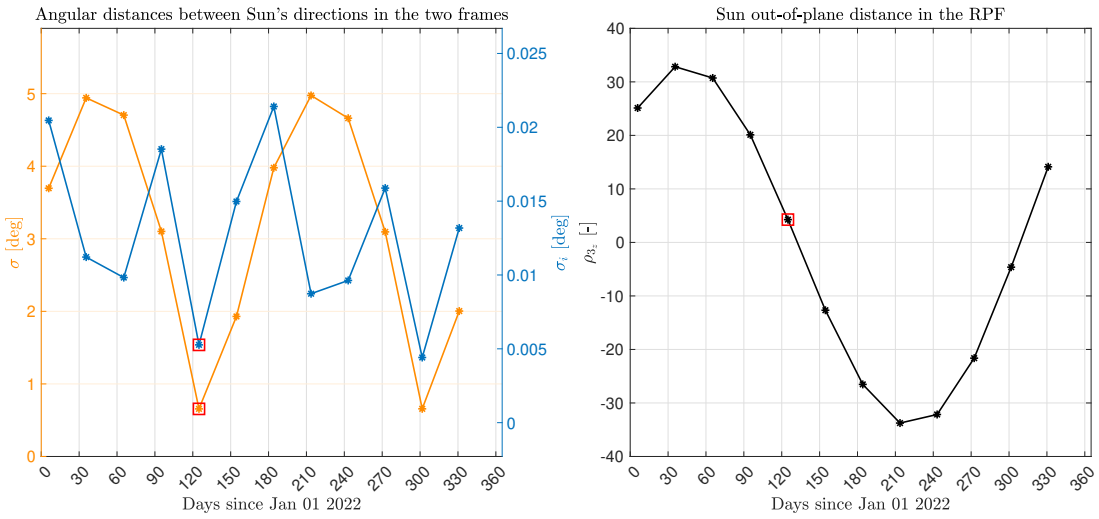

Figure 7.3: Typical solution to the Frames Alignment problem during the course of a year (*red square*), in terms of the angles σ and σ_i (*left*), and the Sun's out-of-plane coordinate ρ_{3_z} (*right*); asterisks denote the local minima of σ within each month

Figure 7.4 represents the trajectories of the Sun in the two models, where also the positions at the departure and at the alignment time are spotted, with a circle and an asterisk, respectively. It is evident, that even if an almost perfect match is achieved at the alignment epoch, an error is present at the departure, where both σ_o and σ_i are not negligible.

The nonzero out-of-plane angle is due to the spiraling trajectory of the Sun, whilst the in-plane error is mainly caused by the different angular velocities of the RPF and the RF. Nonetheless, Fig. 7.4 also points out another advantage of choosing the alignment time as the time of maximum distance from the EMB. In fact, this typically takes place halfway through the transfer, guaranteeing that during all the time of flight, the Sun is close to the Earth–Moon plane. Therefore, the hypothesis of planar geometry of the PBRFBP is justified, making the dynamics of the four-body model a reasonable approximation of the complete n-body model. In turn, this increases the quality of the initial seed trajectory. On the contrary, for example, setting $t_a = t_i$ would mean that the Sun will be far from the (x, y)-plane in the final phase of the transfer, with negative consequences on the quality of the first guess orbit.

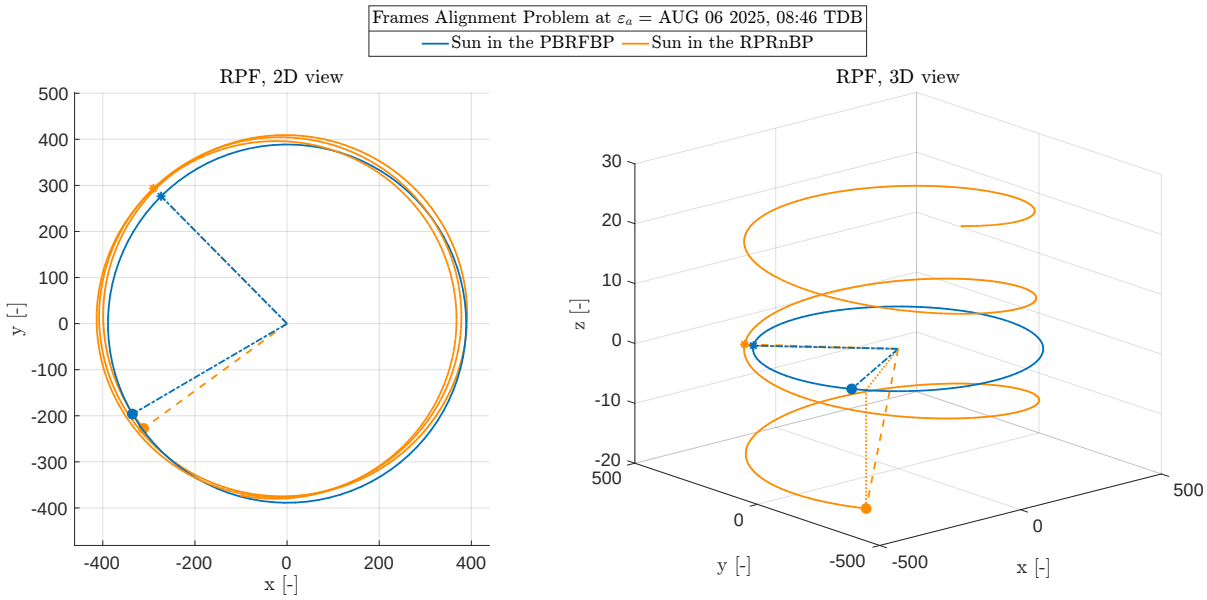

Figure 7.4: Trajectories of the Sun in the two models during the time of a transfer; departure and alignment times are spotted with a circle and an asterisk, respectively

7.1.3. Building the Initial Seed Trajectory

The first guess solution for the multiple shooting problem Γ_n is obtained by transforming γ_4, so converting the states $\{t, \mathbf{r}, \mathbf{v}\}$ into $\{\tau, \boldsymbol{\rho}, \boldsymbol{\eta}\}$ by means of the procedure explained in section 6.2.2. Then, the states composing Γ_n are propagated in the solar system dynamics.

Figure 7.5 shows the four transformations necessary to pass from the RF to the RPF. Here, the conversion is applied to all the states forming the trajectory for a better representation but actually is sufficient to transform s states evenly spaced in time.

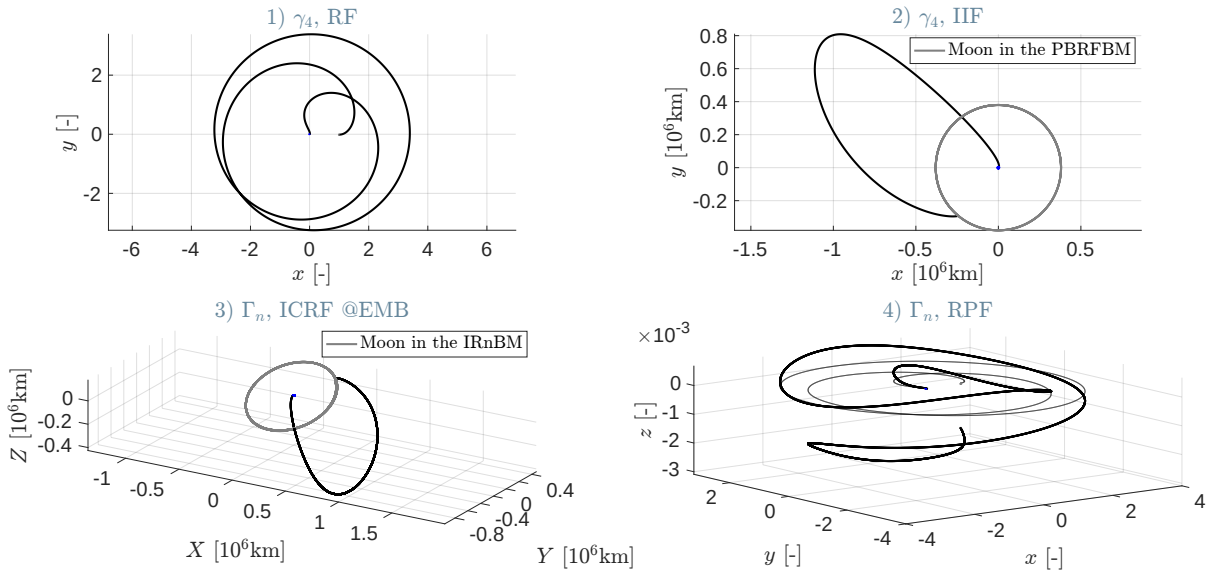

Figure 7.5: Transformations used to modify a trajectory from the RF to the RPF. The first step is to define the trajectory γ_4 in the RF (*top-left*); then the transfer is expressed in an inertial frame (*top-right*); subsequently the Frames Alignment problem is solved and the states composing Γ_n are represented in the ICRF (*bottom-left*); ultimately Γ_n is converted to the RPF (*bottom-right*) using the transformation in section 5.1.3

An initial seed trajectory generated by propagating s nodes of Γ_n in the n-body model is depicted in Fig. 7.6. The states at each node (black dot) are integrated up to the time of the next node; for easier interpretation, the color of each segment is associated with the time of its initial condition. It is evident that the seed trajectory is not continuous (i.e., unfeasible), and it also departs from the curve Γ_n (continuous black line, obtained by transforming all the states of γ_4). Indeed, the underlying dynamical models are different, and the major dissimilarities are at the departure and arrival, where the gradient of the pseudopotential is highly nonlinear.
Even so, note that the in-plane behavior of the four-body model is very similar to the one of the complete model (left graph), and also the scale of the z-axis in the right graph is enlarged. Therefore, one can confirm that the PBRFBP is appropriate to catch the basic dynamics characterizing the Sun–Earth–Moon problem. Moreover, the more nodes are considered, the shorter the propagation time of each state, and the two trajectories (colored and black curves) progressively overlap; however, the cost for this is a higher number of variables in the following NLP algorithm.

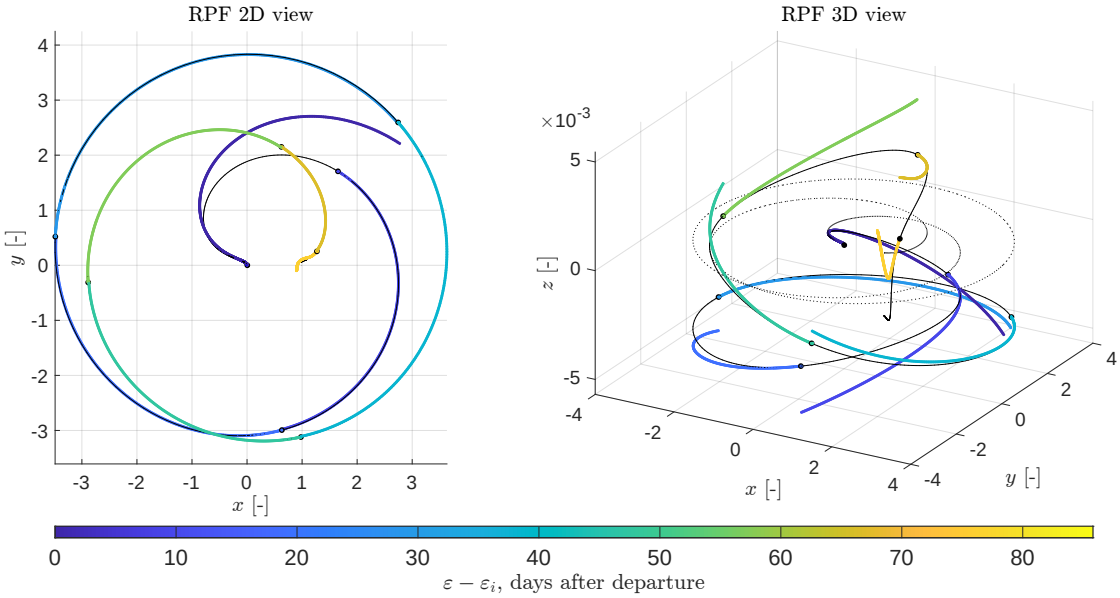

Figure 7.6: Example of a discontinuous initial seed trajectory (colored curves) obtained propagating 10 nodes of Γ_n (black dots); the color of each segment is associated to the time of its initial condition; the continuous black line is Γ_n, and the dashed black line is its projection onto the (x, y)-plane

7.1.4. Multiple Shooting Implementation

The multiple shooting formulation is employed to iteratively modify the initial seed trajectory until a feasible transfer is obtained. Problem 6.3 is implemented within a numerical framework and solved with Matlab® built-in function `fmincon`.

The tolerances on the minimum step and the constraints are set to 10^{-9} adimensional units so that the maximum discontinuity on the position at a node is less than 0.5 m. Instead, the values for the first-optimality and function tolerance are both set to 10^{-5} adimensional units, corresponding to ~ 0.01 m/s.

The jacobians of the nonlinear equality constraints and the objective function are cheeked against Matlab® central finite differences. The worst case relative error is in the order of 10^{-5} adimensional units[3], but the computational time required to evaluate the analytical gradients is much lower. Moreover, since the departure and arrival constraints $\mathbf{h}_{\mathcal{D}}$ and $\mathbf{h}_{\mathcal{A}}$ are expressed in terms of inertial dimensional quantities, they are opportunely divided by a reference length and velocity (see Table 1) to make their scale comparable with the other dimensionless quantities of the problem.

For the same reasons reported in the section 4.4, an `active-set` algorithm is used first,

[3]The higher differences are found in the STM where the dynamics is highly nonlinear, i.e., in the proximity of a primary body.

and then an `interior-point` strategy is employed to refine a solution that did not converge. Nonetheless, it is observed that sometimes the solver takes too large steps, so a relative bound of 0.3 is set on the line search step length. This prevents the final solutions from being much different from the initial guesses, or that the cost diverges because the spacecraft escapes definitely the Earth–Moon system.

Concerning the number of nodes s used to sample a trajectory, a strict rule is not defined. Despite this, as the number of nodes gets lower, the chances of convergence decrease, especially when flybys are performed. On the contrary, a high number of unknowns should be avoided for numerical efficiency. Experimental evidence suggested that a good compromise is to place a node every two or three days of transfer time. Thus, for the solution of interest (i.e., low-energy transfers), a total number of nodes ranging from 30 to 40 is commonly used.

7.2. Analysis of the Results

Finally, some examples of Earth–Moon trajectories in the real solar system are presented. All the following figures show the initial guess solution together with the final feasible[4] transfer returned by the multiple shooting algorithm. Additionally, also the values of the cost and the time of flight of the two trajectories are reported, where the parameters of the initial solution are those of the transfer in the four-body model. The nodes of the solutions are marked with dots, and the trajectories are reported both in the RPF and the ECI2000 frame. The former highlights the variations in the NLP variables produced by the multiple shooting method, while the latter is more suitable to clearly identify the nature of each transfer (direct, exterior, with lunar gravity assist, etc).

Before analyzing some sample solutions, the crucial role of the Frames Alignment problem is emphasized. Indeed, numerical results confirm that the convergence of the algorithm is strictly dependent on the quality of the initial seed trajectory. For instance, even just by choosing an alignment epoch corresponding to a local minimum of σ (and not the absolute minimum, see Fig. 7.3), could make the algorithm converge to a pointless solution, either unfeasible or with a very high cost.

7.2.1. Exterior Transfers

Figure 7.7 shows a low-energy transfer targeting a polar orbit around the Moon without any prescribed right ascension of the ascending node. The SC path is made of an initial

[4]The feasibility of a solution is related not only to the constraints of the NLP problem, but it is also checked that the spacecraft does not impact either the Earth or the Moon.

lunar flyby, a corrective maneuver and a final ballistic capture at the Moon. Note how the continuation algorithm preserves both the geometrical features of the trajectory as well as its time of flight and cost. Here, in particular, the cost of the final solution is even lower than the one of the initial transfer in the four-body model.

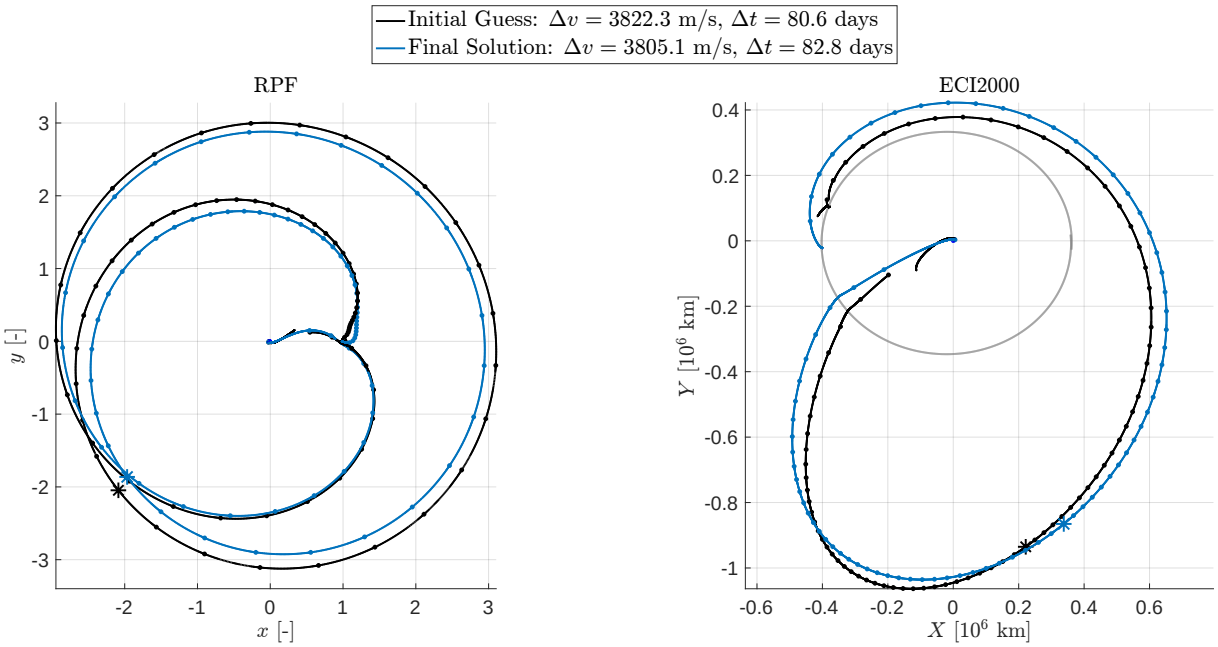

Figure 7.7: Low-energy transfer in the RPRnBP with an initial lunar gravity assist; the asterisks denote the positions of the midcourse maneuvers

Consider now a low-energy WSB transfer without any lunar gravity assist or intermediate maneuver. In theory, this class of transfers is the hardest to be adapted to the n-body model, because the Sun's perturbation plays a key role in determining the path of the spacecraft, and small variations could produce large discrepancies.
Nevertheless, the multiple shooting scheme successfully transforms also this kind of trajectories, as shown in Fig. 7.8. Here the same seed orbit is employed to generate a WSB transfer to a polar lunar orbit (Fig. 7.8a) and to an equatorial lunar orbit (Fig. 7.8b). The costs of the two solutions also highlight the flexibility of low-energy transfers, which can target very different lunar orbits at the same departure epoch and use little difference in fuel ($\sim$ 8 m/s). Furthermore, the similarity of two paths provides several opportunities to utilize a single launch vehicle for placing various spacecrafts into distinct orbits around the Moon, as in the GRAIL mission [31].

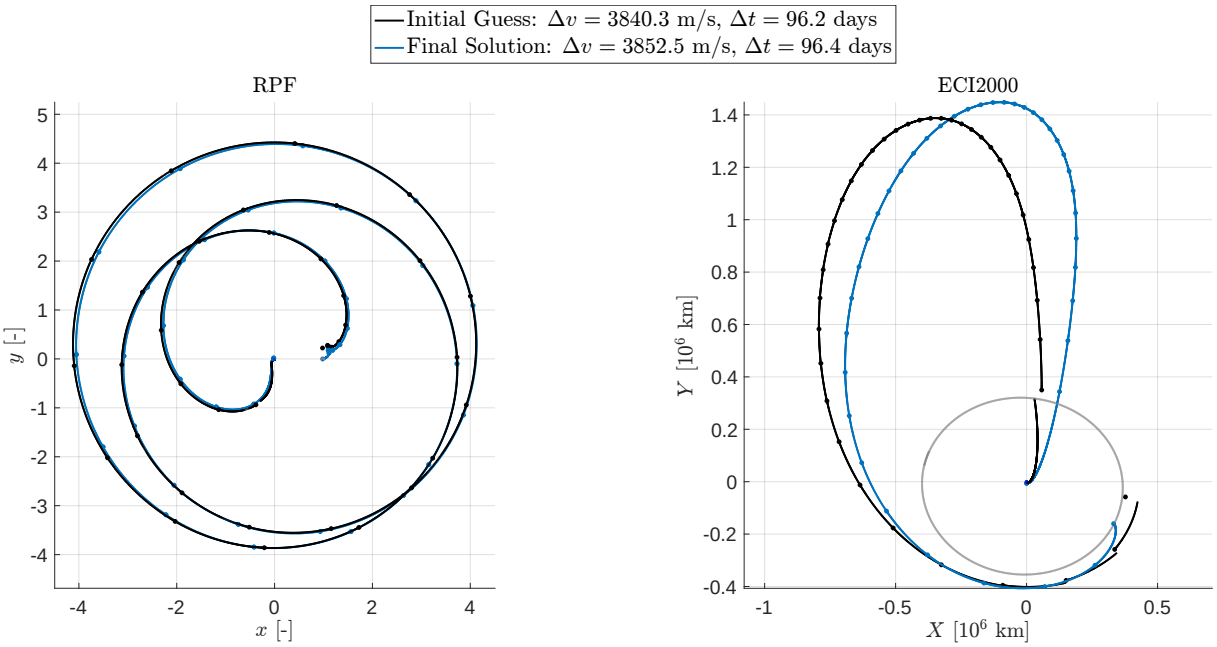

(a) Departure date Jul 27, 2025, arrival to a polar lunar orbit

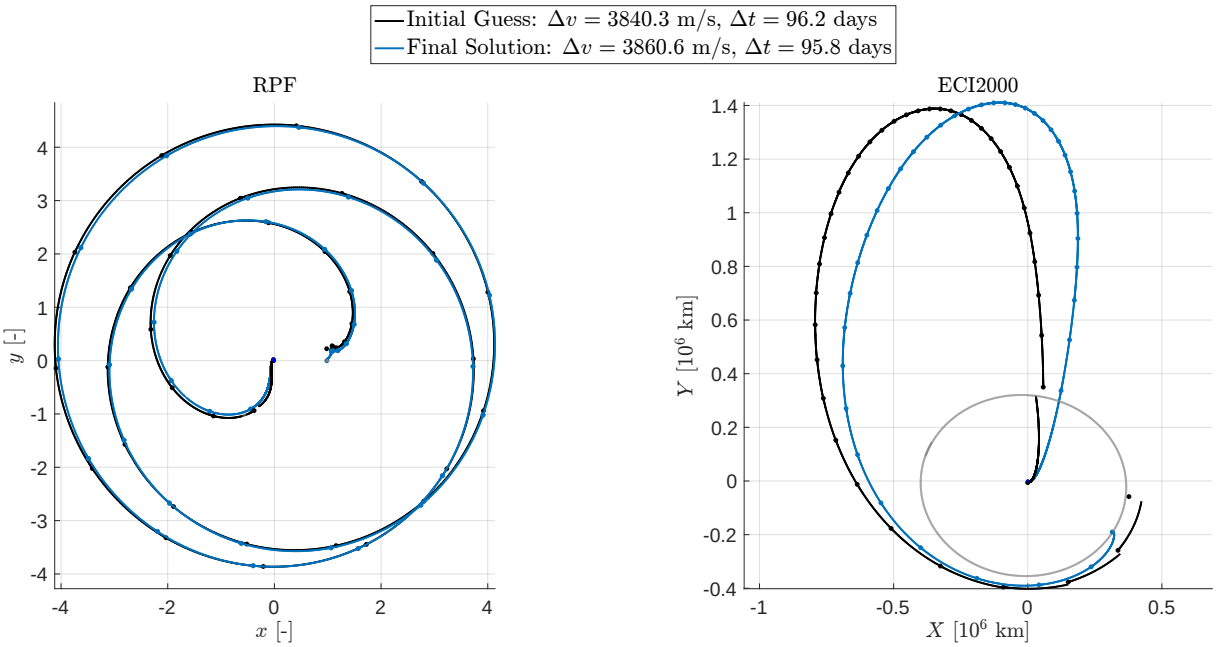

(b) Departure date Jul 27, 2025, arrival to an equatorial lunar orbit

Figure 7.8: Low-energy WSB transfers in the RPRnBP targeting different lunar orbits

7.2.2. Interior Transfers

For the sake of completeness, hereafter two samples of interior transfers successfully continued by the algorithm are also reported. Figure 7.9 shows a direct transfer, while the spacecraft performs an Earth flyby in Fig. 7.10.

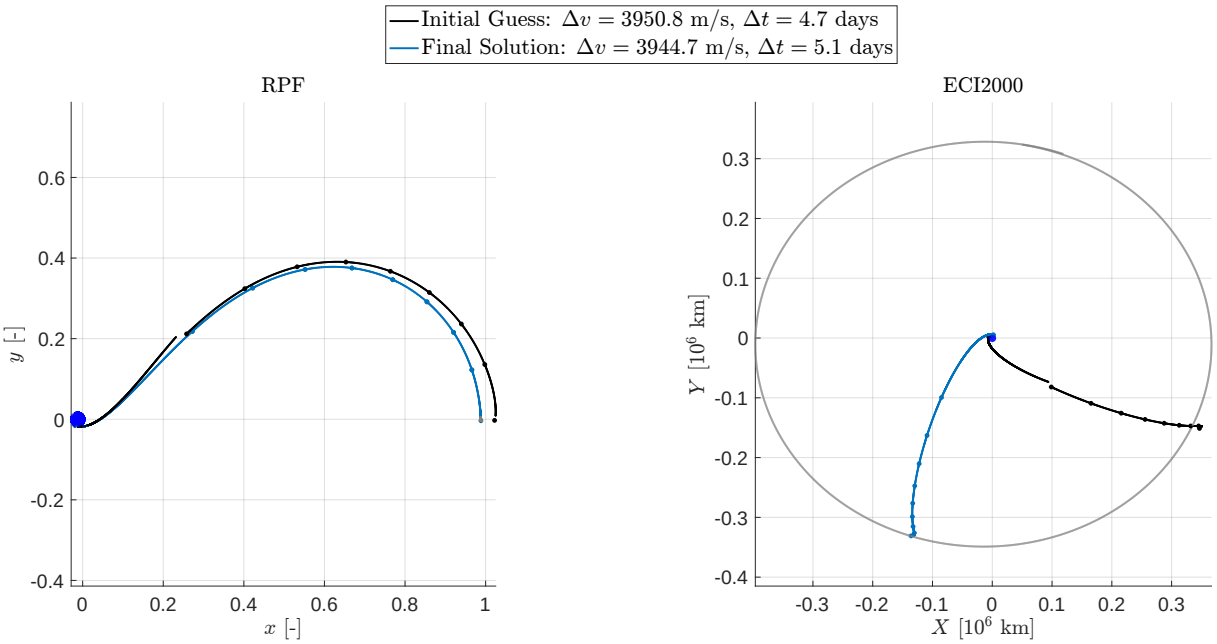

Figure 7.9: Direct interior transfer to a polar lunar orbit in the RPRnBP

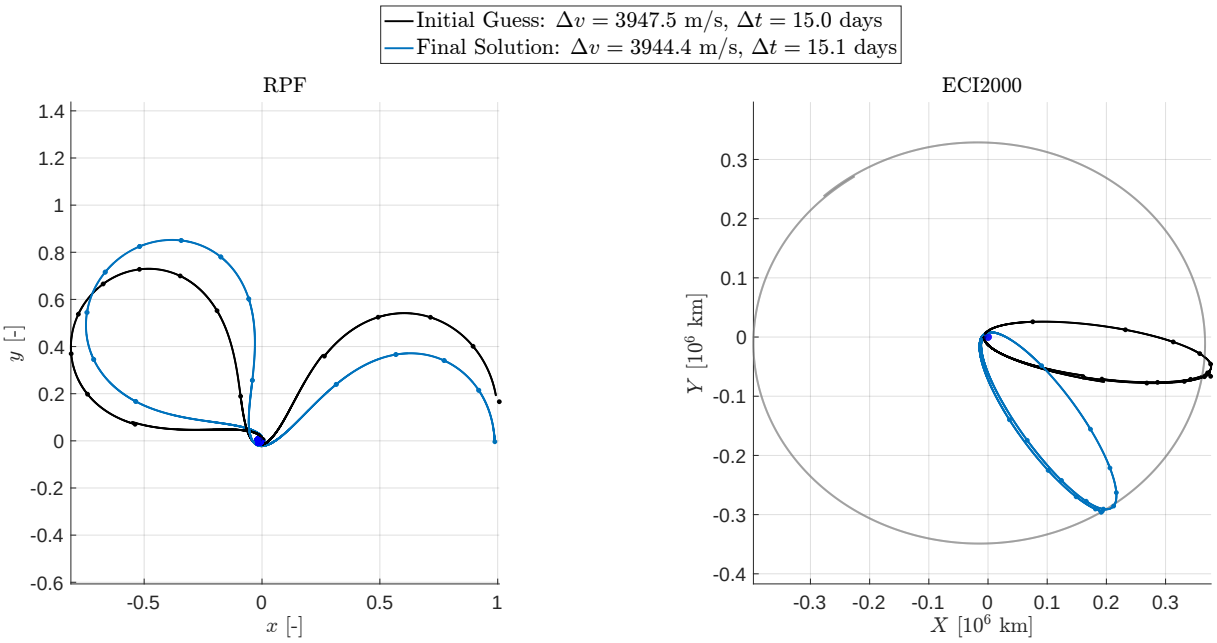

Figure 7.10: Interior transfer with Earth flyby to a polar lunar orbit in the RPRnBP

8 | Conclusions

To conclude, the outcomes of this study are employed to address the research questions outlined in the introduction. Furthermore, critical evaluations are made, and potential prospects for future improvements are explored.

8.1. Part I

With the beginning of a new phase of lunar exploration, improving transfer trajectories is a crucial measure towards achieving more cost-effective and fuel-efficient missions.
In the first part of the thesis, Primer Vector theory was successfully applied to refine time-fixed, two-impulse, Earth–Moon transfers. For the first time, a set of analytical necessary conditions for the optimality of a fuel-efficient solution was derived in a four-body model (Chapter 2). These were applied to over 280 000 transfers from [62], to identify sub-optimal solutions which deserve improvement. In addition, a criterion for the insertion of a midcourse impulse was stated, and employed to generate several three-impulse trajectories, which resulted in lower fuel consumption compared to the original two-impulse transfers (Chapter 3). Then, a parameter optimization problem was solved to refine each three-impulse solution in the neighborhood of each reference trajectory. The entire process was implemented in a numerical framework, and more than 10 000 trajectories were successfully improved using an automated procedure (Chapter 4).

8.1.1. Summary of the Results

A summary of the results pertaining to the first research question, covered in the first part of the thesis, is presented in Fig. 8.1. Here, three-impulse transfers are reported in the $(\Delta t, \Delta v)$ plane, with the color of each point indicating the improvement achieved by adding a midcourse impulse. Instead, black dots represent two-impulse transfers that were not optimized further, either because they were already optimal, or their trajectories were deemed irrelevant for a real mission to the Moon. To answer the research question, the incorporation of a third impulse generally leads to a small percentage variation in the total cost of the final solutions. Additionally, some families of highly intriguing trajectories,

such as direct-interior transfers and very efficient low-energy exterior transfers (top-left and bottom-right corners of Fig. 8.1), were already optimal and did not require a third impulse. Nonetheless, intermediate maneuvers are beneficial for transfers with a moderate time of flight (e.g., 50-60 days) that involve an initial lunar flyby. In these cases, the additional degrees of freedom allow the spacecraft to take full advantage of the lunar gravity assist, and still to achieve a feasible transfer by modifying the SC path after the Moon encounter. As a result, in such scenarios, the largest improvements in the cost are obtained, which are in the range of tens m/s (red dots in Fig. 8.1).

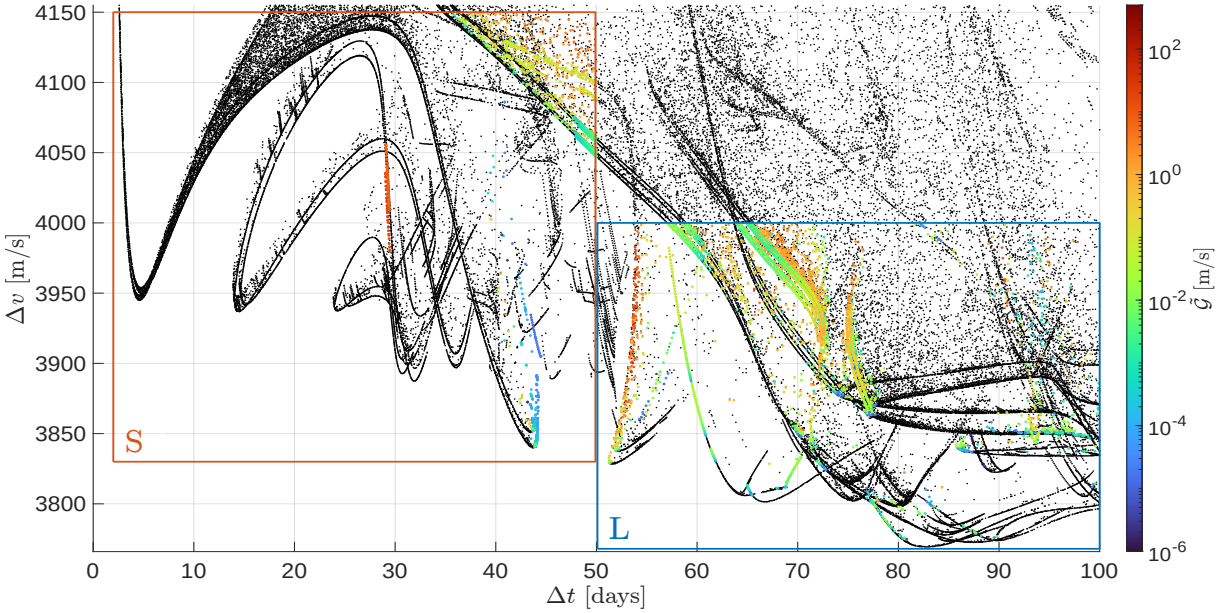

Figure 8.1: Multi-impulse Earth–Moon transfers shown in a (Δt, Δv) graph. Black dots represent two-impulse solutions, while colored dots are three-impulse trajectories; the color is related to the improvement provided by the additional impulse with respect to the original two-impulse transfer

8.2. Part II

As space missions become more complex, high-fidelity models are employed to design unique trajectories. However, simplified models offer a deeper grasp of the dynamics of the cislunar environment, and are more suitable to perform extensive optimization searches. Hence, transition from easier formulations to more complete models is a crucial step in planning future lunar missions.

The second part of the thesis described a procedure to continue a multi-impulsive trajectory from a four-body model to an ephemerides-based model of the complete solar system. The continuation problem described in Chapter 6 was adapted to a real mission to a lunar

circular orbit, whose radius, inclination and right ascension can be selected in advance. It was shown how obtaining a feasible final trajectory heavily relies on the quality of the initial guess. For this reason, an algorithm based on the Sun's positions in the two models was developed to find a proper epoch when to plant the initial seed orbit (see Chapter 7). Then, with a series of transformations through different reference frames, the initial guess trajectory was built. Lastly, a direct multiple-burn, multiple-shooting method was applied to refine the orbit until a desired transfer was achieved. Importance was given to the numerical efficiency of the algorithm, so all jacobians of the objective functions as well as the constraints were derived analytically.

8.2.1. Summary of the Results

The overall process was applied to address the second research question, and thus to design Earth–Moon low-energy transfers in a complete model of the solar system, starting from some trajectories in a four-body model. The sample solutions reported in Chapter 7 show how this procedure was successful in generating various kinds of low-energy transfer, including exterior long transfers with a duration of almost 90 days, and more complicated trajectories with an initial lunar gravity assist and an intermediate correcting maneuver after the Moon encounter. The main attractive feature of these trajectories, i.e., the lower cost compared to direct ones, was preserved during the transformation to the ephemeris-based model. For instance, Fig. 7.7 represents an exterior transfer with $\Delta v = 3805$ m/s (almost 150 m/s cheaper than a Hohmann transfer). The similarity in the cost, time of flight and geometry of the transfer between the two models is a further proof that the PBRFBP is an accurate approximation of the complete cislunar environment, and could be employed to design nominal low-energy trajectories for real missions to the Moon.

8.3. Limitations and Future Work

Some of the limitations of the present thesis, which pave the way for future works, are stated in the following.

Primer Vector Theory Only some outcomes of the Primer Vector theory were employed in this study to optimize Earth–Moon transfers. Future works could expand the class of solutions including transfers with terminal costs and more than three-impulsive maneuvers. Indeed, the procedure presented in the thesis could be employed iteratively until the primer vector satisfies all Lawden's necessary conditions. In this case, the implementation of a direct multiple shooting approach could be beneficial to move efficiently in space and time the intermediate impulses as well as the departure and arrival state.

Multiple Shooting Algorithm The multiple shooting algorithm could be easily extended to a higher number of intermediate maneuvers. In this case, a regularization method could be employed to remove the singularities of the objective function gradient. Moreover, other constraints could be included, for example due to the particular propulsion system of the spacecraft, or to accommodate any mission requirement. Also the nature of the boundary conditions could be modified as desired (changing the orbital plane, the altitude, etc) and a comparative analysis on the different departure or arrival orbits could be conduced to test some features of low-energy transfers.

Design of Earth–Moon Transfers The procedure presented consists in picking up a specific trajectory from the four-body model and reproducing it in the real solar system, looking for the best epoch when the configurations of the celestial bodies are similar in the two models. Consequently, this approach is not suitable when the mission must be launched within a prescribed time window. By the way, without upsetting the entire procedure, a method could be implemented to design a transfer at a prescribednt epoch by exploiting the rich database of solutions provided by [62]. Indeed, the Frame Alignment problem could be reversed, and solved to find the geometry which best overlaps a given configuration in the real solar system among all the thousands of solutions in the four-body model. Moreover, the research area in the (Δt, Δv) plane could be restricted by choosing specific ranges of cost and transfer duration (e.g., to target an exterior low-energy transfer). Finally, once the best trajectory is identified, this can be continued to the n-body model with the same multiple shooting method, adding some constraints on the departure or arrival epochs.

Bibliography

[1] Charles Acton Jr. Ancillary data services of NASA's navigation and ancillary information facility. *Planetary and Space Science*, 44(1):65–70, 1996. doi:10.1016/0032-0633(95)00107-7.

[2] Edward Belbruno. Lunar capture orbits, a method of constructing Earth–Moon trajectories and the lunar GAS mission. In *19th International Electric Propulsion Conference*, page 1054, 1987. doi:10.2514/6.1987-1054.

[3] Edward Belbruno and John Carrico. Calculation of weak stability boundary ballistic lunar transfer trajectories. In *Astrodynamics Specialist Conference*, 2000. doi:10.2514/6.2000-4142.

[4] Edward Belbruno and James K. Miller. Sun-perturbed Earth-to-Moon transfers with ballistic capture. *Journal of Guidance, Control, and Dynamics*, 16(4):770–775, 1993. doi:10.2514/3.21079.

[5] Edward Belbruno, Francesco Topputo, and Marian Gidea. Resonance transitions associated to weak capture in the restricted three-body problem. *Advances in Space Research*, 42(8):1330–1351, 2008. doi:10.1016/j.asr.2008.01.017.

[6] Edward Belbruno, Marian Gidea, and Francesco Topputo. Geometry of weak stability boundaries. *Qualitative Theory of Dynamical Systems*, 12:53–66, 2013. doi:10.1007/s12346-012-0069-x.

[7] Julia Lea Bell. *Primer vector theory in the design of optimal transfers involving libration point orbits*. PhD thesis, Purdue University, 1995.

[8] Miguel Bello-Mora, Filippo Graziani, Paolo Teofilatto, Christian Circi, Manfredi Porfilio, and Martin Hechler. A systematic analysis on weak stability boundary transfers to the moon. In *International Astronautical Congress, 51 st, Paper No. IAF-00-A.6.03, Rio de Janeiro, Brazil*, 2000.

[9] John T. Betts. Survey of numerical methods for trajectory optimization. *Journal of Guidance, Control, and Dynamics*, 21(2):193–207, 1998. doi:10.2514/2.4231.

[10] Robin Biesbroek and Guy Janin. Ways to the Moon. *ESA bulletin*, 103:92–99, 2000.

[11] Erik M. Bollt and James D. Meiss. Targeting chaotic orbits to the Moon through recurrence. *Physics Letters A*, 204(5-6):373–378, 1995. doi:10.1016/0375-9601(95)00502-T.

[12] Roberto Capuzzo-Dolcetta and Marco Giancotti. A study of low-energy transfer orbits to the Moon: towards an operational optimization technique. *Celestial Mechanics and Dynamical Astronomy*, 115:215–232, 2013. doi:10.1007/s10569-012-9458-3.

[13] Angelo Cervone, Francesco Topputo, Stefano Speretta, Alessandra Menicucci, Erdem Turan, Pierluigi Di Lizia, Mauro Massari, Vittorio Franzese, Carmine Giordano, et al. LUMIO: A CubeSat for observing and characterizing micrometeoroid impacts on the Lunar far side. *Acta Astronautica*, 195:309–317, 2022. doi:10.1016/j.actaastro.2022.03.032.

[14] Christian Circi and Paolo Teofilatto. On the dynamics of weak stability boundary lunar transfers. *Celestial Mechanics and Dynamical Astronomy*, 79:41–72, 2001. doi:10.1023/A:1011153610564.

[15] Christian Circi and Paolo Teofilatto. Weak stability boundary trajectories for the deployment of lunar spacecraft constellations. *Celestial Mechanics and Dynamical Astronomy*, 95:371–390, 2006. doi:10.1007/s10569-006-9020-2.

[16] Bruce A. Conway. *Spacecraft Trajectory Optimization*. Cambridge Aerospace Series. Cambridge University Press, 2010. doi:10.1017/CBO9780511778025.

[17] Diogene A. Dei Tos and Francesco Topputo. On the advantages of exploiting the hierarchical structure of astrodynamical models. *Acta Astronautica*, 136:236–247, 2017. doi:10.1016/j.actaastro.2017.02.025.

[18] Diogene A. Dei Tos and Francesco Topputo. Trajectory refinement of three-body orbits in the real solar system model. *Advances in Space Research*, 59(8):2117–2132, 2017. doi:10.1016/j.asr.2017.01.039.

[19] Diogene A. Dei Tos and Francesco Topputo. High-fidelity trajectory optimization with application to saddle-point transfers. *Journal of Guidance, Control, and Dynamics*, 42(6):1343–1352, 2019. doi:10.2514/1.G003838.

[20] Pooja Dutt. A review of low-energy transfers. *Astrophysics and Space Science*, 363 (12):253, 2018. doi:10.1007/s10509-018-3461-4.

[21] William Folkner, James Williams, Dale Boggs, Ryan Park, and Petr Kuchynka. The

planetary and lunar ephemerides de430 and de431. *Interplanetary Network Progress Report*, 196(1):42–196, 2014.

[22] Revaz V. Gamkrelidze. Discovery of the maximum principle. *Journal of Dynamical and Control Systems*, 5(4):437–451, 1999. doi:10.1023/A:1021783020548.

[23] Philip E. Gill, Walter Murray, and Margaret H. Wright. *Practical Optimization.* Society for Industrial and Applied Mathematics, Philadelphia, PA, 2019. doi:10.1137/1.9781611975604.

[24] Carmine Giordano. *Analysis, design, and optimization of robust trajectories for limited-capability small satellites.* PhD thesis, Politenico di Milano, 2021.

[25] Gerard Gómez, Jaume Llibre, R Martínez, and Carles Simó. *Dynamics and Mission Design Near Libration Points.* WORLD SCIENTIFIC, 2001. doi:10.1142/4402.

[26] Gerard Gómez, Josep Masdemont, and Josè M. Mondelo. Solar system models with a selected set of frequencies. *Astronomy & Astrophysics*, 390(2):733–749, 2002. doi:10.1051/0004-6361:20020625.

[27] Josè J. Guzmán, Laurie Mailhe, Conrad Schiff, et al. Primer vector optimization: survey of theory, new analysis and applications. In *53rd International Astronautical Congress: The World Space Congress-2002*, 2002.

[28] Ernst Hairer, Gerhard Wanner, and Syvert Nørsett. *Classical Mathematical Theory.* Springer Berlin Heidelberg, 1993. doi:10.1007/978-3-540-78862-1_1.

[29] Morris Handelsman. Optimal free-space fixed-thrust trajectories using impulsive trajectories as starting iteratives. *AIAA Journal*, 4(6):1077–1082, 1966. doi:10.2514/3.3607.

[30] Richard F. Hartl, Suresh P. Sethi, and Raymond G. Vickson. A survey of the maximum principles for optimal control problems with state constraints. *SIAM review*, 37(2):181–218, 1995. doi:10.1137/1037043.

[31] Sara Hatch, Min-kun Chung, Julie Kangas, Stacia Long, Ralph Roncoli, and Theodore Sweetser. Trans-lunar cruise trajectory design of GRAIL (Gravity Recovery and Interior Laboratory) mission. *AIAA/AAS Astrodynamics Specialist Conference*, page 8384, 2010. doi:10.2514/6.2010-8384.

[32] William Gary Heckathorn. *Optimal, Impulsive, Direct Ascent, Time-Fixed Orbital Interception.* PhD thesis, University of Illinois at Urbana-Champaign, 1985.

[33] Albert L. Herman and Bruce A. Conway. Optimal, low-thrust, Earth–Moon or-

bit transfer. *Journal of Guidance, Control, and Dynamics*, 21(1):141–147, 1998. doi:10.2514/2.4210.

[34] Magnus R. Hestenes. *Calculus of variations and optimal control theory*. Wiley, 1968.

[35] Lisa Ann Hiday. *Optimal transfers between libration-point orbits in the elliptic restricted three-body problem*. PhD thesis, Purdue University, 1992.

[36] Donald J. Jezewski. Primer vector theory and applications. In *NASA Technical Report*, 1975.

[37] Donald J. Jezewski and Harvey L. Rozendaal. An efficient method for calculating optimal free-space n-impulse trajectories. *AIAA journal*, 6(11):2160–2165, 1968. doi:10.2514/3.4949.

[38] Wang Sang Koon, Martin Lo, Jerrold Marsden, and Shane Ross. Low energy transfer to the Moon. *Celestial Mechanics and Dynamical Astronomy*, 81(1-2):63–73, 2001. doi:10.1023/A:1013359120468.

[39] Derek F. Lawden. *Optimal Trajectories for Space Navigation*. Butterworths mathematical texts. Butterworths, 1963.

[40] Paul Lion and Morris Handelsman. Primer vector on fixed-time impulsive trajectories. *Aiaa Journal*, 6(1):127–132, 1968. doi:10.2514/3.4452.

[41] James M. Longuski, José J mán, and John E. Prussing. *Optimal control with aerospace applications*. Space Technology Library. Springer New York, NY, 2014. doi:10.1007/978-1-4614-8945-0.

[42] Maud W. Makemson. Determination of selenographic positions. *The moon*, 2(3): 293–308, 1971. doi:10.1007/BF00561882.

[43] Belinda G. Marchand, Kathleen C. Howell, and Roby S. Wilson. Improved corrections process for constrained trajectory design in the n-body problem. *Journal of Spacecraft and Rockets*, 44(4):884–897, 2007. doi:10.2514/1.27205.

[44] Brian P. McCarthy and Kathleen C. Howell. Four-body cislunar quasi-periodic orbits and their application to ballistic lunar transfer design. *Advances in Space Research*, 71(1):556–584, 2023. doi:10.1016/j.asr.2022.09.020.

[45] Giorgio Mingotti, Francesco Topputo, and Franco Bernelli Zazzera. Efficient invariant-manifold, low-thrust planar trajectories to the Moon. *Communications in Nonlinear Science and Numerical Simulation*, 17(2):817–831, 2012. doi:10.1016/j.cnsns.2011.06.033.

[46] Kenta Oshima, Francesco Topputo, and Tomohiro Yanao. Low-energy transfers to the moon with long transfer time. *Celestial Mechanics and Dynamical Astronomy*, 131(1):4, 2019. doi:10.1007/s10569-019-9883-7.

[47] Jeffrey S. Parker and Rodney L. Anderson. Targeting low-energy transfers to low lunar orbit. *Acta Astronautica*, 84:1–14, 2013. doi:10.1016/j.actaastro.2012.10.033.

[48] Jeffrey S. Parker and Rodney L. Anderson. *Low-energy lunar trajectory design*, volume 12. John Wiley & Sons, 2014. ISBN 978-1-118-85531-7.

[49] Jeffrey S. Parker, Rodney L. Anderson, and Andrew Peterson. Surveying ballistic transfers to low lunar orbit. *Journal of Guidance, Control, and Dynamics*, 36(5): 1501–1511, 2013. doi:10.2514/1.55661.

[50] Lei Peng, Yuanzhen Wang, Guangming Dai, Yamin Chang, and Fangjie Chen. Optimization of the Earth-Moon low energy transfer with differential evolution based on uniform design. In *IEEE Congress on Evolutionary Computation*, pages 1–8. IEEE, 2010. doi:10.1109/CEC.2010.5586384.

[51] Henry Pernicka et al. A search for low Delta-V Earth-to-Moon trajectories. *Astrodynamics Conference, 1994*, pages 530–537, 1994. doi:10.2514/6.1994-3772.

[52] Ettore Perozzi and Alessio Di Salvo. Novel spaceways for reaching the Moon: an assessment for exploration. *Celestial Mechanics and Dynamical Astronomy*, 102: 207–218, 2008. doi:10.1007/s10569-008-9156-3.

[53] Donald A. Pierre. *Optimization theory with applications*. Courier Corporation, 1986.

[54] Lev Semenovich Pontryagin. *Mathematical theory of optimal processes*. CRC press, 1987.

[55] Yi Qi and Shijie Xu. Optimal Earth–Moon transfers using lunar gravity assist in the restricted four-body problem. *Acta Astronautica*, 134:106–120, 2017. doi:10.1016/j.actaastro.2017.02.002.

[56] Rodica Roman and Iharka Szucs-Csillik. Generalization of levi-civita regularization in the restricted three-body problem. *Astrophysics and Space Science*, 349(1):117–123, 2014. doi:10.1007/s10509-013-1628-6.

[57] Ralph Roncoli and Kenneth Fujii. Mission design overview for the Gravity Recovery and Interior Laboratory (GRAIL) mission. In *AIAA/AAS Astrodynamics Specialist Conference*, page 8383, 2010. doi:10.2514/6.2010-8383.

[58] Lawrence F. Shampine and Mark W. Reichelt. The matlab ode suite. *SIAM journal on scientific computing*, 18(1):1–22, 1997. doi:10.1137/S1064827594276424.

[59] Carles Simó, Gerard Gómez, Àngel Jorba, and Josep Masdemont. The bicircular model near the triangular libration points of the rtbp. *From Newton to Chaos: modern techniques for understanding and coping with chaos in n-body dynamical systems*, pages 343–370, 1995. doi:10.1007/978-1-4899-1085-1_34.

[60] Theodore H. Sweetser. An estimate of the global minimum DV needed for Earth–Moon transfer. *AAS Paper 91-101*, 1991.

[61] Victor Szebehely. Theory of orbits, the restricted problem of three bodies, acad. *Press, New York*, page 8, 1967. doi:10.1016/B978-0-12-395732-0.X5001-6.

[62] Francesco Topputo. On optimal two-impulse Earth–Moon transfers in a four-body model. *Celestial Mechanics and Dynamical Astronomy*, 117(3):279–313, 2013. doi:10.1007/s10569-013-9513-8.

[63] Francesco Topputo, Diogene Alessandro Dei Tos, Karthik Venkatesh Mani, Simone Ceccherini, Carmine Giordano, Vittorio Franzese, and Yang Wang. Trajectory design in high-fidelity models. In *7th International Conference on Astrodynamics Tools and Techniques (ICATT)*, pages 1–9, 2018.

[64] Bradley J. Wall and Bruce A. Conway. Shape-based approach to low-thrust rendezvous trajectory design. *Journal of Guidance, Control, and Dynamics*, 32(1):95–101, 2009. doi:10.2514/1.36848.

[65] Ryan Whitley and Cesar Ocampo. Direct multiple shooting optimization with variable problem parameters. In *47th AIAA Aerospace Sciences Meeting Including the New Horizons Forum and Aerospace Exposition*, page 803, 2009. doi:10.2514/6.2009-803.

[66] Kazuyuki Yagasaki. Computation of low energy Earth-to-Moon transfers with moderate flight time. *Physica D: Nonlinear Phenomena*, 197(3-4):313–331, 2004. doi:10.1016/j.physd.2004.07.005.

[67] Kazuyuki Yagasaki. Sun-perturbed Earth-to-Moon transfers with low energy and moderate flight time. *Celestial Mechanics and Dynamical Astronomy*, 90:197–212, 2004. doi:10.1007/s10569-004-0406-8.

[68] Hiroshi Yamakawa, Jun'ichiro Kawaguchi, Nobuaki Ishii, and Hiroki Matsuo. Numerical study of gravitational capture orbit in the Earth–Moon system. *Advances in the Astronautical Sciences*, 79:1113 – 1132, 1992.

A | Appendix

This appendix collects the analytical expressions of some important derivatives used in the thesis, as well as the proof of a result used in Chapter 3.

A.1. Four-Body Pseudopotential Derivatives

Hereafter, the analytical expression of the partial derivatives of the pseudo-potential Ω of the PBRFBP, defined in Eq. (2.8), are reported.

The first-order partial derivatives of Ω appearing at the right-hand side of the equation of motions (see Eq. (2.7)) are:

$$\frac{\partial \Omega}{\partial x} = x - \frac{1-\mu}{{d_1}^3}(x+\mu) - \frac{\mu}{{d_2}^3}(x+\mu-1) - \frac{m_S}{{d_3}^3}(x-\rho\cos(\omega_S t)) - \frac{m_S}{\rho^2}\cos(\omega_S t) \tag{A.1}$$

$$\frac{\partial \Omega}{\partial y} = y - \frac{1-\mu}{{d_1}^3}y - \frac{\mu}{{d_2}^3}y - \frac{m_S}{{d_3}^3}(y-\rho\sin(\omega_S t)) - \frac{m_S}{\rho^2}\sin(\omega_S t). \tag{A.2}$$

Together with them, also the second-order partial derivatives of Ω, useful for the computation of the state transition matrix, are reported:

$$\begin{aligned}\frac{\partial^2 \Omega}{\partial x^2} = {} & 1 + \frac{1-\mu}{{d_1}^3} - \frac{\mu}{{d_2}^3} + \frac{3\mu}{2{d_2}^5}(x+\mu-1)^2 + \frac{3}{2{d_1}^5}(1-\mu)(x+\mu)^2 \\ & - \frac{m_S}{{d_3}^3} + \frac{3m_S}{{d_3}^5}(x-\rho\cos(\omega_S t))^2\end{aligned} \tag{A.3}$$

$$\frac{\partial^2 \Omega}{\partial y^2} = 1 - \frac{1-\mu}{{d_1}^3} - \frac{\mu}{{d_2}^3} + \frac{3\mu y^2}{2{d_2}^5} + \frac{3y^2}{2{d_1}^5}(1-\mu) - \frac{m_S}{{d_3}^3} + \frac{3m_S}{{d_3}^5}(y-\rho\sin(\omega_S t))^2 \tag{A.4}$$

$$\begin{aligned}\frac{\partial^2 \Omega}{\partial x\,\partial y} = {} & \frac{\partial^2 \Omega}{\partial y\,\partial x} = \frac{3y}{{d_1}^5}(1-\mu)(x+\mu) + \frac{3\mu y}{{d_2}^5}(x+\mu-1) \\ & + \frac{3m_S}{{d_3}^5}(x-\rho\cos(\omega_S t))(y-\rho\sin(\omega_S t)).\end{aligned} \tag{A.5}$$

A.2. First-Order Magnitude Difference

This section aims to demonstrate that the first-order difference between the magnitudes of an arbitrary vector on a perturbed and reference path is

$$\mathrm{dx} = \pm \frac{\overline{\mathbf{x}}^\top \delta \overline{\mathbf{x}}}{\|\overline{\mathbf{x}}\|} \ . \tag{A.6}$$

Proof. Let the scalar quantity dx represent this difference:

$$\mathrm{dx} = \|\mathbf{x}\| - \|\overline{\mathbf{x}}\| \ , \tag{A.7}$$

where $\mathbf{x}$ and $\overline{\mathbf{x}}$ are the quantities evaluated on the perturbed and reference trajectories, respectively. Assuming small perturbations, the difference between the two is indicated by $\delta\mathbf{x} = \mathbf{x} \pm \overline{\mathbf{x}}$. Hence,

$$\begin{aligned}
\mathrm{dx} &= \|\overline{\mathbf{x}} \pm \delta\mathbf{x}\| - \|\overline{\mathbf{x}}\| && \text{(A.8)}\\
&= \left[(\overline{\mathbf{x}} \pm \delta\mathbf{x})^\top (\overline{\mathbf{x}} \pm \delta\mathbf{x})\right]^{\frac{1}{2}} - \left[\overline{\mathbf{x}}^\top \overline{\mathbf{x}}\right]^{\frac{1}{2}} && \text{(A.9)}\\
&= \left[\overline{\mathbf{x}}^\top \overline{\mathbf{x}}\right]^{\frac{1}{2}} \left\{ \left[\frac{(\overline{\mathbf{x}} \pm \delta\mathbf{x})^\top (\overline{\mathbf{x}} \pm \delta\mathbf{x})}{\overline{\mathbf{x}}^\top \overline{\mathbf{x}}} \right]^{\frac{1}{2}} - 1 \right\} && \text{(A.10)}\\
&= \|\overline{\mathbf{x}}\| \left\{ \left[\frac{\overline{\mathbf{x}}^\top \overline{\mathbf{x}}}{\|\overline{\mathbf{x}}\|^2} \pm 2\frac{\delta\overline{\mathbf{x}}^\top \overline{\mathbf{x}}}{\|\overline{\mathbf{x}}\|^2} + \frac{\delta\overline{\mathbf{x}}^\top \delta\overline{\mathbf{x}}}{\|\overline{\mathbf{x}}\|^2} \right]^{\frac{1}{2}} - 1 \right\} \ . && \text{(A.11)}
\end{aligned}$$

Neglecting second and higher-order terms in the small perturbation quantity $\delta\mathbf{x}$,

$$\mathrm{dx} = \|\overline{\mathbf{x}}\| \left\{ \left[1 \pm 2\frac{\delta\overline{\mathbf{x}}^\top \overline{\mathbf{x}}}{\|\overline{\mathbf{x}}\|^2} + \ldots \right]^{\frac{1}{2}} - 1 \right\} \ . \tag{A.12}$$

Utilizing a binomial expansion to simplify,

$$\mathrm{dx} = \|\overline{\mathbf{x}}\| \left\{ 1 \pm \frac{1}{2} \frac{2\delta\overline{\mathbf{x}}^\top \overline{\mathbf{x}}}{\|\overline{\mathbf{x}}\|^2} + \ldots - 1 \right\} \ . \tag{A.13}$$

Finally, truncating dx in order to retain only first-order terms, yields the final result

$$\mathrm{dx} \approx \pm \frac{\overline{\mathbf{x}}^\top \delta\overline{\mathbf{x}}}{\|\overline{\mathbf{x}}\|} \ . \tag{A.14}$$

□

A.3. Parameters of the Rotopulsating Frame

Hereafter, the analytical expressions for the first and second time derivatives of Eqs. (5.6), (5.8) and (5.9) used to describe the RPF are reported. Recall, that the state of each celestial body $\mathbf{R}_i$, $\mathbf{V}_i$ are discrete numerical values and are taken from ephemerides at a specific epoch ε. Nonetheless, for brevity, the dependence upon the epoch is omitted, and it is also useful to define the relative states between the two primaries as

$$\mathbf{R}_{21} = \mathbf{R}_2 - \mathbf{R}_1 \ , \tag{A.15a}$$

$$\mathbf{V}_{21} = \mathbf{V}_2 - \mathbf{V}_1 \ , \tag{A.15b}$$

$$\mathbf{A}_{21} = \mathbf{A}_2 - \mathbf{A}_1 \ , \tag{A.15c}$$

$$\mathbf{J}_{21} = \mathbf{J}_2 - \mathbf{J}_1 \ , \tag{A.15d}$$

where the quantities $\mathbf{A}_i$ and $\mathbf{J}_i$ are the acceleration and the jerk (i.e., the third time derivative of the position $\mathbf{R}_i$) of the i-th celestial bodies in the ICRF. These last can be computed from the universal gravitational law:

$$\mathbf{A}_i = \sum_{j \in S,\, j \neq i} \mu_j \frac{\mathbf{R}_j - \mathbf{R}_i}{\|\mathbf{R}_j - \mathbf{R}_i\|^3} \ , \tag{A.16a}$$

$$\mathbf{J}_i = \sum_{j \in S,\, j \neq i} \mu_j \left(\frac{\mathbf{V}_j - \mathbf{V}_i}{\|\mathbf{R}_j - \mathbf{R}_i\|^3} - \frac{(\mathbf{R}_j - \mathbf{R}_i)^\top (\mathbf{V}_j - \mathbf{V}_i)}{\|\mathbf{R}_j - \mathbf{R}_i\|^5} (\mathbf{R}_j - \mathbf{R}_i) \right) \ . \tag{A.16b}$$

The derivatives of the relative Earth–Moon distance $\mathbf{b}$ are:

$$\dot{\mathbf{b}} = \frac{m_1 \mathbf{V}_1 + m_2 \mathbf{V}_2}{m_1 + m_2} \ , \tag{A.17a}$$

$$\ddot{\mathbf{b}} = \frac{m_1 \mathbf{A}_1 + m_2 \mathbf{A}_2}{m_1 + m_2} \ . \tag{A.17b}$$

The derivatives of the adimensionalization factor k are:

$$\dot{k} = \frac{\mathbf{R}_{21}^\top \mathbf{V}_{21}}{k} \ , \tag{A.18a}$$

$$\ddot{k} = \frac{k(\mathbf{V}_{21}^\top \mathbf{V}_{21} + \mathbf{R}_{21}^\top \mathbf{A}_{21}) - \dot{k} \mathbf{R}_{21}^\top \mathbf{V}_{21}}{k^2} \ . \tag{A.18b}$$

Let define the relative angular momentum $\mathbf{h}_{21}$ as

$$\mathbf{h}_{21} = \mathbf{R}_{21} \times \mathbf{V}_{21} \ . \tag{A.19}$$

The derivatives of its modulus $h_{21} \equiv \|\mathbf{h}_{21}\|$ are

$$\dot{h}_{21} = \frac{(\mathbf{R}_{21} \times \mathbf{V}_{21})^\top (\mathbf{R}_{21} \times \mathbf{A}_{21})}{h_{12}} \ , \tag{A.20a}$$

$$\ddot{h}_{21} = \frac{h_{21}\left[(\mathbf{R}_{21} \times \mathbf{A}_{21})^2 + (\mathbf{R}_{21} \times \mathbf{V}_{21})^\top (\mathbf{V}_{21} \times \mathbf{A}_{21} + \mathbf{R}_{21} \times \mathbf{J}_{21})\right]}{h_{12}^2} - \frac{\dot{h}_{21}(\mathbf{R}_{21} \times \mathbf{V}_{21})^\top (\mathbf{R}_{21} \times \mathbf{A}_{21})}{h_{12}^2} \ . \tag{A.20b}$$

The first derivatives of the rotation matrix C are:

$$\dot{\mathbf{e}}_1 = \frac{k\mathbf{V}_{21} - \dot{k}\dot{\mathbf{R}}_{21}}{k^2} \ , \tag{A.21a}$$

$$\dot{\mathbf{e}}_2 = \dot{\mathbf{e}}_3 \times \mathbf{e}_1 + \mathbf{e}_3 \times \dot{\mathbf{e}}_1 \ , \tag{A.21b}$$

$$\dot{\mathbf{e}}_3 = \frac{h_{21}(\mathbf{R}_{21} \times \mathbf{A}_{21}) - \dot{h}_{21}(\mathbf{R}_{21} \times \mathbf{V}_{21})}{h_{21}^2} \ . \tag{A.21c}$$

The second derivatives of the rotation matrix C are:

$$\ddot{\mathbf{e}}_1 = \frac{(2\dot{k}^2 - k\ddot{k})\mathbf{R}_{21} - 2k\dot{k}\mathbf{V}_{21} + k^2\mathbf{A}_{21}}{k^3} \ , \tag{A.22a}$$

$$\ddot{\mathbf{e}}_2 = \ddot{\mathbf{e}}_3 \times \mathbf{e}_1 + 2(\dot{\mathbf{e}}_3 \times \dot{\mathbf{e}}_1) + \mathbf{e}_3 \times \ddot{\mathbf{e}}_1 \ , \tag{A.22b}$$

$$\ddot{\mathbf{e}}_3 = \frac{(2\dot{h}_{21}^2 - h_{21}\ddot{h}_{21})\mathbf{R}_{21} \times \mathbf{V}_{21} - 2h_{21}\dot{h}_{21}\mathbf{R}_{21} \times \mathbf{A}_{21}}{h_{21}^3} + \frac{h_{21}^2(\mathbf{R}_{21} \times \mathbf{J}_{21} + \mathbf{V}_{21} \times \mathbf{A}_{21})}{h_{21}^3} \ . \tag{A.22c}$$